DISSERTATION

NOVEL THERAPEUTICS, ASSOCIATED ADVERSE EFFECTS, AND CHANGES IN IMMUNE RESPONSES DURING PULMONARY INFECTION WITH *MYCOBACTERIUM TUBERCULOSIS*

Submitted by

Malik Zohaib Ali

Graduate Degree Program in Cell and Molecular Biology

In the partial fulfillment of the requirements

For the Degree of Doctor of Philosophy

Colorado State University

Fort Collins, Colorado

Spring 2024

Doctoral Committee:

Advisor: Mercedes Gonzalez-Juarrero

Randall J. Basaraba
Julie A. Moreno
Chaoping Chen

ABSTRACT

NOVEL THERAPEUTICS, ASSOCIATED ADVERSE EFFECTS, AND CHANGES IN IMMUNE RESPONSES DURING PULMONARY INFECTION WITH *MYCOBACTERIUM TUBERCULOSIS*

Patients diagnosed with multidrug resistant (MDR) or extensively drug resistant (XDR) tuberculosis (TB) have limited treatment options. The Nix-TB clinical trial evaluated a new 6-month regimen containing three-oral-drugs; bedaquiline (B), pretomanid (Pa) and linezolid (L) collectively termed as BPaL for the treatment of TB. This regimen achieved remarkable results as almost 90% of the participants suffering from MDR- or XDR-TB had favorable outcomes. Despite the extraordinary outcomes, many patients also developed severe adverse effects (AEs) which were associated with the long-term administration of the oxazolidinone protein synthesis inhibitor linezolid. Spectinamide 1599 (S) is also a potent protein synthesis inhibitor of *Mycobacterium tuberculosis* (Mtb) with an excellent safety profile, but which lacks oral bioavailability. In chapter 2, we hypothesized that inhaled spectinamide 1599, combined with BPa — BPaS regimen —, has similar efficacy to that of BPaL regimen while simultaneously avoiding the L-associated AEs. The BPaL and BPaS regimens were compared in the BALB/c (permissive resistant) and C3HeB/FeJ (permissive susceptible) murine chronic TB efficacy models. Both regimens promoted similar bactericidal effects in lung and spleen of both models after 4 weeks. However, treatment with BPaL resulted in significant weight loss and the complete blood count suggested development of anemia.

These effects were not similarly observed in mice treated with BPaS. BPaL treatment also decreased myeloid to erythroid ratio and increased concentration of proinflammatory cytokines in bone marrow compared to mice receiving BPaS regimen. During therapy both regimens improved the lung lesion burden, reduced neutrophil and cytotoxic T cell counts while increased the number of B and helper and regulatory T cells. This combined data suggests that inhaled spectinamide 1599 combined with BPa is an effective TB therapy that avoids L-associated AEs.

The granuloma formation is the pathological hallmark of TB, and several studies suggest that there are temporal and spatial changes in their distinct immune responses. These changes differ not only from one granuloma to another in a single individual but also depend on the severity of the disease. In chapter 3, we attempted to understand longitudinal changes in immune cells, their relationships, and their spatial distribution in granulomas of Mtb infected BALB/c and C3HeB/FeJ mouse models using a novel technique of multispectral imaging microscopy. Multiplex fluorescence immunohistochemistry (mfIHC) is unique in its ability to provide both expression and location of several immune cells along with their co-localization in a single tissue section while preserving tissue architecture and spatial context. The results showed that as the infection progresses, there are also dynamic changes in the immune phenotypes forming the granulomas and those located within the parenchymal tissue. Moreover, the histologically similar granulomas manifested complexity in their immune cell composition mainly due to the presence of adaptive immune responses. The advanced cellular granulomas in BALB/c TB model were mainly predominated by CD4 and CD8 T cells, Ly6G stained neutrophils, B220 B cells and all these were surrounded by F4/80

macrophages. With time post infection, there was an increased uniform recruitment of CD4 and Foxp3 T cells, F4/80 macrophages and Ly6G neutrophils within granulomas compared to parenchymal tissue where IFNγ and IL-10 secreting cells were in abundance. Moreover, B220 B cells and CD8 T cells also showed increased but heterogeneous distribution among the advancing granulomas especially B220 B cells formed clusters. The spatial analysis showed an increased median distance for Ly6G neutrophils, whereas this distance was decreased for B220 B cells when measured from CD4 and CD8 cells. In summary, combining the spatial and temporal data in addition to the mere cell counts helps to uncover interactions and relationships between different immune cells within the granuloma.

ACKNOWLEDGMENTS

First, I would like to thank my advisor Dr. Mercedes Gonzalez-Juarrero for providing me with an opportunity to work in her laboratory and for her consistent support and guidance during this program. Members of the Gonzalez-Juarrero laboratory were actively involved in achieving this milestone and I would like to especially thank Amanda Walz, Camron Pearce, Ha Lam, Jamie Philp, and John Paterson for their assistance along with so many others. Special thanks to Dr. Amy MacNeil for her support in the blood and bone marrow work and to Dr. Kimberly Jordan and her team (UC Denver) for helping in staining for multiplex fluorescence immunohistochemistry. Further, I am also obliged to the members of the Henao laboratory, especially Dr. Taru Dutt, for her persistent help. I would also like to thank to the members of my advisory committee, Drs. Randall J. Basaraba, Julie A. Moreno and Chaoping Chen for their valuable input and assistance throughout the program. Additionally, I would like to extend my gratitude to Dr. Howard Liber (R), the former director of Cell and Molecular Biology (CMB) - Graduate Program, for accepting me in the program and especially Dr. Carol Wilusz, the current director of CMB for her continuous support along the way. It is also pertinent to mention the emotional support offered by my parents, siblings, in-laws, and members of the Fort Collins community throughout this program. Lastly, I would like to acknowledge the US Fulbright Program and Colorado State University for providing me with the opportunity to pursue my graduate degree program.

DEDICATION

I dedicate this dissertation to my dear wife, for all her love and assistance, especially during this degree program and to my lovely daughter and boys.

TABLE OF CONTENTS

CHAPTER 1

Literature Review

Epidemiology of Tuberculosis

Tuberculosis (TB) is one of the oldest known infectious diseases (1) but still today it is the 13th leading cause of death in the world while 2nd due to a single infectious agent after the COVID-19 pandemic (2). Approximately, one quarter of the world's population is infected with *Mycobacterium tuberculosis* (Mtb; the causative agent of TB) but in most people the infection remains in a latent state and does not develop disease. In 2021, 10.6 million new cases of TB along with 1.4 million deaths were reported. Out of the new TB cases, 86% occurred within the 30 highest TB burden countries. India, China, Indonesia, the Philippines, Pakistan, Nigeria, Bangladesh, and South Africa are among the eight countries that accounted for more than two thirds of new TB cases (3).

People of all ages are at risk of developing TB; however, this disease affects mainly the healthiest and most productive segment of the population (adults aged 15-49 years) (3,4). Its epidemiological control is further complicated by the fact that over 95% of TB cases and deaths occur in developing countries with high disproportion of socioeconomic indicators. There are many factors that exacerbate this disease including conditions that affect the immune system, under or malnutrition (5) and use of alcohol and smoking among others. Risk of TB disease increases 3.3 and 1.6 times in people smoking tobacco and drinking alcohol respectively (3). Coinfection of Mtb with human immunodeficiency virus (HIV) increases by 16 (uncertainty interval: 14-18) times the risk of developing active TB (6). Out of the 1.4 million deaths reported in 2021,

nearly 187,000 people were HIV-associated TB cases. The global incidence of this co-infection has increased from 70% (2019) to 73% (2020) and the highest HIV-associated TB incidence (85%) is currently found in the World Health Organization (WHO) African Region. Among the 10 million new cases of TB, 1.9 million are associated within the undernourished population and unfortunately, within this population there are 3 times (relative uncertainty interval 3.1 – 3.3) higher risk of developing active TB disease.

During the last decade, the global incidence of TB has decreased steadily at about 2% per year, yet this decline only achieves half of the expectations of the WHO End TB Strategy for 2035 (2,7). The End TB Strategy is a WHO program for control of TB worldwide. Using as benchmark data from 2015, the End TB strategy aims by 2035 to have reduced mortality and morbidity by 95% and 90% respectively, along with zero TB-affected families facing catastrophic costs due to TB. Apart from HIV infections, drug resistance to TB is also a contributing factor affecting control of this disease (8). Long treatment duration, poor drug quality, inadequate chemotherapy, history of TB treatment, and lack of patient compliance with the treatment accounted for the development of drug resistance to Mtb (9). Drug resistance develops when a patient is not responding to rifampicin (rifampicin resistant or RR-TB), both isoniazid and rifampicin (multidrug-resistant or MDR-TB), or resistant to isoniazid and rifampicin, plus any fluoroquinolone and at least one of the three injectables second-line drugs i.e., amikacin, kanamycin, or capreomycin (extensively drug-resistant or XDR-TB).

Currently, drug resistance TB is a major global public health crisis and a health security threat that drives the ongoing TB epidemic and contributes to higher morbidity and mortality. Out of 10 million new cases of TB in 2021, 450,000 are attributed to

MDR- or XDR-TB (2). The treatment of MDR- and XDR-TB is complex, challenging, and expensive and in the best-case scenario, it can take between 18 months to more than 2 years. From 2019 to 2020, the global burden of drug resistant TB declined by 22%, but due to the COVID-19 pandemic, the enrolment for treatment of MDR/RR-TB patients dropped by nearly 15% (from 177,100 to 150,359) meaning that only about 1 of 3 MDR/RR-TB patients are getting treatment. This scenario makes TB disease more complicated to control (10).

The incidence of newly reported TB cases in the United States has fallen steadily since 1993 to its lowest level ever; in 2020, the incidence was reported as 2.2/100,000 population (a total of 7,163 TB cases) (11). This steady decline in the number of cases, 2-3% annual decrease since 2010 – a stunning public health accomplishment- can be attributed to a multitude of factors that encompass not only advances in medical science, especially in infectious diseases research, but also in social and economic policies. Improvement in living standards such as increased public sanitation, disinfection of community drinking water, pasteurization of milk, decline in poverty, malnutrition, homelessness, and overcrowding collectively created a healthier environment leading to lower the prevalence of TB even before the advent of Golden Era of TB drug discovery. The advancement in medicine which includes access to the leading health care, extensive TB screening via skin testing and the implementation of effective multidrug chemotherapy further assisted to reduce the burden of this disease. However, after declining for nearly three decades, the number of TB cases has risen in the United States since 2020 due to the COVID-19 pandemic as happened worldwide.

A Concise History of Tuberculosis

The origins of human tuberculosis (TB) are not yet completely understood, still it is believed that TB is one of the oldest known infectious diseases of humankind. It is hypothesized that the early progenitor of Mtb might have infected early hominids in East Africa about three million years ago (12–14). Based on the molecular analysis, it is suggested that the first infection of Mtb to humans occurred about 70,000 years ago during the migration of hunter-gatherers to the European subcontinent (15). Although, the first written documents on TB were found in India and China dating back to 3,300 B.C., and 2,300 B.C. respectively, more recent paleopathological studies in skeletal remains in Heidelberg, Germany, found mycobacteria dating back to as early as 5,000 B.C. Additional evidence was found in Egyptian mummies from 3,700 B.C. showing skeletal deformities typical of TB (also referred to as Pott's disease), and in Europe from 2,500 – 1,500 B.C. (12,13,16,17).

Until European colonization, it was believed that the Americas were free from TB and that TB spread with the arrival of Europeans, however Garcia-Frias in 1940 reported that the disease was already present there. Histo-morphological, biochemical, and molecular biology studies revealed acid-fast positive bacilli and Mtb DNA in mummies (2,000 B.C. to A.D. 1,500) from Peru and skeletal remains dated to 150 B.C. from native Americans living in West Central Illinois and in Ohio (18,19).

Tuberculosis has been a sporadic disease and played a minor role in human infectious diseases until approximately 10,000 years ago when it became endemic. Low population densities in the form of small isolated communal bands of hunter-gathers limited person-to-person interaction could not support the widespread dissemination

and high infection rates observed in the new world TB pandemic. Being a persistent pathogen, Mtb survived throughout human existence until the conditions became favorable for its pandemic spread. With the advent of large agrarian societies, cities, and ultimately, close contact between people led this “crowd” pathogen to spread, reaching its epidemic apex during the 18th and 19th centuries. Further, malnutrition, unsanitary, and poor socioeconomic settings during the industrialization era fueled TB epidemic and optimized the rapid transmission of an aerosolized pathogen in the form of an active infectious disease pathogen (15,20,21).

After isolation of the tubercle bacilli by Robert Koch and later on with the discovery of BCG (Bacillus Calmette-Guérin) vaccine, followed by the antibiotic (anti-tuberculosis drugs) era, there has been a progressive decline in high-burden of this disease (12). Though the global trend in the estimated TB incidence rate between 2000 and 2019 has dropped steadily, TB is still a major worldwide public health problem. To eradicate this disease by the year 2035, as per the commitment of WHO for End TB Strategy, it is imperative that we improve drug treatment and vaccine therapeutics, diagnostics, and prevention strategies (2,10).

***Mycobacterium tuberculosis*: The causative agent of Tuberculosis**

Tuberculosis is caused by a bacterium that belongs to the Family Mycobacteriaceae and the genus Mycobacterium. While most mycobacteria are nonpathogenic, more than 20 mycobacterial species cause disease in humans. *Mycobacterium tuberculosis* (Mtb), among them, is the most potential causative agent of TB. It is a member of the Mtb complex, a cluster of closely related Mycobacterium species. These species are the primary cause of TB in humans and animals (22–24).

Their close relationship has been demonstrated using the latest techniques of gene sequencing, mass spectrometry and PCR (25–28).

The Mtb is a facultative intracellular pathogen that primarily infects macrophages and dendritic cells (29). It is a non-spore forming, nonmotile, obligate aerobic, and straight or slightly curved rod-shaped bacillus of “0.2–0.6 μm by 1.0–10.0” μm. It is a slow growing organism with a generation time of 12-24 hours under optimal conditions (24,29,30). This organism possesses an extremely complex cell envelope made of 60% of lipids, primarily of long chain mycolic acids. The high lipid content of the cell envelope of Mtb prevents penetration of dyes and accordingly defines its classification as gram positive or negative bacterium. Furthermore, this thick layer of lipids also hinders penetration of antimicrobials as well as effective interaction with the host immune system, therefore, the thick wall of Mtb plays an important role in pathogenesis. Moreover, within the host cell, Mtb can shut down its metabolic and replicative states and is capable of surviving under harsh conditions of extreme pH and anaerobic conditions; all together allowing this bacillus to remain dormant and to survive intracellularly for decades. More importantly, when inside the host macrophages and surviving in a dormant state for decades, this bacillus retains its capacity to resume growth. At this stage, the host may become infectious and develop clinical symptoms; also referred as active TB disease (21,31–33). Altogether, this bacillus is an extraordinarily difficult pathogen to protect against and it has survived successfully for thousands of years among the human population.

Tuberculosis transmission and its Pathophysiology

Tuberculosis in humans is caused by *Mycobacterium tuberculosis* (Mtb) which mainly affects the lungs (pulmonary TB), however, under certain circumstances Mtb can disseminate to and infect other body organs (extra pulmonary TB). Although one third of the world population is infected with Mtb, the majority (90%) do not show clinical symptoms and are non-infectious. In the clinics, this stage of infection is referred to as latent TB (LTB). It is estimated that only 10% of the LTB population is at risk of developing active TB (ATB) disease. The LTB population progresses to ATB when it becomes immunocompromised, old aged, suffer from stress, when infected with HIV, or in response to immunosuppressive drug treatment (10).

The pathogenesis of TB is a complicated process that involves a complex interaction between the host immune system and bacterial virulence factors. A healthy individual can be infected by uptaking Mtb via inhalation, ingestion, damaged skin, or mucous membranes (34) but inhalation is generally the most common route of infection (29,35). Primary infection occurs when a patient with ATB coughs and creates aerosols of aqueous droplets containing virulent bacilli that in turn are inhaled by a nearby healthy individual. Usually, the aerosolized aqueous droplets are between 1-5 µm in diameter and contain one or few infectious bacilli (36). Perhaps, only a single bacillus is capable of transmitting infection in susceptible individuals, but repeated exposure is most often required to develop infection in less susceptible individuals. The confirmation of infection in an individual is associated with detectable cell-mediated immunity. Upon inhalation, this organism can reach deep in the terminal lung airways, alveoli, bypassing the innate lung physiological barriers, where it can persist in the extracellular matrix and

inside the cells. In the highly aerated environment of the lungs, the first immune cells to encounter this organism are the alveolar macrophages (AM). These cells have the capacity to phagocytose Mtb and to form a phagosome (37). In most instances, the phagosome fuses with a lysosome to produce a phagolysosome. The latter provides the infected cells with an armamentarium of hydrolytic enzymes capable of killing bacterial pathogens by interfering with their metabolic pathways. As discussed above, however, Mtb has evolved special mechanisms to hijack the macrophage defense systems and among those, in many instances this bacillus can avoid phagosome-lysosome fusion and it can create its own primary cellular niche within macrophages. Within the phagosome, the bacillus can survive intracellularly for long periods of time; a state that clinically is referred to as LTB infection (34,38,39). In the initial stage of TB development, Mtb-laden macrophages and dendritic cells may be transported across the alveolar barrier through lymphatics and vasculatures to almost any organ of the body and infect them (extrapulmonary TB).

Failure to contain bacterial replication by the immune system facilitates the escape of Mtb into the extracellular milieu. In this environment the bacillus can actively replicate and can secrete proteins and lipids that interact with host's cells (23,40). These host-bacterial interactions activate recruitment to the site of infection of immune cells which organize to form a wall that surround the infected cells and develop into a lesion called tuberculous granuloma. The granuloma is the hallmark pathological structure of TB (41). Especially in advance disease states, the histopathological examination of human lungs manifests a dynamic and diverse spectrum of TB lesions (12,14,37,44) ranging from non-capsulated, pulmonary cellular granulomas containing

immune cell aggregates to the highly organized necrotic encapsulated granulomas with caseous material with or without a cavity (45,46). Even within a single individual, infection can result in histomorphologically distinct granulomas where each progresses independently of others based on their immune microenvironments (IME) (44). A study by Kaplan et al. revealed heterogeneous morphology, cell composition and distribution of acid-fast bacilli (AFB) in human patients (47). Histologically the structure of a granuloma consists mainly of macrophages, polymorphonuclear neutrophils (PMNs), highly differentiated cells such as multinucleated giant cells, epithelioid cells and foamy cells, all these cells being interspaced or surrounded by a rim of lymphocytes (48). The granulomatous necrotic area is mostly acellular which may contain caseum and be surrounded by a fibrotic tissue layer. AFB can be observed in foamy macrophages and in large quantities at the luminal surface of a cavity (47).

Despite decades of research, the role of the granuloma is not clear (49) and traditionally, it is thought to be host-protective in nature by limiting the infection into a confined area (50) but studies from animal models revealed that it can provide a niche in which Mtb can proliferate. This dual but opposite role of the granuloma suggest there are distinctly diverse IME for each granuloma (51). As infection progresses in time, the granuloma increases in size, and varies in cellular composition.

Animal Models of Tuberculosis

Since the identification of Mtb as a presumable causative agent of TB and to demonstrate his famous postulates, Robert Koch chose the mouse, guinea pig and others species as “animal models” (102–104). The Koch’s postulates established that an infectious agent must 1) be present in every case of a disease, 2) but absent when

there is no disease, 3) be isolated and grow in a pure culture and, 4) be able to cause disease upon reinoculation in an experimental animal model (102,105). Nowadays, the extreme urgency for development of new drug therapies and vaccines justifies the use of animal models because *in vitro* models cannot recapitulate the complex immune and physiological phenomena occurring *in vivo*. Yet no animal model is capable of recapitulating the entire pathological aspects of human TB (103,106,107). A lot of determinants are involved in choosing the most suitable animal model e.g. goals of the study, how well the animal model recapitulates features of infection and disease (e.g. pathogenesis, immunity) in humans, therapeutic aspects (drug and vaccine efficacy), cost and availability of reagents and of course, size of the animals and ethical regulations. Today, the animal models most frequently used in TB studies are the mouse, guinea pig, rabbit, and the nonhuman primates (NHP) (103,108,109), though each model has advantages and disadvantages, altogether they help in advancing TB research. Specialized laboratory facilities of biosafety levels (BSL-3), approval of protocols from critical supervising committees and agencies (e.g., Institutional Animal Care and Use Committee, Office of Laboratory Animal Welfare, etc.), well trained personnel to collect relevant, clear, and translatable data and to treat animals humanely and the availability of reagents for experiments are the main prerequisites for working with animal models.

Mouse Models

Mice are used as TB animal model because of their availability in a wide variety of inbred, outbred, transgenic and genetically deficient mouse strains, and, of course, because of their small size, easy handling and their cost-effectiveness (104,110,111).

For this dissertation, BALB/c and C3HeB/FeJ mouse models have been chosen for several reasons explained below.

BALB/c Mouse Model

BALB/c mice are frequently used as a preclinical animal model for TB studies. After a low-dose aerosol (LDA) infection with Mtb (50-100 CFU per lung), these mice develop several uniform pulmonary granulomas that are non-necrotic and non-capsulated (37,111) where the bacilli are present. The granuloma lesions in BALB/c mice are composed primarily of epithelioid macrophages, lymphocytes and small number of neutrophils (112,113). These mice have decreased inter-mouse variability and therefore provide enhanced power of experimental statistics. Furthermore, the bacilli are located mostly intracellularly within macrophages in granulomas. The BALB/c TB model while assessing the efficacy of the drug for bacilli within an intracellular environment, it lacks extracellular bacilli, necrotic and encapsulating granulomas and therefore it could bias and potentially overestimate the effect of the drug under study (114–118).

C3HeB/FeJ Mouse Model

C3HeB/FeJ mice are highly susceptible to Mtb infection. The susceptibility and early death of C3HeB/FeJ mice to Mtb infection is attributed to the *Intracellular Pathogen Resistance 1* (*Ipr1*) gene present on chromosome 1 locus, sst1 (super-susceptibility to tuberculosis 1). The *Ipr1* gene is an important mediator of innate immunity which promotes the activation of macrophages against intracellular pathogens and, therefore, is involved in the control of macrophage stress responses. It switches

cell death pathway of the infected macrophages from necrosis to a well-known highly controlled form of suicide, apoptosis (119–121). Studies on characterization of the *sst1*/*lpr1*-mediated pathway in macrophages show that *lpr1* loss of function makes sst1 macrophages of C3HeB/FeJ mice more susceptible to rapid TB progression and death by necrosis upon infection with Mtb (120).

C3HeB/FeJ mice, unlike BALB/c, develop advanced lung pathology with virulent Mtb (35). Following a low dose aerosol (LDA) infection, these mice develop heterogenous pulmonary granulomas; some are similar to those seen in BALB/c mice while other granulomas are highly organized encapsulated caseous necrotic lesions that resemble the necrotic granulomas present in some human patients with active TB (37). Within the necrotic core of the granulomas, the majority of the bacilli remain extracellular and among necrotic cell debris (115,122,123). The necrotic core is surrounded by a rim of foamy cells laden with intracellular bacilli. The development of these granulomas depends on their respective local immune and inflammatory microenvironment (44). Based on the leading work by Dr. Igor Kramnik in describing and adopting these mice for TB research, C3HeB/FeJ mice are also referred to as the Kramnik mouse model (124).

Following 2-3 weeks post LDA infection, C3HeB/FeJ mice develop small foci of inflammation (early granulomas) composed primarily of myeloid cells especially macrophages and neutrophils. After 3-5 weeks, these mice develop three distinct types of granulomas classified as Type I, Type II and Type III lesions (123). Briefly, the Type I lesions are highly organized, solid, fibrous, encapsulated caseous necrotic granulomas very similar to those found in some active cases of human TB. They can be seen as

early as 5 weeks post LDA infection and mainly composed of central accumulation of foamy macrophages and neutrophils along with peripherally located collections of epithelioid macrophages and lymphocytes. During 7-10 weeks of infection, these lesions progress to a highly organized architecture in which the central core of granuloma becomes a hypoxic microenvironment (115,125) with neutral pH (126) and filled with densely packed neutrophils and necrotic debris. The interior of the core is surrounded by a rim of foamy macrophages encapsulated with fibrous tissue while the outer zone has fibroblasts and epithelioid cells intermixed with activated macrophages and lymphocytes in the surroundings (123). Previous studies (125) showed that these mice develop cavities in lung granulomas at 8-14 weeks post infection. To understand cavitation of lesions, some studies infected these mice with different strains of Mtb and found that the rate of cavity formation was influenced by the Mtb strain used.

Type II lesions appear after 3 weeks of LDA infection as small clusters of granulocytes and epithelioid macrophages. Like type I granuloma, type II is primarily composed of neutrophils with few lymphocytes but lack fibrotic and collagen structure. When they appear in the infected animals, type II granulomas grow rapidly between 5-7 weeks and soon many small granulomas consolidate and occupy a large area, sometimes the whole lobe. In the later stages, these lesions appear as polymorphonuclear alveolitis similar to some outcomes also found in humans (127) and show various stages of central caseous necrosis. Histological inspection reveals the presence of a considerable number of extracellular bacteria in these lesions (123). Animals developing Type II granulomas have poor survival outcomes and succumb to infection between 4-7 weeks post infection.

Type III lesions are mainly cellular inflammatory granulomas and primarily composed of epithelioid and foamy macrophages and a large number of lymphocytes present as aggregates or dispersed throughout the lesion. However, unlike type I and II, type III granulomas do not contain caseous necrosis and possess a rather small number of neutrophils where bacilli are mainly located inside the macrophages (123).

The Mtb infection progresses rapidly in C3HeB/FeJ mice, and their pulmonary bacterial load measured as colony forming unit (CFU) reaches 7 $\log_{10}$ CFU at day 30 following LDA infection with the Erdman strain. Compared to BALB/c which show substantially less CFU (6 $\log_{10}$) at day 40, the mortality rate is also high in these mice ranging from 10-40% between 28 to 45 days post-infection. However, the surviving mice live an additional 14 weeks with minimum mortality (123).

Drug Therapy in Tuberculosis

Treatment for DS-TB patients

In 1944, two antibiotics, streptomycin and para-amino salicylic acid (PAS) were used for first time in the treatment of TB (130). Between 1952 and 1970, referred to as the Golden Era of TB drug discovery, another four drugs were introduced as standard therapy to cure TB. The four drugs are isoniazid (H), rifampicin (R), ethambutol (E) and pyrazinamide (Z) and the combined regimen is collectively known as HREZ. This regimen is still used today to cure drug sensitive TB (DS-TB). The HREZ regimen, recommended by Center for Disease Control (CDC), is also known as the first-line anti-TB drugs or standard TB chemotherapy in which each drug has its unique role (131). The standard TB chemotherapy consists of an intensive phase of 2-months with HREZ

followed by a continuation phase of 4-months with isoniazid and rifampicin. This 6-9 month regimen transformed TB from a potentially deadly disease to a curable disease, however, this standard regimen remains far from optimal due to the development of Mtb resistance (132).

Isoniazid, a prodrug, also known as isonicotinic acid hydrazide (INH), has been the most important potent bactericidal drug in TB standard chemotherapy since 1952. It kills about 95% of bacilli during the first two days of treatment. This prodrug is activated by the catalase-peroxidase katG enzyme of Mtb. The active INH compound acts on bacterial cell wall synthesis by hindering its mycolic acid synthesis via inhA enzyme (133). Mutation in *katG* and *inhA* genes are the two main molecular mechanisms of resistance to INH in Mtb (134,135).

Rifampicin (RIF) has remained the most important drug for the treatment of TB since 1965 for its bactericidal properties and ability to reduce treatment duration. This drug is a protein synthesis inhibitor that forms a drug-enzyme complex by binding to β-subunit of bacterial RNA polymerase leading to the suppression of RNA synthesis and, ultimately, cell death (134). Many studies showed the sterilizing activity of RIF in combination with INH in mice (136). Resistance to RIF by mutation in the *rpoB* gene that codes for the β-subunit. This mutation leads to conformational changes in the RNA polymerase and decreases its affinity for the drug (134,135).

Ethambutol (EMB) is a synthetic compound used against Mtb since 1960s (137). It is a bacteriostatic drug that damages Mtb cell wall by interfering with the biosynthesis of arabinogalactan (134,138). Studies show the synergy of EMB with other anti-TB

drugs like INH (138) and RIF (139). The well recognized mechanism associated with the resistance to EMB is mutations in the *embB* gene (134,135,140,141).

Pyrazinamide (PZA) has been a critical frontline drug against Mtb since 1952 (134). It is a prodrug that is converted to its active form pyrazinoic acid by pyrazinamidase enzyme present in Mtb. The antimycobacterial activity of pyrazinoic acid is unclear but it may inhibit mycolic acid biosynthesis by inactivating fatty acid synthase, a key enzyme in fatty acid synthesis, and therefore it disrupts bacterial cell wall function (135). PZA like RIF is unique in reducing the treatment duration from previously 9-12 months to 6 months (142,143). Mutation in the *pncA* gene encoding pyrazinamidase is characterized as the most common type of resistance against PZA (134,135,142,143).

In the early therapeutic history of TB, the HREZ regimen performed very well and was able to shorten the lengthy treatment duration to 6-9 months. However, improper administration of HREZ or noncompliance with this lengthy treatment have resulted in development of drug-resistant-TB (DR-TB) and current treatment failures in patients with active DR-TB are fueling the dissemination of Mtb drug-resistant (DR) strains.

Treatment for DR-TB patients

DR-TB is further classified as RR-TB, MDR-TB and XDR-TB. The long duration and complexity of the treatment results in a high healthcare cost and remains a public health crisis (144). Despite administration of very long therapies with critical associated side effects, the outcomes in MDR- and XDR-TB patients are extremely poor, and these patients have limited treatment options. To address the urgent need of developing a

highly efficacious multidrug regimen for MDR- and XDR-TB treatment, the TB Alliance and other research organizations are searching for new multidrug regimens that are tested as a unit using *in vitro* and *in vivo* models. Following this approach, a number of promising new TB regimens are being evaluated in clinical trials. One of the promising combinations is the Nix-TB regimen.

The Novel Nix-TB Regimen for MDR- and XDR-TB patients

The Nix-TB regimen is a 6-month novel treatment protocol of 3 oral drugs: bedaquiline (B), pretomanid (Pa) and linezolid (L). This multidrug combination is referred to as the BPaL or Nix-TB regimen (145) because it was first tested in the Nix-TB trial conducted in South Africa. This regimen was a breakthrough cure for patients with XDR-TB or MDR-TB who failed or were intolerant of prior therapy including HIV positive patients with a CD4 count of 50 or higher (146). The Nix-TB regimen in animal models demonstrated better efficacy for drug susceptible TB compared to the standard TB chemotherapy (147–151). In this regimen, each drug has potent preclinical and clinical anti-TB activity with minimal pre-existing resistance.

Bedaquiline (B) is a novel compound approved by the United States FDA in 2012 to cure pulmonary MDR- and XDR-TB in combination with other anti-TB drugs (152) though it is also effective against DS-TB (153). This drug inhibits the proton transfer of bacterial ATP synthase enzyme by binding to its subunit c and has demonstrated bactericidal effect. This binding is highly specific to the ATP synthase enzyme of Mtb and therefore, it is unlikely to produce target-based toxicity in the host cells (154). Compared to conventional TB regimes, in mice B alone or in combination with other TB drugs (INH, PZA, clofazimine) have improved the treatment outcome by 30% (155). B is

equally effective against replicating and nonreplicating Mtb and both INH- and RR Mtb strains (135). A recent study on the cost-effectiveness analysis showed that addition of B to MDR-TB regimen improves health outcomes and reduces costs in high TB burden countries (156). However, the use of B is associated with several safety concerns in patients including increased mortality and heart- and liver-related adverse reactions (10,151).

Pretomanid (Pa), an interesting prodrug with anti-TB activity, belongs to nitroimidazole and blocks Mtb cell wall production by inhibiting mycolic acid biosynthesis (146,157). Its anti-TB activity works against both actively replicating and hypoxic non-replicating (persistent) Mtb. The novel mechanism of this drug includes the generation of reactive nitrogen species such as nitric oxide (NO) that functions as a “suicide bomb”. NO either directly damages the bacterial DNA or inhibits the energy metabolism by blocking the ATP synthase enzyme thus causing anaerobic killing (157). Pa was recently approved by the US FDA as an anti-TB drug as part of a combination regimen with B and linezolid for the treatment of pulmonary MDR- and XDR-TB (146).

Linezolid (L) is a synthetic drug that belongs to the oxazolidinone class of drugs and binds to a site on the bacterial 23S ribosomal RNA of the 50S subunit. The unique mechanism of binding of this drug prevents the formation of 70S ribosomal unit and therefore results in inhibition of protein synthesis (135,158,159). L was recently approved for treatment of MDR-TB and XDR-TB (160).

Collectively, the three drugs in BPaL regimen showed the remarkable outcomes (90% effectiveness for 6 months of treatment) of curing XDR- and treatment intolerant MDR-TB patients, but many side effects were observed in the clinical trial. Among the

BPaL regimen, the long-term administration of L is responsible for myelosuppression (48%), peripheral neuropathy and optic neuritis (81%) and anemia (37%) (161). To avoid and understand these toxicities, several studies have evaluated dose modifications of L within the BPaL regimen (146,162). Along with the adverse effects (AEs) noted, L has also been reported in many studies for its resistance against Mtb (163,164). Therefore, based on these observations, researchers are working to modify the BPaL regimen to improve its efficacy against DR-TB and minimize its AEs.

A follow-up trial, the ZeNix, was aimed to adjust the BPaL regimen for L doses and duration for patients in South Africa, Russia, Georgia and Moldova. This trial also had remarkable results; it cured 84-91% patients (9 to 26 weeks therapy respectively) and resulted in fewer AEs than those observed in the Nix-TB trial along with fewer treatment interruptions or discontinuations (162). Other trials such as the TB-PRACTECAL clinical trial showed promising results with the addition of moxifloxacin (BPaLM) and clofazimine (BPaLC) to the BPaL regimen (165). Therefore, in 2019 the approval of BPaL regimen by the United States Food and Drug Administration that is affective against highly DR-TB patients (146) was one of the steps taken towards achieving WHO goal to end TB and spread of drug resistance.

Current Guidelines of WHO on DR-TB Treatment

WHO categorized the drugs to be used for DR-TB treatment into three groups. Group A contains fluoroquinolone (levofloxacin or moxifloxacin), bedaquiline, and linezolid while Group B encompasses clofazimine, and cycloserine or terizidone and Group C consists of ethambutol, delamanid, pyrazinamide, imipenem/cilastatin or meropenem, amikacin or streptomycin, ethionamide or prothionamide and para-

aminosalicylic acid (166,167). According to the guidelines released in 2020, WHO prefers all-oral drugs for DR-TB treatment based on the drug susceptibility test and the treatment history of patients. An 18-month treatment consists of two phases; a 6-month intensive phase comprised of four TB drugs three of which belong to Group A and at least one from Group B. However, if a four-drug regimen cannot be achieved with drugs from Group A and B, the agents from Group C will be considered for this formation. The continuation phase follows the remaining treatment duration with a total of at least three drugs except bedaquiline and this phase may be modified according to the treatment response.

In December 2022, WHO updated the guidelines which contain recommendations on treatment of MDR/RR-TB. The novelty of updated guidelines was the addition of two new multidrug regimens. (1) A 6-month BPaL regimen which may be used with moxifloxacin (BPaLM) or without in case of documented resistance to fluoroquinolones (in patients with pre-XDR-TB). (2) A 9-month all-oral bedaquiline-containing regimen for patients in whom resistance to fluoroquinolones has been excluded but who are not eligible for BPaLM. This treatment approach consists of two phases; the intensive phase which utilizes a combination of bedaquiline with fluoroquinolone, ethionamide (or linezolid at the dosage of 600 mg daily), ethambutol, high-dose isoniazid, pyrazinamide and clofazimine, followed by a continuation phase comprises of fluoroquinolone, clofazimine, ethambutol, and pyrazinamide. The longer (18-month) treatments, as above, remain a valid option in all cases in which shorter regimens cannot be implemented due to intolerance, drug-drug interactions, XDR-TB, extensive forms of extrapulmonary TB, or previous treatment failure.

Routes of Drug Administration in Tuberculosis

Different routes of administration provide varying concentrations of drugs at target sites in the body. Ideally a drug should penetrate to the target site at therapeutic concentration for activity without causing toxicity. Systemic toxicities are frequently observed with parental and oral drugs and may lead to side effects and lack of patient compliance with the treatment (168).

Inhalational Route

Inhalation or direct administration of aerosolized antibiotics in Mtb infected lungs, the main site of Mtb infection, has recently gained attention (169). This promising route of delivery provides high local concentration of drug with lower systemic exposures than oral or injection administration and as a result can reduce systemic toxicity (170,171).

Spectinamides are semisynthetic analog of spectinomycin with potent anti-tubercular activity due to their ability to avoid drug efflux by Rv1258c transporters present on the surface of Mtb (172,173). Spectinamides are active under hypoxic conditions and have shown excellent activity against MDR- and XDR-TB (155,174). One of the lead compounds, spectinamide 1599 (1599) has demonstrated promising results both *in vitro* and *in vivo* studies with lack of cross-resistant with existing TB drugs. Having poor oral bioavailability, 1599 has to be administered via parenteral route (154,155,174).

Spectinamide 1599 shows synergism when combined with classical and non-classical TB drugs. *In vitro*, it shows efficacy with clarithromycin, doxycycline, and clindamycin (154). Co-administration of 1599 in different mouse models shows

synergistic activity with most of the first-line TB drugs e.g. RIF and PZA or BDQ and PZA [202] and clarithromycin (154). Despite the efficacious results, one of the limitations of using 1599 as injectable is risk of lack of patient compliance with the long treatment duration. However, due to its hydrophilic nature, 1599 can be delivered directly to the lungs (intrapulmonary IPA) as “inhalational therapy” with high efficacy when combined with other frontline TB drugs (128,172,175). A comparative study of drug administration routes demonstrated that 1599 has 48 times higher exposure in mouse lungs by inhalation than subcutaneous injection and it could be the reason for increased efficacy of this drug when administered via inhalation (128,175). Moreover, like other members within the aminocyclitol group (tobramycin and amikacin) also used as inhalation therapy, 1599 shows a great potential to be used as dry powder inhalation therapy (176).

Future Perspective of Tuberculosis Chemotherapy

Over the last two decades of intensified research, there has been tremendous progress in DR-TB treatment. However, the recent pandemic of COVID-19 has caused disruptions across the TB health care system by posing challenges in diagnosis, appropriate treatment and reporting of such patients through national disease surveillance systems, altogether leading to an increase in TB cases globally. The collaborative efforts from academia, pharmaceutical industry and non-profit organizations have led to the approval of new promising anti-TB drugs such as bedaquiline and pretomanid. Moreover, improvement management of toxicities and adverse effects and the development of shorted regimens using all-oral drug regimens have improved the outcomes and retention of DR-TB patients in TB care. The BPaL and

BPaLM regimens are the first ever 6-month all-oral treatment for MDR/XDR-TB patients. Many other studies, including the study discussed in chapter 2 of this thesis are underway aiming to develop short-course, injection-free, low pill burden regimes with reduced toxicity that are more efficacious in sterilizing Mtb and, ultimately, avoiding relapse. Regardless of these developments, some uncertainties remain and therefore must be considered while progressing forward. Drug resistance may emerge to the new drugs suggesting that the use of new core drugs such as bedaquiline and pretomanid must be used based on the defined recommendation and within defined regimens to prevent further resistance acquisition. Research on the growing pipeline for anti-TB drug candidates should result in the development of new promising agents. While rapid and proficient diagnostic approaches are essential to offer improved clinical outcomes to the patients, treatment should be based on drug susceptibility testing and treatment history of the patients. Markers for progression of latent TB to the active pulmonary form and markers for drug response and prediction of relapse, along with animal models capable of assessing treatment shortening potential of new regimens in the clinics are required.

References

1. Smith I. *Mycobacterium tuberculosis* pathogenesis and molecular determinants of virulence. Clin Microbiol Rev. 2003;16(3):463–96.
2. Chakaya J, Khan M, Ntoumi F, Aklillu E, Fatima R, Mwaba P, et al. Global Tuberculosis Report 2020 – Reflections on the Global TB burden, treatment and prevention efforts. Int J Infect Dis. 2021;113:S7–12.
3. WHO. Global TB report. 2022.
4. Kawatsu L, Yoshiyama T, Kato S. Tuberculosis in the Elderly. Essent Tuberc. 2021;253–8.
5. Ockenga J, Fuhse K, Chatterjee S, Malykh R, Rippin H, Pirlich M, et al. Tuberculosis and malnutrition: The European perspective. Clin Nutr. 2023;42(4):486–92.
6. Komrower D, Thillai *M. tuberculosis* and HIV co-infection. Clin Tuberc A Pract Handb. 2015;157–70.
7. Drain PK, Bajema KL, Dowdy D, Dheda K, Naidoo K, Schumacher SG, et al. Incipient and subclinical tuberculosis: A clinical review of early stages and progression of infection. Clin Microbiol Rev. 2018;31(4).
8. Wright A, Zignol M, Van Deun A, Falzon D, Gerdes SR, Feldman K, et al. Epidemiology of antituberculosis drug resistance 2002-07: an updated analysis of the Global Project on Anti-Tuberculosis Drug Resistance Surveillance. Lancet. 2009;373(9678):1861–73.
9. Caminero JA. Multidrug-resistant tuberculosis: Epidemiology, risk factors and case finding. Int J Tuberc Lung Dis. 2010;14(4):382–90.
10. WHO. Global TB Report 2021.
11. Deutsch-Feldman M, Pratt RH, Price SF, Tsang CA, Self JL. Tuberculosis — United States, 2020 [Internet]. Vol. 70. 2021. Available from: https://www.census.gov/data/tables/time-series/demo/popest/2010s-national-
12. Barberis I, Bragazzi NL, Galluzzo L, Martini M. The history of tuberculosis: From the first historical records to the isolation of Koch's bacillus. J Prev Med Hyg. 2017;58(1):E9–12.
13. Gutierrez MC, Vincent V, Brisse S, Brosch R, Fabre M, Marmiesse M, et al. Ancient Origin and Gene Mosaicism of the Progenitor of *Mycobacterium tuberculosis* [Internet]. Vol. 1, PLoS Pathogens. 2005. Available from: https://doi.org/10.1371/journal.ppat.0010005.g001
14. Laennec RTH. A treatise on the diseases of the chest. First Amer. Philadelphia: William Brown Printer, Philadelphia; 1823.
15. Comas I, Coscolla M, Luo T, Borrell S, Holt KE, Kato-Maeda M, et al. Out-of-

Africa migration and Neolithic coexpansion of *Mycobacterium tuberculosis* with modern humans. Nat Genet. 2013;45(10):1176–82.

16. Cave BYAJ. The Evidence for the Incidence of Tuberculosis in Ancient Egypt. Br J Tuberc. 1939;33(3):142–52.

17. Kapur V, Whittam TS, Musser JM. Is *Mycobacterium tuberculosis* 15, 000 years old? J Infect Dis. 1994;170(5):1348–9.

18. Bernardo A, Wilmar S, Arthur A, Todd H. Pre-Columbian tuberculosis in Northern Chile: Molecular and skeletal evidence. Am J Phyaiscal Antrhropology. 1995;98(1):37–45.

19. Prat J, Souza S. Prehistoric Tuberculosis in the Americas – Brewminate_ A Bold Blend of News and Ideas. 2003.

20. McGrath JW. Social networks of disease spread in the lower illinois valley: A simulation approach. Am J Phys Anthropol. 1988;77(4):483–96.

21. Barbier M, Wirth T. The evolutionary history, demography, and spread of the *Mycobacterium tuberculosis* complex. Tuberc Tuber Bacillus Second Ed. 2017;(1):453–73.

22. Ahamad N, Gupta S, Parashar D. Using Omics to Study Leprosy, Tuberculosis, and Other Mycobacterial Diseases. Front Cell Infect Microbiol. 2022;12(February):1–15.

23. Kanabalan RD, Lee LJ, Lee TY, Chong PP, Hassan L, Ismail R, et al. Human tuberculosis and *Mycobacterium tuberculosis* complex: A review on genetic diversity, pathogenesis and omics approaches in host biomarkers discovery. Microbiol Res [Internet]. 2021;246(December 2020):126674. Available from: https://doi.org/10.1016/j.micres.2020.126674

24. Yamada H, Chikamatsu K, Aono A, Murata K, Miyazaki N, Kayama Y, et al. Fundamental Cell Morphologies Examined With Cryo-TEM of the Species in the Novel Five Genera Robustly Correlate With New Classification in Family Mycobacteriaceae. Front Microbiol. 2020;11(November):1–11.

25. Niemann S, Harmsen D, Rusch-Gerdes S, Richter E. Differentiation of clinical *Mycobacterium tuberculosis* complex isolates by gyrB DNA sequence polymorphism analysis. J Clin Microbiol. 2000;38(9):3231–4.

26. Bayraktar B, Bulut E, Bariş AB, Toksoy B, Dalgic N, Celikkan C, et al. Species distribution of the *Mycobacterium tuberculosis* complex in clinical isolates from 2007 to 2010 in Turkey: A prospective study. J Clin Microbiol. 2011;49(11):3837–41.

27. Bajaj AO, Saraswat S, Knuuttila JEA, Freeke J, Stielow JB, Barker AP. Accurate Identification of Closely Related *Mycobacterium tuberculosis* Complex Species by High Resolution Tandem Mass Spectrometry. Front Cell Infect Microbiol. 2021 Jun 22;11.

28. Lin CR, Wang HY, Lin TW, Lu JJ, Hsieh JCH, Wu MH. Development of a two-step nucleic acid amplification test for accurate diagnosis of the *Mycobacterium tuberculosis* complex. Sci Rep. 2021 Dec 1;11(1).

29. Delogu G, Sali M, Fadda G. The biology of *Mycobacterium tuberculosis* infection. Mediterr J Hematol Infect Dis. 2013;5(1).

30. Koch R, Brock T. The Etiology of Tuberculosis. Rev Infect Dis. 1982;4(6):1270–4.

31. Brennan PJ. Structure, function, and biogenesis of the cell wall of *Mycobacterium tuberculosis*. Tuberculosis. 2003;83(1–3):91–7.

32. Wayne LG, Hayes LG. An in vitro model for sequential study of shiftdown of *Mycobacterium tuberculosis* through two stages of nonreplicating persistence. Infect Immun. 1996;64(6):2062–9.

33. Wayne LG, Sohaskey CD. Nonreplicating persistence of *Mycobacterium tuberculosis*. Annu Rev Microbiol. 2001;55:139–63.

34. Zhai W, Wu F, Zhang Y, Fu Y, Liu Z. The immune escape mechanisms of *Mycobacterium Tuberculosis*. Int J Mol Sci. 2019;20(2).

35. Pan H, Yan B, Rojas M, Shebzukhov Y V, Zhou H, Kobzik L, et al. Ipr1 gene mediates innate immunity to tuberculosis. Nature. 2006;434(7034):767–72.

36. Patterson B, Wood R. Is cough really necessary for TB transmission? Tuberculosis [Internet]. 2019;117(January):31–5. Available from: https://doi.org/10.1016/j.tube.2019.05.003

37. Kramnik I, Beamer G. Mouse models of human TB pathology: roles in the analysis of necrosis and the development of host-directed therapies. Semin Immunopathol. 2016;38(2):221–37.

38. Archana, Dietzold J, Verma S, Bhagavathula M. Toll-like Receptor 2 Prevents Neutrophil-Driven Immunopathology during Infection with *Mycobacterium tuberculosis* by Curtailing CXCL5 Production. Infect Immun. 2019;87(3):e00760-18.

39. Upadhyay S, Mittal E, Philips JA. Tuberculosis and the art of macrophage manipulation. Pathog Dis. 2018;76(4):1–12.

40. Palucci I, Delogu G. Host Directed Therapies for Tuberculosis: Futures Strategies for an Ancient Disease. Chemotherapy. 2018;63(3):172–80.

41. Kaplan G, Post FA, Moreira AL, Wainwright H, Kreiswirth BN, Tanverdi M, et al. *Mycobacterium tuberculosis* Growth at the Cavity Surface: A Microenvironment with Failed Immunity. Infect Immun. 2003;71(12):7099–108.

42. Pai M, Behr MA, Dowdy D, Dheda K, Divangahi M, Boehme CC, et al. Tuberculosis. Nat Rev Dis Prim. 2016;2.

43. McCaffrey EF, Donato M, Keren L, Chen Z, Delmastro A, Fitzpatrick MB, et al. The immunoregulatory landscape of human tuberculosis granulomas. Nat

Immunol. 2022;23(2):318–29.

44. Rosenthal IM, Tasneen R, Peloquin CA, Zhang M, Almeida D, Mdluli KE, et al. Dose-ranging comparison of rifampin and rifapentine in two pathologically distinct murine models of tuberculosis. Antimicrob Agents Chemother. 2012;56(8):4331–40.

45. Grosset J. *Mycobacterium tuberculosis* in the extracellular compartment: An underestimated adversary. Antimicrob Agents Chemother. 2003;47(3):833–6.

46. Xu G, Wang J, Gao GF, Liu CH. Insights into battles between *Mycobacterium tuberculosis* and macrophages. Protein Cell. 2014;5(10):728–36.

47. O'Garra A, Redford P, McNab F, Bloom C, Wilkinson R, Berry M. The Immune Response in Tuberculosis. Annu Rev Immunol. 2013;(31):475–527.

48. Ravimohan S, Kornfeld H, Weissman D, Bisson G. Tuberculosis and lung damage: From epidemiology to pathophysiology. Eur Respir Rev. 2018;27(147).

49. Abengozar-Muela M, Esparza M, Garcia-Ros D, Vásquez C, Echeveste J, Idoate M, et al. Diverse immune environments in human lung tuberculosis granulomas assessed by quantitative multiplexed immunofluorescence. Mod Pathol. 2020;33(12):2507–19.

50. Lombard R, Doz E, Carreras F, Epardaud M, Le Vern Y, Buzoni-Gatel D, et al. IL-17RA in non-hematopoietic cells controls CXCL-1 and 5 critical to recruit neutrophils to the lung of mycobacteria-infected mice during the adaptive immune response. PLoS One. 2016;11(2).

51. Vono M, Lin A, Norrby-Teglund A, Koup R, Liang F, Lore K. Neutrophils Acquire the Capacity for Antigen Presentation to Memory CD4+ T Cells in Vitro and Ex Vivo. Blood. 2017;129(14):1991–2001.

52. Borkute RR, Woelke S, Pei G, Dorhoi A. Neutrophils in tuberculosis: Cell biology, cellular networking and multitasking in host defense. Int J Mol Sci. 2021;22(9).

53. Muefong CN, Sutherland JS. Neutrophils in Tuberculosis-Associated Inflammation and Lung Pathology. Front Immunol. 2020;11(May):1–9.

54. Capuano S, Croix DA, Pawar S, Zinovik A, Myers A, Lin PL, et al. Experimental *Mycobacterium tuberculosis* infection of cynomolgus macaques closely resembles the various manifestations of human *M. tuberculosis* infection. Infect Immun. 2003;71(10):5831–44.

55. Morel C, Badell E, Abadie V, Robledo M, Setterblad N, Gluckman JC, et al. *Mycobacterium bovis* BCG-infected neutrophils and dendritic cells cooperate to induced specific T cell responses in humans and mice. Eur J Immunol. 2008;38(2):437–47.

56. Nouailles G, Dorhoi A, Koch M, Zerrahn J, Weiner J, Faé KC, et al. CXCL5-secreting pulmonary epithelial cells drive destructive neutrophilic inflammation in tuberculosis. J Clin Invest. 2014;124(3):1268–82.

57. Kang DD, Lin Y, Moreno JR, Randall TD, Khader SA. Profiling early lung immune responses in the mouse model of tuberculosis. PLoS One. 2011;6(1).

58. Mayadas TN, Cullere X, Lowell CA. The multifaceted functions of neutrophils. Annu Rev Pathol Mech Dis. 2014;9:181–218.

59. Seiler P, Aichele P, Raupach B, Odermatt B, Steinhoff U, Kaufmann SHE. Rapid neutrophil response controls fast-replicating intracellular bacteria but not slow-replicating *Mycobacterium tuberculosis*. J Infect Dis. 2000;181(2):671–80.

60. Eruslanov EB, Lyadova I V., Kondratieva TK, Majorov KB, Scheglov I V., Orlova MO, et al. Neutrophil responses to *Mycobacterium tuberculosis* infection in genetically susceptible and resistant mice. Infect Immun. 2005;73(3):1744–53.

61. Dallenga T, Repnik U, Corleis B, Eich J, Reimer R, Griffiths GW, et al. *M. tuberculosis*-Induced Necrosis of Infected Neutrophils Promotes Bacterial Growth Following Phagocytosis by Macrophages. Cell Host Microbe. 2017;22(4):519-530.e3.

62. Romero MM, Balboa L, Basile JI, López B, Ritacco V, De La Barrera SS, et al. Clinical isolates of *Mycobacterium tuberculosis* differ in their ability to induce respiratory burst and apoptosis in neutrophils as a possible mechanism of immune escape. Clin Dev Immunol. 2012;2012.

63. Lyadova IV. Neutrophils in Tuberculosis: Heterogeneity Shapes the Way? Mediators Inflamm. 2017;2017.

64. Cheng P, Li S, Chen H. Macrophages in lung injury, repair and fibrosis. Cells. 2021;10(2):1–17.

65. Kopf M, Schneider C, Nobs SP. The development and function of lung-resident macrophages and dendritic cells. Nat Immunol. 2015;16(1):36–44.

66. Shim D, Kim H, Shin SJ. *Mycobacterium tuberculosis* Infection-Driven Foamy Macrophages and Their Implications in Tuberculosis Control as Targets for Host-Directed Therapy. Front Immunol. 2020;11(May):1–10.

67. Killick KE, Ní Cheallaigh C, O'Farrelly C, Hokamp K, Machugh DE, Harris J. Receptor-mediated recognition of mycobacterial pathogens. Cell Microbiol. 2013;15(9):1484–95.

68. Yao S, Huang D, Chen CY, Halliday L, Wang RC, Chen ZW. CD4+ T cells are required to contain early extrathoracic TB dissemination and sustain multi-effector functions of CD8+ T and CD3- lymphocytes. J Immunol. 2014;192(5):2120–32.

69. Lin, Philana Ling and JF. CD8 T cells and *Mycobacterium tuberculosis* infection. Semin Immunol. 2015;37(3):239–49.

70. Maphasa RE, Meyer M, Dube A. The Macrophage Response to *Mycobacterium tuberculosis* and Opportunities for Autophagy Inducing Nanomedicines for Tuberculosis Therapy. Front Cell Infect Microbiol. 2021;10(February):1–22.

71. Abrahem R, Chiang E, Haquang J, Nham A, Ting YS, Venketaraman V. The role of dendritic cells in TB and HIV infection. J Clin Med. 2020;9(8):1–15.

72. Mellman I. Dendritic cells: master regulators of the immune response. Cancer Immunol Res. 2013;1(3):145–9.

73. Steinman RM, Bonifaz L, Fujii SI, Liu K, Bonnyay D, Yamazaki S, et al. The innate functions of dendritic cells in peripheral lymphoid tissues. Adv Exp Med Biol. 2005;560:83–97.

74. Hudrisier D, Neyrolles O. Antigen Smuggling in Tuberculosis. Cell Host Microbe. 2014;15:657–9.

75. Mellman I, Steinman RM. Dendritic cells: Specialized and regulated antigen processing machines. Cell. 2001;106(3):255–8.

76. Berger AC, Roche PA. MHC class II transport at a glance. J Cell Sci. 2009;122(1):1–4.

77. Morris D, Gonzalez B, Khurasany M, Kassissa C, Luong J, Kasko S, et al. Characterization of dendritic cell and regulatory T cell functions against *Mycobacterium tuberculosis* infection. Biomed Res Int. 2013;2013.

78. Moreira-Teixeira L, Mayer-Barber K, Sher A, O'Garra A. Type I interferons in tuberculosis: Foe and occasionally friend. J Exp Med. 2018;215(5):1273–85.

79. Chan J, Mehta S, Bharrhan S, Chen Y, Achkar JM, Casadevall A, et al. The role of B cells and humoral immunity in *Mycobacterium tuberculosis* infection. Adv Exp Med Biol. 2014;783:225–50.

80. Sakai S, Mayer-Barber KD, Barber DL. Defining features of protective CD4 T cell responses to *Mycobacterium tuberculosis*. Curr Opin Immunol. 2014;29(1):137–42.

81. Diedrich CR, Mattila JT, Klein E, Janssen C, Phuah J, Sturgeon TJ, et al. Reactivation of latent tuberculosis in cynomolgus macaques infected with SIV is associated with early peripheral T cell depletion and not virus load. PLoS One. 2010;5(3):1–12.

82. Lin PL, Rutledge T, Green AM, Bigbee M, Fuhrman C, Klein E, et al. CD4 T cell depletion exacerbates acute *Mycobacterium tuberculosis* while reactivation of latent infection is dependent on severity of tissue depletion in cynomolgus macaques. AIDS Res Hum Retroviruses. 2012;28(12):1693–702.

83. Serbina NV, Lazarevic V, Flynn JL. CD4+ T Cells Are Required for the Development of Cytotoxic CD8+ T Cells During *Mycobacterium tuberculosis* Infection. J Immunol. 2001;167(12):6991–7000.

84. Serbina NV. CD8+ CTL from lungs of *Mycobacterium tuberculosis*-infected mice express perforin in vivo and lyse infected macrophages. J Immunol. 2000;165(1):353–63.

85. Patankar YR, Sutiwisesak R, Boyce S, Lai R, Lindestam Arlehamn CS, Sette A, et al. Limited recognition of *Mycobacterium tuberculosis*-infected macrophages by polyclonal CD4 and CD8 T cells from the lungs of infected mice. Mucosal Immunol. 2020;13(1):140–8.

86. Prezzemolo T, Guggino G, La Manna MP, Di Liberto D Di, Dieli F, Caccamo N. Functional signatures of human CD4 and CD8 T cell responses to *Mycobacterium tuberculosis*. Front Immunol. 2014;5:1–13.

87. Hongliang Yang, Nicole A. Kruh-Garcia and KMD. Purified Protein Derivatives of Tuberculin - Past, Present, and Future. FEMS Immunol Med Microbiol. 2012;66(3):273–80.

88. Stegelmann F, Bastian M, Swoboda K, Bhat R, Kiessler V, Krensky AM, et al. Coordinate Expression of CC Chemokine Ligand 5, Granulysin, and Perforin in CD8+ T Cells Provides a Host Defense Mechanism against *Mycobacterium tuberculosis*. J Immunol. 2005;175(11):7474–83.

89. Cardona P, Cardona PJ. Regulatory T Cells in *Mycobacterium tuberculosis* Infection. Front Immunol. 2019;10:1–11.

90. Qureshi OS, Zheng Y, Nakamura K, Attridge K, Manzotti C, Schmidt EM, et al. Trans-endocytosis of CD80 and CD86: a molecular basis for the cell extrinsic function of CTLA-4. Science (80-). 2011;332(6029):600–3.

91. Khattri R, Cox T, Yasayko SA, Ramsdell F. An essential role for Scurfin in CD4+CD25+T regulatory cells. J Immunol. 2017;198(3):993–8.

92. Fontenot JD, Gavin MA, Rudensky AY. Foxp3 programs the development and function of CD4+CD25+ regulatory T cells. J Immunol. 2017;198(3):986–92.

93. Maglione PJ, Xu J, Chan J. B Cells Moderate Inflammatory Progression and Enhance *Mycobacterium tuberculosis*. J Immunol. 2007;178(11):7222–34.

94. Catharine M. Bosio, Donald Gardner and KLE. Infection of B Cell-Deficient Mice with CDC 1551, a Clinical Isolate of *Mycobacterium tuberculosis*: Delay in Dissemination and Development of Lung Pathology. J Immunol. 2000;164(12):6417–25.

95. Phuah JY, Mattila JT, Lin PL, Flynn JL. Activated B cells in the granulomas of nonhuman primates infected with *Mycobacterium tuberculosis*. Am J Pathol. 2012;181(2):508–14.

96. Rahman S, Rehn A, Rahman J, Andersson J, Svensson M, Brighenti S. Pulmonary tuberculosis patients with a vitamin D deficiency demonstrate low local expression of the antimicrobial peptide LL-37 but enhanced FoxP3+ regulatory T cells and IgG-secreting cells. Vol. 156, Clinical Immunology. 2015. p. 85–97.

97. Loxton AG. Bcells and their regulatory functions during Tuberculosis: Latency and active disease. Mol Immunol. 2019 Jul 1;111:145–51.

98. Maglione PJ, Chan J. How B cells shape the immune response against

Mycobacterium tuberculosis. Eur J Immunol. 2009;39(3):676–86.

99. Lund FE, Randall TD. Effector and regulatory B cells: modulators of CD4+ T cell immunity. Nat Rev Immunol. 2010;10(4):236–47.

100. Cambau E, Drancourt M. Steps towards the discovery of *Mycobacterium tuberculosis* by Robert Koch, 1882. Clin Microbiol Infect. 2014;20:196–201.

101. Dharmadhikari AS, Nardell EA. What animal models teach humans about tuberculosis. Am J Respir Cell Mol Biol. 2008;39(5):503–8.

102. Gupta UD, Katoch VM. Animal models of tuberculosis. Tuberculosis. 2005;85(5–6):277–93.

103. Cohen J. Introduction to Infectious Diseases [Internet]. Fourth Edi. Infectious Diseases, 2-Volume Set. Elsevier Ltd; 2017. 1–4 p. Available from: http://dx.doi.org/10.1016/B978-0-7020-6285-8.00001-0

104. Une Y, Mori T. Tuberculosis as a zoonosis from a veterinary perspective. Comp Immunol Microbiol Infect Dis. 2007;30(5–6):415–25.

105. Basaraba RJ, Hunter RL. Pathology of tuberculosis: How the pathology of human tuberculosis informs and directs animal models. Tuberc Tuber Bacillus Second Ed. 2017;117–29.

106. Bucsan AN, Mehra S, Khader SA, Kaushal D. The current state of animal models and genomic approaches towards identifying and validating molecular determinants of *Mycobacterium tuberculosis* infection and tuberculosis disease. Pathog Dis. 2019;77(4):1–17.

107. Zhan L, Tang J, Sun M, Qin C. Animal models for tuberculosis in translational and precision medicine. Front Microbiol. 2017;8(1–12).

108. Cooper AM. Mouse model of tuberculosis. Cold Spring Harb Perspect Med. 2015;5(2):1–9.

109. Orme IM. The mouse as a useful model of tuberculosis. Tuberculosis. 2003;83:112–5.

110. Hernandez-Pando R, Aguilar D, Hernandez MLG, Orozco H, Rook GAW. Pulmonary tuberculosis in BALB/c mice with non-functional IL-4 genes: Changes in the inflammatory effects of TNF-α and in the regulation of fibrosis. Eur J Immunol. 2004;34(1):174–83.

111. Lee C, Homer RJ, Zhu Z, Lanone S, Wang X, Koteliansky V, et al. Interleukin-13 induces tissue fibrosis by selectively stimulating and activating transforming growth factor β1. J Exp Med. 2001;194(6):809–21.

112. Harper J, Skerry C, Davis SL, Tasneen R, Weir M, Kramnik I, et al. Mouse model of necrotic tuberculosis granulomas develops hypoxic lesions. J Infect Dis. 2012;205(4):595–602.

113. Driver ER, Ryan GJ, Hoff DR, Irwin SM, Basaraba RJ, Kramnik I, et al. Evaluation

of a mouse model of necrotic granuloma formation using C3HeB/FeJ mice for testing of drugs against *Mycobacterium tuberculosis*. Antimicrob Agents Chemother. 2012;56(6):3181–95.

114. Irwin SM, Gruppo V, Brooks E, Gilliland J, Scherman M, Reichlen MJ, et al. Limited activity of clofazimine as a single drug in a mouse model of tuberculosis exhibiting caseous necrotic granulomas. Antimicrob Agents Chemother. 2014;58(7):4026–34.

115. Aly S, Wagner K, Keller C, Malm S, Malzan A, Brandau S, et al. Oxygen status of lung granulomas in *Mycobacterium tuberculosis* -infected mice. J Pathol. 2006;210:298–305.

116. Tsai MC, Chakravarty S, Zhu G, Xu J, Tanaka K, Koch C, et al. Characterization of the tuberculous granuloma in murine and human lungs: Cellular composition and relative tissue oxygen tension. Cell Microbiol. 2006;8(2):218–32.

117. Wang Y, Yang C, He Y, Zhan X, Xu L. Ipr1 modified BCG as a novel vaccine induces stronger immunity than BCG against tuberculosis infection in mice. Mol Med Rep. 2016;14(2):1756–64.

118. Pichugin A, Yan BS, Sloutsky A, Kobzik L, Kramnik I. Dominant role of the sst1 locus in pathogenesis of necrotizing lung granulomas during chronic tuberculosis infection and reactivation in genetically resistant hosts. Am J Pathol. 2009;174(6):2190–201.

119. Yan B-S, Pichugin A, Jobe O, Helming L, Eruslanov EB, Gutiérrez-Pabello JA, et al. Progression of Pulmonary Tuberculosis and Efficiency of Bacillus Calmette-Guérin Vaccination Are Genetically Controlled via a Common sst1 -Mediated Mechanism of Innate Immunity. J Immunol. 2007;179(10):6919–32.

120. Lanoix JP, Lenaerts AJ, Nuermberger EL. Heterogeneous disease progression and treatment response in a C3HeB/FeJ mouse model of tuberculosis. Dis Model Mech. 2015;8(6):603–10.

121. Irwin SM, Driver E, Lyon E, Schrupp C, Ryan G, Gonzalez-Juarrero M, et al. Presence of multiple lesion types with vastly different microenvironments in C3HeB/FeJ mice following aerosol infection with *Mycobacterium tuberculosis*. Dis Model Mech. 2015;8(6):591–602.

122. Kramnik I, Dietrich WF, Demant P, Bloom BR. Genetic control of resistance to experimental infection with virulent *Mycobacterium tuberculosis*. Proc Natl Acad Sci U S A. 2000;97(15):8560–5.

123. Ordonez AA, Tasneen R, Pokkali S, Xu Z, Converse PJ, Klunk MH, et al. Mouse model of pulmonary cavitary tuberculosis and expression of matrix metalloproteinase-9. Dis Model Mech. 2016;9(7):779–88.

124. Lanoix JP, Ioerger T, Ormond A, Kaya F, Sacchettini J, Dartois V, et al. Selective inactivity of pyrazinamide against tuberculosis in C3HeB/FeJ mice is best explained by neutral pH of caseum. Antimicrob Agents Chemother.

2016;60(2):735–43.

125. Canetti G. Pathogenesis of Tuberculosis in Man. Ann New York Acad Sci. :13–8.

126. Gonzalez-Juarrero M, Lukka PB, Wagh S, Walz A, Arab J, Pearce C, et al. Preclinical Evaluation of Inhalational Spectinamide-1599 Therapy against Tuberculosis. ACS Infect Dis. 2021;7(10):2850–63.

127. Singh AK, Gupta UD. Animal models of tuberculosis: Lesson learnt. Indian J Med Res [Internet]. 2018;147:456–63. Available from: http://www.ncbi.nlm.nih.gov/pubmed/23144490

128. Chakraborty S and RK. Tuberculosis Drug Development: History and Evolution of the Mechanism-Based Paradigm. Cold Spring Harb Perspect Med. 2015;5:a021147.

129. Mitchison DA. Role of individual drugs in the chemotherapy of tuberculosis. Int J Tuberc Lung Dis. 2000;4(9):796–806.

130. Nahid P, Dorman SE, Alipanah N, Barry PM, Brozek JL, Cattamanchi A, et al. Official American Thoracic Society/Centers for Disease Control and Prevention/Infectious Diseases Society of America Clinical Practice Guidelines: Treatment of Drug-Susceptible Tuberculosis. Clin Infect Dis. 2016;63(7):e147-95.

131. Arun KB, Madhavan A, Abraham B, Balaji M, Sivakumar KC, Nisha P, et al. Acetylation of isoniazid is a novel mechanism of isoniazid resistance in *Mycobacterium tuberculosis*. Antimicrob Agents Chemother. 2021;65(1).

132. Palomino JC, Martin A. Drug resistance mechanisms in *Mycobacterium tuberculosis*. Antibiotics. 2014;3(3):317–40.

133. Bardal S, Waechter J, Martin D. Chapter 18 Infectious diseases. In: Applied Pharmacology. Saunders; 2011. p. 233–91.

134. Grobbelaar M, Louw GE, Sampson SL, Helden PD van, Donald PR, Warren RM. Evolution of rifampicin treatment for tuberculosis. Infect Genet Evol. 2019;74(103937):1–9.

135. Forbes M, Kuck NA, Peets EA. Mode of Action of Ethanibutol. J Bacteriol. 1962;84(5):1099–103.

136. Chen Zhu, Yu Liu, Lihua Hu, Min Yang and Z-GH. Molecular mechanism of the synergistic activity of ethambutol and isoniazid against *Mycobacterium tuberculosis*. J Biol Chem. 2018;293(43):16741–50.

137. Rastogi N, Goh KS, Horgen L, Barrow WW. Synergistic activities of antituberculous drugs with cerulenin and trans-cinnamic acid against *Mycobacterium tuberculosis*. FEMS Immunol Med Microbiol. 1998;21(2):149–57.

138. Coloma MJ, Morrison SL. The emb operon, a gene cluster of *Mycobacterium tuberculosis* involved in resistance to ethambutol. 1990;27(5):159–63.

139. Sreevatsan S, Stockbauer KE, Pan X, Kreiswirth BN, Moghazeh SL, Jacobs WR,

et al. Ethambutol resistance in *Mycobacterium tuberculosis*: Critical role of embB mutations. Antimicrob Agents Chemother. 1997;41(8):1677–81.

140. Zhang Y, Wade MM, Scorpio A, Zhang H, Sun Z. Mode of action of pyrazinamide: Disruption of *Mycobacterium tuberculosis* membrane transport and energetics by pyrazinoic acid. J Antimicrob Chemother. 2003;52(5):790–5.

141. Zhang Y, Shi W, Zhang W, Mitchison D. Mechanisms of Pyrazinamide Action and Resistance. Microbiol Spectr [Internet]. 2014;2(4):1–12. Available from: https://www.ncbi.nlm.nih.gov/pmc/articles/PMC4268777/pdf/nihms594851.pdf

142. Campbell JR, Nsengiyumva P, Chiang LY, Jamieson F, Khadawardi H, Mah HKH, et al. Costs of Tuberculosis at 3 Treatment Centers, Canada, 2010–2016. Emerg Infect Dis. 2022;28(9):1814–23.

143. FDA news release. FDA approves new drug for treatment-resistant forms of tuberculosis that affects the lungs. https://www.fda.gov/news-events/press-announcements/fda-approves-new-drug-treatment-resistant-forms-tuberculosis-affects-lungs. 2019.

144. Conradie F, Diacon AH, Ngubane N, Howell P, Everitt D, Crook AM, et al. Treatment of Highly Drug-Resistant Pulmonary Tuberculosis. N Engl J Med. 2020;382(10):893–902.

145. Mudde SE, Alsoud RA, Meijden A Van Der, Upton AM, Lotlikar MU, Simonsson USH, et al. Predictive Modeling to Study the Treatment-Shortening Potential of Novel Tuberculosis Drug Regimens, Toward Bundling of Preclinical Data. J Infect Dis. 2022;225:1876–85.

146. Berg A, Clary J, Hanna D, Hartley D, Ammerman N, Ramey M. Model-Based Meta-Analysis of Relapsing Mouse Model Studies from the Critical Path to Tuberculosis Drug Regimens Initiative Database. Antimicrob Agents Chemother. 2022;66(3):e01793-21.

147. Xu J, Li S, Almeida D V, Tasneen R, Barnes-boyle K, Converse PJ, et al. Contribution of Pretomanid to Novel Regimens Containing Bedaquiline with either Linezolid or Moxifloxacin and Pyrazinamide in Murine Models of Tuberculosis. Antimicrob Agents Chemother. 2019;63(5):e00021-19.

148. Tasneen R, Betoudji F, Tyagi S, Li SY, Williams K, Converse PJ, et al. Contribution of oxazolidinones to the efficacy of novel regimens containing bedaquiline and pretomanid in a mouse model of tuberculosis. Antimicrob Agents Chemother. 2016;60(1):270–7.

149. Larkins-Ford J, Degefu YN, Van N, Sokolov A, Aldridge BB. Design principles to assemble drug combinations for effective tuberculosis therapy using interpretable pairwise drug response measurements. Cell Reports Med. 2022;3(9).

150. Mbuagbaw L, Guglielmetti L, Hewison C, Bakare N, Bastard M, Caumes E, et al. Outcomes of bedaquiline treatment in patients with multidrug-resistant tuberculosis. Emerg Infect Dis. 2019;25(5):936–43.

151. Pontali E, Sotgiu G, D'Ambrosio L, Centis R, Migliori GB. Bedaquiline and multidrug-resistant tuberculosis: A systematic and critical analysis of the evidence. Eur Respir J [Internet]. 2016;47(2):394–402. Available from: http://dx.doi.org/10.1183/13993003.01891-2015

152. Bruhn DF, Scherman MS, Liu J, Scherbakov D, Meibohm B, Böttger EC, et al. In vitro and in vivo evaluation of synergism between anti-tubercular spectinamides and non-classical tuberculosis antibiotics. Sci Rep [Internet]. 2015;5:1–10. Available from: http://dx.doi.org/10.1038/srep13985

153. Lee RE, Hurdle JG, Liu J, Bruhn DF, Matt T, Scherman MS, et al. Spectinamides: A New Class of Semisynthetic Anti-Tuberculosis Agents that Overcome Native Drug Efflux. Nat Med. 2017;20(2):152–8.

154. Lu X, Smare C, Kambili C, El Khoury AC, Wolfson LJ. Health outcomes of bedaquiline in the treatment of multidrug-resistant tuberculosis in selected high burden countries. BMC Health Serv Res [Internet]. 2017;17(1):1–12. Available from: http://dx.doi.org/10.1186/s12913-016-1931-3

155. Manjunatha U, Boshoff HI, Barry CE. The mechanism of action of PA-824: Novel insights from transcriptional profiling. Commun Integr Biol [Internet]. 2009;2(3):215–8. Available from: http://www.ncbi.nlm.nih.gov/pubmed/19641733%0Ahttp://www.pubmedcentral.nih.gov/articlerender.fcgi?artid=PMC2717523

156. Roger C, Roberts JA, Muller L. Clinical Pharmacokinetics and Pharmacodynamics of Oxazolidinones. Clin Pharmacokinet. 2018;57(5):559–75.

157. Colca JR, McDonald WG, Waldon DJ, Thomasco LM, Gadwood RC, Lund ET, et al. Cross-linking in the living cell locates the site of action of oxazolidinone antibiotics. J Biol Chem [Internet]. 2003;278(24):21972–9. Available from: http://dx.doi.org/10.1074/jbc.M302109200

158. WHO. Global Tuberculosis Report 2018 [Internet]. 2018. Available from: https://apps.who.int/iris/handle/10665/274453

159. TB-Alliance. Update on Pretomanid , in Combination with Bedaquiline and Linezolid (the BPaL Regimen) in Drug-Resistant TB. 2022.

160. Conradie F, Bagdasaryan TR, Borisov S, Howell P, Mikiashvili L, Ngubane N, et al. Bedaquiline–Pretomanid–Linezolid Regimens for Drug-Resistant Tuberculosis. N Engl J Med. 2022;387(9):810–23.

161. Nambiar R, Tornheim JA, Diricks M, Bruyne K De, Sadani M, Shetty A, et al. Linezolid resistance in *Mycobacterium tuberculosis* isolates at a tertiary care centre in Mumbai, India. Indian J Med Res. 2021;154:85–9.

162. Richter E, Rüsch-Gerdes S, Hillemann D. First linezolid-resistant clinical isolates of *Mycobacterium tuberculosis*. Antimicrob Agents Chemother. 2007;51(4):1534–6.

163. Berry C, du Cros P, Fielding K, Gajewski S, Kazounis E, McHugh TD, et al. TB-

PRACTECAL: study protocol for a randomised, controlled, open-label, phase II–III trial to evaluate the safety and efficacy of regimens containing bedaquiline and pretomanid for the treatment of adult patients with pulmonary multidrug-resistant tubercul. Trials [Internet]. 2022;23(1):1–16. Available from: https://doi.org/10.1186/s13063-022-06331-8

164. Tiberi S, Scardigli A, Centis R, D'Ambrosio L, Muñoz-Torrico M, Salazar-Lezama MÁ, et al. Classifying new anti-tuberculosis drugs: rationale and future perspectives. Int J Infect Dis. 2017;56:181–4.

165. WHO. WHO consolidated guidelines on tuberculosis. WHO Press. 2022.

166. Wu S, Zhang Y, Sun F, Chen M, Zhou L, Wang N, et al. Adverse events associated with the treatment of multidrug-resistant tuberculosis: A systematic review and meta-analysis. Am J Ther. 2016;23(2):e521–30.

167. Misra A, Hickey AJ, Rossi C, Borchard G, Terada H, Makino K, et al. Inhaled drug therapy for treatment of tuberculosis. Tuberculosis. 2011;91(1):71–81.

168. Braunstein M, Hickey AJ, Ekins S. Why Wait? The Case for Treating Tuberculosis with Inhaled Drugs. Pharmacol Res. 2020;36(12):166.

169. Matthieu B, Matthieu J, Nicolas G, Patrice G, Srine M, William C, et al. Comparison of intrapulmonary and systemic pharmacokinetics of colistin methanesulfonate (CMS) and colistin after aerosol delivery and intravenous administration of CMS in critically ill patients. Antimicrob Agents Chemother. 2014;58(12):7331–9.

170. Liu J, Bruhn DF, Lee RB, Zheng Z, Janusic T, Scherbakov D, et al. Structure-activity relationships of spectinamide antituberculosis agents: A dissection of ribosomal inhibition and native efflux avoidance contributions. ACS Infect Dis. 2017;3(1):72–88.

171. Bruhn DF, Scherman MS, Liu J, Scherbakov D, Meibohm B, Böttger EC, et al. In vitro and in vivo evaluation of synergism between anti-tubercular spectinamides and non-classical tuberculosis antibiotics. Sci Rep. 2015;5:1–10.

172. Robertson GT, Scherman MS, Bruhn DF, Liu J, Hastings C, McNeil MR, et al. Spectinamides are effective partner agents for the treatment of tuberculosis in multiple mouse infection models. J Antimicrob Chemother. 2017;72(3):770–7.

173. Rathi C, Lukka PB, Wagh S, Lee RE, Lenaerts AJ, Braunstein M, et al. Comparative pharmacokinetics of spectinamide 1599 after subcutaneous and intrapulmonary aerosol administration in mice. Tuberculosis [Internet]. 2019;114:119–22. Available from: https://doi.org/10.1016/j.tube.2018.12.006

174. Hickey AJ, Misra A, Fourie PB. Dry powder antibiotic aerosol product development: Inhaled therapy for tuberculosis. J Pharm Sci [Internet]. 2013;102(11):3900–7. Available from: http://dx.doi.org/10.1002/jps.23705

CHAPTER 2

Preclinical *in vivo* Assessment of Replacing Linezolid with Spectinamide 1599 in the Nix-TB Regimen

Introduction

Human tuberculosis (TB) is caused by *Mycobacterium tuberculosis* (Mtb) (1,2). TB is a curable disease; however, it requires long-term multi drug chemotherapy. The standard TB chemotherapy comprises of four anti-TB drugs such as isoniazid (INH), rifampicin (RIF), ethambutol (EMB) and pyrazinamide (PZA). These drugs are used for the treatment of drug-susceptible TB (DS-TB) which requires a treatment course of ~6-9 months (3,4). Lack of patient compliance, substandard quality of antibiotics, difficult management of multidrug therapies and malnutrition are the major factors contributing to the development of drug resistance against TB (5,6). Drug resistance in TB patients is clinically attributed to patients that do not respond to RIF (RIF resistant or RR-TB) or to both drugs, RIF and INH (multidrug-resistant or MDR-TB). When patients are already MDR and do not respond also to any fluoroquinolone and at least to one of the three injectables second-line drugs i.e., amikacin, kanamycin, or capreomycin, they are clinically diagnosed as extensively drug-resistant or XDR-TB.

In 2021, there were 10.6 million new cases of TB diagnosed and among those, 450,000 cases were also diagnosed as MDR- or XDR-TB. MDR- and XDR-TB takes several months to more than 2 years of multidrug therapy with limited treatment options (7). The long treatment duration and complexity of these regimens result in a high

healthcare cost and thus the treatment of MDR-TB remains a public health crisis (8). In addition to problems associated with the length, cost, and intensity of treatment, the outcomes are extremely poor, especially in MDR- and XDR-TB (9). In this scenario, the World Health Organization (WHO) proposed the End TB Strategy. Using the 2015 data as a benchmark, this program aims to control TB worldwide by 2035. The latter will be achieved by reducing mortality and morbidity by 95% and 90% respectively, along with zero TB-affected families facing catastrophic costs due to TB.

More recently, the United States Food and Drug Administration (FDA) approved a 6-month novel treatment regimen of 3 oral drugs: bedaquiline (B), pretomanid (Pa) and linezolid (L) referred to as BPaL regimen. In this regimen, each drug has potent preclinical and clinical anti-TB activity with minimal pre-existing resistance. Preclinical studies in animal models demonstrated the better efficacy of BPaL regimen for DS-TB compared to the standard TB chemotherapy (8,10,11). The BPaL regimen was tested in the Nix-TB clinical trial (12) conducted in South Africa. The trial enrolled patients with XDR-TB as well as treatment-intolerant or non-responsive MDR-TB, including HIV positive patients with a CD4 count of 50 or higher were enrolled. The treatment regimen showed remarkable results by curing 95 out of 107 patients though it had a high rate of adverse effects (AEs). A follow up trial, the ZeNix (13), designed to fine-tune linezolid doses was conducted in South Africa, Russia, Georgia, and Moldova and this trial enrolled 181 patients (including 20% HIV+) with drug resistant TB. The ZeNix resulted in a high success rate like Nix-TB trial and had fewer AEs. Therefore, approval of the BPaL regimen was one of the steps taken towards achieving WHO goal to end TB and spread of drug resistance.

Bedaquiline (B) is a novel anti-TB drug recommended by WHO for the treatment of MDR- and XDR-TB (14). This is the only anti-TB drug that binds to the subunit c of ATP synthase enzyme and thereby targets the energy metabolism of Mtb (15). It has significant minimum inhibitory concentrations (MICs) both against DS-TB and drug-resistant TB in combination with other TB drugs (14) and it is equally effective against replicating and nonreplicating Mtb and against both INH- and rifampicin-resistant Mtb strains (16). Some studies have reported that B also activates host macrophage innate immune resistance to Mtb infection (17,18). B alone or in combination with other anti-TB drugs such as PZA, moxifloxacin and clofazimine improves the efficacy of treatment in murine models when compared to the standard TB chemotherapy (19,20). A study on the cost-effectiveness analysis in selected high TB burden countries showed that addition of B to MDR-TB regimen improves the health outcomes and reduces cost (21). It is pertinent to mention as well that in some patients, administration of B is associated with several safety concerns including heart- and liver-related drug reactions leading, in few instances, to death (15).

Pretomanid (Pa) is a prodrug which is metabolically activated by Mtb nitroreductase enzyme. The active form of Pa acts against both replicating and hypoxic, and non-replicating Mtb by its two unique mechanisms of action (22–24). In aerobic state, Pa blocks Mtb cell wall production by inhibiting protein and lipid synthesis by a mechanism which decreases the availability of keto mycolic acids (25). While in anaerobic conditions, the therapeutic action of Pa against Mtb is to produce nitric oxide (NO) and it functions as “suicide bomb", by inhibiting cytochrome c oxidase that leads to a significant reduction in ATP concentrations in the cell (23,25). Based on the

promising published data, Pa was recently approved by WHO for the treatment of drug resistant TB in combination with B and linezolid. The AEs data of Pa is still incomplete but the most common effects reported in trails include gastrointestinal, dermatological and musculoskeletal events along with consistent reversible increase in serum creatinine and transient liver enzyme elevation (26–28).

Linezolid (L) is a synthetic antibiotic that belongs to the oxazolidinone group and functions as a protein synthesis inhibitor. This drug binds to a site on bacterial 23S ribosomal RNA of 50S subunit and thereby prevents the formation of 70S ribosomal unit (29,30). L is a protein inhibitor in prokaryotic cells, but it also binds to mitochondrial ribosomes, leading to mitochondrial protein inhibition and mitochondrial toxicity. The later results in activation of the Nlrp3 inflammasome and *in vivo* inflammatory response associated with suppression of bone marrow myeloid precursors, which is consistent with the hematologic anomalies seen in patients (31–33). It was recently categorized as Group A drug by WHO for the treatment of MDR-TB and XDR-TB (34). L associated AEs encompasses bone marrow myelosuppression, anemia, peripheral and optic neuropathy leading to disability and blindness often of irreversible nature (33,35).

Spectinomycin, an aminocyclitol antibiotic, is a broad spectrum antibiotic used mainly for treatment of *Nisseria gonorrhoeae* (36). Although the efficacy of spectinomycin against Mtb is poor due to the efflux of drug by Rv1258c transporters present on the surface of Mtb, it has a high safety profile with no known ototoxicity and nephrotoxicity (37,38). The poor activity of spectinomycin against Mtb was compensated for by its structural modification leading to the development of a series of semisynthetic analogues called spectinamides (2,39). Spectinamides potent anti-

tubercular activity is attributed to its ability to evade the drug efflux and unlike spectinomycin, they bind selectively with bacterial 30S ribosomes (helix 34 of 16S rRNA) but not with the mammalian mitochondrial 30S (40,41). Moreover, spectinamides are active under hypoxic conditions and have shown excellent activity against MDR- and XDR-TB in in vitro models (19,42). However, poor oral availability of spectinamides has limited its usage to injectables.

Spectinamide 1599 (S), one of the lead compounds, has demonstrated promising results both *in vitro* and *in vivo* studies and it lacks cross-resistance with existing anti-TB drugs (19,40–44). Moreover, S shows synergy when combined with classical and non-classical tuberculosis drugs. One study (41) showed *in vitro* synergy of S with clarithromycin, doxycycline and clindamycin and *in vivo* with clarithromycin. Co-administration of S subcutaneously (SC) in different mouse models shows synergistic activity with most of the anti-TB drugs such as RIF, PZA, B and P (19).

Inhalation or direct administration of aerosolized antibiotics to the lung, main site of Mtb infection, has being studied for decades as an alternative to systemic drug administration. Despite the efficacious results, one of the limitations of using S as injectable is the risk of lack of patient compliance with long duration of TB treatment (45). Direct administration of S has been tested in preclinical *in vivo* studies using liquid formulation of the drug. These studies have shown that monotherapy of S or combination with PZA have high efficacy and good tolerability (46,47). A comparative study assessing biodistribution of the drug in relation to the administration route demonstrated that S has 48 times higher exposure in mouse lungs via inhalation than by subcutaneous injection; the latter may explain the increased efficacy of this drug via

intrapulmonary aerosol (43,47). Moreover, like other members of aminocyclitol group (tobramycin and amikacin) administered as inhalation therapy (48), S shows potential to be used as a dry powder inhalation therapy (48). Therefore, in this study, we propose to replace L in the BPaL regimen with S as BPaS regimen. We hypothesize that inhalational administration of S if combined with BPa (BPaS regimen) has higher or similar efficacy than the BPaL regimen. Furthermore, the BPaS regimen avoids the adverse effects observed during administration of the BPaL regimen.

Materials and Methods

Mice and Mtb infection

Female C3HeB/FeJ and BALB/c mice at 6-8 weeks of age were purchased from the Jackson Laboratories (Bar Harbor, ME). Before infection, mice were rested for at least one week inside the BSL3 laboratory at Colorado State University (CSU). All protocols and use of these animals were reviewed and approved by the Institutional Animal Care and Use Committee (IACUC) at CSU. *Mycobacterium tuberculosis* (Mtb) Erdman strain was used to infect the animals. Briefly, animals were infected using a low dose aerosol (LDA) infection of Mtb (ATCC 35801) using the inhalation exposure system (Glas-Col, Terre Haute, IN). The nebulizer attached to the Glass- Col chamber was loaded with five mL of an inoculum solution ($2x10^6$ colony forming units (CFU)/mL) and the Glass-Col unit was calibrated to deliver ~50-100 CFU to the lungs of each mouse located inside the chamber. To confirm the bacterial deposition into the lungs, mice (n=5) were euthanized after infection and their lung homogenates were plated onto 7H11 agar plates followed by incubation at 37 °C for 3-4 weeks until the colonies were

visible to the naked eye on the agar and were enumerated. Likewise, the CFU in serial dilutions of the inoculum were also determined as explained above. Clinical observations of these mice (e.g., inactivity, rough fur, hunched posture, increased respiratory rate or effort) were monitored daily and their live body weights were taken weekly. As per IACUC protocol, mice were sacrificed if the loss of body weight was <20% of the initial weight.

Drug preparation and treatment

Bedaquiline fumarate (B: cat#B165121) and linezolid (L: cat#L3453) were obtained from LKT laboratories (St. Paul, MN), pretomanid (Pa: cat#140130) from ChemShuttle (Burlingame, CA) and spectinamide 1599 (dihydrochloride) was provided by Dr. Lee at St. Jude Children's Research Hospital (Memphis, TN). B was administered at 25 mg per kg (mpk) whereas Pa and L were dosed at 100mpk each and 1599 at 50mpk and 100mpk in BALB/c and C3HeB/FeJ TB models respectively. The drugs were formulated in weekly batches according to the live body weights of the animals, aliquoted for single daily dosing and stored at 4 °C in the dark. All drugs were administered once daily for 5 days/week for 4 weeks by oral (gavage) administration except S which was administered 3 days/week on the alternate days by intrapulmonary aerosol using MicroSprayer® aerosolized (Penn Century). The drug treatments were started at 4 weeks post infection in BALB/c while 8-9 weeks post infection in C3HeB/FeJ TB models. B was administered in the morning, Pa one hour after B and, L and S at least 4 hours after Pa. The timeline and drug regimen are given in Figure 2.1.

C3HeB/FeJ TB Model

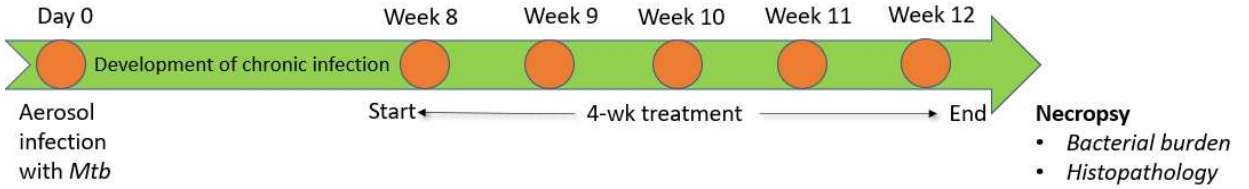

Group	Drug	Dose (mg/kg)	Route	Mice	Treatment (week)	
					Frequency	Duration
1	No treatment	NA	NA	5-10	5 days	4
2	B+Pa	25/100	Oral			
3	B+Pa+L	25/100/100	Oral			
4	B+Pa+S	25/100/100	Oral + IT			
5	Linezolid	100	Oral			
6	Spectinamide-1599	100	IT			

IT = Intra tracheal

BALB/c TB Model

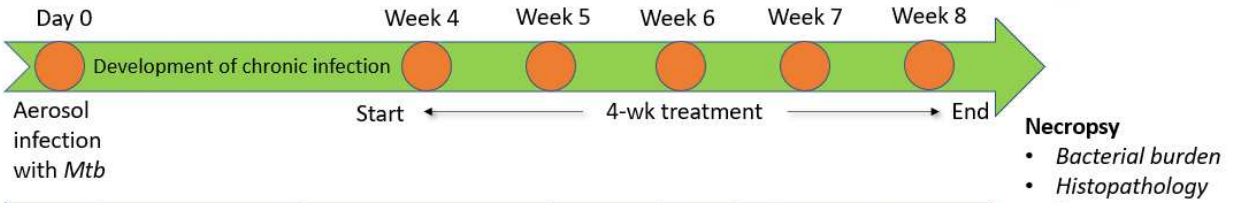

Group	Drug	Dose (mg/Kg)	Route	Mice	Treatment (week)	
					Frequency	Duration
1	No treatment	NA	NA	5-10	5 days	4
2	B+PA+L	25/100/100	Oral			
3	B+PA+S	25/100/50	Oral + IT			
4	Linezolid	100	Oral			
5	Spectinmide-1599	50	IT			
6	Vehicle	Saline	Oral			

IT = Intra tracheal

Figure 2.1. Experimental design of the studies. (Top) C3HeB/FeJ mice were infected with Mtb (C3HeB/FeJ TB model) and rested for 8 weeks. Mice were randomly divided into 6 groups and treated with monotherapy or combination therapy for 4 weeks starting from week 9 post infection to week 12. (Bottom) BALB/c mice were randomly divided into 8 groups after infection with Mtb (BALB/c TB model). Animals were treated for 2 weeks (combination therapy) and 4 weeks (monotherapy and combination therapy). For both studies, mice were euthanized at the end of the drug-treatment and organs were collected for further analysis.

The drugs were prepared as reported previously (19). B was prepared in an acidified solution. Briefly, B was taken into a brand-new Pyrex glass flask. A 20% 2-hydroxypropyl-β-cyclodextrin (Sigma) solution [prepared with autoclaved Milli-Q water and filter sterilized through a 0.2 µM filter] was added into the flask. Calculated volume of freshly prepared 1N HCl solution was added dropwise until the solution became clear. The flask was completely covered by aluminum foil and stirred overnight with the addition of a brand-new Teflon coated magnetic stir bar (VWR). Next day, if the solution was still cloudy, more 1N HCl was added, whilst warming the solution to a maximum of 37°C. The pH of B solution was adjusted to 3.5 with dropwise addition of freshly made 1N NaOH if necessary. The batch was then aliquoted with a glass pipette into amber glass vials.

The Pa was suspended in 10% 2-hydroxypropyl-β-cyclodextrin (Sigma) in a conical tube and rotated overnight using an orbital shaker (Orbital Genie). Next day, the suspension was sonicated twice with a Vibra Cell probe Sonicator for 10 minutes at 25% amplitude and 15 minutes at 30% amplitude to make sure the homogeneous mixing of Pa. During this process the drug tube was kept on ice. In between sonication steps, frozen 10% w/v soybean lecithin (MP Biomedicals, Irvine, CA) was added, and the suspension tube was stirred for 10 minutes at room temperature.

The L was suspended in 5% v/v polyethylene glycol 200 [PEG 200, Sigma] in a conical tube and grinded with a tissue grinder. Then 95% v/v methylcellulose (Sigma) in the distilled water was added and the tube was placed on an orbital shaker overnight at a slow rotation of 25 rpm.

The S was dissolved in 0.22 µm filtered endotoxin free 0.9% saline water (Teknova) and then aliquoted.

Necropsy of animals

After 4-weeks of treatment, BALB/c and C3HeB/FeJ mice were euthanized by CO_2 narcosis, the thoracic cavity was opened and whole blood was collected via cardiac puncture in EDTA containing tubes. Lung, spleen, and long bones were collected from each mouse for further processing and analysis.

Assessment of treatment efficacy in the lungs

The efficacy of treatment was assessed by determining the reduction in bacterial burden [measured as colony forming unit; CFU] in the lung and spleen of animals at the end of drug treatment. Lungs were homogenized using the Next Advance Bullet Blender (Averill Park, NY). Briefly, the whole lung was placed into two 1.5 mL sterile, safe lock Eppendorf tubes (half lung in each tube) containing 0.5 mL sterile 1xPBS and 3 × 3.2 mm sterile stainless-steel beads. Thereafter the tubes were placed in the Bullet Blender and homogenized for 4 min at 800 rpm. Lung homogenate from both tubes were mixed and plated in a serial 10-fold dilutions onto 7H11 agar plates supplemented with 0.4% activated charcoal to reduce the carryover effect of drugs and incubated for 6-8 weeks before the final CFU count. The remaining lung homogenate samples were centrifuged, and the supernatant was collected and stored at -80°C for further evaluation of their cytokine and chemokines content.

Histopathological evaluation and lesion scoring

A separate group of mice were sacrificed and their whole lungs were fixed in 4% paraformaldehyde (PFA) for 48 hours and embedded in paraffin for histopathology purposes. Sections were cut at 5 µm, stained with hematoxylin and eosin [H&E (Leica Biosystems)] and scanned at 40X magnification using the multispectral automated PhenoImager (Akoya Biosciences Inc.) for histopathological evaluation. The extent of the lesion burden in the lungs was quantified using blinded digital images and an open-source QuPath software for image analysis. For each tissue section, a region of interest (ROI) was generated at low magnification with a custom tissue detecting algorithm using decision forest training and classification to differentiate tissue versus background based on color and area. Lesions were identified within tissue ROIs at high magnification with an additional custom-made algorithm using decision forest training and classification based on staining intensity, color normalization and deconvolution, area, and morphological features. Percent lesion calculations were integrated into the same algorithm and calculated from tissue area and lesion area as designated by the ROI and lesions detected.

Bone marrow histopathology

The sternum and femur and tibia bones from both limbs of each mouse were collected. Muscles in the bones were removed as much as possible with the help of scissors and forceps. The sternum and one femur were fixed in 4% PFA and processed for histology. To evaluate the myelosuppressive effect of the drugs, bone sections were cut at 5 µm and stained with H&E. The number of myeloid and erythroid cells from 5 different regions of the bone were blinded and then counted by a veterinary pathologist.

The rest of the bones were used to collect bone marrow. Briefly, a 0.6 mL sterile eppendorf tube punctured at the bottom with the help of a 26-gauge needle was inserted into a 1.5 mL sterile eppendorf tube. One end of the epiphysis of the long bones was cut open to expose the bone marrow and placed down into the small eppendorf tube-system. The tubes were centrifuged at 10,000 x g for 15 seconds and the marrow was collected from the base of the large eppendorf tube. The bone marrow was resuspended in PBS and centrifuged again. Thereafter, the supernatant was collected and stored at -80 °C for evaluation of cytokines and chemokines content while the bone marrow cells were saved in 4% PFA and freezing media for further use in clinical pathology analysis and flow cytometry, respectively.

Processing of blood

For complete blood count (CBC) analysis of C3HeB/FeJ animals during the treatment, blood was collected via submandibular vein as described previously (49). Briefly, the mouse was held by the scruff of the neck and their submandibular vein was lanced with a sterile single-use mouse Goldenrod lancet (4 mm). The blood was collected in K2-EDTA tubes and 50-100 µL aliquots were immediately analyzed in VETSCAN® HM5 hematology analyzer (Zoetis).

At the time of necropsy, the thoracic cavity of each mouse was opened and whole blood was collected via cardiac puncture in K2-EDTA containing tubes. After adding an equal volume of PBS, the sample was centrifuged at 800 × g for 10 min at 25 °C with the brake off (deceleration = 0). The top plasma layer was collected and stored at -80 °C for evaluation of their cytokines and chemokine content. The buffy coat was collected, washed and the erythrocytes were lysed using RBC lysis buffer (Miltenyi,

CA). The cells were washed and resuspended in 500 µL of complete DMEM media (Corning) to perform flow cytometry analysis.

Determination of cytokine and chemokine concentrations

Multiplex immunoassay using plasma, lung homogenates and bone marrow supernatants was performed using a Luminex bead-based multiplex ELISA kit (ProcartaPlex Mouse Cytokine & Chemokine Panel 1 26plex, reference # EPXR260-26088-901, Invitrogen). Each sample was normalized to the total protein concentration determined by Bicinchoninic acid (BCA) assay (Thermo Fisher). The BCA and Luminex assays were performed according to the manufacturer's instructions and the final stained samples were fixed with 4% PFA prior to acquisition. Sample data were acquired on a MAGPIX instrument running xPONENT 4.3 software (Luminex Corp.) and analyzed using a five-parameter logistic model with an 80-120% standard acceptance range. LLOQ indicates the lower limit of quantification for assay; extrapolated values below the LLOQ were evaluated at the LLOQ. Heatmaps of the cytokine and chemokine concentration levels in the samples were generated using R pheatmap package. Correlation analyses of cytokines and chemokines content with bacterial burden in the lung and spleen data were performed using the corrplot package in R.

Analysis of immune cell populations via flow cytometry

A single cell suspension of bone marrow, blood, and lung from C3HeB/FeJ TB model was prepared as described previously (3). Cells were counted using Countess 3 cell counter (Invitrogen) and 1 x 10^6 cells were added to a 96-well V-bottom plate (Greiner Bio-One, cat#651-180). Viability staining was performed by incubating cells

with 100 µl of Zombie NIR (Biolegend, cat# 423106) viability dye (1:2000 dilution prepared in PBS) for 15 minutes in the dark. Cells were washed twice, and Fc receptors were blocked using 1:200 dilution of anti-mouse CD16/32 antibody (Biolegend, cat# 156604). Cells were finally stained with predetermined optimal concentrations of specific antibodies (Table 2.1) for 30 minutes in the dark at 4^{o}C. Cells were washed to remove excess antibody, fixed using 4% PFA and resuspended in 300 µL of flow cytometry staining (FACS) buffer. Samples were acquired using Cytek Aurora^{TM} 4-Laser spectral flow cytometer where 100,000 events were recorded. Data were analyzed in FlowJo software (BD Biosciences) using manual gating (50).

Multiplex fluorescence immunohistochemistry

Five µm sections of formalin fixed paraffin embedded (FFPE) lung tissues were stained for multiplex fluorescence immunohistochemistry (mfIHC) by the Imaging Core at the University of Colorado, Anschutz Medical Campus, Denver. The mfIHC was performed for a panel of 6-color antibodies + DAPI using Opal-plex Tyramide Signal Amplification (TSA) technique in Leica Bond III autostainer. The protocol and details of antibodies and Opal fluorophores used are given in Table 2.2. Each antibody was optimized in our lab using Opal 3-Plex Anti-Rb Detection Kit (Akoya Biosciences Inc. cat# NEL830001KT) and stained with automated LabSat^{TM} Research (Lunaphore Technologies SA, Epredia). Slides were scanned using multispectral automated PhenoImager^{TM} (Akoya Biosciences) and analyzed for different immune cell populations using the inForm® tissue Finder (Version 2.4.8) and Phenochart^{TM} (Version 1.0.12) software (Akoya Biosciences).

Table 2.1. List of the antibodies used for flow cytometry.

Antibodies	Source	Identifier
Anti-mouse LY6G PerCP	BioLegend	Cat# 127654; RRID: AB_11218876
Anti-mouse CD14 PerCP Cy5.5	Invitrogen	Cat# 120606; RRID: AB_493267
Anti-mouse NKp46/CD335 PE	BioLegend	Cat# 137604; RRID: AB_2566163
Anti-mouse B220/ CD45R PE-Cy7	BioLegend	Cat# 103222; RRID: AB_2573837
Anti-mouse CD8 FITC	BioLegend	Cat# 100706; RRID: AB_394458
Anti-mouse CD34 PE-Dazzle 594	BioLegend	Cat# 128616; RRID: AB_11219403
Anti-mouse TER119 APC	BD Pharmingen	Cat# 561033; RRID: AB_10900980
Anti-mouse γδ-TCR APC Fire 750	BioLegend	Cat# 118129; RRID: AB_755986
Anti-mouse LY6C Alexa Fluor 700	BioLegend	Cat# 128024; RRID: AB_2869739
Anti-mouse CD4 BV421	BioLegend	Cat# 100544; RRID: AB_2562555
Anti-mouse MHC-II BV480	BD Biosciences	Cat# 566088; RRID: AB_2562612
Anti-mouse CD11b Pacific Blue	BioLegend	Cat# 101224; RRID: AB_2565937
Anti-mouse CD3e BV510	BioLegend	Cat# 100353; RRID: AB_2563056
Anti-mouse CD45 BV570	BioLegend	Cat# 103136; RRID: AB_2814047
Anti-mouse CD19 BV605	BioLegend	Cat# 115540; RRID: AB_2563289
Anti-mouse CCR2 BV711	BD Biosciences	Cat# 747964; RRID: AB_2660295
Anti-mouse CC11c BV785	BioLegend	Cat# 117335; RRID: AB_2073247

Statistical analysis. The lung and spleen bacterial burden data were expressed as CFU which were Log_{10}-transformed and analyzed using GraphPad Prism version 9.5.1 (GraphPad software, La Jolla, CA). The statistical analysis was performed using a Tukey's multiple comparison test as part of either one-way or two-way ANOVA and mixed-model effects where necessary. The correlation analyses were performed using the spearman's correlation test. Flow cytometry and mfIHC data were graphed in R studio and statistical evaluation was performed using stats package in R.

Table 2.2. List of the antibodies and Opal fluorophores used for multiplex fluorescence immunohistochemistry.

Antibody	Specie	Type	Company	Catalog #	Concentration	pH	Opal
CD8	Rabbit	mAb	CST	D4W2Z	1:400	6	480
CD4	Rat	mAb	Thermo Fisher	4SM95	1:200	6	520
B220	Rat	mAb	BD Pharm	RA3-6B2	1:500	6	570
Foxp3	Rabbit	mAb	R&D	MAB8214	1:200	6	620
Ly6G	Rabbit	mAb	CST	87048	1:100	6	690
F4/80	Rabbit	mAb	CST	D4C8V	1:100	6	780

Results

This study evaluated the comparative efficacy and adverse effects (AEs) of linezolid (L) and spectinamide 1599 (S) in combination with bedaquiline (B) and pretomanid (Pa) as BPaL and BPaS regimens respectively. Two mouse TB models were used: the C3HeB/FeJ and the BALB/c TB models. Mice were infected with a low-dose aerosol infection of Mtb and treated with L or S monotherapy or with a combination

therapy of BPaL or BPaS drug combinations for 4 weeks. The efficacy of each regimen was determined by comparative analysis of the bacterial burden between infected animals not receiving therapy and those treated with the BPaL or BPaS regimens. To study drug related AEs, live body weight of animals, complete blood count (CBC), bone marrow and lung histopathology along with changes in the profile of immune cell populations of animals were monitored.

Monotherapy of linezolid or spectinamide 1599 show similar efficacy in the C3HeB/FeJ TB model

To compare the efficacy of monotherapy, Mtb infected C3HeB/FeJ (n=6 mice received linezolid (L; 100 mpk administered 5/7 a week orally) or spectinamide 1599 (S; 100mpk administered 3/7 a week on alternate days via intrapulmonary aerosol delivery) for 4 weeks. At the end of treatments, the animals were sacrificed, and their lung and spleen bacterial burden (measured as CFU) were enumerated (Figure 2.2). As expected in for the C3HeB/FeJ TB model, L (7.30 ± 0.45 $\log_{10}$) and S (6.90 ± 0.48 $\log_{10}$) treated mice had similar lung CFU compared to untreated (UnRx) (7.81 ± 0.36 $\log_{10}$) control (2.2A). In spleen, however, L (4.49 ± 0.10 $\log_{10}$) treated mice had significantly ($p<0.05$) lower CFU compared to UnRx (5.43 ± 0.27 $\log_{10}$) mice whereas no significant difference ($p<0.05$) was found between L and S (4.94 ± 0.11 $\log_{10}$) treated mice (2.2B).

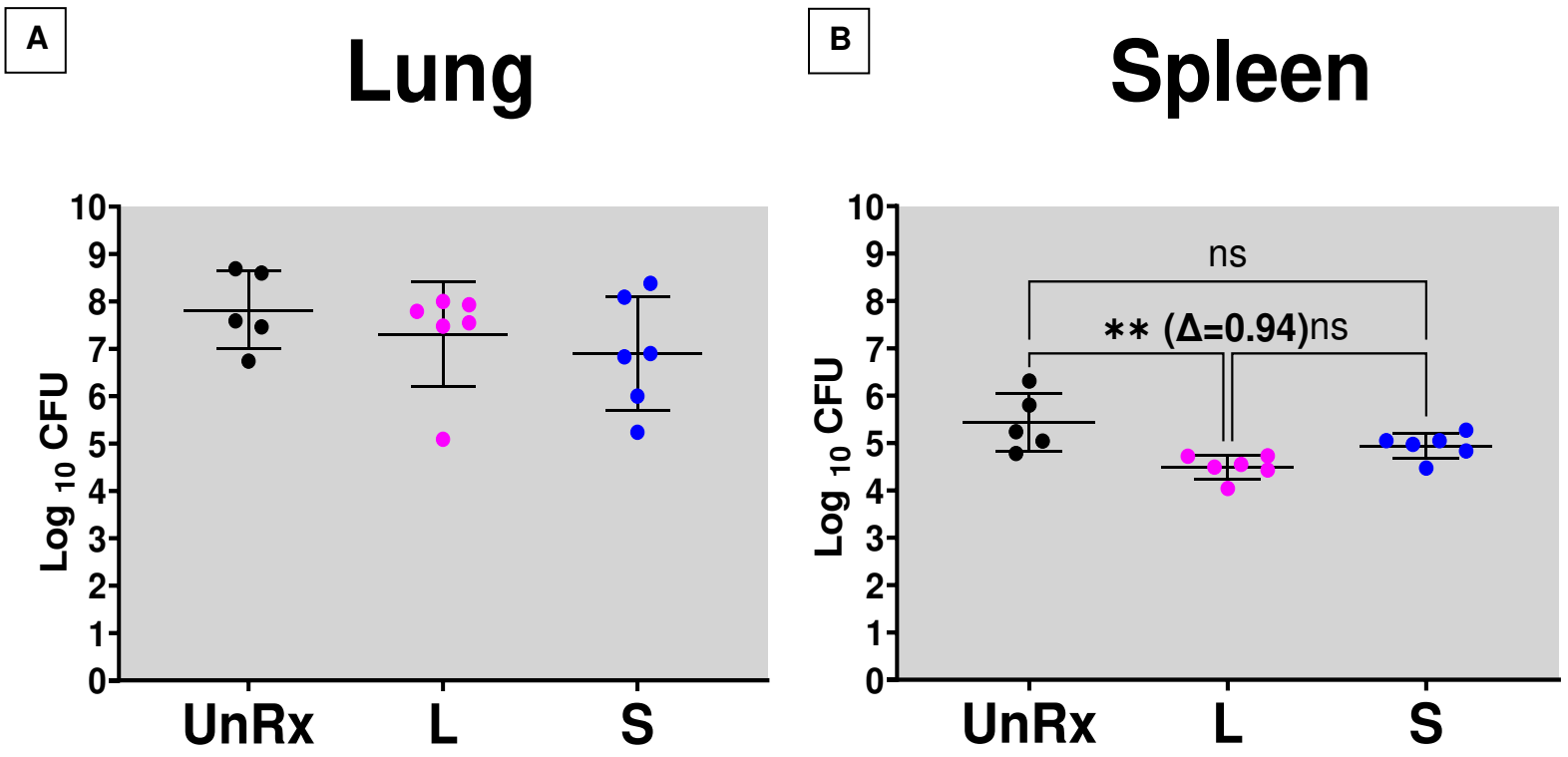

Figure 2.2. Bacterial burden (measured as $\log_{10}$ CFU per lung is in Y-axis) in Mtb infected C3HeB/FeJ mice treated with monotherapy. (A) *In vivo* efficacy data shows that linezolid (L) and spectinamide 1599 (S) treated mice had similar lung CFU as in untreated (UnRx) control. (B) In spleen, mice treated with L had significantly decreased CFU compared to UnRx control, but no significant difference was observed between in the number of CFU between L and S treated mice. ns = non-significant, ** = $p < 0.005$

Combination therapy of BPaL or BPaS have similar efficacy in the C3HeB/FeJ TB model

We further tested and compared the efficacy of combination therapy wherein linezolid (L) in BPaL regimen was replaced with inhaled spectinamide 1599 (S) (aka BPaS regimen). Mtb infected C3HeB/FeJ mice were treated with BPaL (B= 25mpk; Pa= 100mpk and L= 100mpk all administered 5/7 a week via oral gavage) or BPaS (BPa as in BPaL and S= 100mpk administered 3/7 a week on alternate days via intrapulmonary aerosol delivery) regimen for 4 weeks and their lung and spleen were cultured on agar plates for enumeration of the CFU. The comparative analysis from combined data of three independent studies is shown in Figure 2.3 and results of individual studies are shown in Figure 2.3i-iii. Two of the three studies contained an extra group of BPa only as a reference control. Compared to untreated control (7.48 ± 0.12 $\log_{10}$), mice in the BPa (5.49 ± 0.42 $\log_{10}$), BPaL (4.76 ± 0.38 $\log_{10}$) and BPaS (4.98 ± 0.35 $\log_{10}$) treatment groups had significantly ($p<0.05$) reduced the total number of lungs CFU (2.3A). Importantly among all three treatment groups, there was no significant difference between the lungs CFU. Similar results were obtained in spleen where BPa (1.54 ± 0.18 $\log_{10}$), BPaL (1.70 ± 0.14 $\log_{10}$) and BPaS (1.76 ± 0.22 $\log_{10}$) had significantly lowered the number of CFU compared to UnRx (5.69 ± 0.12 $\log_{10}$) control (2.3B). However, most of the spleen CFU remained below the limit of detection (LOD) of the assay.

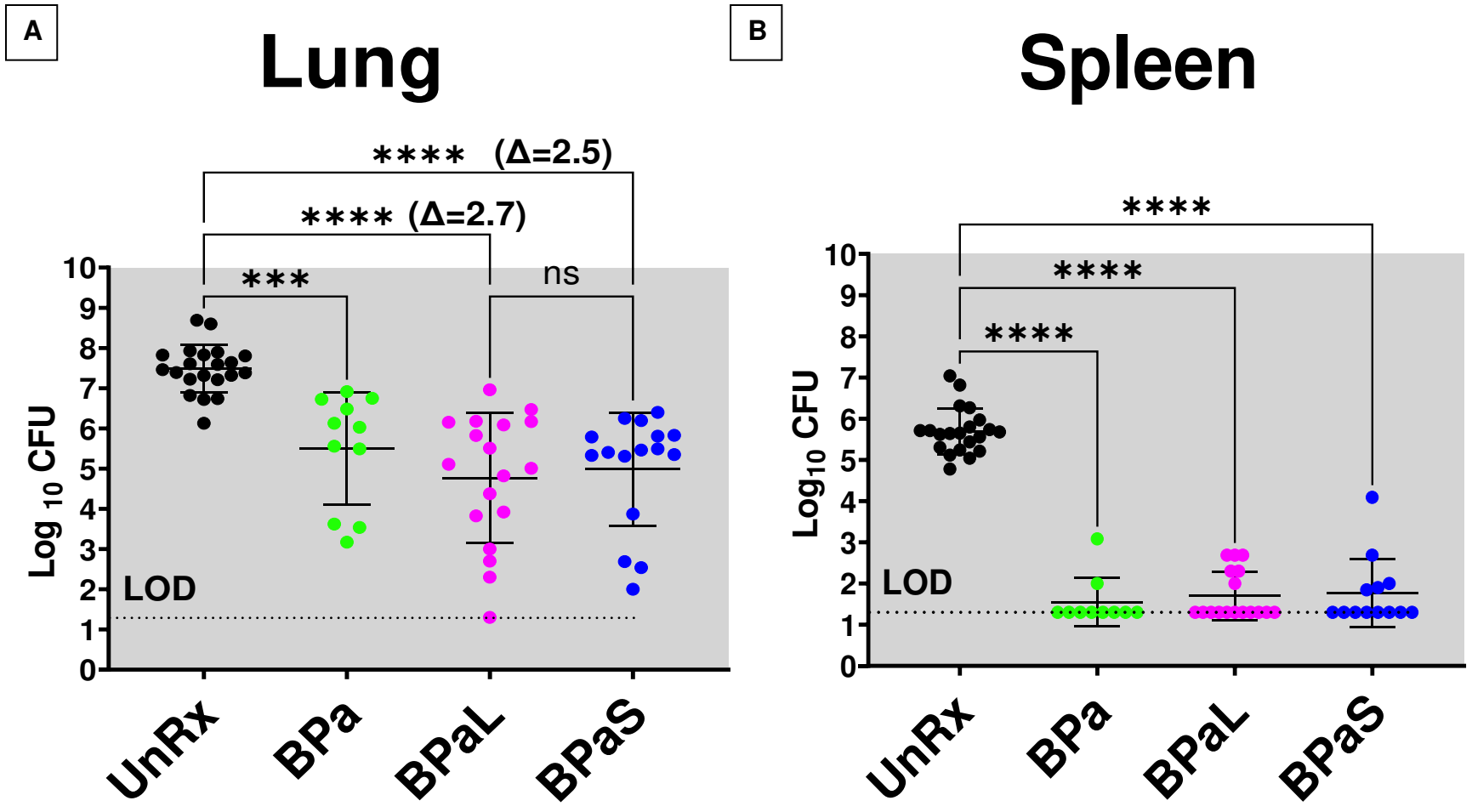

Figure 2.3. Bacterial burden (CFU) in Mtb infected C3HeB/FeJ mice treated with combination therapy. The graphs represent the combined data from three independent studies. The Y-axes show log_{10} CFU in lung (A) and spleen (B) of mice after 4 weeks of treatment with one of the multidrug combination regimens (BPa, BPaL and BPaS) and untreated (UnRx) control. No significant difference was observed among the treatment groups. The BPa group was included in one of the two studies. LOD: limit of detection, ns = non-significant, *** = $p < 0.0005$, **** = $p < 0.00005$

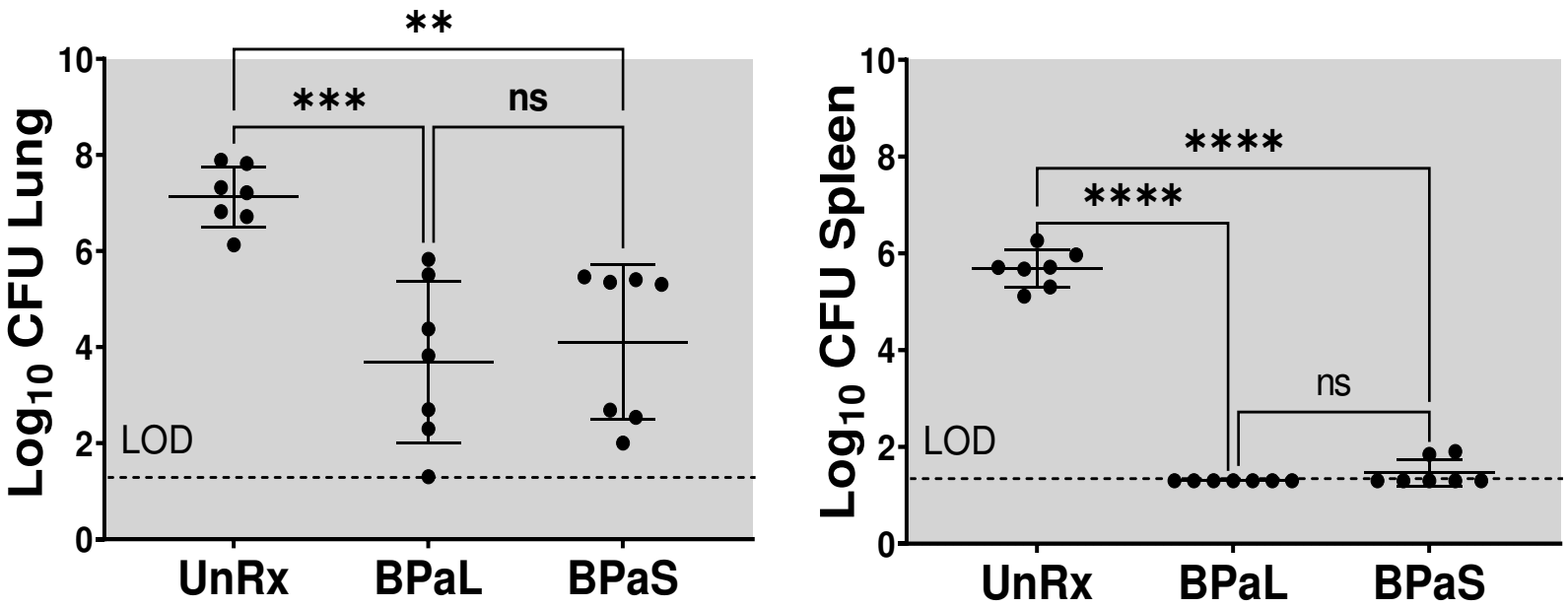

Figure 2.3i (C3HeB/FeJ Study 1). Lung and spleen bacterial burden (CFU) in Mtb infected C3HeB/FeJ mice treated with BPaL and BPaS regimen for 4 weeks. n = 7, LOD: limit of detection, ns = non-significant, ** = $p < 0.005$, *** = $p < 0.0005$, **** = $p < 0.00005$

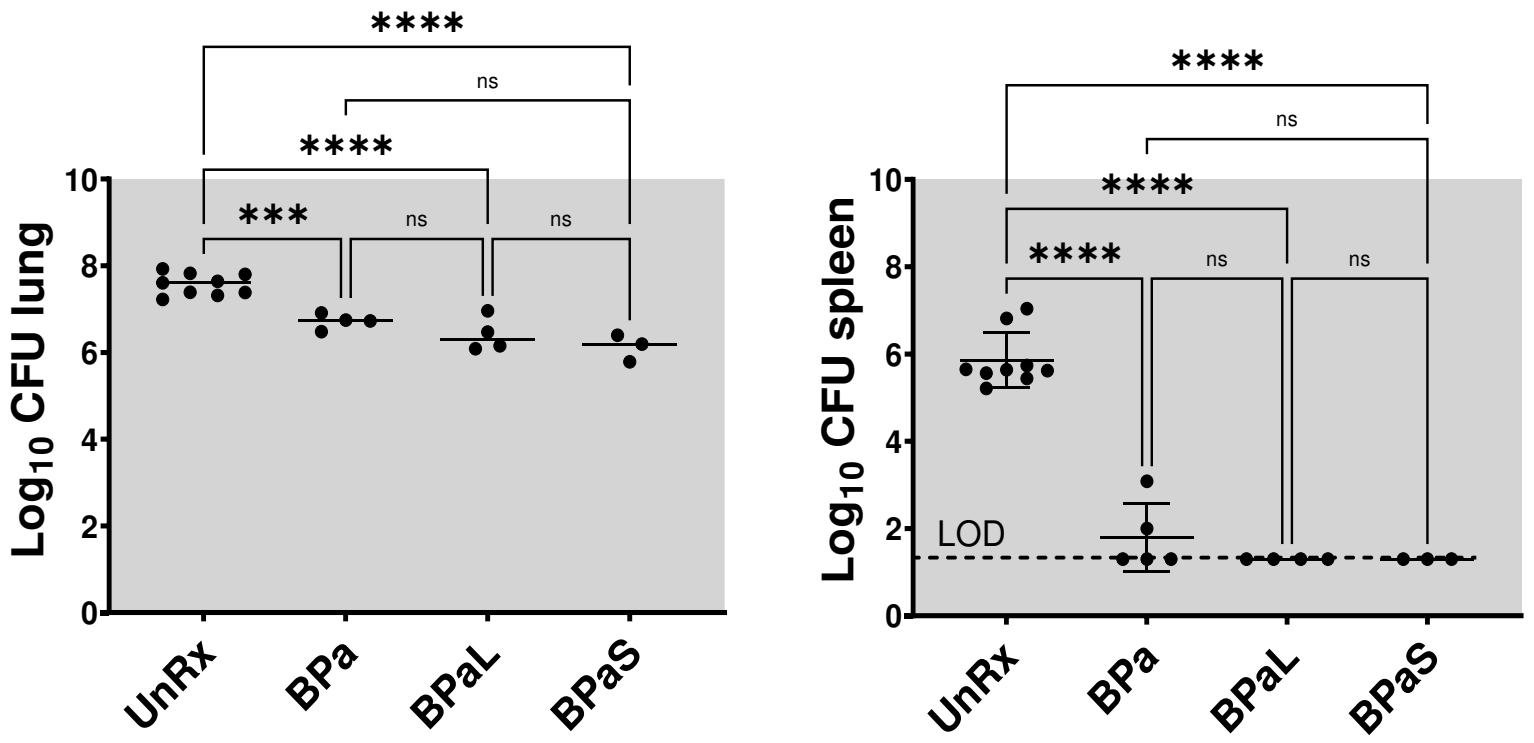

Figure 2.3ii (C3HeB/FeJ Study 2). Lung and spleen bacterial burden (CFU) in Mtb infected C3HeB/FeJ mice treated with BPaL and BPaS regimen for 4 weeks. n = 3-9, LOD: limit of detection, ns = non-significant, *** = $p < 0.0005$, **** = $p < 0.00005$

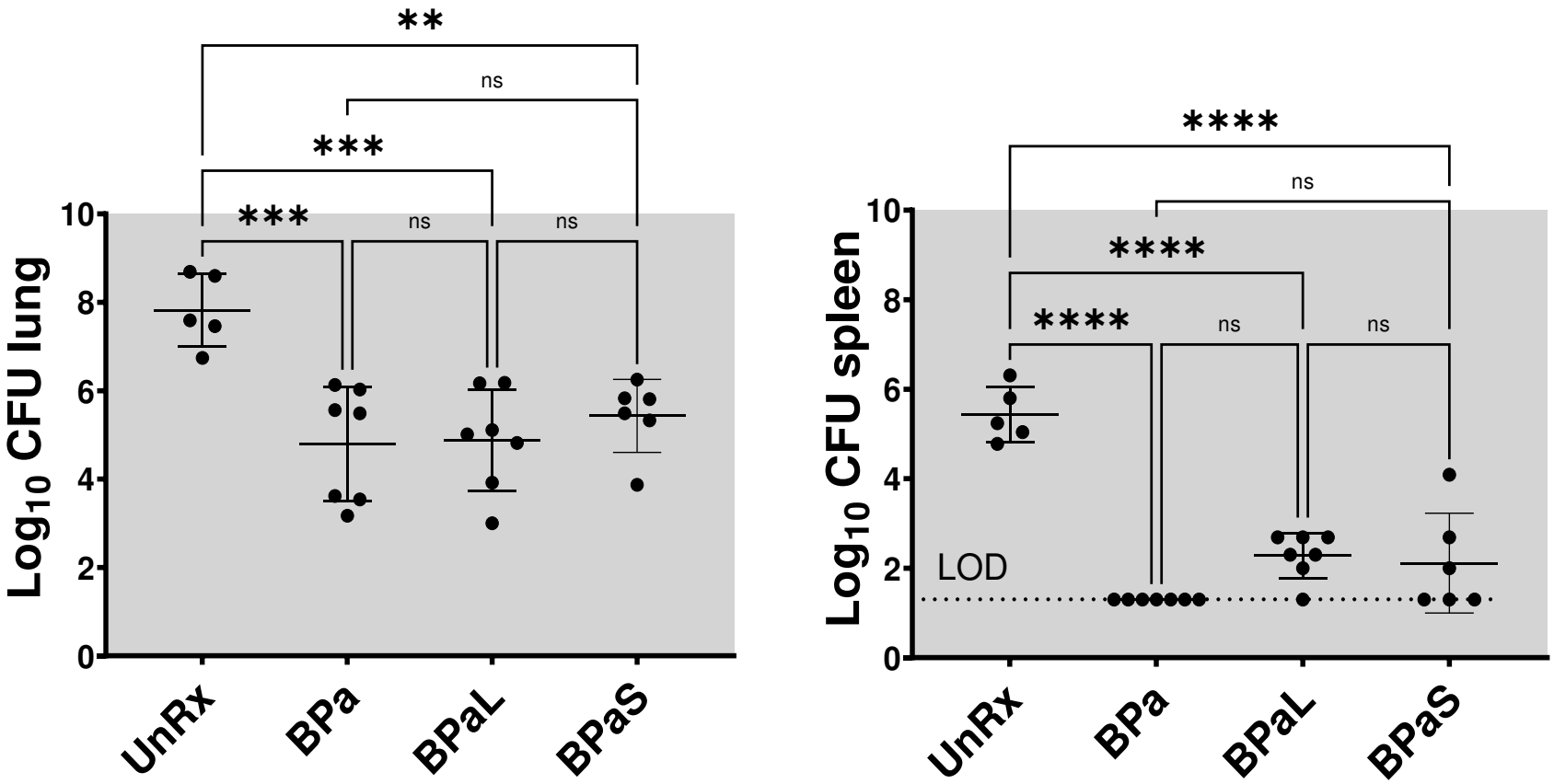

Figure 2.3iii (C3HeB/FeJ Study 3). Lung and spleen bacterial burden (CFU) in Mtb infected C3HeB/FeJ mice treated with BPaL and BPaS regimen for 4 weeks. n = 7, LOD: limit of detection, ns = non-significant, ** = $p < 0.005$, *** = $p < 0.0005$, **** = $p < 0.00005$

Monitoring of adverse effects during drug treatment in the C3HeB/FeJ TB model

The Nix-TB clinical trial (12) reported severe adverse effects (AEs) in many patients which were associated with the long-term administration of L in BPaL regimen. These AEs included peripheral neuropathy (81% of patients) and alteration in bone marrow precursor cells [myelosuppression (48%)]; consistent with the hematologic anomalies [anemia (37% of study population)] seen in the Nix-TB trial and decrease in hemoglobin. Therefore, the potential AEs in the current study during drug therapy were monitored at several levels 1) change in the live body weight; 2) lung histopathology and lesion scoring 3) evaluation of complete blood count (CBC), 4) clinical pathology to study myelosuppression in bone marrow and 5) change in immune cell populations at lung, spleen, bone marrow and blood level.

1. ***Change in the live body weight in the C3HeB/FeJ TB model***

a) ***Monotherapy of linezolid or spectinamide 1599 does not affect the live body weight of mice***

First the effect of monotherapy on the live body weight of Mtb infected C3HeB/FeJ (n=6) mice was evaluated. Mice were treated for 4 weeks with linezolid (L; 100mpk administered 5/7 a week orally) or spectinamide 1599 (S; 100 mpk administered 3/7 a week on alternate days via intrapulmonary aerosol) and their live body weight was monitored on weekly basis. The results demonstrated that there was not statistically significant ($p<0.05$) difference in the live body weight among all groups during monotherapy treatment (Figure 2.4).

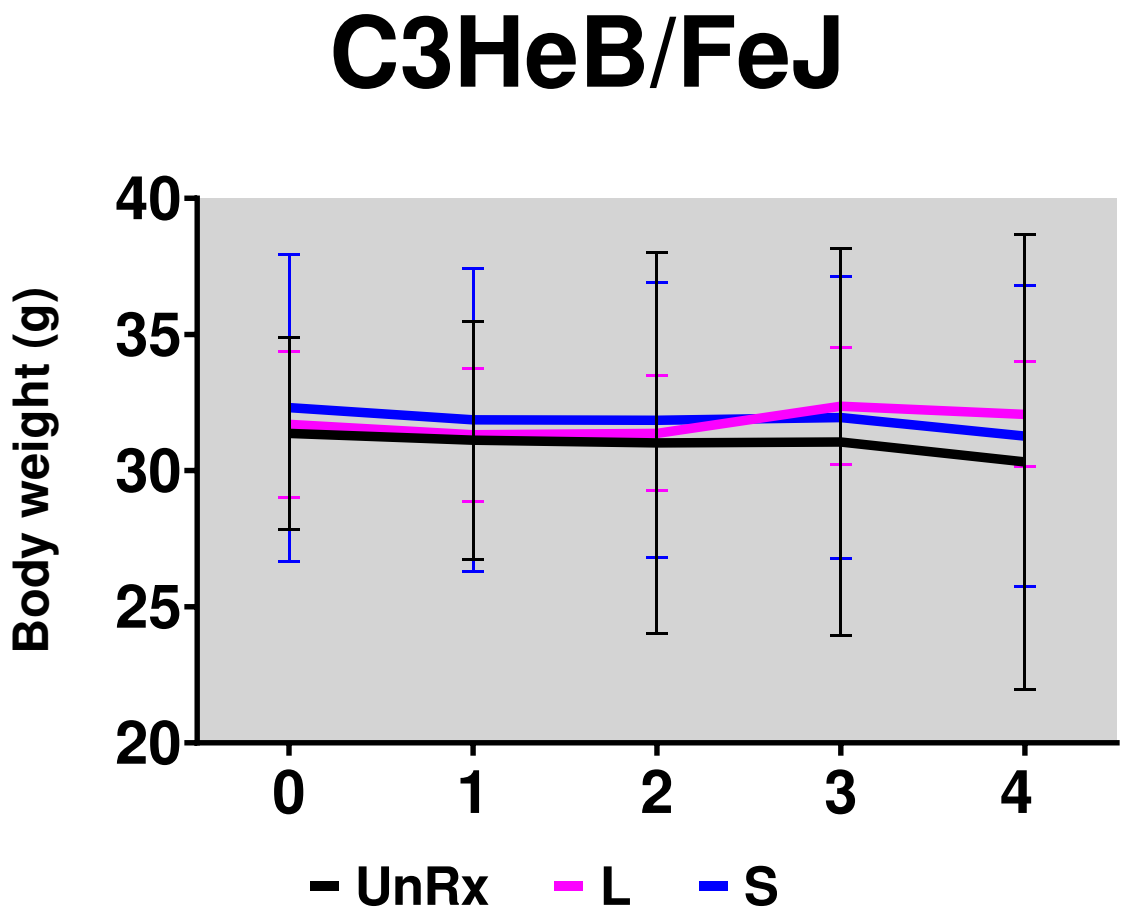

Figure 2.4. Change in the average live body weight of Mtb infected C3HeB/FeJ mice during monotherapy treatment. Mice were treated with linezolid (L) or spectinamide 1599 (S) for 4 weeks. No significant difference was observed among the groups (n=5). $p < 0.05$

b) BPaL therapy decreases the live body weight of mice

The average live body weight of Mtb infected C3HeB/FeJ mice treated with combination therapy of BPaL or BPaS summarized in Figure 2.5 shows the combined data from three independent studies. The result of individual study is given in Figure 2.5i A-C. Two of the three studies contained an extra group of BPa only as a reference control. All mice tolerated well the BPa, BPaL and BPaS regimens as the loss in the body weight ranged only between 2.37-5.13%. By the end of therapy, mice treated with BPaL regimen significantly ($p<0.05$) decreased their live body weight compared to BPa, BPaL and untreated (UnRx) groups.

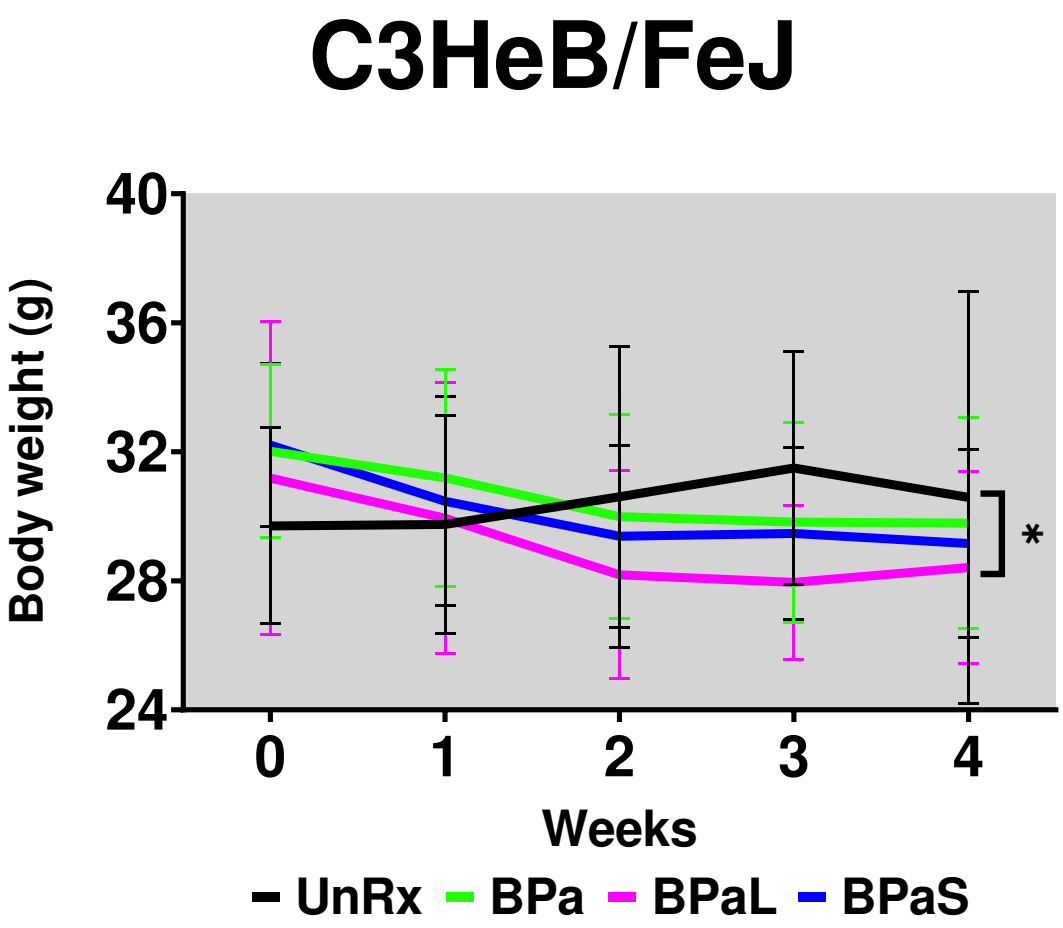

Figure 2.5. Change in the average live body weight of Mtb infected C3HeB/FeJ mice during drug treatment. Mice treated with BPaL regimen had significantly decreased their live body weight compared to BPa, BPaL and untreated (UnRx) groups. The graph represents the combined data from three independent studies and two of the three studies contained an extra group of BPa. $p < 0.05$

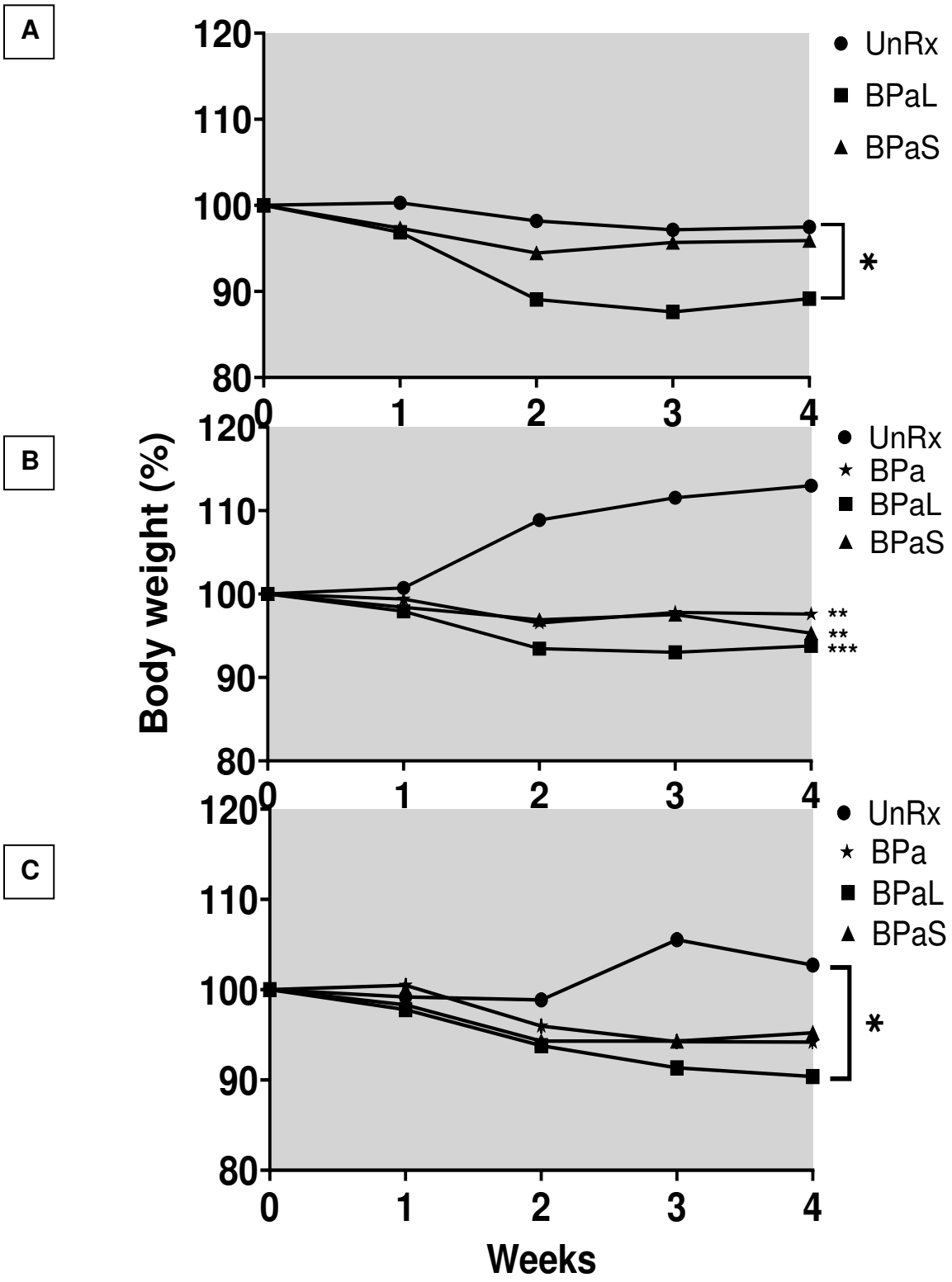

Figure 2.5i**.** Change in the average live body weight of Mtb infected C3HeB/FeJ mice during drug treatment. (A) Study 1, n = 7 (B) study 2, n = 3-9 (C) study 3, n – 7 are presented and the combined results of these studies are shown in Figure 2.5. * = $p < 0.05$, ** = $p < 0.005$, *** = $p < 0.0005$

2. BPaL and BPaS therapy result in significantly lower lesion burden in the C3HeB/FeJ TB model

The lung samples from Mtb infected C3HeB/FeJ mice treated with the BPaL or BPaS regimen were processed for histopathology and lesion scoring. As was expected by the lung CFU, the untreated (UnRx) mice produced well-formed TB lesions (granuloma) typical of C3HeB/FeJ model that occupied most of the lung tissue area as depicted by their lesion scores (Figure 2.6). The C3HeB/FeJ mice displayed a diverse spectrum of granulomatous lesions from cellular infiltrate to granulocytic pneumonia to highly organized granulomas with collagen encapsulation and central caseous necrosis that can also be seen in some human patients (51). However, BPaL and BPaS therapy significantly decreased the number and size of TB lesions, importantly, without showing any difference ($p<0.05$) between the treatments (Figure 2.6).

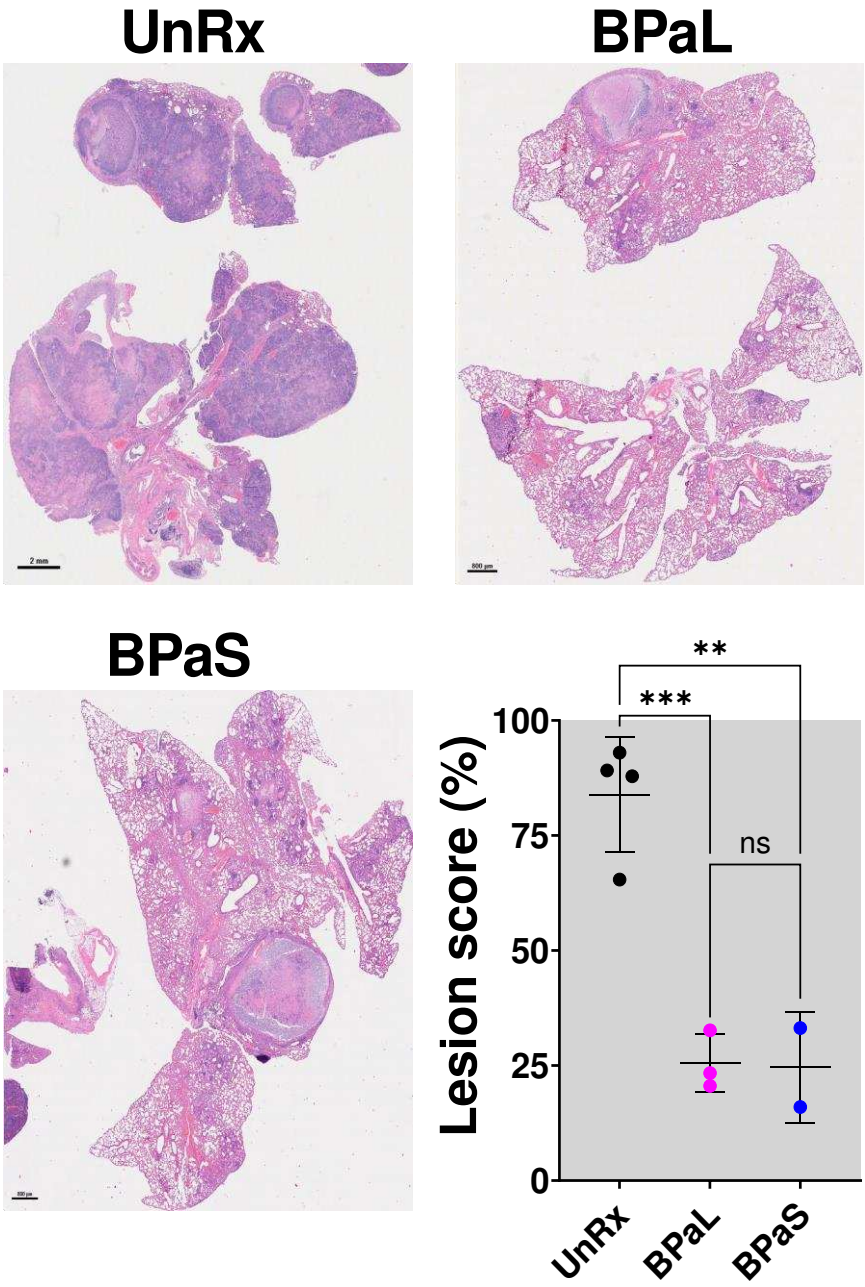

Figure 2.6. Change in the lung histopathology and lesion score of Mtb infected C3HeB/FeJ mice during drug treatment. BPaL and BPaS treatment significantly decreased the lesion size and number compared to UnRx control and their lesion scores reflect that change. H&E, 20X. ns = non-significant, ** = $p < 0.005$, *** = $p < 0.0005$

3. BPaL therapy but not BPaS decreases hemoglobin concentration in the C3HeB/FeJ TB model

As shown above, the L associated BPaL regimen significantly ($p<0.05$) decreased the live body weights of mice, we further analyzed blood of Mtb infected C3HeB/FeJ mice during therapy for their complete blood count (CBC) profile to see if the hematological changes seen in the Nix-TB trial are consisted with the use of BPaL.

The results obtained from mice treated with monotherapy of L or S for 4 weeks are given in Table 2.3 and summarized in Figure 2.7. The L treatment compared to UnRx control and S, significantly ($p<0.05$) increased red blood cell distribution width (RDWs), however, both L and S significantly ($p<0.05$) decreased mean corpuscular hemoglobin concentration (MCHC) compared to UnRx control.

The effect of combination therapy of BPaL or BPaS on CBC profile was analyzed at 1-, 2- and 4-weeks (Figure 2.8). None of the 20 parameters of CBC were changed after the first two weeks of therapy. However, BPaL regimen decreased ($p<0.05$) hemoglobin (HBG) concentration and mean platelet volume (MPV) at 4 weeks compared to UnRx and BPa controls respectively. Similar results for MCHC and RDWs were observed for BPaL and BPaS regimen as were seen in monotherapy (Figure 2.7). The consistent alteration in RDWs and MCHC both in mono- and combination therapy along with the decrease in HBG caused by BPaL regimen suggest the development of mild anemia in C3HeB/FeJ mice, interestingly, no such difference ($p<0.05$) was associated with BPa control.

Table 2.3. Changes (Mean ± SEM) in CBC parameters of Mtb infected C3HeB/FeJ mice after 4-week monotherapy

CBC	UnRx	L	S
WBC (10^9/L)	7.35 ± 1.44	5.39 ± 0.51	4.94 ± 0.72
Lymphocyte (10^9/L)	2.818 ± 0.31	3.56 ± 0.57	2.39 ± 0.39
Monocyte (10^9/L)	0.676 ± 0.19	0.28 ± 0.03	0.33 ± 0.06
Neutrophil (10^9/L)	3.858 ± 1.29	1.23 ± 0.08	2.21 ± 0.58
Lymphocyte% auto	43.24 ± 7.47	69.23 ± 2.47 [a]	49.82 ± 6.65
Monocyte% auto	8.68 ± 0.96	5.58 ± 0.79	6.88 ± 1.21
Neutrophil% auto	48.08 ± 6.57	29.17 ± 4.95	43.3 ± 6.46
RBC (10^12/L)	11.23 ± 0.41	10.73 ± 0.13	10.04 ± 0.77
HGB (g/dL)	13.62 ± 0.14	13.8 ± 0.18	12.58 ± 0.9
HCT (%)	53.36 ± 1.2	56.65 ± 0.76	52 ± 3.46
MCV (fl)	47.8 ± 2.51	52.83 ± 0.74	52.2 ± 1.98
MCH (pg)	12.2 ± 0.49	12.85 ± 0.17	12.56 ± 0.35
MCHC (g/dL)	25.54 ± 0.39	24.3 ± 0.16 [a]	24.2 ± 0.35 [a]
RDWc (%)	21.34 ± 0.89	21.8 ± 0.62	19.46 ± 0.56
RDWs (fl)	37.2 ± 1.01	42.72 ± 0.8 [a]	37.48 ± 0.89
Platelets (10^9/L)	325.8 ± 32.18	297.7 ± 26.54	303 ± 34.12
MPV (fl)	7.1 ± 0.37	7.25 ± 0.18	7.74 ± 0.16
PCT (%)	0.234 ± 0.03	0.21 ± 0.02	0.23 ± 0.02
PDWc (%)	33.62 ± 1.83	33.28 ± 1.02	33.94 ± 0.91
PDWs (fl)	10.78 ± 1.61	10.15 ± 0.76	10.62 ± 0.74

CBC, complete blood count; WBC, white blood cell; RBC, red blood cell; HGB, hemoglobin; HCT, hematocrit; MCV, mean cell volume; MCH, mean cell hemoglobin; MCHC, MCH concentration; RDW, red cell distribution width; MPV, mean platelet volume; PCT, platelet crit; PDWc, platelet cell distribution width coefficient of variation; PDWs, platelet cell distribution width standard deviation; L, linezolid; S, spectinamide 1599.

[a] Statistically significant at $p < 0.05$

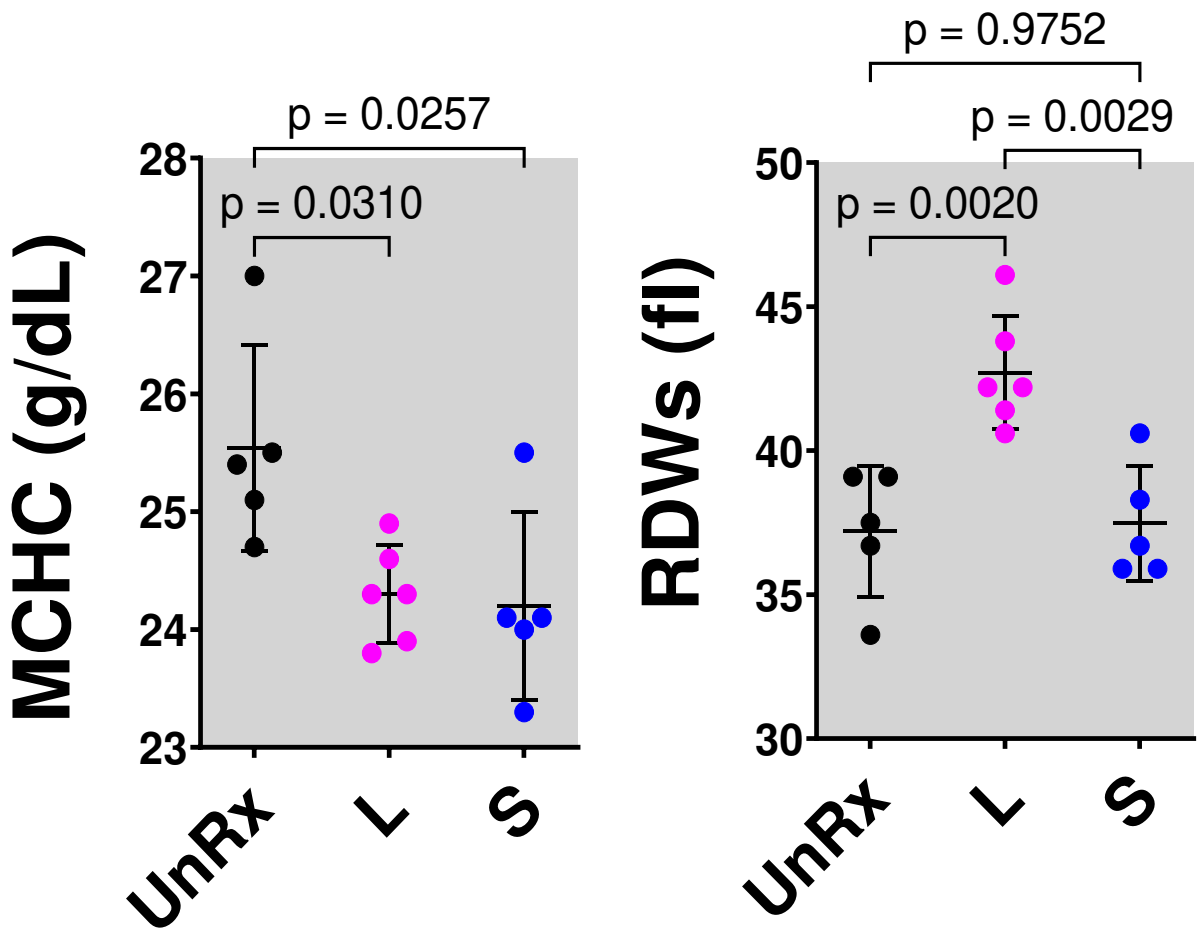

Figure 2.7. Change in the CBC profile of Mtb infected C3HeB/FeJ mice during monotherapy treatment. Mice were treated with linezolid (L) or spectinamide 1599 (S) for 4 weeks. $p < 0.05$

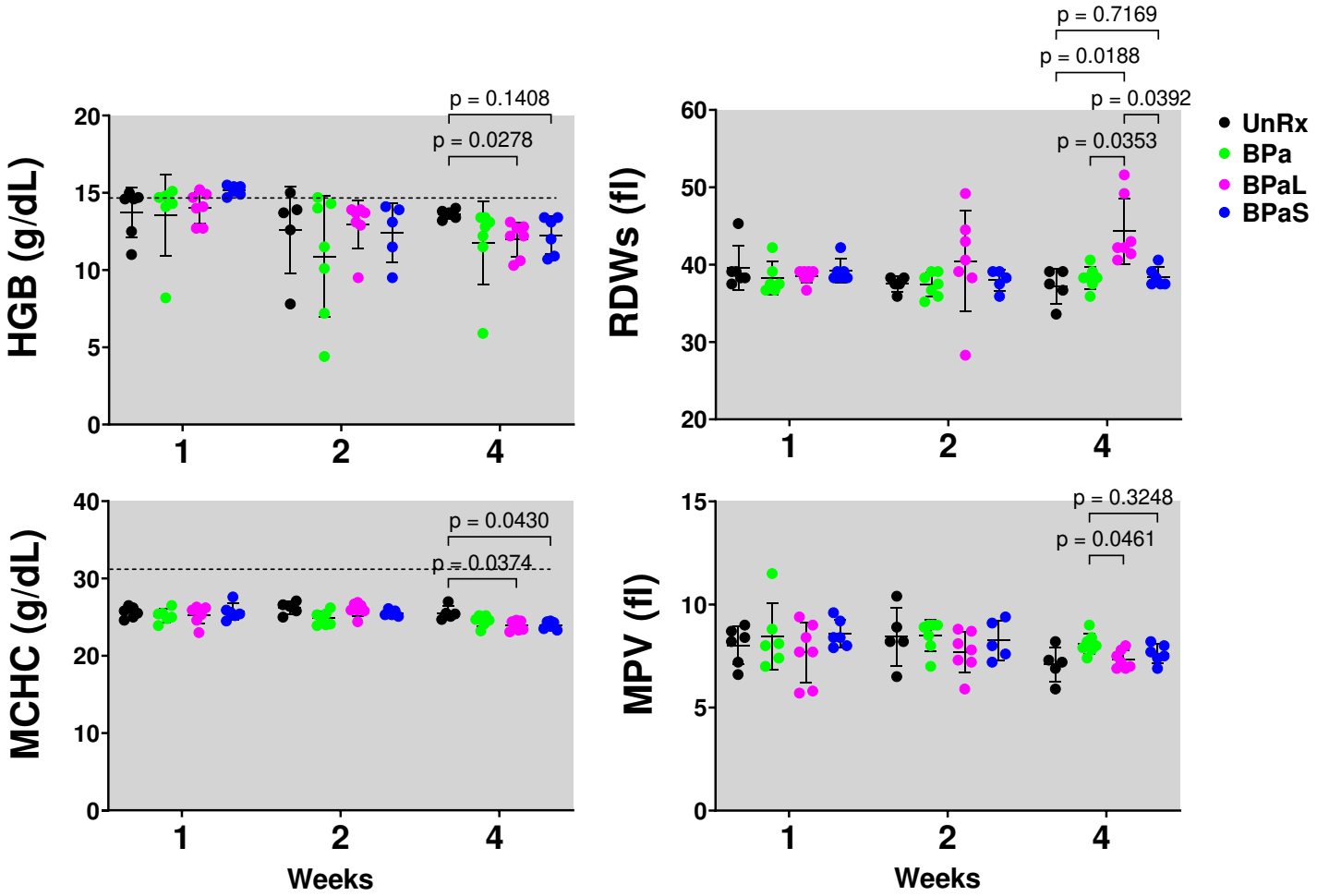

Figure 2.8. Change in the CBC profile of Mtb infected C3HeB/FeJ mice during combination treatment. Mice were treated with either BPaL or BPaS for 4 weeks. A horizontal dotted line indicates the lower end of the reference interval for C3HeB/FeJ mice. $p < 0.05$

4. *BPaL therapy decreases the ratio of myeloid to erythroid cells in bone marrow of the C3HeB/FeJ TB model*

To further evaluate if the drugs have a myelosuppressive effect, we performed hematopathology analysis of bone marrow of Mtb infected C3HeB/FeJ mice and treated with either BPa, BPaL or BPaS regimens as above (Figure 2.9). The number of myeloid (M) and erythroid (E) precursors cells were calculated from H&E stained sections (2.9A) and thereafter their M:E ratio was calculated. BPa and BPaL therapies significantly ($p<0.05$) decreased the content of M cells while increasing the number E cells counted for 300 bone marrow cells in 5 different regions. Hence, the corresponding M:E ration in bone marrow of animals treated with BPaL or BPa were lower compared to those from UnRx control (2.9B). Importantly, bone marrow of animals treated with BPaS therapy did not show difference in the content of M or E cells.

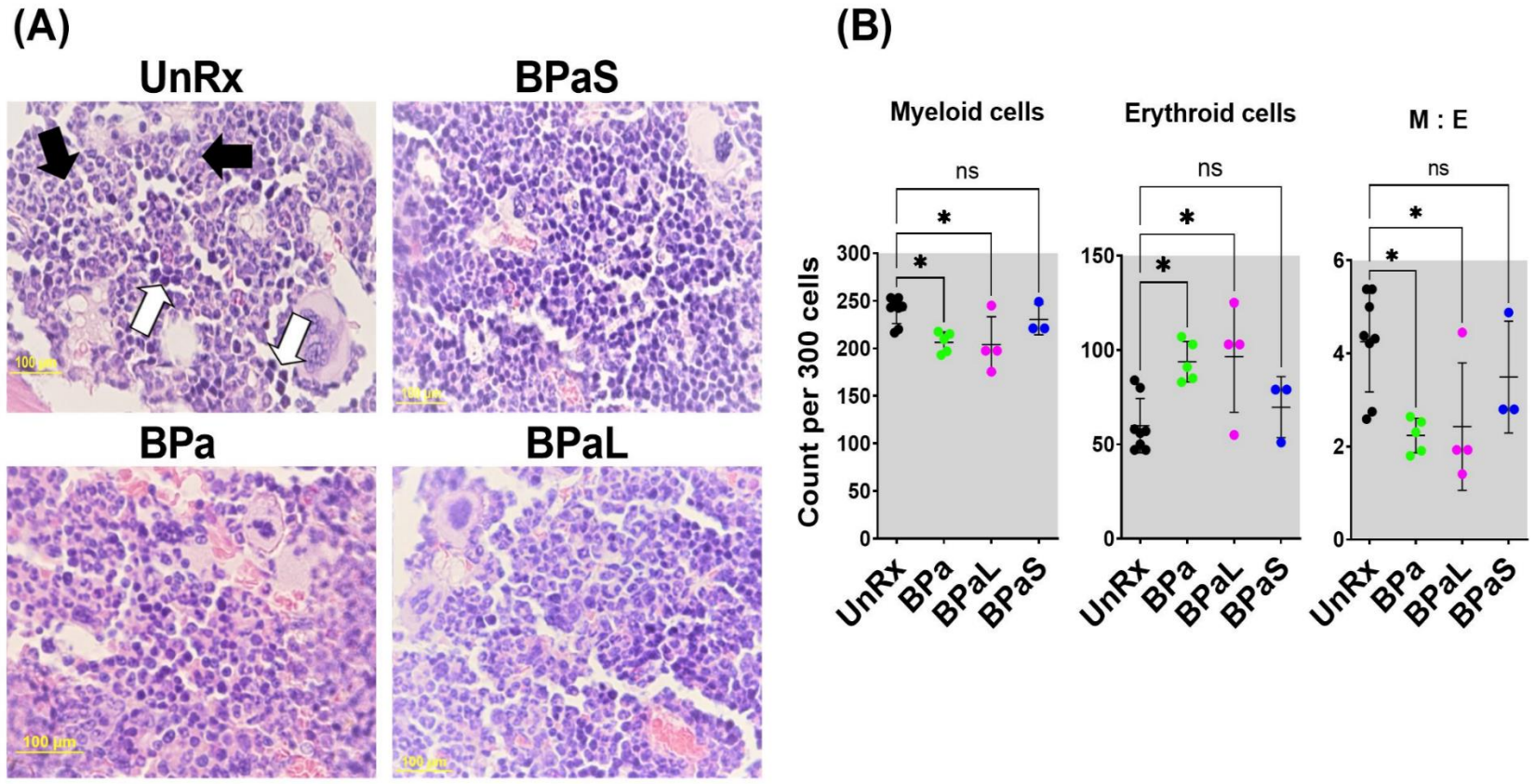

Figure 2.9. BPaL and BPa therapy cause alteration in M:E ratio in Mtb infected C3HeB/FeJ mice after 4 weeks of treatment. BPaL and BPa treatment caused a significant drop in the number of myeloid (M) cells (black arrows, A in UnRx) while increase in erythroid (E) cells (white arrows, A in UnRx) in bone marrow as compared to untreated (UnRx) and BPaS groups. H&E image at 20X; scale bar 100 µm; ns = non-significant, $p < 0.05$

5. *BPaL therapy triggers proinflammatory cytokine and chemokine response in bone marrow of the C3HeB/FeJ TB model*

a. *Change in the total protein concentration*

A comparative analysis for the concentration of cytokine and chemokine in bone marrow, plasma, and lung samples from Mtb infected C3HeB/FeJ mice treated with BPaL or BPaS regimen was measured. First the total protein (TP) concentration in lung homogenate and bone marrow supernatant was calculated to normalize its concentration for Luminex assay (Figure 2.10). The plasma samples, however, did not require TP measurement as their matrix was self-normalizing. The TP concentration in the lung samples was significantly ($p<0.05$) reduced in BPaL and BPaS groups compared to UnRx control, and there was no significant difference between both the treatment groups (2.10A). Contrary, total protein concentration in bone marrow supernatants remained unaltered among the groups (2.10B).

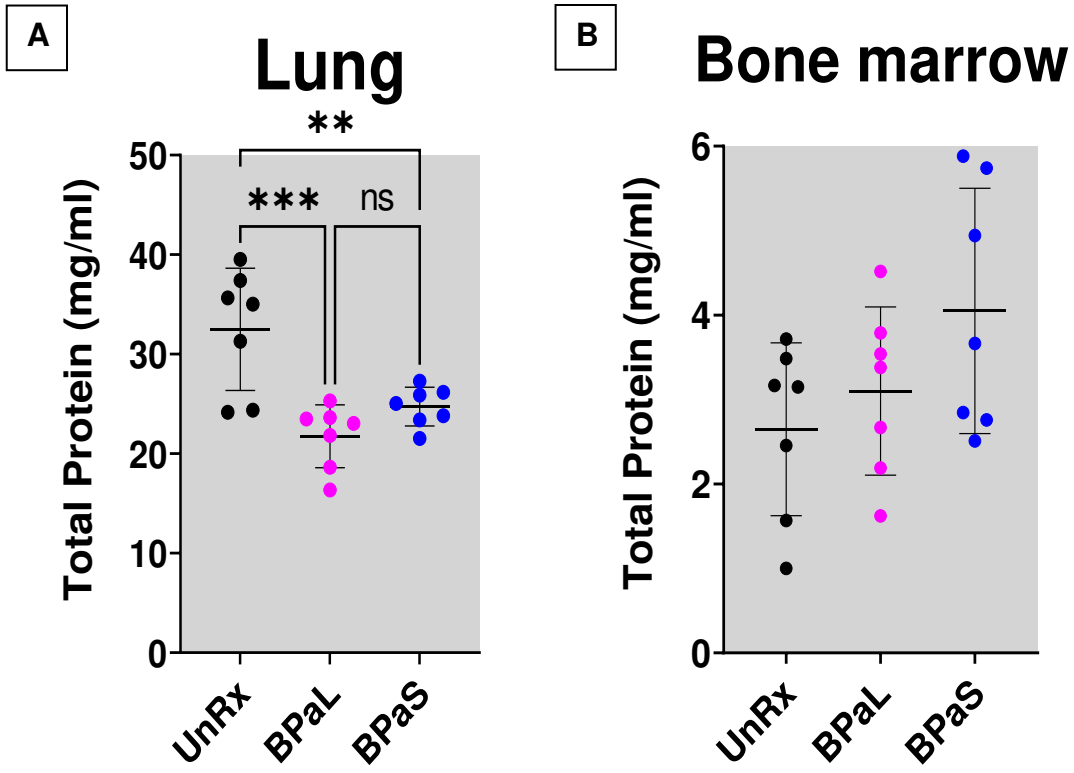

Figure 2.10. Change in the total protein (TP) concentration in lung and bone marrow from Mtb infected C3HeB/FeJ mice during drug treatment. (A) Mice treated with BPaL and BPaS regimen significantly decreased TP concentration in lung compared to untreated (UnRx) control. (B) TP concentration in bone marrow remained unchanged after the drug treatment. ns = non-significant, ** = $p < 0.05$, *** = $p < 0.0005$

b. *Change in the cytokine and chemokine response*

The 26 cytokines and chemokines in bone marrow supernatant from Mtb infected C3HeB/FeJ mice showed significant difference for IL-1β, IL-12p70, IL-23, TNF alpha, GRO alpha (CXCL1), MP-2 alpha (CXCL2), MP-1 alpha (CCL3), RANTES (CCL5), MCP-3 (CCL7), Eotaxin (CCL11) and IP-10 (CXCL10) between BPaL and BPaS treatment groups at the end of 4 weeks. BPaL treatment group showed significantly higher concentration of pro-inflammatory cytokines and chemokines than BPaS group (Figure 2.11).

When plasma samples from these animals were analyzed using the same methodology as for bone marrow (discussed above), only MCP-3 (CCL7) chemokine showed significant ($p<0.05$) difference between both treatment groups and its level was higher in the BPaS than in the BPaL group (Figure 2.12). However, the lung homogenate samples showed no significant differences between treatment groups for these cytokines and chemokines (Figure 2.13).

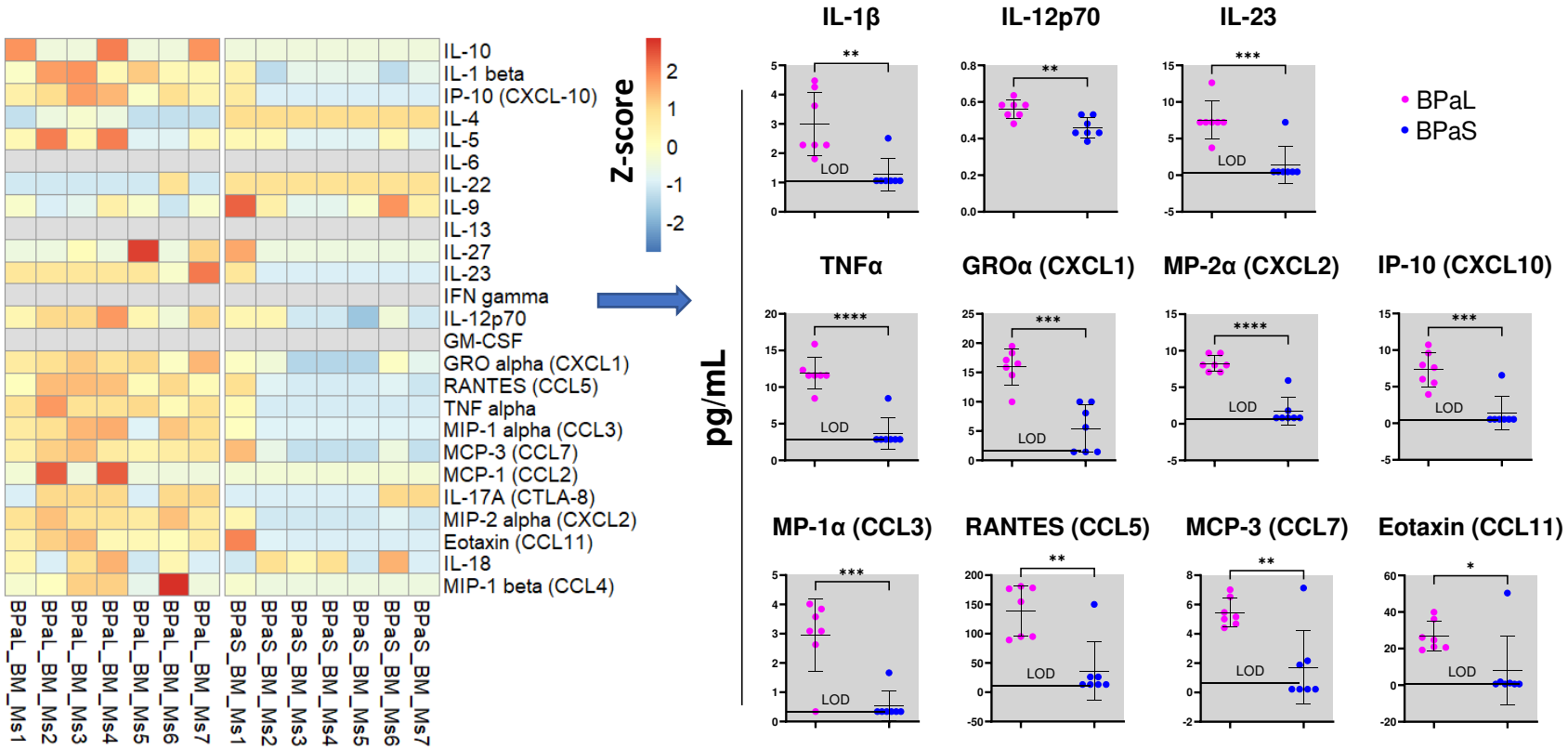

Figure 2.11. Measurement of 26 cytokines and chemokines in bone marrow (BM) supernatants of Mtb infected C3HeB/FeJ mice treated with BPaL or BPaS regimen. The BPaL mice showed significantly higher concentration of proinflammatory cytokines and chemokines compared to BPaS treated mice after 4 weeks. LOD = limit of detection, * = $p < 0.05$, ** = $p < 0.005$, *** = $p < 0.0005$, **** = $p < 0.00005$

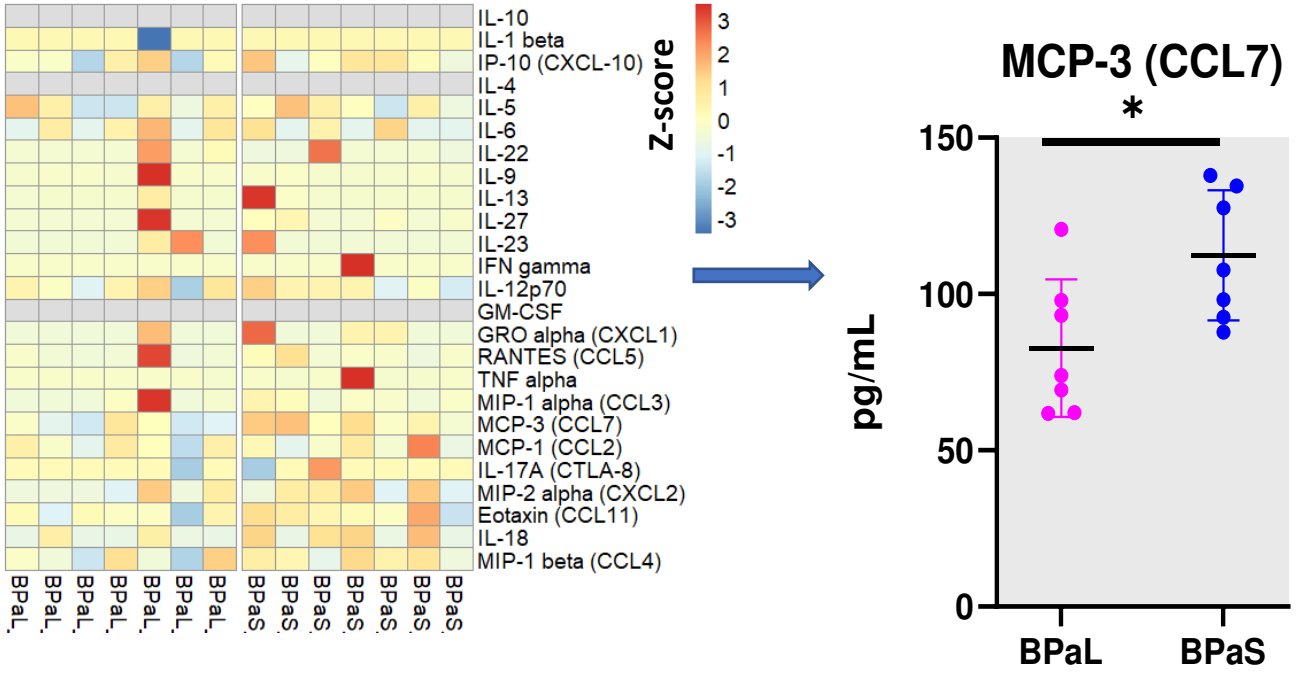

Figure 2.12. Measurement of 26 cytokines and chemokines in plasma of Mtb infected C3HeB/FeJ mice treated with BPaL or BPaS regimen. MCP-3 was found to be significantly different between the treatment groups after 4 weeks. $p < 0.05$

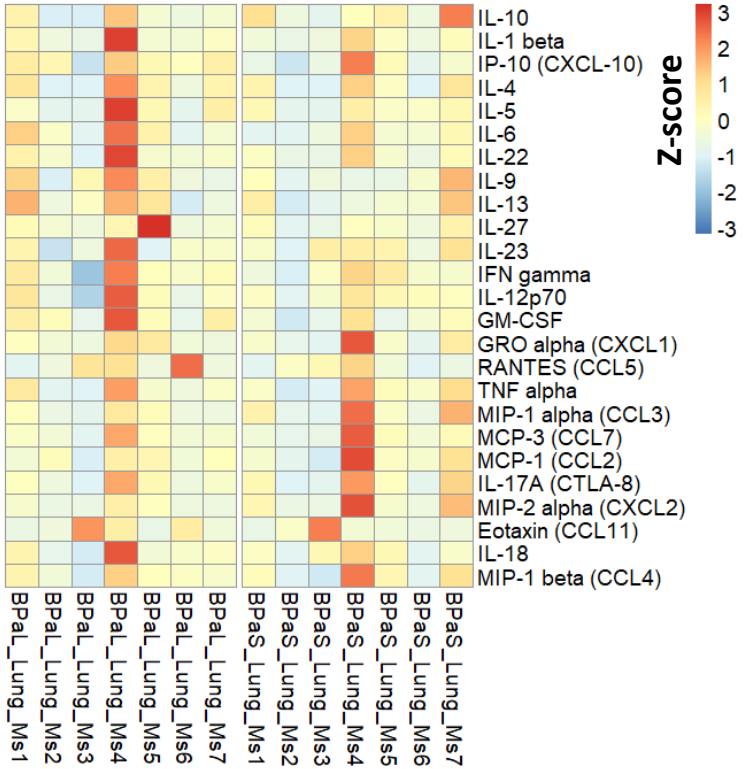

Figure 2.13. Measurement of 26 cytokines and chemokines in lung homogenate of Mtb infected C3HeB/FeJ mice treated with BPaL or BPaS regimen. As depicted by the z-score, no significant difference was observed between the groups after 4 weeks of treatment.

c. Correlation between lung CFU and cytokines and chemokines

We further investigated a correlation factor between lung bacterial burden (CFU), and 26 cytokines and chemokines from bone marrow supernatant, plasma and lung homogenate samples from BPaL and BPaS treatment groups. The Spearman's correlation analysis revealed that most of the cytokines and chemokines from bone marrow (Figure 2.14), plasma (Figure 2.15) and lung (Figure 2.16) samples were positively correlated with the lung CFU except for IL-5 in lung and Eotaxin (CCL11) in plasma samples and these were correlated negatively. However, IL-4, IL-13 and GM-CSF did not show any correlation as their concentration in bone marrow samples was detected at the limit of detection (LOD) of the assay. Similar results for IL-4, IL-10, IL-23 and GM-CSF concentration in plasma samples were observed.

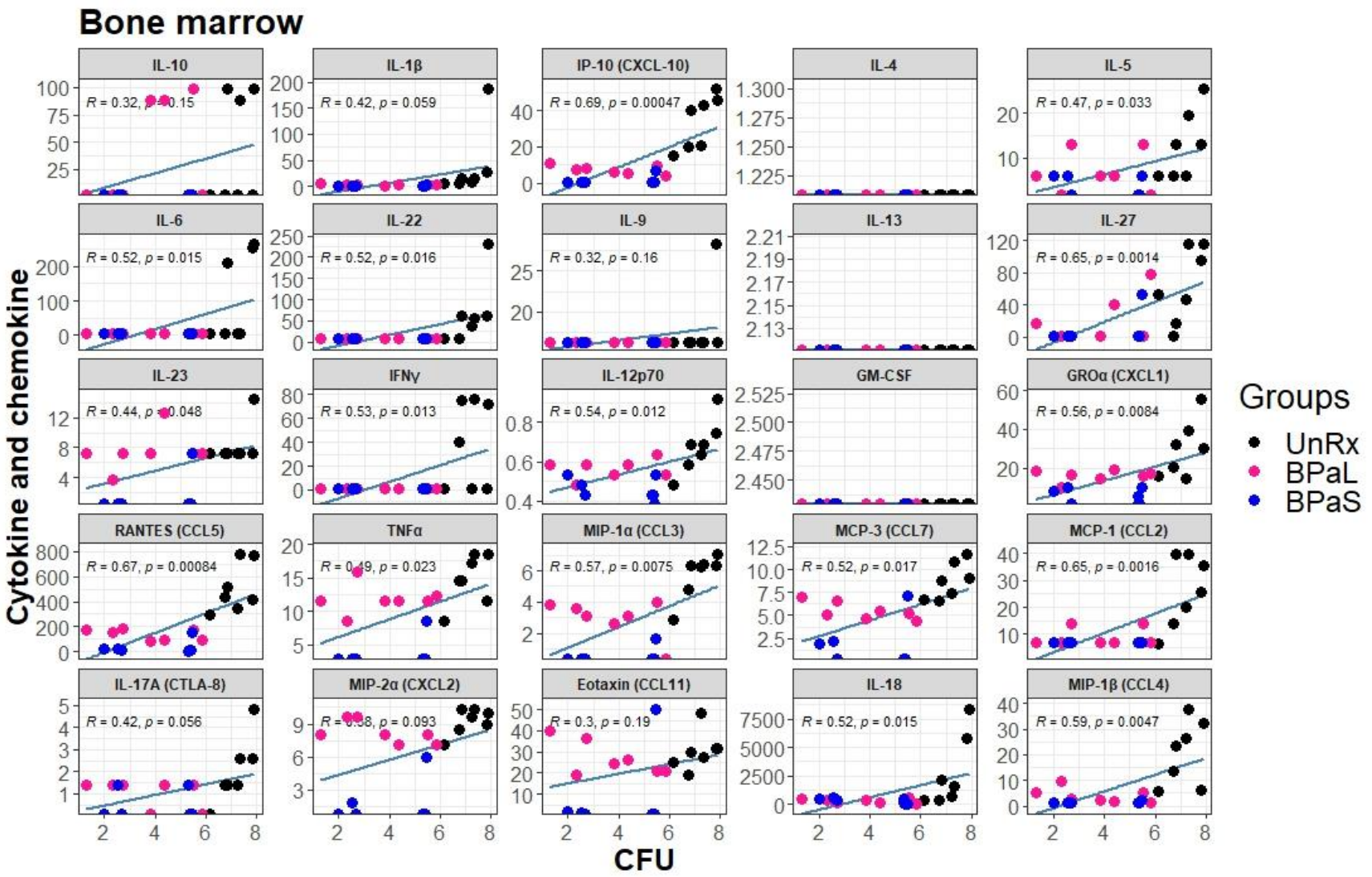

Figure 2.14. Spearman's correlation analysis between lung bacterial burden and bone marrow cytokines and chemokines profile in Mtb infected C3HeB/FeJ mice treated with BPaL or BPaS regimen.

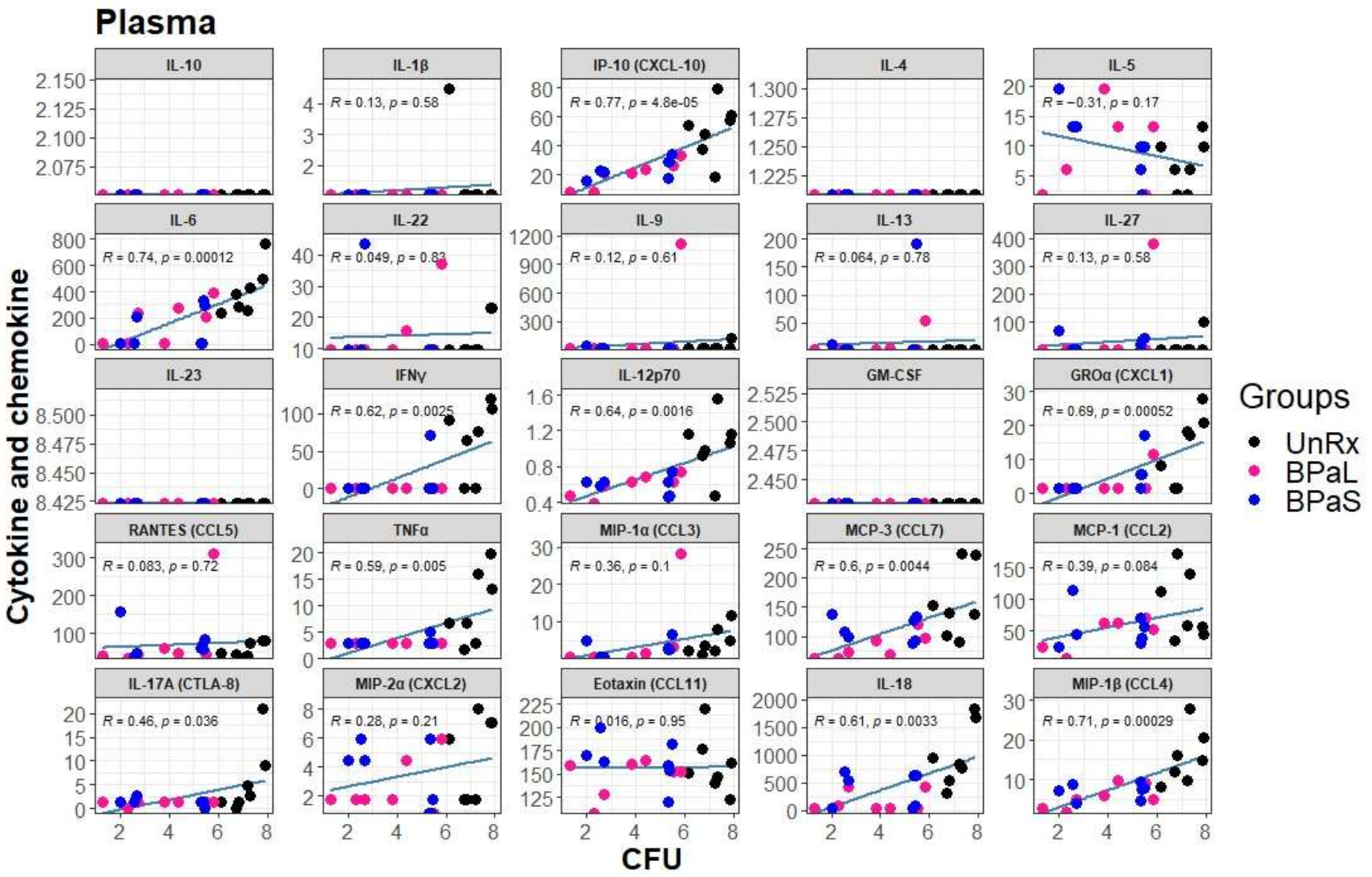

Figure 2.15. Spearman's correlation analysis between lung bacterial burden and plasma cytokines and chemokines profile in Mtb infected C3HeB/FeJ mice treated with BPaL or BPaS regimen.

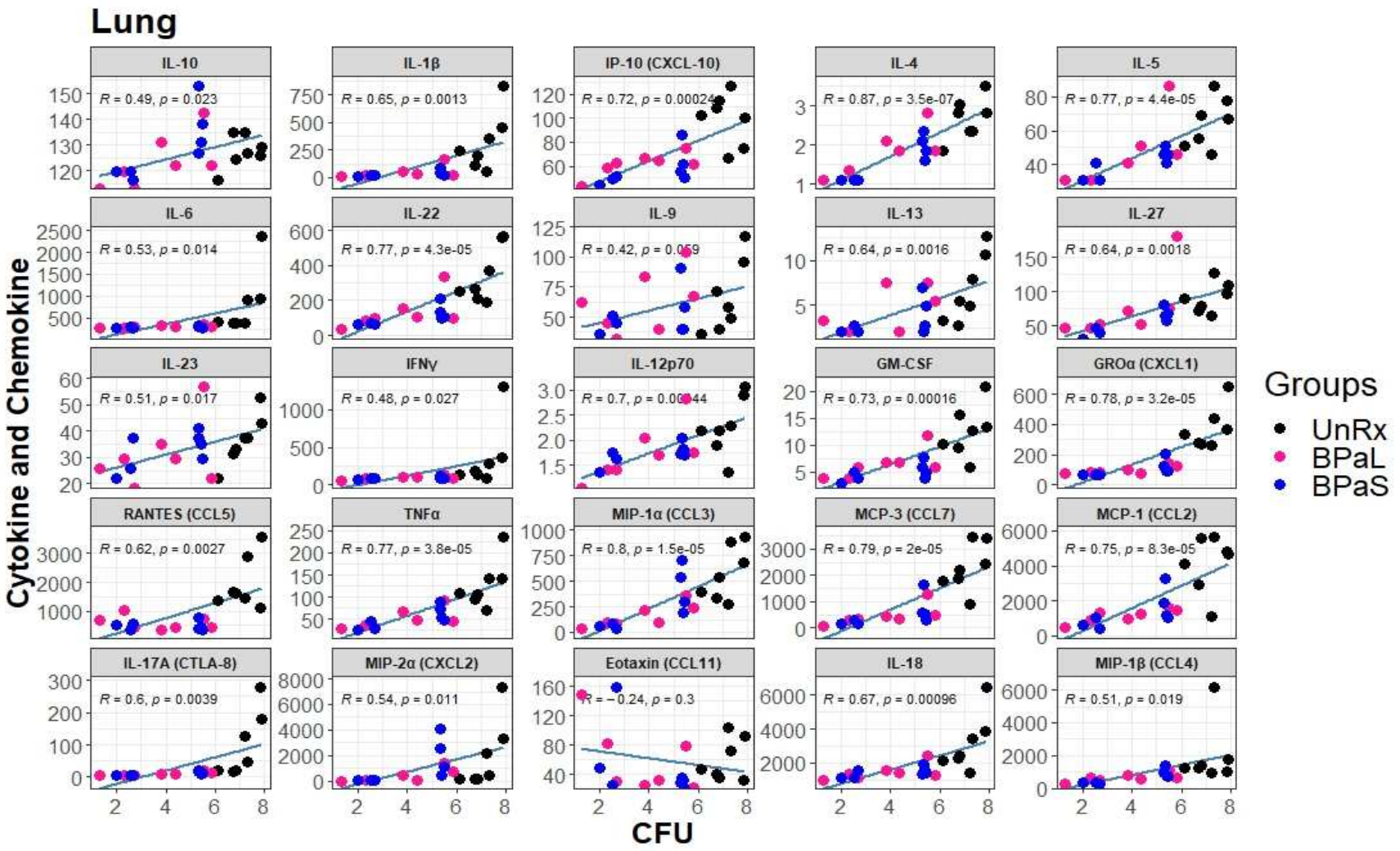

Figure 2.16. Spearman's correlation analysis between lung bacterial burden and lung cytokines and chemokines profile in Mtb infected C3HeB/FeJ mice treated with BPaL or BPaS regimen.

6. *BPaL and BPaS therapy affect the profile of immune cell populations in bone marrow, lung and blood of the C3HeB/FeJ TB model*

We further assessed the environment of immune cells using flow cytometry in bone marrow, blood, and lungs from each group of Mtb-infected C3HeB/FeJ mice. The bone marrow (Figure 2.17) results revealed that as compared to UnRx control, there was a significant decrease in the percentage of inflammatory myeloid phenotypes (CD45+CD3-CD11b+CD11c-Ly6C+CCR2+, CD45+CD3-CD11b+CD11c-Ly6C+CCR2+MHC-II+ and CD45+CD3-D14+CCR2+) in response to therapy with either BPa, BPaL, or BPaS. In contrast, neutrophils (CD45+CD3-CD11b+CD11c-Ly6C+Ly6G^{high}), precursor T cells (CD45+CD3+) and B cells (CD45+CD3-CD19+B220-) were significantly increased in either BPa, BPaL, or BPaS treatment groups compared to UnRx control in bone marrow. This reduced inflammatory response in treatment groups is also consistent in blood shown by significantly reduced inflammatory myeloid cells (CD45+CD3-CD11b+CD11c-Ly6C+CCR2+) (Figure 2.18A). Interestingly, the response to therapy in the lungs (Figure 2.18B) was manifested by a significant increase of CD3+CD4+ T helper cells and B-1 cells (CD3-CD19+) and a reverse trend for CD3+CD8+ and γδ-T cells (CD3+CD8+γδTCR+).

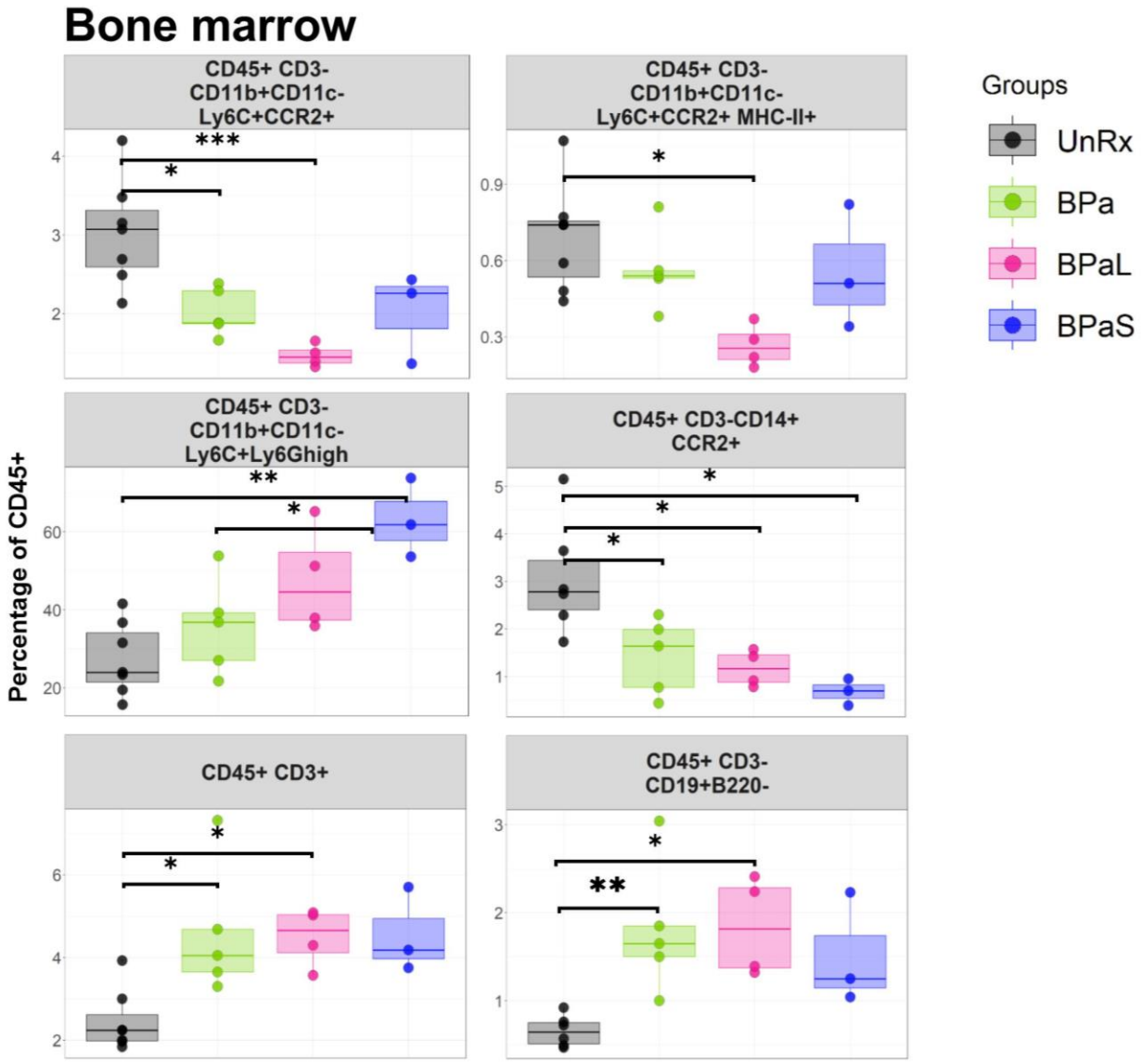

Figure 2.17. Change in the immune cell populations in bone marrow of Mtb infected C3HeB/FeJ mice during drug treatment. Statistical significance was calculated using one-way ANOVA with Tukey's test for multiple comparisons. * = $p < 0.05$, ** = $p < 0.005$, *** = $p < 0.0005$

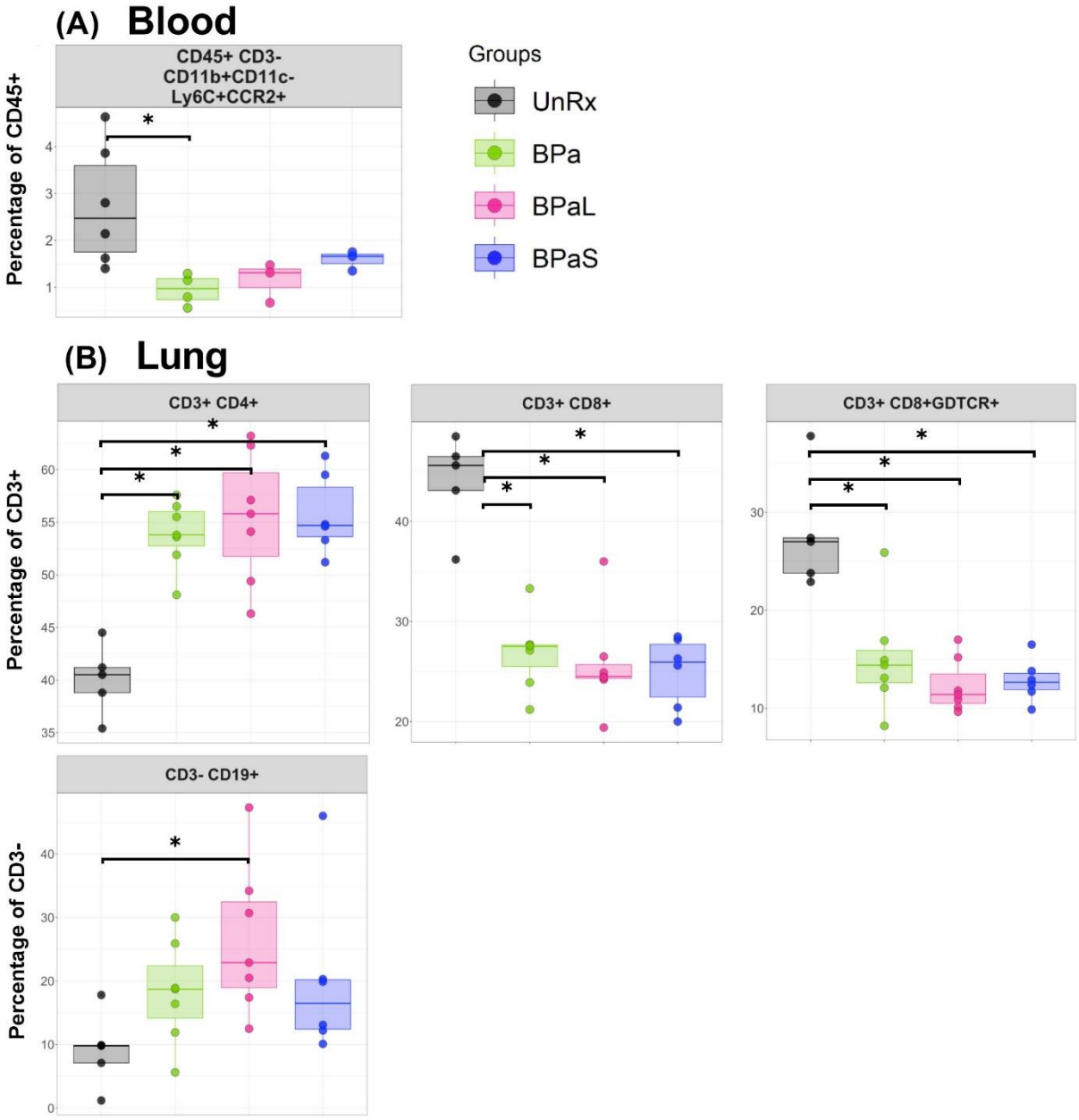

Figure 2.18. Change in the immune cell populations in blood and lung samples of Mtb infected C3HeB/FeJ mice during drug treatment. Statistical significance was calculated using one-way ANOVA with Tukey's test for multiple comparisons. $p < 0.05$

7. Change in the distribution of lung immune cells during BPaL and BPaS therapy in the C3HeB/FeJ TB model

Changes in the distribution of immune cells in the lungs of C3HeB/FeJ mice from each group was studied using multiplex fluorescence immunohistochemistry (mfIHC). A 7-color composite image for cell markers (B220, CD4, CD8, Foxp3, F4/80 and Ly6G) along with DAPI is shown in Figure 2.19 while their single-color staining is shown in Figure 2.20. Figure 2.19 shows a typical necrotic TB granuloma comprised of central necrosis, peripheral rim and parenchyma. The analysis of mfIHC images (Figure 2.21A & 2.22) revealed that BPaL and BPaS treatment significantly and dramatically lowered the number of neutrophils (count based on Ly6G+) compared to UnRx control, however, F4/80+ cells were observed significantly higher in BPaS compared to UnRx control. Interestingly, the spearman's correlation plot (Figure 2.21B) shows that a significant decrease in Ly6G+ neutrophils positively correlated with an increase of other immune cells.

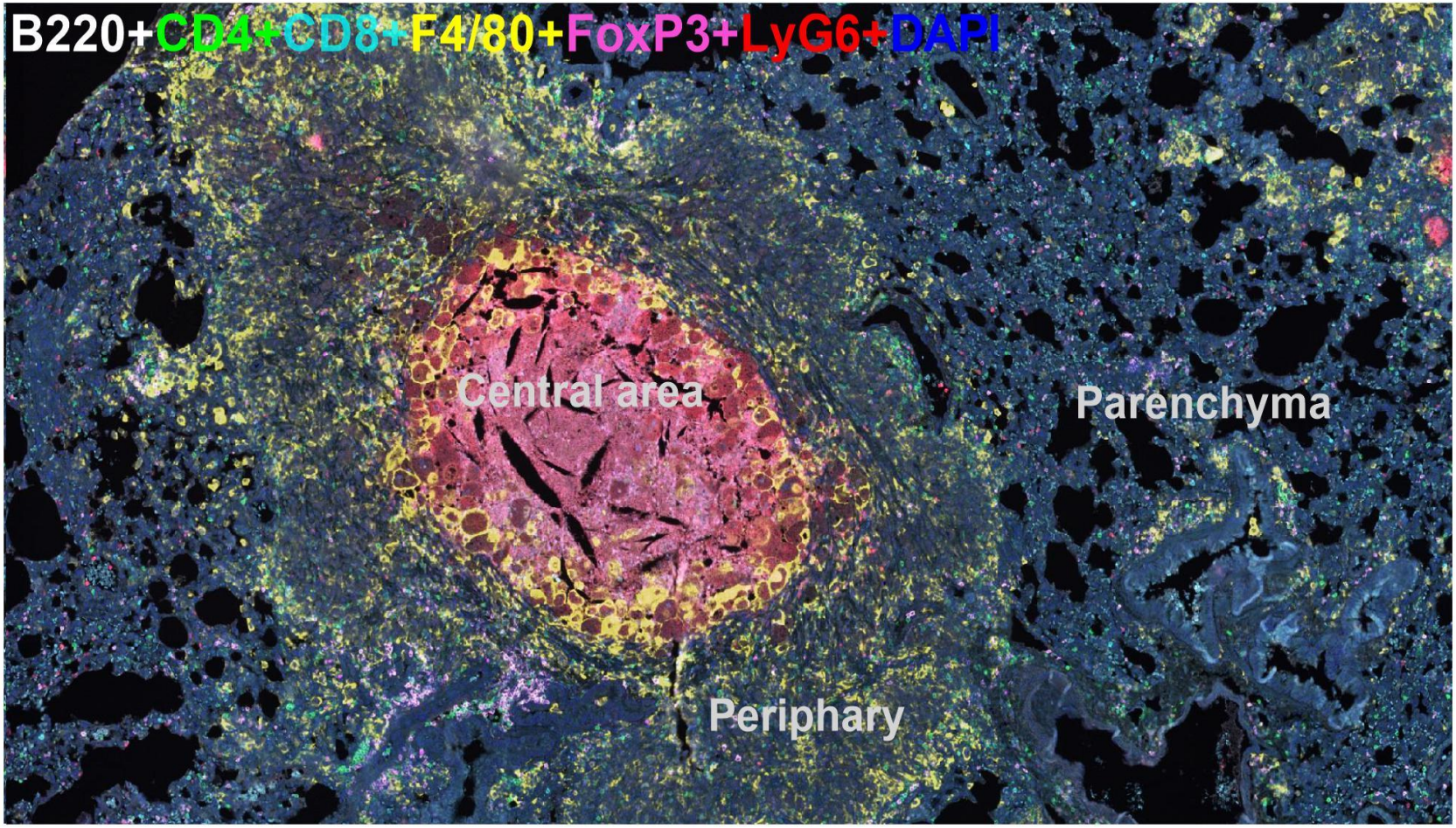

Figure 2.19. A lung composite image stained with multiplex immunohistochemistry displays different immune cell markers along with DAPI in a necrotic TB granuloma. The central and peripheral regions of granuloma and the parenchyma of lung are also shown.

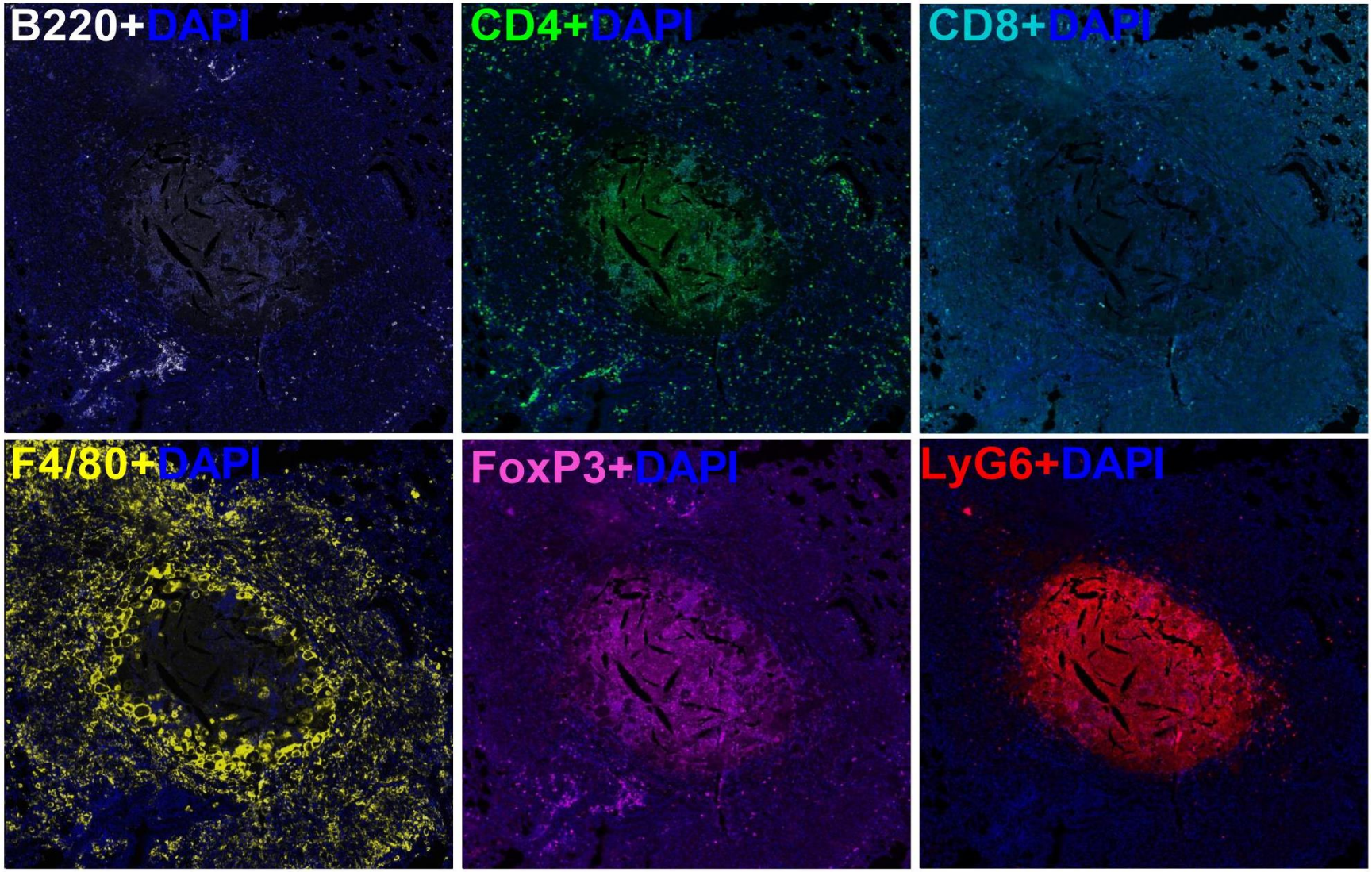

Figure 2.20. A single-color composite image of individual markers with DAPI showing distribution of each immune cell population in a TB granuloma (shown in Figure 2.19). The full composite image of these individual markers is shown in Figure 2.19.

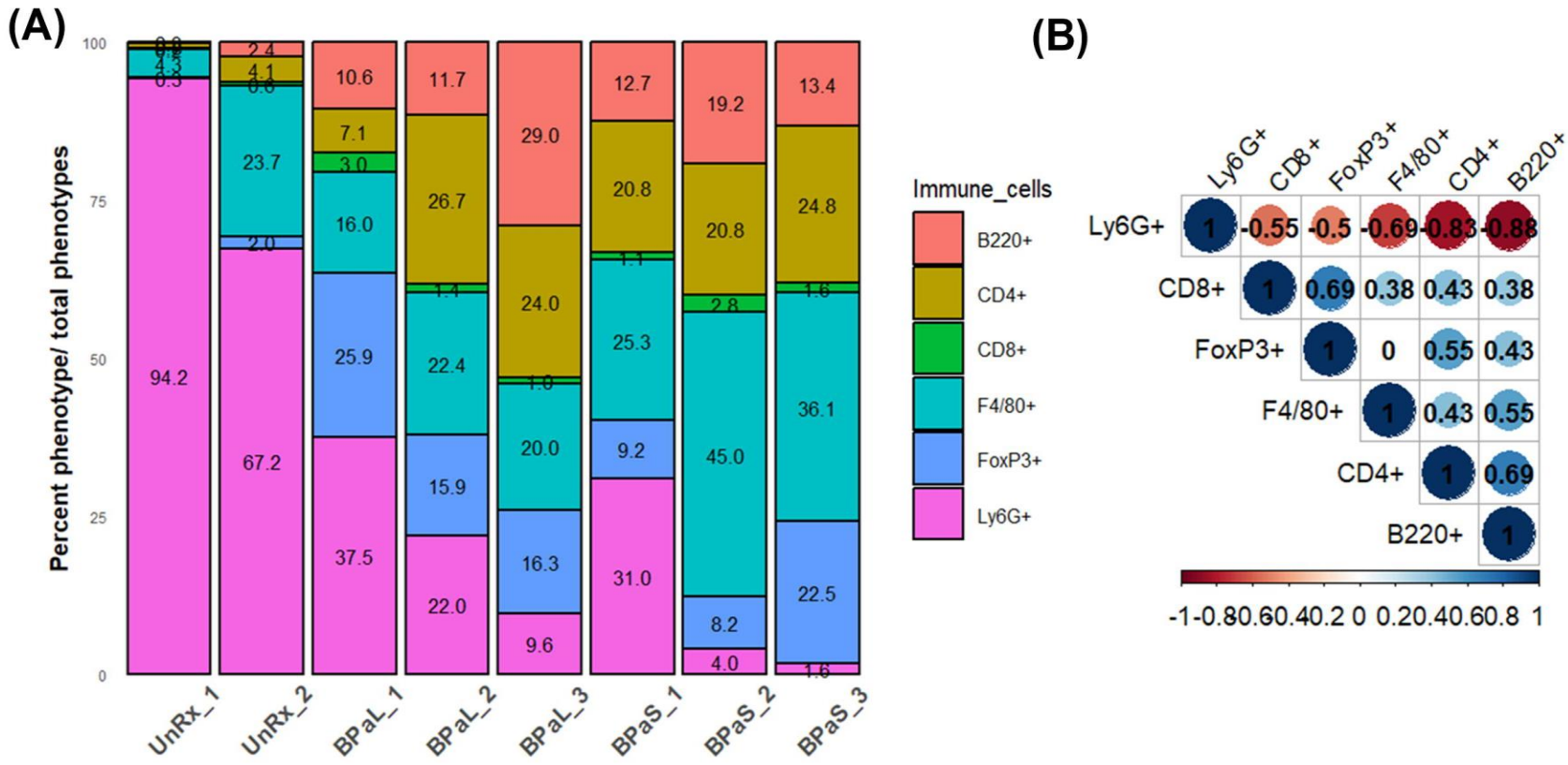

Figure 2.21. Change in the immune cell populations in lungs from Mtb infected C3HeB/FeJ mice during drug treatment. (A) Cell population (%) of several immune cells per total number of their phenotypes was calculated in untreated (UnRx) and treated (BPaL and BPaS) groups based on a panel of 6-color antibodies + DAPI. (B) Spearman's correlation matrix for immune cell populations (B220, CD4, CD8, F4/80, Foxp3, Ly6G) showing all relationships. A coefficient with a value of either +1 (blue), 0 (white), or -1 (red) indicates a perfect association, no association, and a perfect negative association of ranks, respectively. Numbers indicate the correlation coefficient.

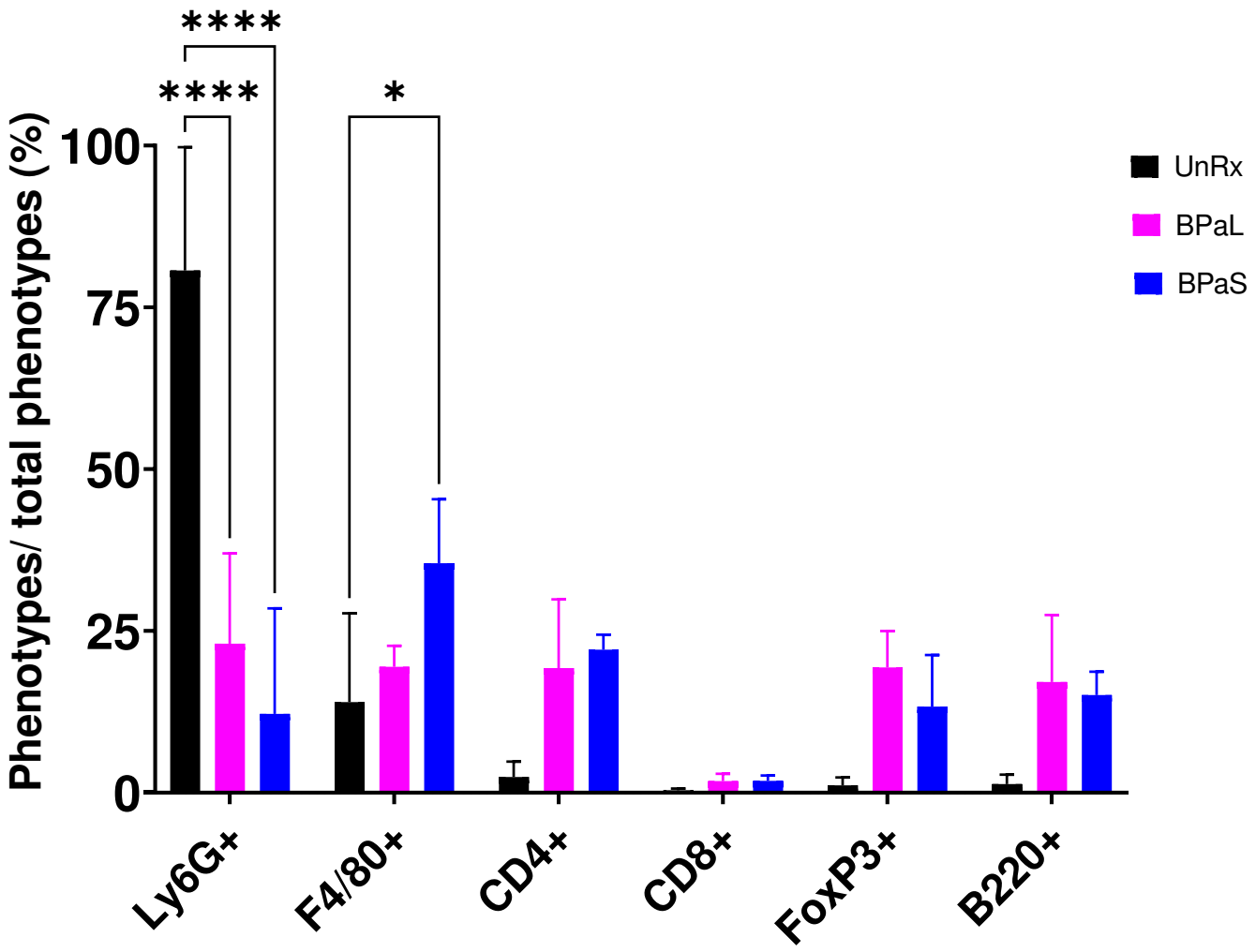

Figure 2.22. Immune cell populations in lung samples of Mtb infected C3HeB/FeJ TB model after 4 weeks therapy. Statistical significance was calculated using two-way ANOVA with Tukey's test for multiple comparisons and $p < 0.05$ was considered significant.

Monotherapy of linezolid and spectinamide 1599 show similar efficacy in the BALB/c TB model

The bactericidal effect of monotherapy of linezolid (L) and spectinamide 1599 (S) was tested in Mtb infected BALB/c mice. Animals received L or S for 4 weeks and at the end of treatment their lung and spleen bacterial burden was measured by enumerating the colony forming units (CFU) (Figure 2.23). The results showed that compared to UnRx (5.40 ± 0.07 $\log_{10}$) and vehicle (5.49 ± 0.20 $\log_{10}$) controls, animals in L (4.57 ± 0.16 $\log_{10}$) and S (4.63 ± 0.06 $\log_{10}$) treated groups had significantly ($p<0.05$) lowered lung CFU (2.23A). Importantly, no statistically significant difference was observed between either treatment group. Bacterial burden in spleen after 4 weeks of L and S treatment showed no change in CFU, and all the groups behaved alike (2.23B).

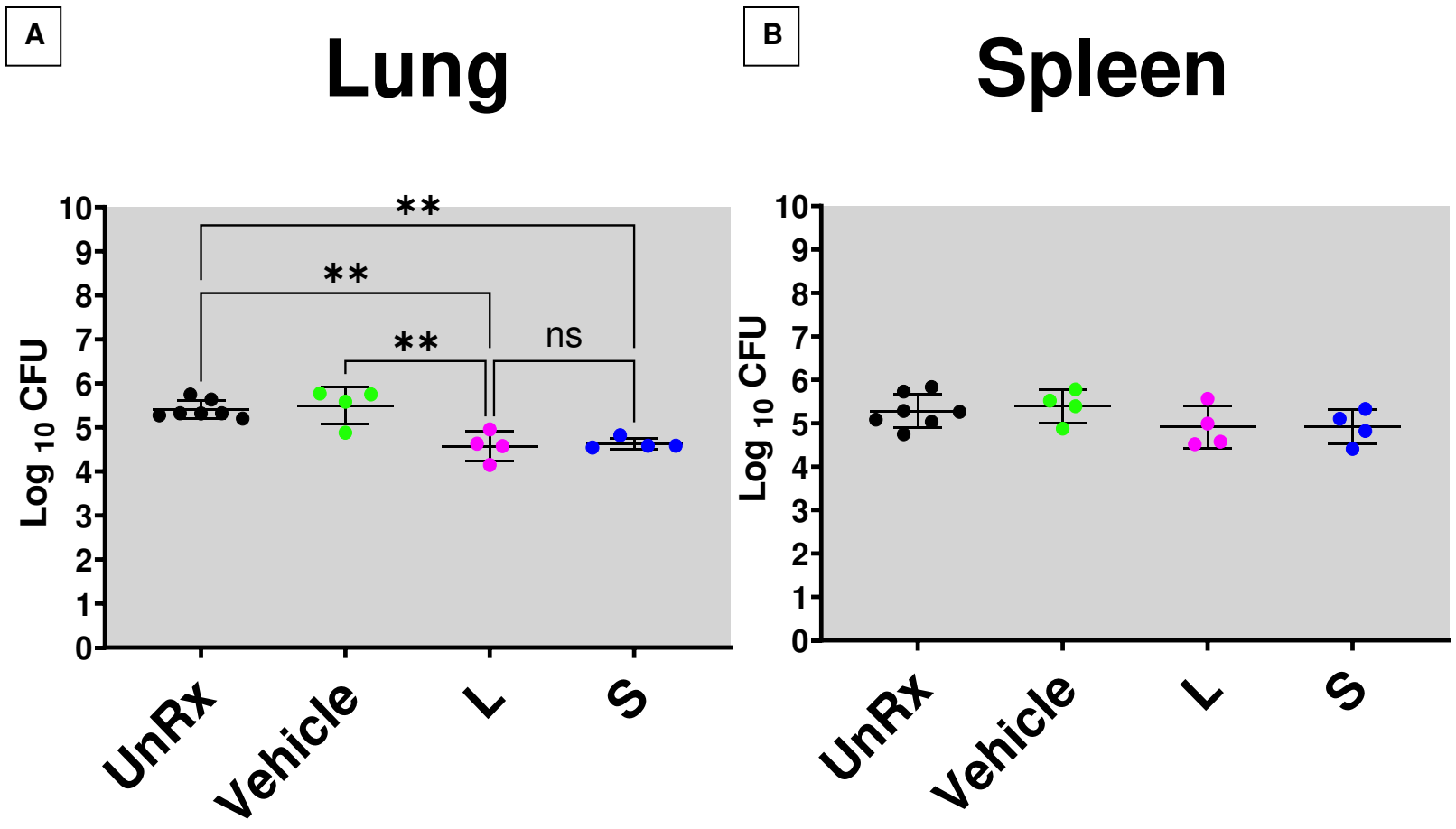

Figure 2.23. Bacterial burden (CFU) in Mtb infected BALB/c mice treated with monotherapy of linezolid (L) and spectinamide 1599 (S). L and S significantly decreased lung CFU (A) compared to untreated (UnRx) and vehicle controls and no significant difference was observed between both treatment groups. In the spleen, there was no difference in CFU(B). ns = non-significant, ** = $p < 0.005$

Combination therapy of BPaL or BPaS have similar efficacy in the BALB/c TB model

The effect of combination therapy on lung and spleen bacterial burden (CFU) of Mtb infected BALB/c mice was measured at the end of 4 weeks of drug treatment. The comparative analysis of lung CFU of combined data from two independent studies is shown in Figure 2.24 and the results of each individual study are shown in Figure 2.24i&ii. The combined results demonstrated that compared to untreated (UnRx) (5.24 ± 0.17 $\log_{10}$) control, mice in BPaL (1.29 ± 0.13 $\log_{10}$) and BPaS (1.44 ± 0.17 $\log_{10}$) treated groups significantly ($p<0.05$) reduced the lungs CFU (2.24A). Importantly, no significant difference was observed between the treatment groups. Similarly, in spleen, 4 weeks of BPaL and BPaS treatments reduced CFU below the level of detection (LOD) compared to UnRx (5.68 ± 0.38 $\log_{10}$) control (2.24B).

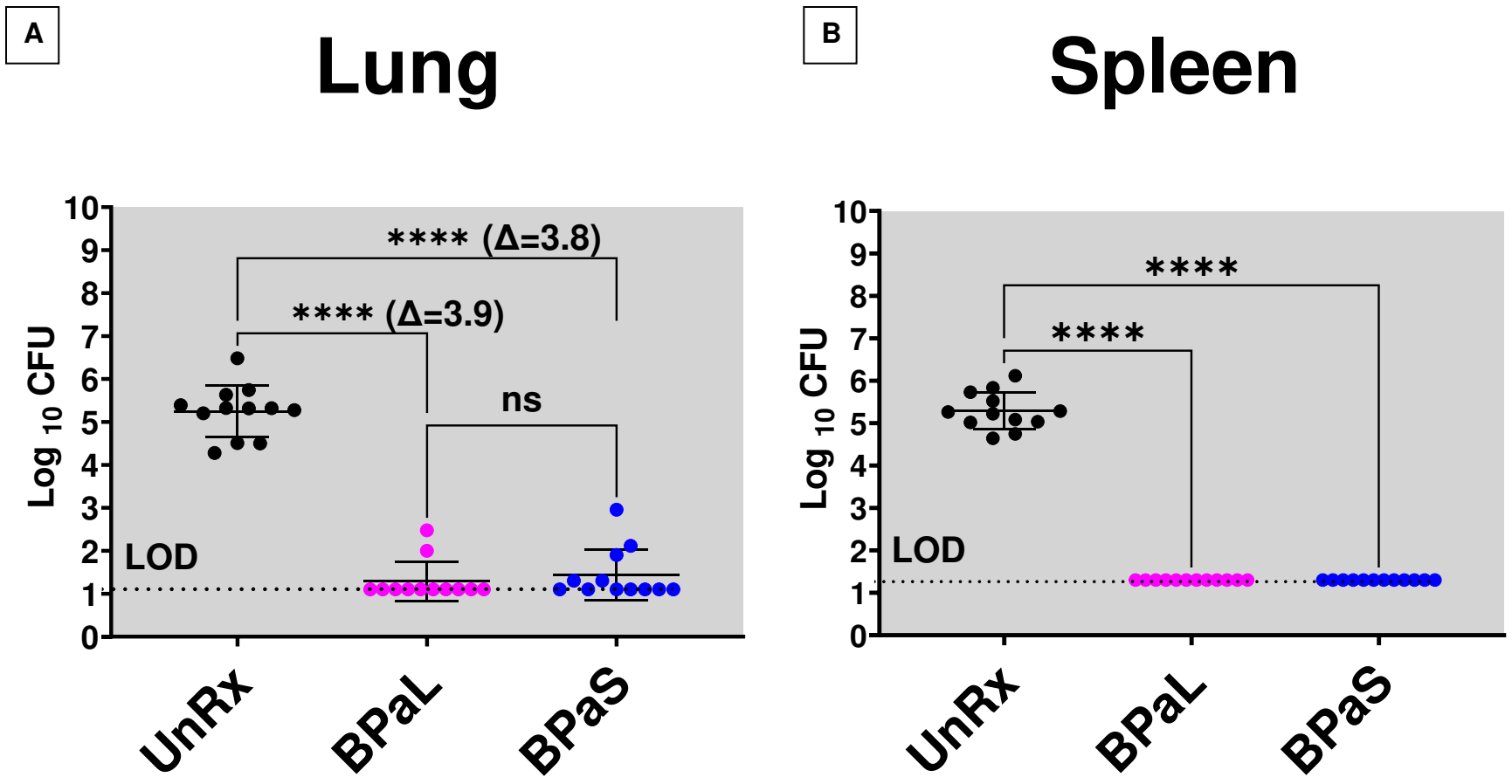

Figure 2.24. Bacterial burden (CFU) in Mtb infected BALB/c mice treated with BPaL or BPaS regimen. Both treatment regimens significantly lowered the CFU in lung (A) and spleen (B) after 4 weeks compared to untreated (UnRx) control. No significant difference was observed between either treatment groups in lung or spleen. The graphs represent combined data from two independent studies. LOD: limit of detection; ns = non-significant, **** = $p < 0.00005$

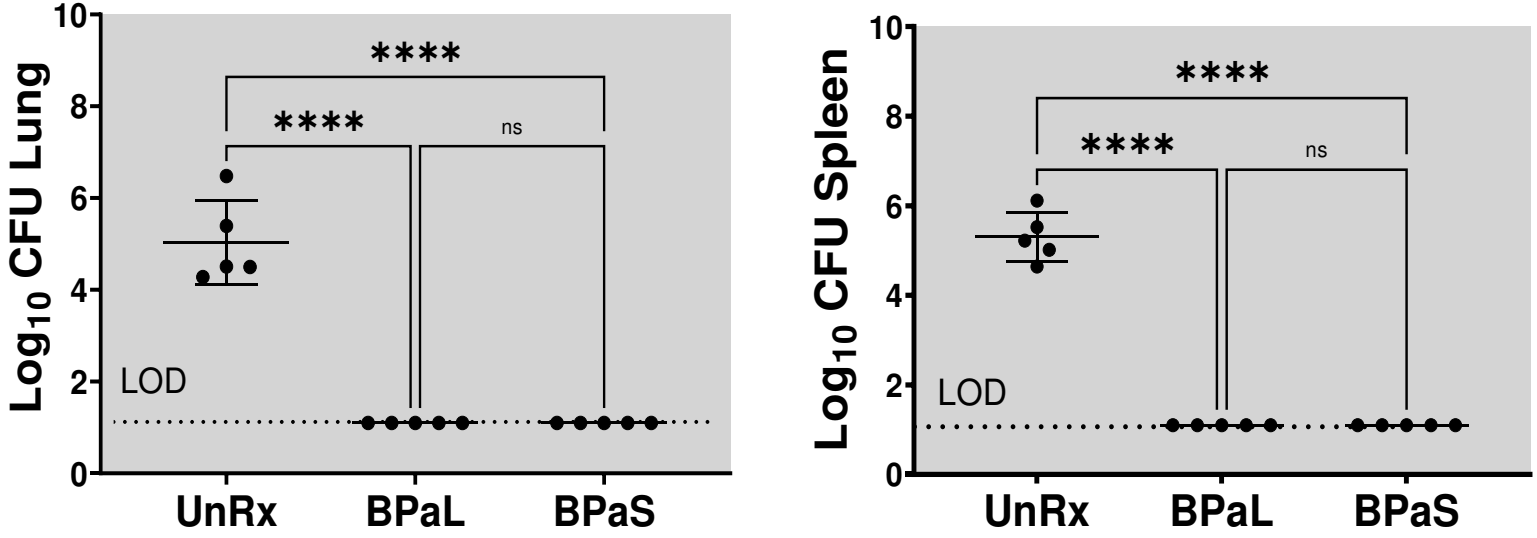

Figure 2.24i (BALB/c Study 1). Lung and spleen bacterial burden (CFU) in Mtb infected BALB/c mice treated with BPaL or BPaS regimen for 4 weeks. n = 5, LOD: limit of detection, ns = non-significant, **** = $p < 0.00005$

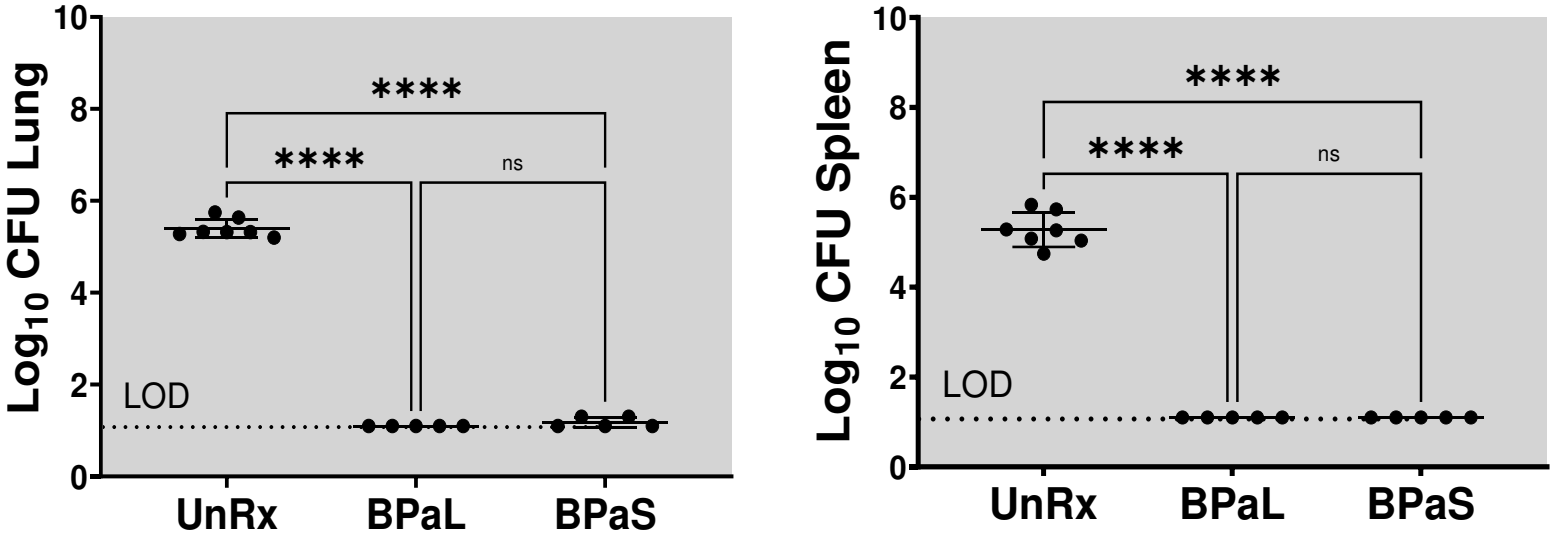

Figure 2.24ii (BALB/c Study 2). Lung and spleen bacterial burden (CFU) in Mtb infected BALB/c mice treated with BPaL or BPaS regimen for 4 weeks. n = 7, LOD: limit of detection, ns = non-significant, **** = $p < 0.00005$

Monitoring of adverse effects during drug treatment in the BALB/c TB model

1. ***Changes in the live body weight in the BALB/c TB model during treatment***
    a. ***Monotherapy of linezolid or spectinamide 1599 does not affect the live body weight of mice***

First the effect of monotherapy on the average live body weight of Mtb infected mice was evaluated. Mice were treated with linezolid (L) or spectinamide 1599 (S) alone for 4 weeks and their average live body weight was measured on a weekly basis. The results demonstrated that the live body weight of Mtb infected BALB/c mice treated with L or S was not affected during the 4 weeks of monotherapy treatment (Figure 2.25).

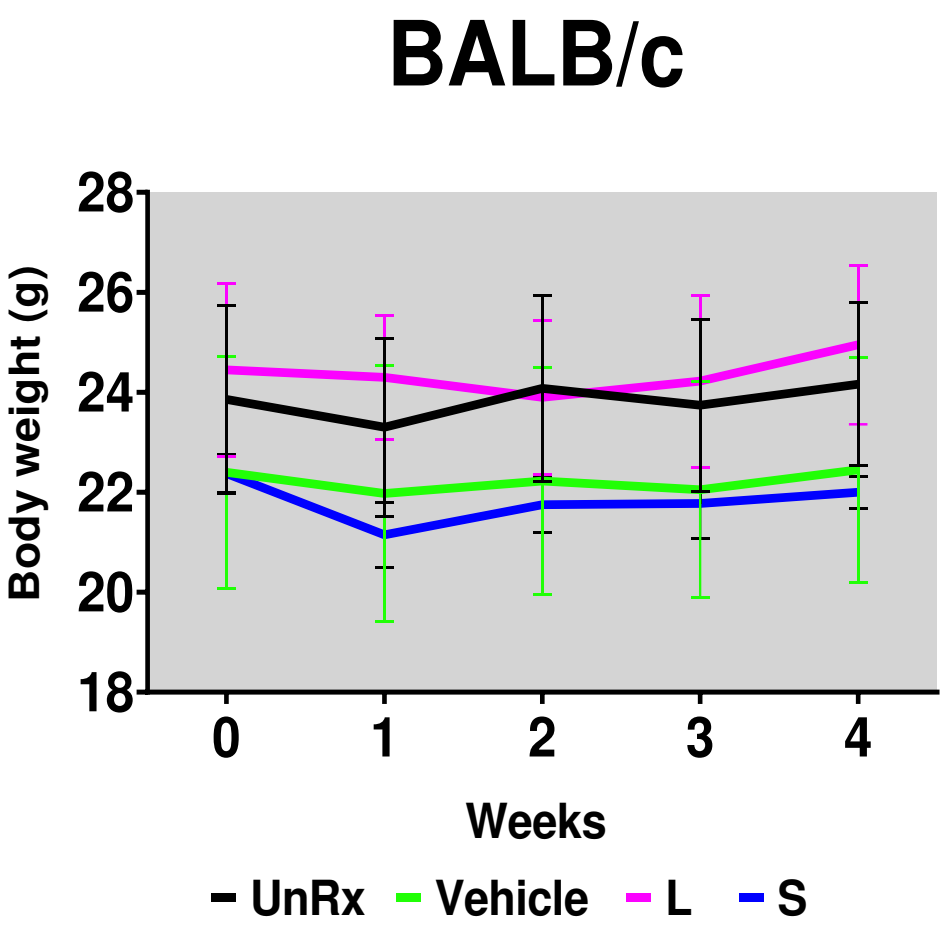

Figure 2.25. Change in the average live body weight of Mtb infected BALB/c mice during monotherapy. Mice treated with linezolid (L) or spectinamide 1599 (S) alone while untreated (UnRx) and vehicle groups served as control. No significant difference was observed among the groups after monotherapy. $p < 0.05$

b. BPaL therapy decreases the live body weight of mice

The average live body weight of Mtb infected female BALB/c mice summarized in Figure 2.26 is the combination of two independent studies and the results of individual studies are given in Figures 2.26i. The combined results showed that BPaL and BPaS treatments were well tolerated as change (%) in the live body weight of mice only ranged between 2.28-3.85%. The BPaL treatment significantly ($p<0.05$) decreased average live body weight of mice compared to untreated (UnRx) and BPaS treated animals. However, there was no significant ($p<0.05$) difference between UnRx and BPaS treatment groups.

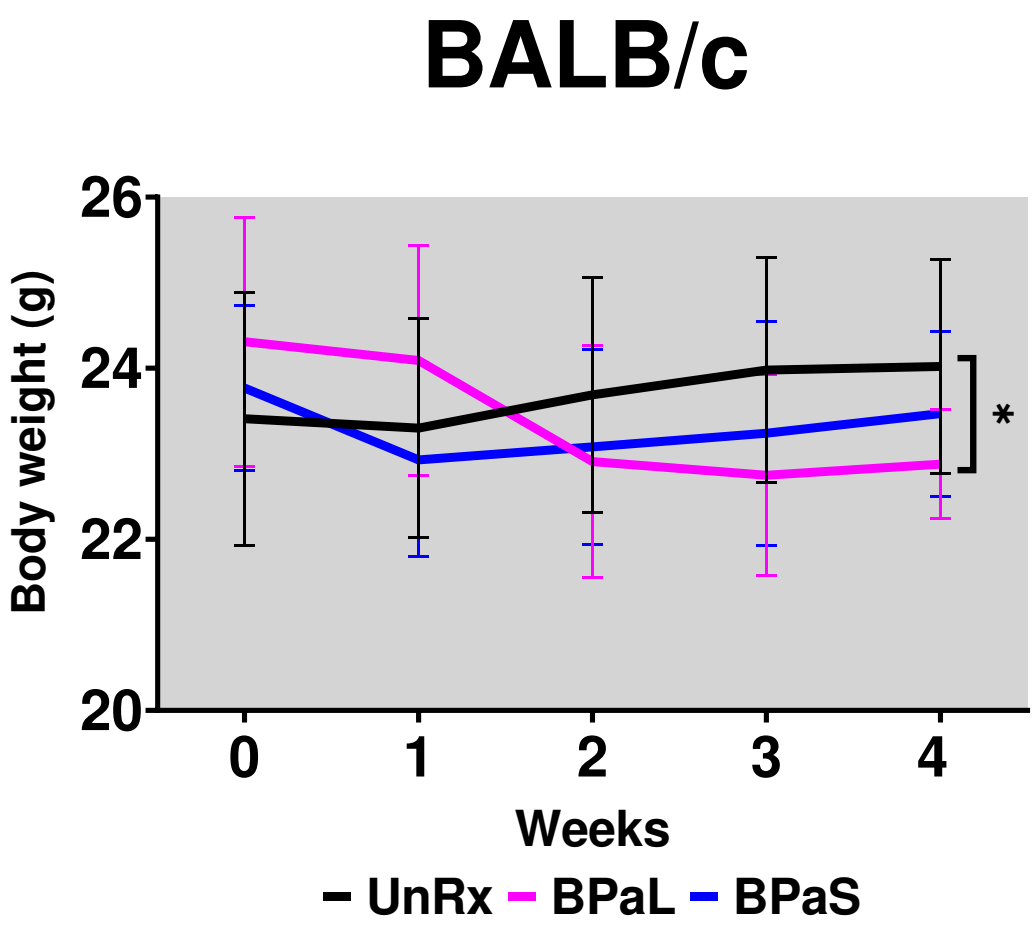

Figure 2.26. Change in the average live body weight of Mtb infected BALB/c mice during drug treatment. Mice treated with BPaL regimen significantly decreased their live body weight compared to untreated (UnRx) control and BPaS groups. The graph represents the combined data from two independent studies. $p < 0.05$

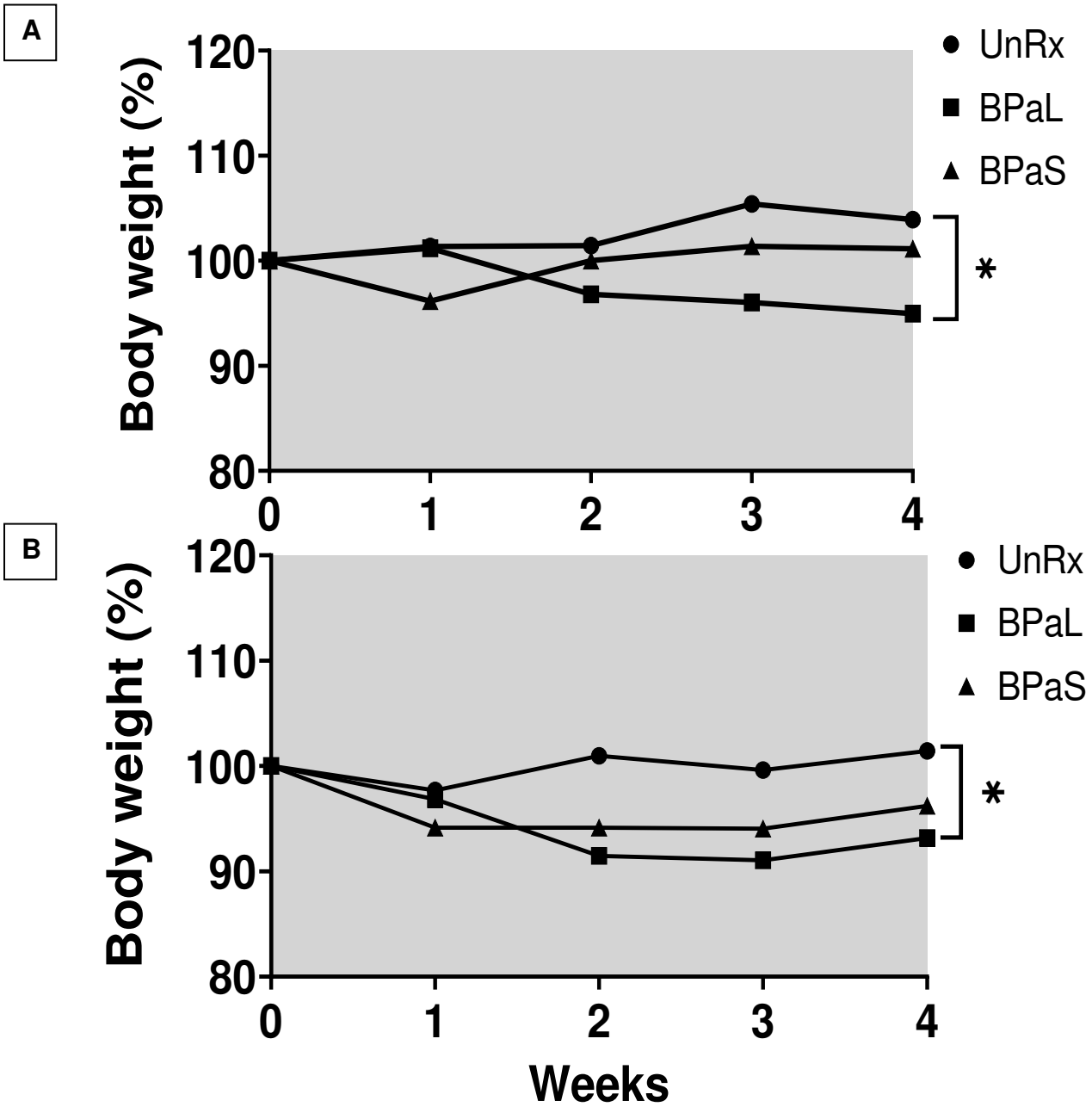

Figure 2.26i. Change in the average live body weight of Mtb infected BALB/c mice during drug treatment. (A) Study 1, n =7 (B) and study 2, n = 5 are presented here and the combined results of these studies are shown in Figure 2.26. $p < 0.05$

2. *BPaL and BPaS therapy result in significantly lower lesion burden in the BALB/c TB model*

The lungs from Mtb infected BALB/c mice treated with BPaL or BPaS regimen were processed for histopathology and lesion scoring. Contrary to C3HeB/FeJ mice, all granulomas in BALB/c mice consisted of cellular aggregations with very homogeneous structure. Importantly, like C3HeB/FeJ, BPaL and BPaS therapy in BALB/c mice significantly decreased the number and size of TB lesions and a significant ($p<0.05$) lesion burden score difference was observed between untreated and drug treatment groups (Figure 2.27).

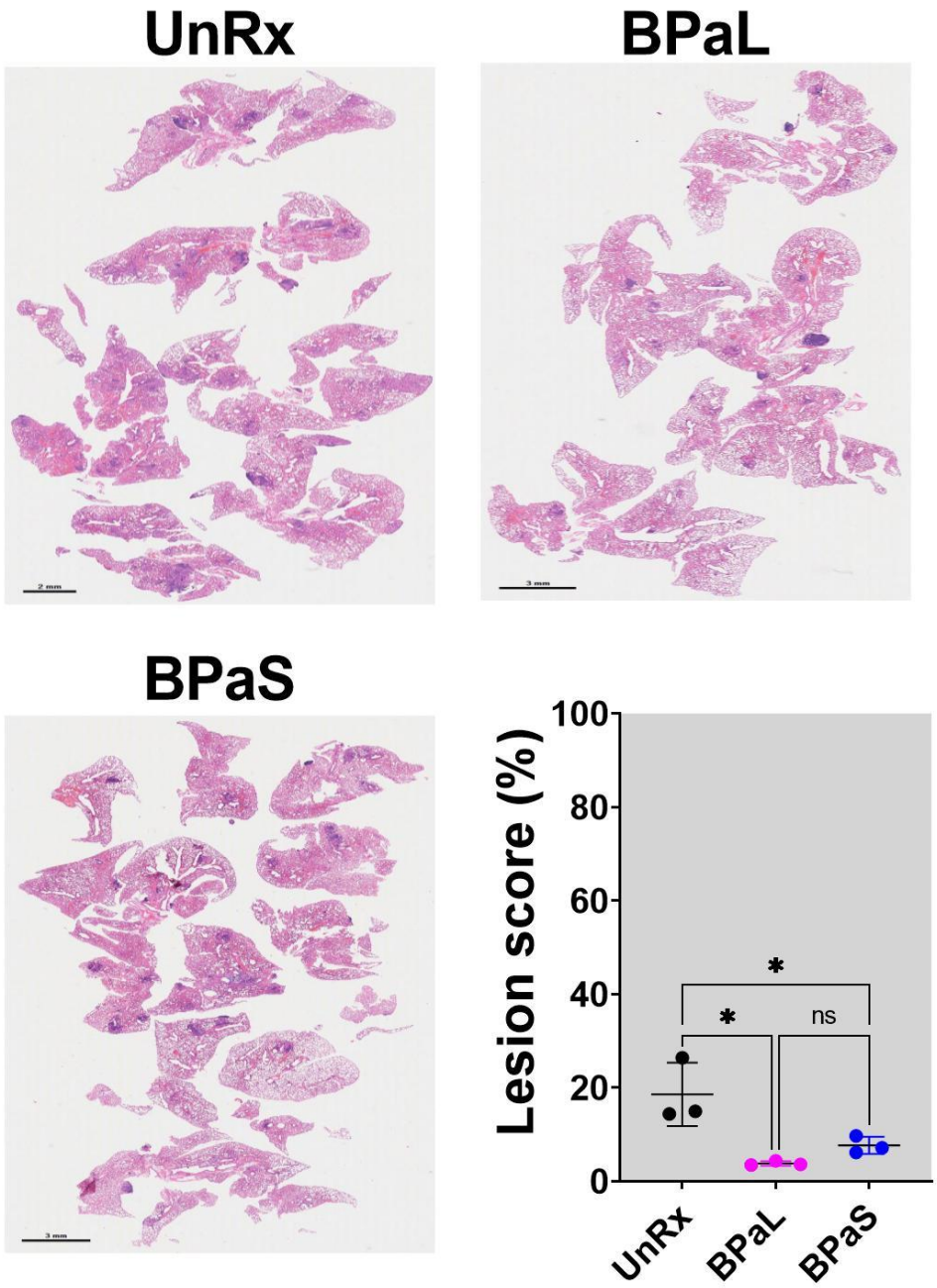

Figure 2.27. Change in the lung histopathology and lesion score of Mtb infected BALB/c mice during drug treatment. BPaL and BPaS treatments significantly decreased the lesion size and number compared to untreated (UnRx) control and their lesion scores reflect that change. H&E, 20X. ns = non-significant, $p < 0.05$

3. *BPaL and BPaS therapy does not alter the cell ratio in bone marrow of the BALB/c TB model*

Hematopathology of bone marrow of Mtb infected BALB/c mice was done at the end of 4 weeks treatment with BPaL and BPaS. The effect of treatments was evaluated by counting the number of myeloid (M) cells and other (O) cell types per 100 bone marrow cells. Both BPaL and BPaS treatments did not alter their numbers (Figure 2.28).

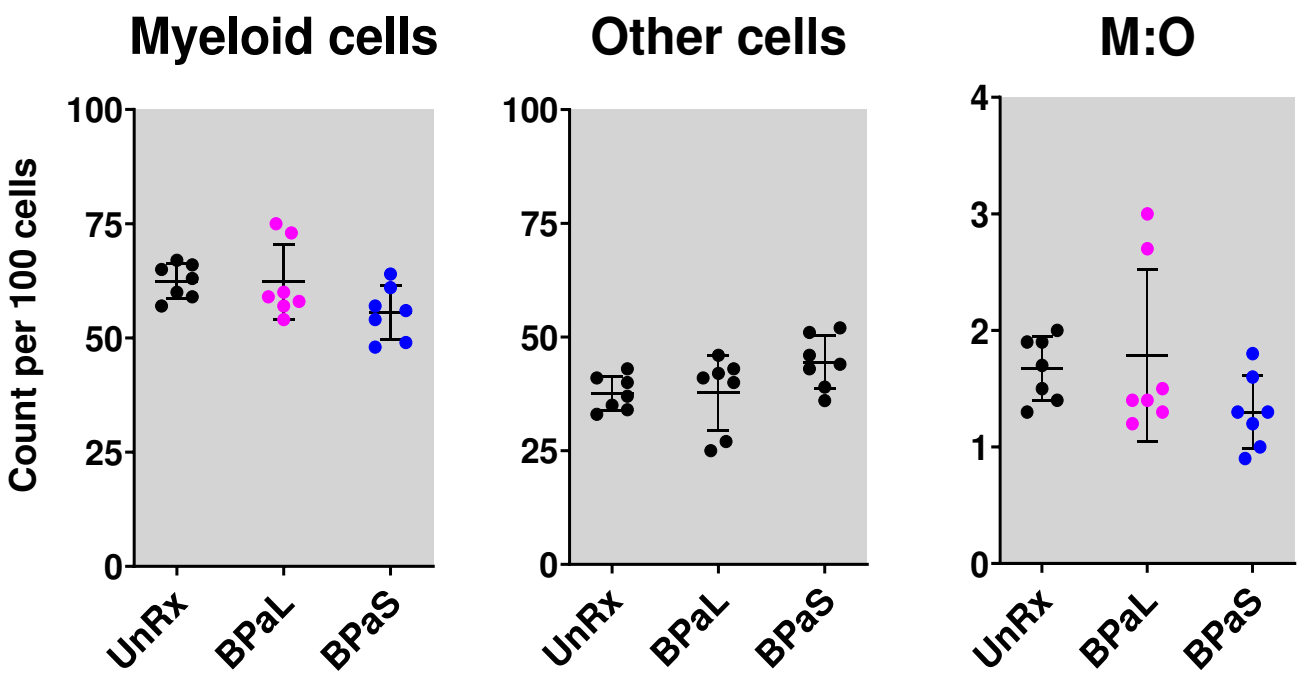

Figure 2.28. Evaluation of bone marrow cells in Mtb infected BALB/c mice after 4 weeks of treatment. The number and ratio of myeloid (M) cells and other (O) cell types remained unaltered after BPaL and BPaS treatments. $p < 0.05$

4. BPaL and BPaS therapy has no effect on cytokine and chemokine response in bone marrow of the BALB/c TB model

a) Change in the total protein concentration

A comparative analysis for the concentration of cytokine and chemokine in bone marrow, plasma, and lung samples from Mtb infected BALB/c mice treated with BPaL or BPaS regimen was measured. First the total protein (TP) concentration in lung homogenate and bone marrow supernatant was calculated to normalize its concentration for Luminex assay. The plasma samples, however, did not require TP measurement as their matrix was self-normalizing. The TP concentrations remained unaltered among the groups both in lung and spleen (Figure 2.29).

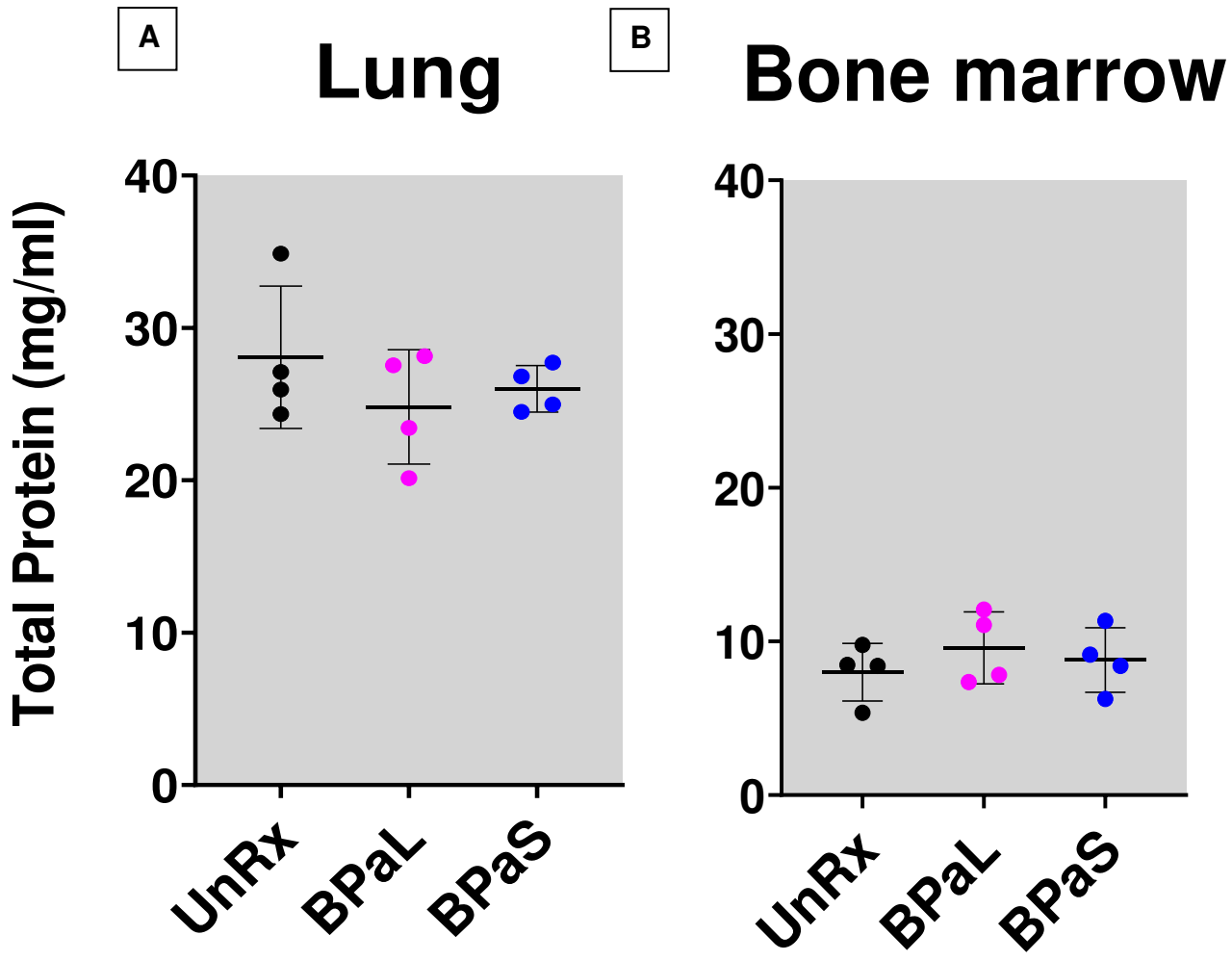

Figure 2.29. Change in the total protein (TP) concentration in lung and bone marrow from Mtb infected BALB/c mice during drug treatment. Mice were treated with BPaL and BPaS regimen but at the end of treatment no significant change was observed in TP concentration in lung (A) and bone marrow (B) samples in untreated (UnRx) and treatment groups.

b) Change in the cytokine and chemokine response

When bone marrow, plasma and lung samples of Mtb infected BALB/c mice were analyzed for 26 cytokines and chemokines, the BPaL and BPaS treatments did not change their concentration as depicted by their z-score in Figure 2.30, 2.31 and 2.32 respectively.

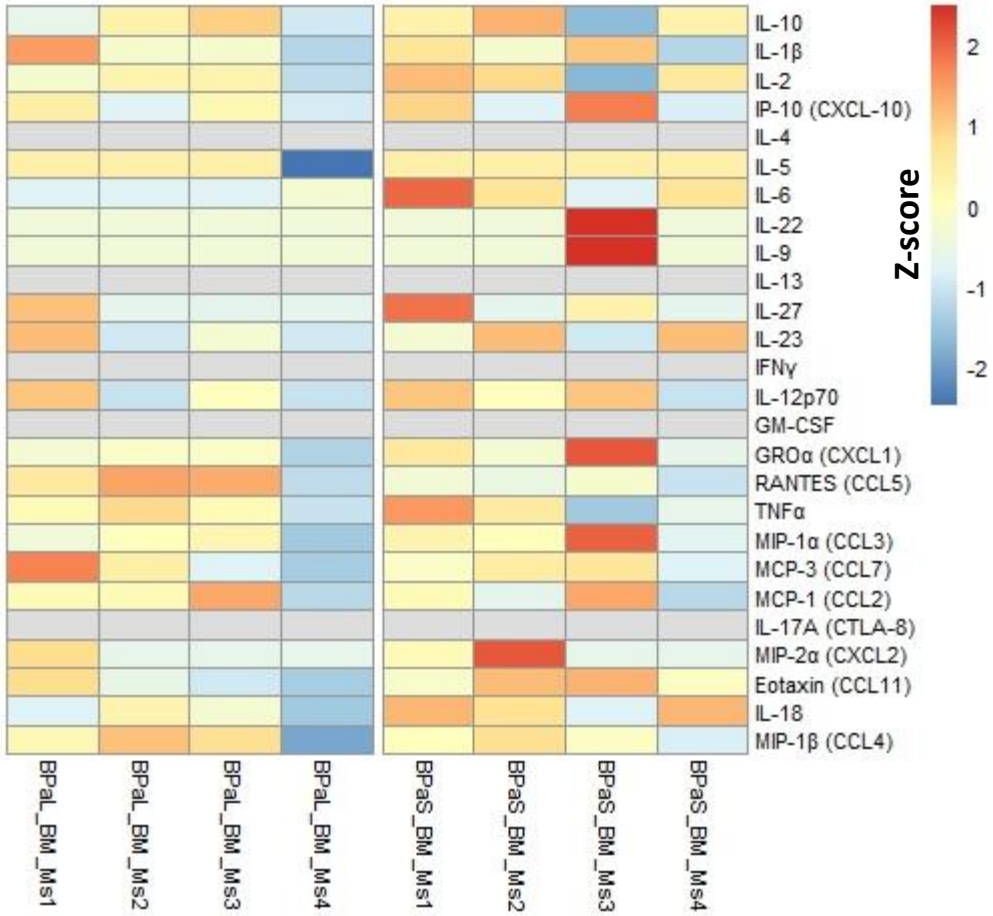

Figure 2.30. Measurement of 26 cytokines and chemokines in bone marrow (BM) supernatants of Mtb infected BALB/c mice treated with BPaL or BPaS regimen. No significant difference was observed for all cytokines and chemokines between the treatment groups after 4 weeks. $p < 0.05$

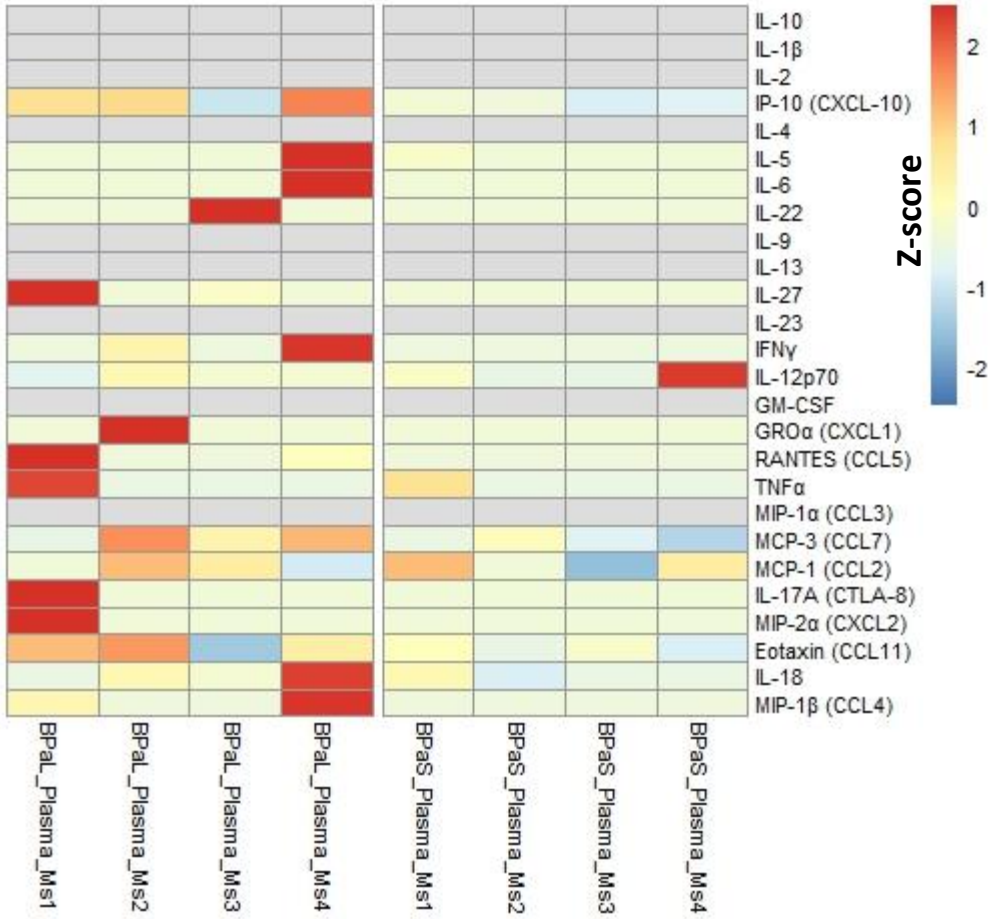

Figure 2.31. Measurement of 26 cytokines and chemokines in plasma of Mtb infected BALB/c mice treated with BPaL or BPaS regimen. No significant difference was observed for all cytokines and chemokines between the treatment groups after 4 weeks. $p < 0.05$

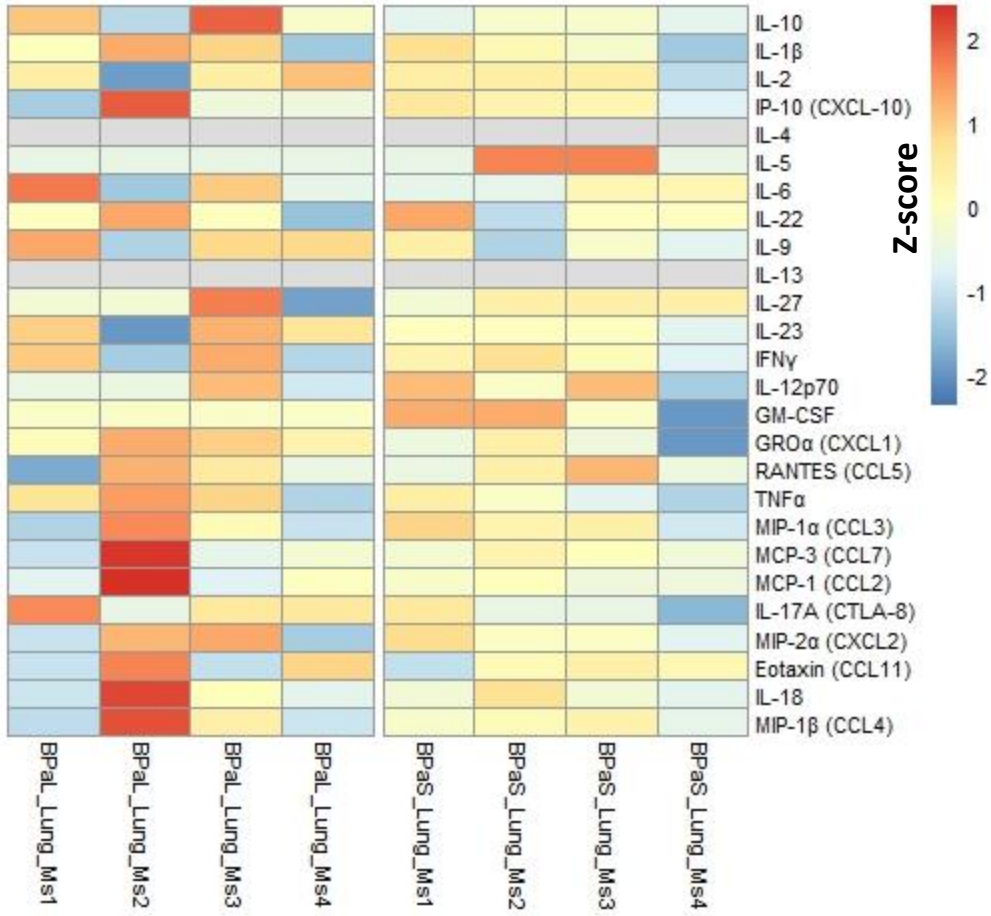

Figure 2.32. Measurement of 26 cytokines and chemokines in lung homogenates of Mtb infected BALB/c mice treated with BPaL or BPaS regimen. No significant difference was observed for all cytokines and chemokines between the treatment groups after 4 weeks. $p < 0.05$

c) *Correlation between lung CFU and cytokines and chemokines*

We further investigated the correlation factor between lung bacterial burden (CFU) and 26 cytokines and chemokines from bone marrow, plasma and lung samples from untreated (UnRx) and treatment (BPaL and BPaS) groups. None of the bone marrow cytokines and chemokines were found significantly (*$p<0.05$*) correlated with lung CFU (Figure 2.33). In plasma samples IL-13 (*$R=0.58$, $p=0.049$*) and IL-27 (*$R=0.64$, $p=0.026$*) were significantly positively correlated with the lung CFU (Figure 2.34). Whereas in the lung samples IP-10 (CXCL-10; *$R=0.71$, $p=0.01$*), GM-CSF (*$R=0.62$, $p=0.032$*), RANTES (CCL5; *$R=0.62$, $p=0.031$*), MCP-3 (CCL7; *$R=0.59$, $p=0.045$*), IL-17A (CTLA-8; *$R=0.69$, $p=0.012$*) and MIP-2 alpha (CXCL2; *$R=0.6$, $p=0.041$*) were positively correlated with lung CFU (Figure 2.35).

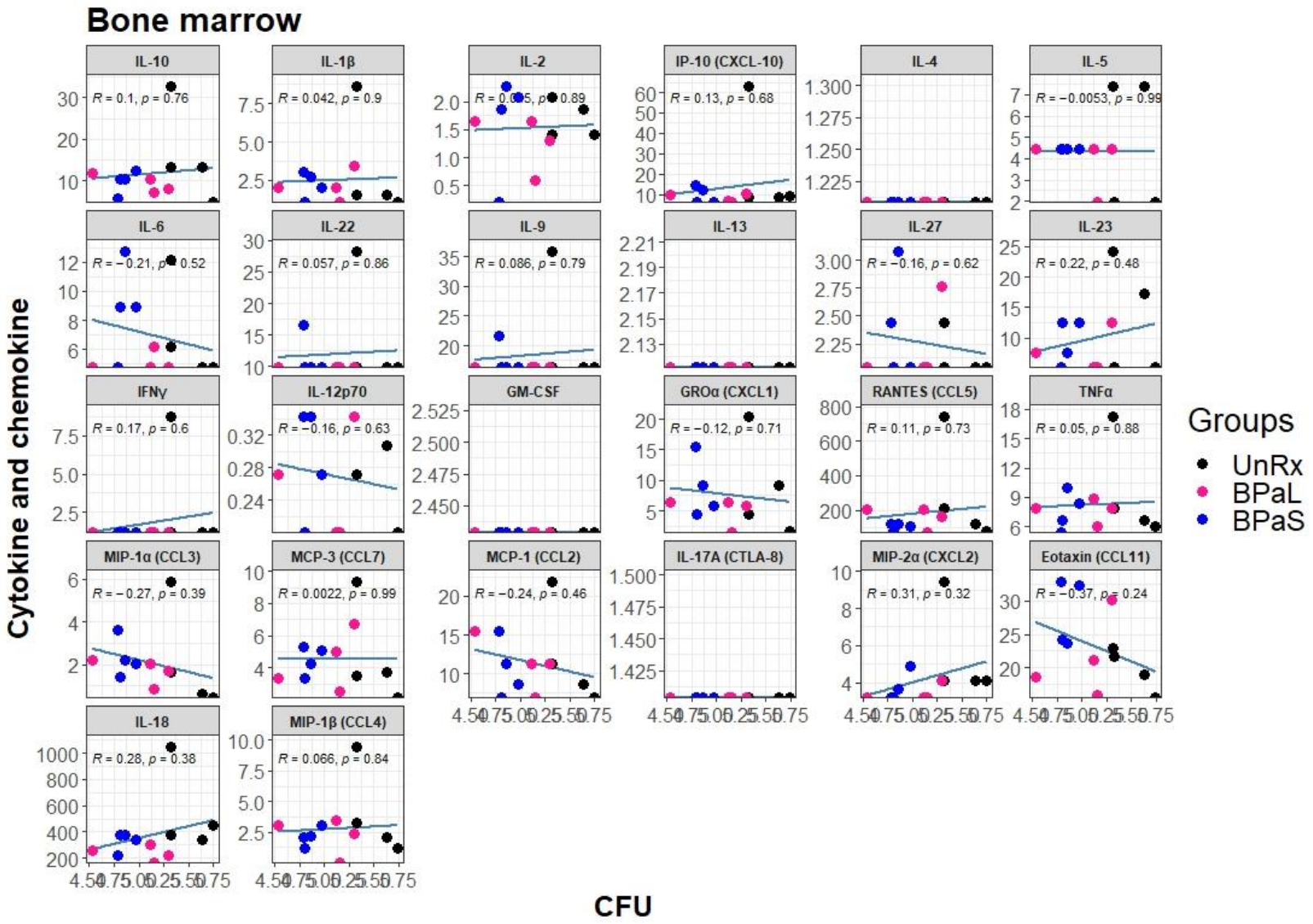

Figure 2.33. Spearman's correlation analysis between lung bacterial burden and bone marrow cytokines and chemokines profile in Mtb infected BALB/c mice treated with BPaL or BPaS regimen.

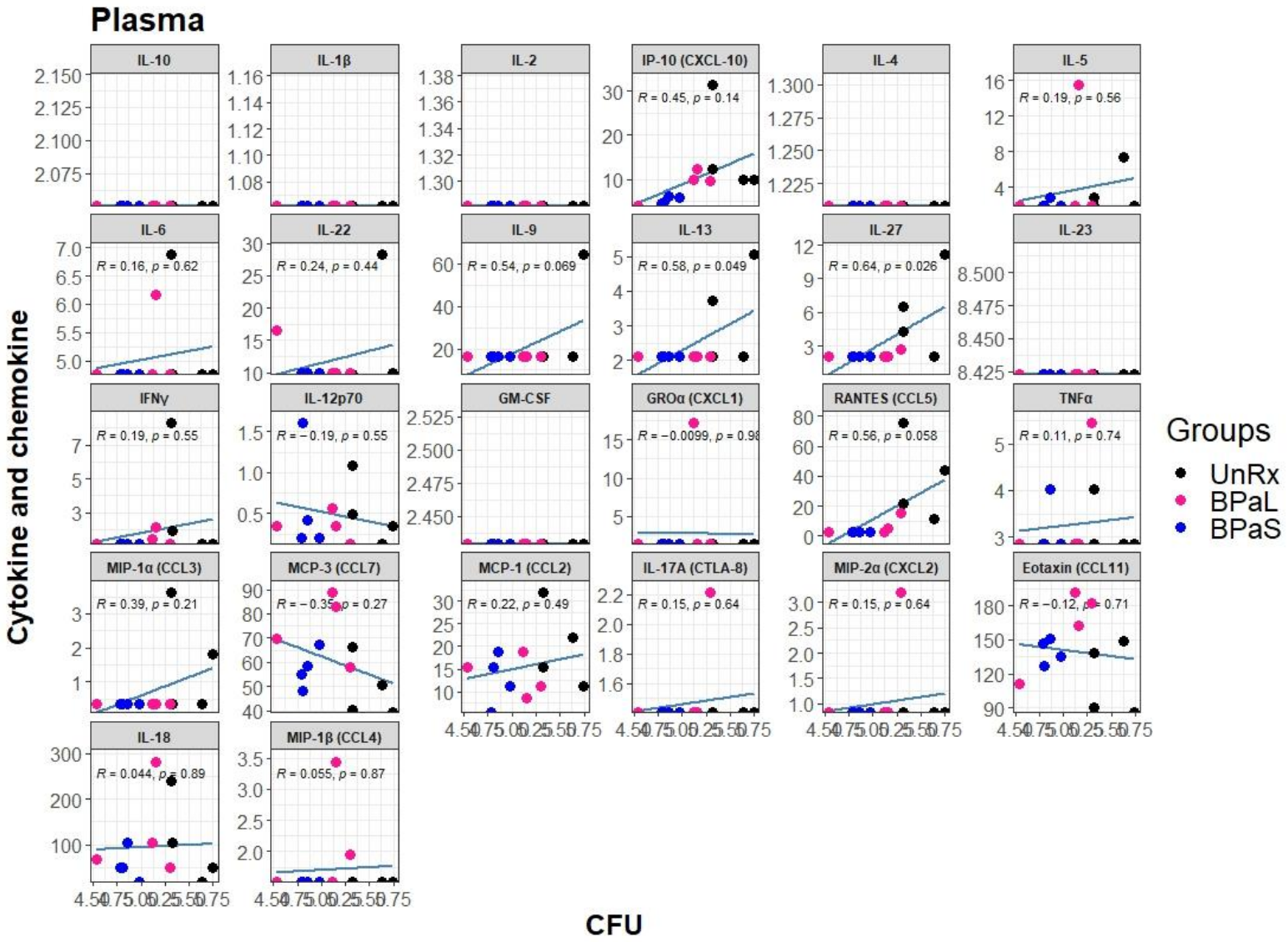

Figure 2.34. Spearman's correlation analysis between lung bacterial burden and plasma cytokines and chemokines profile in Mtb infected BALB/c mice treated with BPaL or BPaS regimen.

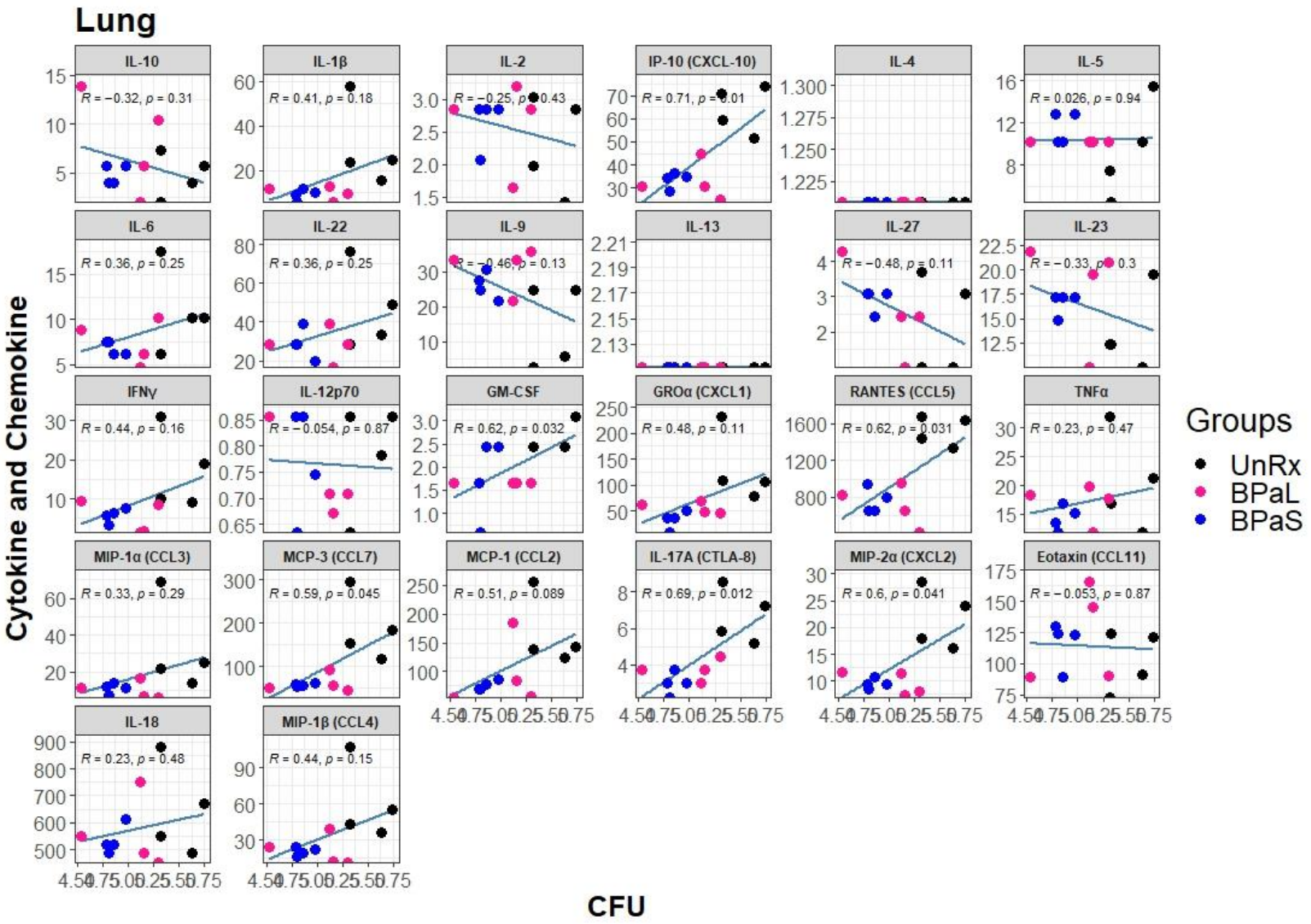

Figure 2.35. Spearman's correlation analysis between lung bacterial burden and lung cytokines and chemokines profile in Mtb infected BALB/c mice treated with BPaL or BPaS regimen.

Discussion

Despite decades of research, there are limited treatment options for MDR- and XDR-TB patients. Fortunately, the BPaL regimen consisting of all-oral drugs such as B, Pa and L showed excellent efficacy in preclinical (11,20,52,53) and clinical trials (12,13), yet there were associated severe AEs linked to long-term administration of L. In an attempt to overcome L-associated AEs, we evaluated a new regimen in which L in BPaL regimen was replaced with inhaled spectinamide 1599 (S), administered at 50 and 100mpk as reported previously (43). S has shown excellent efficacy against MDR- and XDR-TB in in vitro models studies (19,42), has potential for with high safety profile (37,38) and to be used as a dry powder inhalation therapy (48). Therefore, in the current study, we hypothesized that the BPaS regimen has similar efficacy to that of BPaL, while avoiding L-associated AEs.

We used two preclinical chronic TB murine efficacy models (54–56) to investigate BPa, BPaL and BPaS, for efficacy and any associated AEs during the course of 4-weeks of treatment. Based on the diversity of outcomes observed during human TB disease (43) and as no single animal model recapitulates the wide spectrum of human TB pathology (57), we chose the BALB/c and C3HeB/FeJ murine TB models. The BALB /c chronic TB model is representative of a long-term Mtb chronic infection that develops homogenous lung granulomatous lesions that restrain the bacilli within intracellular compartments (58). In contrast, low-dose aerosol Mtb infection of C3HeB/FeJ mouse also results in a chronic infection, but their lungs exhibit a heterogenous spectrum of lesions including granulomas similar to those seen in BALB/c chronic TB model in addition to caseous necrotic lesions surrounded by a fibrotic rim (51,59,60). The

caseum of these necrotic granulomas creates a hypoxic environment and contains abundant extracellular bacilli (51,60,61) in a similar fashion to necrotic granulomas found in some human TB patients. It is believed that fibrotic, necrotic and hypoxic environment of these granulomas creates barriers to drug penetration, alters bacterial phenotype, and together both attributes challenge therapeutic outcomes (54–56,62). Therefore, to better understand the broader implications of drug efficacy and drug associated AEs in scenarios without (BALB/c) and with (C3HeB/FeJ) necrotic granulomas, both murine TB efficacy models were employed.

Overall, our antimicrobial data are in accordance with the granuloma spectrum of both mouse models discussed above where a more robust reduction in lung bacterial burdens was observed in the absence (BALB/c) versus the presence (C3HeB/FeJ) of necrotic lesions. Although the spleen contains culturable Mtb, the pathological response is limited, consisting of microscopic aggregates of macrophages localized within lymphoid white pulp compartments in both models (62). As such, no difference in treatment response for BPa, BPaL, or BPaS was observed in spleen between BALB/c and C3HeB/FeJ mice. The overall lung efficacy observed for monotherapy with L or S administered for 4-weeks was <1 $\log_{10}$ CFU reduction (Figure 2.2 & 2.25), but both multidrug regimens as BPaL or BPaS promoted much higher CFU reduction. Thus, BPaL and BPaS significantly reduced lung burdens by 3.8-4.0 $\log_{10}$ and 2.5-2.7 $\log_{10}$ in BALB/c (Figure 2.26) and C3HeB/FeJ TB (Figure 2.3) models, respectively. The bactericidal effect of S as monotherapy (24) and BPaL (53) in mice is in line with previous reports. We therefore conclude that both regimens promote similar bactericidal effects in murine models lacking, or featuring, advanced pulmonary pathology.

A primary concern with the continued use of BPaL in humans, is the appearance of L-associated AEs including peripheral neuropathy, anemia, myelosuppression, and optic neuritis (12,13). Moreover, among all the hematological anomalies found in the patients worldwide treated with L or BPaL, the most commonly reported anomalies are anemia and myelosuppression (19,57,63,64). Although considered manageable, these AEs required dose reductions or interruptions in treatment of patients with L, which may drive treatment failure and/or further resistance development to B or Pa.

We deployed a host of diverse strategies to investigate regimen efficacy, tolerability, and treatment-associated alterations in hematology and immune function by quantifying the lung and spleen bacterial burdens, live body weight of animals, pulmonary histopathology, CBC profiles, and bone marrow histopathology as measures of treatment response, anemia, and myelosuppression.

Detailed pathological assessment revealed an improvement in the lesion burden score in mice treated with BPaL and BPaS when compared to untreated animals. The improvement of lesion burden strongly correlated with the reduction of bacterial burden in both TB models (Figure 2.6 & 2.29). Thus, we concluded that the potent antimicrobial effect of BPaL and BPaS regimens also results in improvement of the pathological outcome during chronic infection with Mtb. It remains to be determined whether BPaS is equivalent to BPaL in terms of achieving durable relapse-free cure in mice, which was outside of the scope of this initial study.

Weight loss is an important clinical parameter in TB patients as the extent of weight loss determines the severity of disease progression (65). Moreover it is also used in clinics as an indicator of *in vivo* drug efficacy (66). As in a previous study (43),

monotherapy with 4-weeks of L or S did not have a pronounced effect on the live body weight of mice (Figure 2.4 & 2.27). However, L-containing BPaL regimen, but not BPaS, was associated with a significant decrease in the live body weight at week 4 in Mtb-infected BALB/c (Figure 2.28) and C3HeB/FeJ mice (Figure 2.5). A similar inverse relationship between body weight and L exposure was recently reported in human patients (67). Nevertheless, it remains unclear whether the observed change in mice body weight while on 4-weeks of treatment with BPaL versus L alone is the result of stress arising from repeated daily drug administration by oral gavage but arguably the treatment with BPaS also received repeated daily dosing. Therefore, we concluded it might be a regimen-specific effect that will need to be monitored during longer periods of treatments.

Among L-associated hematological side effects, the incidence of anemia is reported at rates of up to 62.5% in MDR and XDR-TB patients (68–70) and the onset of this effect can occur 2 weeks to 2 months post L administration (71). Using a CBC profile of 20 peripheral blood parameters, we showed that mild anemia is associated with 4-weeks of L or BPaL drug treatment in Mtb-infected C3HeB/FeJ mice. In contrast, our preclinical study failed to detect any difference between 4-weeks L or S monotherapy in terms of total red blood cells, white blood cells, platelets, or hemoglobin (HGB) concentrations compared to untreated control group (data not shown). However, L treatment alone increased RDWs and both L and S decreased MCHC (Figure 2.7). In human TB patients treated with anti-TB drugs (72–74), increased RDWs and lower HGB are associated with anemia and these parameters serve as markers of disease prognosis. Interestingly, in our study, such changes were observed in BPaL but not in BPa or BPaS

groups suggesting that L could be the causative agent leading to these changes. As MCHC was also decreased to an equivalent extent in mice receiving 4-weeks of BPaL and BPaS, this suggests that reduction in MCHC is independent of inclusion of an oxazolidinone in a BPa-based combination regimen. Another striking observation is that none of the 20-blood parameters evaluated showed any change after the first two weeks of therapy with BPa, BPaL, or BPaS (Figure 2.8). However, by 4-weeks, a significant drop in HGB and an increase in RDWs was apparent for BPaL group (Figure 2.8). This is interpreted to mean that mild hematological effects observed in mice treated for 4-weeks with L or BPaL are dependent on the number of L-doses administered and are thus, time-dependent. Overall, the onset of these hematological effects when testing an L-containing regimen (BPaL) is in agreement with previous studies (71,75) in human patients.

Toxicity of the oxazolidinones remains a critical issue. The mechanism of L-induced toxicity is attributed to its binding with the host mitochondrial ribosomes leading to mitochondrial toxicities (32). The latter results in activation of Nlrp3 inflammasome (31) and subsequently results in L-mediated bone marrow myelosuppression (64); a phenomenon consistent with the hematologic anomalies seen in patients treated with L for extended time periods. Because spectinamides do not bind to mitochondrial ribosomes there is reduced potential for similar side effects (42) (76). To conclusively test this hypothesis, we performed bone marrow histopathology to quantify M to E ratio (M:E), a parameter that provides information about the relative proportions of myeloid lineage (granulocytes, monocytes, and their precursors) to erythroid lineage (77). The BPa and BPaL regimens altered M:E ratio in C3HeB/FeJ TB model by suppressing myeloid and inducing erythroid lineages (Figure 2.9) whereas no such difference was

observed in mice treated with BPaS compared to untreated control. L was previously shown to impact M:E ratio, although an opposite trend was observed in those studies, which employed 12-days of L administration and a different strain of otherwise healthy mice (31). Time course studies using a single consistent assay method are needed to resolve this discrepancy.

Elevation of interleukin 1β (IL-1β) levels and activation of Nlrp3 inflammasome have been previously linked to myelosuppression (64). A 26-plexed immunoassay on bone marrow samples from Mtb-infected C3HeB/FeJ mice revealed that most of the proinflammatory cytokines and chemokines including IL-1β, IL-12p70 and TNF-α were present at significantly higher concentrations in animals treated with BPaL compared to BPaS (Figure 2.11). The presence of elevated IL-1β was previously reported during monotherapy with L (31),(78). Studies from UnRx Mtb-infected C3HeB/FeJ mice also revealed highly elevated levels of cytokine and chemokine, as expected (Figure 2.14).

Lastly, we examined the effect of BPaL and BPaS regimens with regards to changes in the immune cell profile of bone marrow, blood, and lungs. Similar to changes observed for cytokine profiles, our comparative analysis of cell populations in bone marrow revealed a significant reduction in the number of most immune cell subsets during BPa, BPaL or BPaS treatment compared to UnRx control (Figure 2.17). Two cell subsets showed a specific increase with drug treatment including CD45+CD3+ T-lymphocytes and CD45+CD3-CD19+B220- B-lymphocytes. This quantitative increase in T- and B-lymphocytes suggests changes in adaptive immunity with effective drug treatment in mice. These observations are further supported by quantification of immune cells in lungs which also revealed an increase of T- (CD4, CD8 and Foxp3) and

B-lymphocytes (B220) in BPaL and BPaS treatment groups compared to UnRx control (Figure 2.21). Comparative analysis of immune cell populations in Mtb-infected C3HeB/FeJ mice treated with BPaS and BPaL was similar for all groups except for cells expressing the F4/80 marker, which were significantly higher in mice treated with BPaS (Figure 2.22).

An additional striking finding from this study was a strong concordance between the decrease in lung and spleen bacterial burdens and a corresponding decrease in the number of cells expressing the neutrophil associated marker (Ly6G) (Figure 2.21). This observation further supports profound overall changes in the reorganization of immune cells during therapy with BPaL or BPaS (Figure 2.22). An implication of this finding is that the favorable treatment outcomes may promote a corresponding decline in Ly6G neutrophil population. This finding is noteworthy as the previous studies have suggested a correlation between the presence of Ly6G neutrophils in lungs with higher Mtb load and worsened disease severity, whereas, depletion of this cell population was found to lower Mtb burdens, without affecting other immune cells (79).These observations should be considered with caution given that only a single timepoint was allocated to this study arm.

In support of our original hypothesis, we show that 4-weeks of treatment with BPaS was equivalent to BPaL in terms of bactericidal response in lungs and spleens in two mouse models of increasing pathologic complexity. Hematologic and bone marrow histopathology confirmed a role for L and BPaL in promoting mild anemia and myelosuppression in mice. In contrast, BPaS was not found to promote AEs within the timeframe and dosing interval tested herein. Both regimens also promoted significant

improvement in lung pathology score and quantitative changes of markers of adaptive immunity. Together this data suggests that inhaled spectinamide 1599 is an effective partner agent to BPa and may serve as a potentially safer replacement for L in a modified Nix-TB regimen (BPaS).

This report has several limitations. The studies conducted were not designed as formal safety trials and should be considered accordingly. The studies performed only looked at 1-month of L, BPaL or BPaS treatment, and longer dosing would be necessary to determine if treatment continued to reduce lung bacterial burden and/or resulted in more significant L-associated AEs. Definitive relapse trials are also warranted to understand if BPa + S is as effective as BPa + L in promoting durable cure in mice.

The TB drug development field is working towards developing shorter and safer therapies with a common goal of developing new multidrug regimens of low pill burden that are accessible to patients, of short duration (ideally 2-3 months) and consist of 3-4 drugs of novel mode-of-action with proven efficacy, safety, and limited toxicity. Here we present initial results that are in line with these goals. Further studies with inhaled spectinamide 1599 and BPa are therefore warranted to determine if 2-3 months of treatment with BPaS, further reduces the bacterial burden and leads to sterilizing activity without associated AEs.

References

1. Santos KP, Rodero CF, Ribeiro CM, Gremião MPD, Peccinini RG, Pavan FR, et al. Development of a Mucoadhesive Liquid Crystal System for the Administration of Rifampicin Applicable in Tuberculosis Therapy. Life. 2022;12(1138):1–21.
2. Temrikar ZH, Kodidela S, Kumar S, Liu J, Robertson GT, Lee RE, et al. Characterization of spectinamide 1599 efficacy against different mycobacterial phenotypes. Tuberculosis [Internet]. 2023;140:1–9. Available from: https://doi.org/10.1016/j.tube.2023.102342
3. Dutt TS, Karger BR, Fox A, Youssef N, Dadhwal R, Ali MZ, et al. Mucosal exposure to non-tuberculous mycobacteria elicits B cell-mediated immunity against pulmonary tuberculosis. Cell Rep [Internet]. 2022;41(11):111783. Available from: https://doi.org/10.1016/j.celrep.2022.111783
4. Chakaya J, Khan M, Ntoumi F, Aklillu E, Fatima R, Mwaba P, et al. Global Tuberculosis Report 2020 – Reflections on the Global TB burden, treatment and prevention efforts. Int J Infect Dis. 2021;113:S7–12.
5. Brunaugh AD, Walz A, Warnken Z, Pearce C, Gutierrez JM, Koleng JJ, et al. Respirable Clofazimine Particles Produced by Air Jet Milling Technique Are Efficacious in Treatment of BALB/c Mice with Chronic *Mycobacterium tuberculosis* Infection. Antimicrob Agents Chemother. 2022;66(9):1–19.
6. Ockenga J, Fuhse K, Chatterjee S, Malykh R, Rippin H, Pirlich M, et al. Tuberculosis and malnutrition: The European perspective. Clin Nutr. 2023;42(4):486–92.
7. WHO. Global TB report. 2022.
8. Campbell JR, Nsengiyumva P, Chiang LY, Jamieson F, Khadawardi H, Mah HKH, et al. Costs of Tuberculosis at 3 Treatment Centers, Canada, 2010–2016. Emerg Infect Dis. 2022;28(9):1814–23.
9. Zhang MW, Zhou L, Zhang Y, Chen B, Peng Y, Wang F, et al. Treatment outcomes of patients with multidrug and extensively drug-resistant tuberculosis in Zhejiang, China. Eur J Med Res. 2021;26(1):1–10.
10. Williams K, Minkowski A, Amoabeng O, Peloquin CA, Taylor D, Andries K, et al. Sterilizing activities of novel combinations lacking first- and second-line drugs in a murine model of tuberculosis. Antimicrob Agents Chemother. 2012;56(6):3114–20.
11. Tasneen R, Betoudji F, Tyagi S, Li SY, Williams K, Converse PJ, et al. Contribution of oxazolidinones to the efficacy of novel regimens containing bedaquiline and pretomanid in a mouse model of tuberculosis. Antimicrob Agents Chemother. 2016;60(1):270–7.
12. Conradie F, Diacon AH, Ngubane N, Howell P, Everitt D, Crook AM, et al. Treatment of Highly Drug-Resistant Pulmonary Tuberculosis. N Engl J Med.

2020;382(10):893–902.

13. Conradie F, Bagdasaryan TR, Borisov S, Howell P, Mikiashvili L, Ngubane N, et al. Bedaquiline–Pretomanid–Linezolid Regimens for Drug-Resistant Tuberculosis. N Engl J Med. 2022;387(9):810–23.

14. Mbuagbaw L, Guglielmetti L, Hewison C, Bakare N, Bastard M, Caumes E, et al. Outcomes of bedaquiline treatment in patients with multidrug-resistant tuberculosis. Emerg Infect Dis. 2019;25(5):936–43.

15. Pontali E, Sotgiu G, D'Ambrosio L, Centis R, Migliori GB. Bedaquiline and multidrug-resistant tuberculosis: A systematic and critical analysis of the evidence. Eur Respir J [Internet]. 2016;47(2):394–402. Available from: http://dx.doi.org/10.1183/13993003.01891-2015

16. Bardal S, Waechter J, Martin D. Chapter 18 Infectious diseases. In: Applied Pharmacology. Saunders; 2011. p. 233–91.

17. Lyu XL, Lin TT, Gao JT, Jia HY, Zhu CZ, Li ZH, et al. Effects of Bedaquiline on Antimicrobial Activity and Cytokine Secretion of Macrophages Infected with Multidrug-Resistant *Mycobacterium tuberculosis* Strains. Can J Infect Dis Med Microbiol. 2022;2022:1–9.

18. Giraud-Gatineau A, Coya JM, Maure A, Biton A, Thomson M, Bernard EM, et al. The antibiotic bedaquiline activates host macrophage innate immune resistance to bacterial infection. Elife. 2020;9:1–29.

19. Robertson GT, Scherman MS, Bruhn DF, Liu J, Hastings C, McNeil MR, et al. Spectinamides are effective partner agents for the treatment of tuberculosis in multiple mouse infection models. J Antimicrob Chemother. 2017;72(3):770–7.

20. Xu J, Li SY, Almeida D V., Tasneen R, Barnes-Boyle K, Converse PJ, et al. Contribution of pretomanid to novel regimens containing bedaquiline with either linezolid or moxifloxacin and pyrazinamide in murine models of tuberculosis. Antimicrob Agents Chemother. 2019;63(5):1–14.

21. Lu X, Smare C, Kambili C, El Khoury AC, Wolfson LJ. Health outcomes of bedaquiline in the treatment of multidrug-resistant tuberculosis in selected high burden countries. BMC Health Serv Res [Internet]. 2017;17(1):1–12. Available from: http://dx.doi.org/10.1186/s12913-016-1931-3

22. Malo A, Kellermann T, Ignatius EH, Dooley KE, Dawson R, Joubert A, et al. A validated liquid chromatography tandem mass spectrometry assay for the analysis of pretomanid in plasma samples from pulmonary tuberculosis patients. J Pharm Biomed Anal. 2021;195:1–8.

23. Singh R, Manjunatha U, Boshoff HIM, Young HH, Niyomrattanakit P, Ledwidge R, et al. PA-824 kills nonreplicating *Mycobacterium tuberculosis* by intracellular NO release. Vol. 322, Science. 2008.

24. Pstragowski, M. Zbrzezna, M. and Bujalska-Zadrozny M. Advances in pharmacotherapy of Tuberculosis. Acta Pol - Drug Res [Internet]. 2017;74(1):3–

11. Available from: https://www.embase.com/search/results?subaction=viewrecord&id=L604925228&from=export

25. Manjunatha U, Boshoff HI, Barry CE. The mechanism of action of PA-824: Novel insights from transcriptional profiling. Commun Integr Biol [Internet]. 2009;2(3):215–8. Available from: http://www.ncbi.nlm.nih.gov/pubmed/19641733%0Ahttp://www.pubmedcentral.nih.gov/articlerender.fcgi?artid=PMC2717523

26. Fekadu G, Tolossa T, Turi E, Bekele F, Fetensa G. Pretomanid development and its clinical roles in treating tuberculosis. J Glob Antimicrob Resist. 2022;31:175–84.

27. Occhineri S, Matucci T, Rindi L, Tiseo G, Falcone M, Riccardi N, et al. Pretomanid for tuberculosis treatment: an update for clinical purposes. Curr Res Pharmacol Drug Discov. 2022;3:1–8.

28. Jackson A. Drugs and the Future: Brain Science, Addiction and Society. Academic Press. 2007.

29. Roger C, Roberts JA, Muller L. Clinical Pharmacokinetics and Pharmacodynamics of Oxazolidinones. Clin Pharmacokinet. 2018;57(5):559–75.

30. Colca JR, McDonald WG, Waldon DJ, Thomasco LM, Gadwood RC, Lund ET, et al. Cross-linking in the living cell locates the site of action of oxazolidinone antibiotics. J Biol Chem [Internet]. 2003;278(24):21972–9. Available from: http://dx.doi.org/10.1074/jbc.M302109200

31. Iyer SS, Iyer SS, He Q, He Q, Janczy JR, Janczy JR, et al. Mitochondrial Cardiolipin Is Required for Nlrp3 Inflammasome Activation. Immunity [Internet]. 2013;39(2):311–23. Available from: http://linkinghub.elsevier.com/retrieve/pii/S1074761313003294%5Cnpapers3://publication/doi/10.1016/j.immuni.2013.08.001

32. De Vriese AS, Van Coster R, Smet J, Seneca S, Lovering A, Van Haute LL, et al. Linezolid-induced inhibition of mitochondrial protein synthesis. Clin Infect Dis. 2006;42(8):1111–7.

33. Song T, Lee M, Jeon HS, Park Y, Dodd LE, Dartois V, et al. Linezolid Trough Concentrations Correlate with Mitochondrial Toxicity-Related Adverse Events in the Treatment of Chronic Extensively Drug-Resistant Tuberculosis. EBioMedicine. 2015;2(11):1627–33.

34. WHO. Global TB Report 2018.

35. Singh B, Cocker D, Ryan H, Sloan DJ. Linezolid for drug-resistant pulmonary tuberculosis. Cochrane Database Syst Rev. 2019;2019(3).

36. Holloway WJ. Spectinomycin. Med Clin North Am. 1982;66(1).

37. Owusu E, Amartey BT, Afutu E, Boafo N. Aminoglycoside Therapy for

Tuberculosis: Evidence for Ototoxicity among Tuberculosis Patients in Ghana. Diseases. 2022;10(1):10.

38. De Jager R, Van Altena R. Hearing loss and nephrotoxicity in long-term aminoglycoside treatment in patients with tuberculosis. Int J Tuberc Lung Dis. 2002;6(7):622–7.

39. Kanchugl S, Selmer M. Structural Recognition of Spectinomycin by Resistance Enzyme ANT(9) from Enterococcus faecalis. Antimicrob Agents Chemother. 2020;64(6):e00371-20.

40. Liu J, Bruhn DF, Lee RB, Zheng Z, Janusic T, Scherbakov D, et al. Structure-activity relationships of spectinamide antituberculosis agents: A dissection of ribosomal inhibition and native efflux avoidance contributions. ACS Infect Dis. 2017;3(1):72–88.

41. Bruhn DF, Scherman MS, Liu J, Scherbakov D, Meibohm B, Böttger EC, et al. In vitro and in vivo evaluation of synergism between anti-tubercular spectinamides and non-classical tuberculosis antibiotics. Sci Rep. 2015;5:1–10.

42. Lee RE, Hurdle JG, Liu J, Bruhn DF, Matt T, Scherman MS, et al. Spectinamides: A New Class of Semisynthetic Anti-Tuberculosis Agents that Overcome Native Drug Efflux. Nat Med. 2017;20(2):152–8.

43. Gonzalez-Juarrero M, Lukka PB, Wagh S, Walz A, Arab J, Pearce C, et al. Preclinical Evaluation of Inhalational Spectinamide-1599 Therapy against Tuberculosis. ACS Infect Dis. 2021;7(10):2850–63.

44. Wagh S, Rathi C, Lukka PB, Parmar K, Temrikar Z, Liu J, et al. Model-based exposure-response assessment for spectinamide 1810 in a mouse model of tuberculosis. Antimicrob Agents Chemother. 2021;65(11):1–15.

45. Nirmal A, Sznajder K, Patil R, Shaikh B. Preference of inhalants over pills/injections among pulmonary tuberculosis patients in Western India: A cross-sectional study. J Clin Tuberc Other Mycobact Dis. 2021;23.

46. Matthieu B, Matthieu J, Nicolas G, Patrice G, Srine M, William C, et al. Comparison of intrapulmonary and systemic pharmacokinetics of colistin methanesulfonate (CMS) and colistin after aerosol delivery and intravenous administration of CMS in critically ill patients. Antimicrob Agents Chemother. 2014;58(12):7331–9.

47. Rathi C, Lukka PB, Wagh S, Lee RE, Lenaerts AJ, Braunstein M, et al. Comparative pharmacokinetics of spectinamide 1599 after subcutaneous and intrapulmonary aerosol administration in mice. Tuberculosis. 2019;114:119–22.

48. Hickey AJ, Misra A, Fourie PB. Dry powder antibiotic aerosol product development: Inhaled therapy for tuberculosis. J Pharm Sci [Internet]. 2013;102(11):3900–7. Available from: http://dx.doi.org/10.1002/jps.23705

49. Golde WT, Gollobin P, Rodriguez LL. A rapid, simple, and humane method for submandibular bleeding of mice using a lancet. Lab Anim (NY). 2005;34(9):39–

43.

50. Fox A, Dutt TS, Karger B, Rojas M, Obregón-Henao A, Anderson GB, et al. Cyto-Feature Engineering: A Pipeline for Flow Cytometry Analysis to Uncover Immune Populations and Associations with Disease. Sci Rep. 2020;10(1):1–12.

51. Irwin SM, Driver E, Lyon E, Schrupp C, Ryan G, Gonzalez-Juarrero M, et al. Presence of multiple lesion types with vastly different microenvironments in C3HeB/FeJ mice following aerosol infection with *Mycobacterium tuberculosis*. Dis Model Mech. 2015;8(6):591–602.

52. Bigelow KM, Tasneen R, Chang YS, Dooley KE, Nuermberger EL. Preserved efficacy and reduced toxicity with intermittent linezolid dosing in combination with bedaquiline and pretomanid in a murine tuberculosis model. Antimicrob Agents Chemother. 2020;64(10).

53. Nuermberger EL, Martínez-Martínez MS, Sanz O, Urones B, Esquivias J, Soni H, et al. GSK2556286 Is a Novel Antitubercular Drug Candidate Effective In Vivo with the Potential To Shorten Tuberculosis Treatment. Antimicrob Agents Chemother. 2022;66(6).

54. Harper J, Skerry C, Davis SL, Tasneen R, Weir M, Kramnik I, et al. Mouse model of necrotic tuberculosis granulomas develops hypoxic lesions. J Infect Dis. 2012;205(4):595–602.

55. Irwin SM, Gruppo V, Brooks E, Gilliland J, Scherman M, Reichlen MJ, et al. Limited activity of clofazimine as a single drug in a mouse model of tuberculosis exhibiting caseous necrotic granulomas. Antimicrob Agents Chemother. 2014;58(7):4026–34.

56. Aly S, Wagner K, Keller C, Malm S, Malzan A, Brandau S, et al. Oxygen status of lung granulomas in *Mycobacterium tuberculosis*-infected mice. J Pathol. 2006;210:298–305.

57. Singh AK, Gupta UD. Animal models of tuberculosis: Lesson learnt. Indian J Med Res [Internet]. 2018;147:456–63. Available from: http://www.ncbi.nlm.nih.gov/pubmed/23144490

58. De Groote MA, Gilliland JC, Wells CL, Brooks EJ, Woolhiser LK, Gruppo V, et al. Comparative studies evaluating mouse models used for efficacy testing of experimental drugs against *Mycobacterium tuberculosis*. Antimicrob Agents Chemother. 2011;55(3):1237–47.

59. Dpre, Robertson GT, Ramey ME, Massoudi LM, Carter CL, Zimmerman M, et al. Comparative Analysis of Pharmacodynamics in the C3HeB/FeJ Mouse Tuberculosis Model for DprE1 Inhibitors TBA-7371, PBTZ169, and OPC-167832. Antimicrob Agents Chemother. 2021;65(1):e00583-21.

60. Driver ER, Ryan GJ, Hoff DR, Irwin SM, Basaraba RJ, Kramnik I, et al. Evaluation of a mouse model of necrotic granuloma formation using C3HeB/FeJ mice for testing of drugs against *Mycobacterium tuberculosis*. Antimicrob Agents

Chemother. 2012;56(6):3181–95.

61. Lanoix JP, Lenaerts AJ, Nuermberger EL. Heterogeneous disease progression and treatment response in a C3HeB/FeJ mouse model of tuberculosis. Dis Model Mech. 2015;8(6):603–10.

62. Walter ND, Ernest JP, Dide-Agossou C, Bauman AA, Ramey ME, Rossmassler K, et al. Lung microenvironments harbor *Mycobacterium tuberculosis* phenotypes with distinct treatment responses . Antimicrob Agents Chemother. 2023;67(9):1–15.

63. Minardi ML, Fato I, Di Gennaro F, Mosti S, Mastrobattista A, Cerva C, et al. Common and rare hematological manifestations and adverse drug events during treatment of active tb: A state of art. Microorganisms. 2021;9(7):1–15.

64. Winchell CG, Mishra BB, Phuah JY, Saqib M, Nelson SJ, Maiello P, et al. Evaluation of IL-1 Blockade as an Adjunct to Linezolid Therapy for Tuberculosis in Mice and Macaques. Front Immunol. 2020;11:1–18.

65. Van Crevel R, Karyadi E, Netea MG, Verhoef H, Nelwan RHH, West CE, et al. Decreased plasma leptin concentrations in tuberculosis patients are associated with wasting and inflammation. J Clin Endocrinol Metab. 2002;87(2):758–63.

66. Nikonenko BV, Samala R, Einck L, Nacy CA. Rapid, simple in vivo screen for new drugs active against *Mycobacterium tuberculosis*. Antimicrob Agents Chemother. 2004;48(12):4550–5.

67. Wasserman S, Denti P, Brust JCM, Abdelwahab M, Hlungulu S, Wiesner L, et al. Linezolid pharmacokinetics in South African patients with drug-resistant tuberculosis and a high prevalence of HIV coinfection. Antimicrob Agents Chemother. 2019;63(3).

68. Abebe G, Bonsa Z, Kebede W. Early Safety and Efficacy of Linezolid-Based Combination Therapy among Patients with Drug-Resistant Tuberculosis in North-western Nigeria. Int J Mycobacteriology. 2021;10:129–35.

69. Palomino JC, Martin A. Drug resistance mechanisms in *Mycobacterium tuberculosis*. Antibiotics. 2014;3(3):317–40.

70. Sotgiu G, Centis R, D'Ambrosio L, Alffenaar JWC, Anger HA, Caminero JA, et al. Efficacy, safety and tolerability of linezolid containing regimens in treating MDR-TB and XDR-TB: Systematic review and meta-analysis. Eur Respir J. 2012;40(6):1430–42.

71. Tang S, Yao L, Hao X, Zhang X, Liu G, Liu X, et al. Efficacy, safety and tolerability of linezolid for the treatment of XDR-TB: A study in China. Eur Respir J [Internet]. 2015;45(1):161–70. Available from: http://dx.doi.org/10.1183/09031936.00035114

72. Mirlohi M-S, Nezamodini ZS, Rezvani Z, Kian K. Hematological and liver toxicity of anti-tuberculosis drugs. Electron Physician. 2016;8(9):3592–7.

73. Kassa E, Enawgaw B, Gelaw A, Gelaw B. Effect of anti-tuberculosis drugs on

hematological profiles of tuberculosis patients attending at University of Gondar Hospital, Northwest Ethiopia. BMC Hematol. 2016;16(1):1–11.

74. Luo M, Liu M, Wu X, Wu Y, Yang H, Qin L, et al. Impact of anemia on prognosis in tuberculosis patients. Ann Transl Med. 2022;10(6):329–329.

75. Gerson SL, Kaplan SL, Bruss JB, Le V, Arellano FM, Hafkin B, et al. Hematologic effects of linezolid: Summary of clinical experience. Antimicrob Agents Chemother. 2002;46(8):2723–6.

76. Modongo C, Pasipanodya JG, Zetola NM, Williams SM, Sirugo G, Gumboc T. Amikacin concentrations predictive of ototoxicity in multidrug-resistant tuberculosis patients. Antimicrob Agents Chemother. 2015;59(10):6337–43.

77. Elmore SA. Enhanced Histopathology of the Bone Marrow Susan. Toxicol Pathol [Internet]. 2006;34(5):666–86. Available from: https://www.ncbi.nlm.nih.gov/pmc/articles/PMC3624763/pdf/nihms412728.pdf

78. Jasenosky LD, Scriba TJ, Hanekom WA, Goldfeld AE. T cells and adaptive immunity to *Mycobacterium tuberculosis* in humans. Immunol Rev. 2015;264(1):74–87.

79. Lovewell RR, Baer C, Mishra BB, Smith CM, Christopher M. Granulocytes act as a niche for *Mycobacterium tuberculosis* growth. Mucosal Immunol. 2021;14(1):229–41.

CHAPTER 3

Spatial and temporal profiling of immune responses during pulmonary infection with *Mycobacterium tuberculosis*

Introduction

Tuberculosis (TB) is an infectious disease caused by *Mycobacterium tuberculosis* (Mtb), and it has been recorded since ancient history. In 2021, 1.4 million people died of TB and 10 million new cases of this disease were diagnosed (1). Commonly, a person is infected by inhaling Mtb and thus the bacteria first infects the lungs, however, it can also disseminate to and infect other body organs like kidney, brain, liver, spleen, and bones (2). An estimated one fourth of the world population is infected with Mtb (3) but the majority (90%) lack clinical symptoms and are non-infectious; clinically this stage of infection is diagnosed as latent TB (LTB) (4). Only 10% of the infected world population develop clinical symptoms and can be infectious; clinically these patients are diagnosed with active TB (ATB).

Mtb is an intracellular bacillus that primarily infects macrophages and dendritic cells (DCs), the innate component of the immune system in the lungs. Upon entry into the lungs, alveolar macrophages (AMs) along with other phagocytes (DCs) engulf Mtb (5). Infection of these cells promotes an inflammatory response that leads to recruitment of more macrophages and neutrophils, all of which form a wall surrounding the infected cell. Eventually, as the infection progresses in time, the inflammatory responses recruit several types of lymphocytes at the site of infection. This cell wall surrounding the

infected cells is referred to as a tuberculous granuloma. Thus, the granuloma is a highly organized lesion located within stromal cells of the lungs and which contains focal aggregates of central myeloid cells (mainly macrophages, neutrophils and DCs) that are at various stages of activation and are interspaced or surrounded with T and B lymphocytes (6,7). This structure can further be surrounded by a fibrous capsule of fibroblasts and collagen fibers that separates the immune cells from the uninvolved adjacent healthy tissue or parenchyma (8) and in some instances the core of the granuloma becomes necrotic and is highly infiltrated with neutrophils. The granuloma is considered the hallmark of TB and its main role is to create unique immune microenvironments (IME) that controls dissemination of the bacteria to other organs and to another host (6). However, if IME fails to control the infection, the integrity of the granuloma is lost and the Mtb is free to replicate within and outside cells. Active replication of the bacilli results in uncontrolled inflammatory responses along with extensive lung tissue and airway damage. The latter also facilitates the host expulsion, via coughing, of droplets containing bacilli which are transmitted and implanted into a new host (ATB infection) (9,10).

The Mtb-containing droplets first interact with alveolar macrophages (AMs) located in the alveolar sacs of the lungs. These cells phagocytose Mtb bacilli and often kill them via formation of phagolysosomes and production of antimycobacterial peptides and reactive oxygen and nitrogen intermediaries (ROIs and RNIs respectively) (11). This process, in response, causes mild inflammation in the lungs. The initial containment of the infection may depend on factors such as genetics of the individual and on the inhaled Mtb strain. However, Mtb has also evolved numerous mechanisms

to escape the host defense system by triggering anti-inflammatory responses and blocking the formation of phagolysosomes (12).

Most frequently as soon as the AMs interact and ingest the bacteria, these cells secrete various cytokines; among others the most important are tumor necrosis factor alpha (TNFα), interleukin (IL) 12 and 23 along with a variety of chemokines; CCL2 and CCL5. This initial inflammatory response of the AMs recruit neutrophils, DCs and blood monocytes to the site of infection, all of which are also capable of ingesting and digesting bacteria. Antigen presenting DCs are very important cell populations at this point because after uptaking the bacilli they move quickly from the site of infection to the draining lymph nodes where naïve T lymphocytes reside (13). The DCs at the lymph nodes activate differentiation of naïve T cells into effector T cells that in turn will be recruited back to the forming granuloma in the lungs. At the granuloma, effector T cells recognize the infected macrophages and secrete interferon gamma (IFNγ) which activates macrophages to kill intracellular Mtb via RNIs production (14). However, the latter mechanism has no sterilizing capacity, and some bacteria survive the attack, as a result, a perpetual inflammatory response ensues with a continuous recruitment of more T and B lymphocytes along with regulatory T cells and more myeloid cells; all aiming to balance the antimicrobial and inflammatory responses (and subsequent tissue damage) with anti-inflammatory responses that limit excessive inflammation and tissue damage. Thus, the successful longevity of a granuloma and restraining of bacilli within its wall is possible thanks to the well-balanced environment of pro-inflammatory (e.g. TNFα and IFNγ) and anti-inflammatory (e.g. IL-10) cytokines (15) produced by lymphocytes and macrophages within the granuloma. Overall, as discussed above, the granuloma acts

as a double-edged sword because it limits infection, but it also provides a safe IME for Mtb to survive for long periods of time. In this scenario, more than 90% of the infected individuals are capable of restraining Mtb within granulomas; these individuals are diagnosed with LTB infection and remain asymptomatic.

About 10% of LTB infections can eventually develop ATB. Reactivation may be caused because patients develop immunosuppression or due to the environmental causes such as coinfection with HIV infection, other co-morbidities and aging (16). In this stage, Mtb can actively replicate, disrupt the granuloma structure and become a free-living bacterium within and outside the granuloma and in the extracellular matrix. The latter leads to overriding inflammatory responses, advance pathology and extensive tissue and airway damage that results in pulmonary disease and often leads to cavitation of the lungs.

Human TB manifests a diverse spectrum of granulomas (17) which exhibit morphological heterogeneity both in ATB and LTB disease as revealed by the studies conducted more than 50 years ago (4). Apart from the classic caseous granuloma, granulomas range from the non-necrotizing, neutrophil-rich, mineralized granulomas to the highly organized necrotic encapsulated granulomas with a cavity (7). The heterogeneity of the granulomas is influenced by factors such as the state and number of Mtb, the type of localized immune response, and the overall host disease status (18,19). These findings are supported by the studies conducted in humans (8,20–23) and animal models (10,24,25) all of which reiterate the inherent complexity of this disease. With the progression of time, granulomas increase in size, number, and distribution in the lungs and vary in cellular composition and histological features.

Initially the small cellular aggregates of non-necrotic lesions develop into large mature necrotic granulomas.

Animal models play an important role in basic and translational TB research and, therefore, are frequently used to answer critical questions. There is no single animal model that truly recapitulates the human TB spectrum (4). For example, Mtb infection in BALB/c mice develop into a long-term and very slow chronic infection resulting in uniform pulmonary non-capsulated cellular lesions containing clusters of immune cells (24). On the other hand, Mtb infection in C3HeB/FeJ mice develops into a much rapid and advanced pathology and disease that results in heterogenous pulmonary lesions including cellular granuloma and highly organized encapsulated caseous necrotic lesions (24,25). Each model is well suited to help understand the course of immunopathology in circumstances (BALB/c mice) in which the bacteria remain intracellularly versus other scenarios (C3HeB/FeJ mice) in which bacteria can be found either intracellular or extracellularly in necrotic and encapsulated granulomas and there is rapid progression into advanced disease with early mortality. Most important, it is well reported that the granulomas are not static lesions and over time there are important spatial and temporal changes that lead to changes in their structure and composition. These changes differ not only from one granuloma to another in a single individual but also depend on severity of the disease (4). Thus, longitudinal studies using the BALB/c and C3HeB/FeJ mice also allow us to study spatial and temporal changes of different types of granulomas at different disease states.

Our goal is to understand the *in situ* immunopathological course of different scenarios of TB using the BALB/c and C3HeB/FeJ mouse models of TB. Previous

studies have used similar models to investigate the cellular and molecular composition of the lung immunopathology using flow cytometry, immunoassays, etc. (26–30) but all these approaches use homogenates or isolated cell suspensions of lung tissue which lack the histological context of the granuloma. Therefore, intrinsic interactions *in situ* between cells during formation of the granuloma and their changes over time remain poorly understood. Conventional histopathological techniques such as hematoxylin and eosin (H&E), immunofluorescence (IF) and immunohistochemistry (IHC) are limited in their capacity to study immunopathology. Here, we studied longitudinal relationships of immune cells as well as their unique populations within and around granuloma in BALB/c and C3HeB/FeJ mouse models of TB using a novel technique of multispectral imaging microscopy. Compared to flow cytometry and other techniques, multiplex fluorescence immunohistochemistry (mfIHC) is unique in its ability to provide both expression and location of several immune cells along with their co-localization in a single tissue section while preserving tissue architecture and spatial context.

Materials and Methods

Mice and *Mycobacterium tuberculosis* infection

Female 6-8 weeks old BALB/c and C3HeB/FeJ mice were purchased from the Jackson Laboratories (Bar Harbor, ME). Mice were rested for at least one week at BSL3 laboratory in Colorado State University (CSU) before infection. All protocols and use of these animals were reviewed and approved by the Institutional Animal Care and Use Committee (IACUC) at CSU. Animals were infected with a low dose aerosol infection of

Mycobacterium tuberculosis (Mtb) (Erdman strain; ATCC 35801) using an inhalation exposure system (Glas-Col, Terre Haute, IN) calibrated to deliver ~50-100 colony forming units (CFU) to the lungs. To confirm the bacterial deposition into the lungs, mice (n=5) were euthanized after the aerosol infection and their lung homogenates were plated onto 7H11 agar plates followed by incubation at 37 °C for 3-4 weeks until the colonies were visible to the naked eye on the agar and were enumerated. Likewise, the total CFU of the inoculum was also determined as explained above. Clinical observations of these mice e.g., inactivity, rough fur, hunched posture, increased respiratory rate or effort were monitored daily.

Necropsy of animals

Mtb-infected BALB/c mice (n=5) were sacrificed at 5-, 9- and 11-weeks post infection and C3HeB/FeJ mice (n=3) were sacrificed at 9- and 13-weeks post infection. Mice were terminally euthanized by CO_2 narcosis, then the thoracic cavity was opened, and their lungs collected and processed for further analysis.

Measurement of bacterial burden in the lungs

The bacterial burden was measured as CFU in the lungs of animals. Because the course of infection in BALB/c mice is homogenously distributed between lung lobes, only the left lung lobes (1/3 of the lungs) were collected and prepared for CFU quantitation. On the other hand, because the course of infection in the C3HeB/FeJ mice is heterogeneously distributed, we used the whole lungs for CFU quantitation. Lungs were collected and homogenized using the Next Advance Bullet Blender (Averill Park,

NY) as described previously (31). The lung homogenates were plated in a serial 10-fold dilution onto 7H11 agar plates and incubated for 4-6 weeks before the final CFU count.

Lung histopathology and lesion scoring

The right lung lobes from BALB/c animals and whole lungs from C3HeB/FeJ mice were fixed in 4% paraformaldehyde (PFA) for 48 hours and embedded in paraffin for histopathological evaluation. Formalin fixed paraffin embedded (FFPE) tissues were sectioned at 5 µm, dried overnight at room temperature and then kept at 4 °C until further use. The sections were stained with hematoxylin and eosin (H&E: Leica Biosystems) and scanned at 40X magnification using the multispectral automated PhenoImager (Akoya Biosciences) for lesion scoring. The extent of the lesion burden in the lungs was quantified using blinded digital images and an open-source QuPath software for image analysis. For each tissue section, a region of interest (ROI) was generated at low magnification with a custom tissue detecting algorithm using decision forest training and classification to differentiate tissue versus background based on color and area. Lesions were identified within tissue ROIs at high magnification with an additional custom-made algorithm using decision forest training and classification based on staining intensity, color normalization and deconvolution, area, and morphological features. Percent lesion calculations were integrated into the same algorithm and calculated from tissue area and lesion area as designated by the ROI and lesions detected.

Multiplex fluorescence immunohistochemistry

Five µm sections of FFPE lung tissues were further stained for multiplex fluorescence immunohistochemistry (mfIHC) using a Leica bond autostainer at the Human Immunology & Immunotherapy Initiative (HI^3) core located at the University of Colorado, Denver. mfIHC was conducted using an Opal 7-color automatic IHC kit (Akoya Biosciences) with Tyramide Signal Amplification (TSA) technique. The principle of TSA technique for mfIHC staining is described in Figure 3.1. Briefly, the detection method of antigen is based on the use of fluorophore conjugated to a tyramide molecule in the TSA reagent. In this system, horse-radish peroxidase (HRP) enzyme conjugated with secondary antibody is used to catalyze a reaction between tyramide. Tyrosine residues formed in this process covalently deposit each fluorophore on or near the epitope of interest on the tissue section. Compared to conventional fluorescence IHC, the TSA offers brighter signals by producing a local sea of fluorophores near an HRP-conjugated antibody. Due to the covalent binding, mfIHC staining leaves a permanent fluorescent label in the tissue slide and therefore it allows more colors to be added by sequential labelling. This step is followed by the heat-mediated stripping of primary and secondary antibodies from the tissue slide without removing the fluorophore. A new set of antibodies is then applied to detect the next antigen, and the process is repeated sequentially until all 6 markers of interest are detected in a single tissue section. The main advantage of this detection system is that it does not require specially labeled primary antibodies and can be used with standard unlabeled primary antibodies.

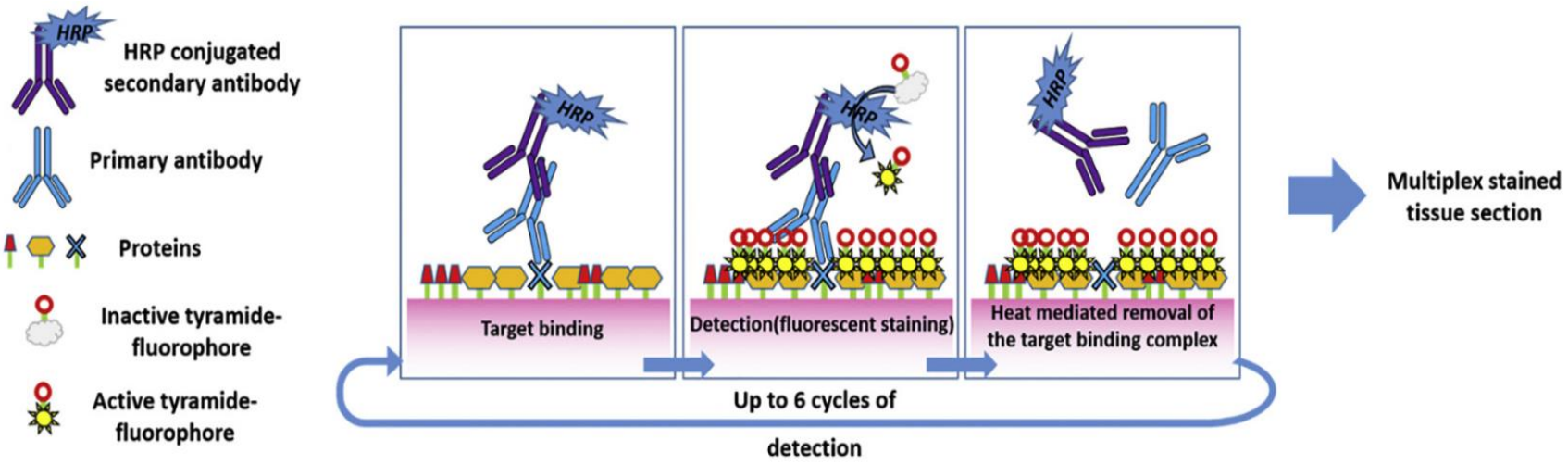

Figure 3.1. Principle of Tyramide Signal Amplification (TSA) technique. Secondary antibody conjugated with HRP enzyme is attached to the primary antibody. HRP enzyme catalyzes the reaction between TSA conjugated fluorophore and converts inactive tyramide fluorophore to active one. Active tyramide molecules then covalently deposit on or near the epitope of interest on the tissue to amplify detection. Heat stripping of primary and secondary antibody complex allows the next round of antibodies to attach with the target (31).

Development of mfIHC assay

Three 7-color panels were developed as described previously (31) and their details are given in Table 3.1. In brief, the staining pattern for each antibody was first optimized using a single color IHC staining on a control slide containing different mouse tissue from lung, spleen, tonsil, and intestine. Based on the known brightness ranking of TSA fluorophores, more abundant antibodies were paired with less bright fluorophores. The ranking of fluorophore brightness is given in Table 3.2. TSA dilutions were titrated as per need starting at the initial recommended dilution of 1:150. Full three panels were validated in HI^3 core before final mfIHC staining. Details of antibodies and Opal reagents are given in Table 3.3.

Whole Slide Scanning

The mfIHC stained sections were scanned for whole slide imaging at 40X using the automated quantitative pathology imaging system (PhenoImager™ HT, Akoya Biosciences). Each channel was set for exposure time using the auto-exposure feature at the region of interest (ROI) for a lung tissue sample. Similarly, the exposure time for each channel for all of the lung samples from different time points were set individually for both strains of mice.

Table 3.1. Details on the antibodies combine with their respective fluorophore in each of 7-color mfIHC staining panel.

Panel	Opal fluorophore						
	480	**520**	**570**	**620**	**690**	**780**	**Nuclear staining**
1	CD8	CD4	B220	Foxp3	DEC-205	F4/80	DAPI
2	CD4	LY6G	IFNγ	CD11c	IL-10	CD8	DAPI
3	CD4	PD-1	OTB	DEC-205	PDL-1	CD8	DAPI

Table 3.2. Brightness ranking of Opal fluorophores.

Opal fluorophore	**Brightness ranking**
Opal 480	Highest
Opal 520	Highest
Opal 570	Medium
Opal 620	Medium
Opal 690	Lowest
Opal 780	Lowest

Table 3.3. Details of the antibodies used in three 7-color mfIHC staining panels.

Antibody	Specie	Type	Company	Cat#	Clone/ Lot#	Concentration	pH
CD4	Rat	mAb	Thermo Fisher	4SM95		1:200	6
CD8	Rabbit	mAb	CST	D4W2Z		1:400	6
B220	Rat	mAb	BD Pharm	RA3-6B2		1:500	6
Foxp3	Rabbit	mAb	R&D	MAB8214	1054C	1:200	9
DEC-205	Rat	mAb	Biorad	MCA949		1:10	6
F4/80	Rabbit	mAb	CST	D4C8V		1:100	6
CD11c	Rabbit	mAb	CST	97585S	D1V9Y	1:300	6
Ly6G	Rabbit	mAb	CST	87048		1:100	6
IFNγ	Rabbit	Polyclonal	Bioss	bs-0480R	BJ07074740	1:200	6
IL-10	Rabbit	Polyclonal	Bioss	bs-20373R	BA01279056	1:200	6
PD-1	Rabbit	mAb	CST	84651T	D7D5W	1:100	6
PDL-1	Rabbit	mAb	MSVA	2083-711R-01	MSVA-711R	1:100	6
OTB	Rabbit	mAb	Otsuka			1:100	6

Image Analysis and autofluorescence removal

The mfIHC stained whole slide scanned (WSS) images were analyzed using Phenochart and inForm Tissue Finder software (Akoya Biosciences). Briefly, the WSS images were loaded in Phenochart (version 1.1.0) and all of the granuloma lesions along with parenchymal tissue were annotated using Stamp feature based on the size of the lesions. At least 5 representative Stamps were chosen to make a project for image analysis. The project was further opened in inForm Tissue Finder software (version 2.4 8) and tissue autofluorescence was removed using a control unstained lung tissue slide (not stained with DAPI and Opal reagents) from the respective mouse strain in this project. The removal of autofluorescence ensures the accurate quantification of different immune cell interactions in the tissue of interest without false-positive signals from the background.

The Stamps with some artifacts like tissue folds, or fluorescence precipitates were manually removed from analysis using Disinterest Region feature. Threshold values for each fluorophore were modified to create uniform view settings of images. The image analysis using inForm Tissue Finder was comprised of 4 different steps and details of each step are given below.

1. Unmixing of images

The first step in image analysis is the preparation of images or spectral unmixing. The inForm unmixes images based on the emission spectra of respective fluorophores and enables the identification and separation of weakly expressing and overlapping signals from background autofluorescence (Figure 3.2). Spectral unmixing separates

the signals from the fluorescent reagents placed on the tissue into individual bins. The advantage of using Vectra Polaris for multiplex image is automatic extraction of the signals from overlapping spectra and therefore no need to worry about spectral overlapping in this system as compared to conventional system where single-color spectral libraries are required for this purpose.

2. Tissue segmentation

The automatic tissue segmentation detects specific tissue types using train-by-example deep learning pattern recognition algorithms. The inForm can segment lung tissue into different tissue types based on the tissue morphologies and fluorescent color. For this study, we segmented the annotated Stamps in granuloma lesions, unaffected parenchyma, and glass (where no tissue was found, and slide was blank) types (Figure 3.2). Quantitative outputs of tissue segmentation included the total number of granuloma lesions identified and the total area occupied by granuloma and parenchymal tissues.

3. Nuclear segmentation

The nuclear segmentation through deep learning approach is based mainly on the DAPI marker in the image (Figure 3.2). As the nucleus is present in nearly all cell types, DAPI being the nuclear marker helps in this segmentation. To further assist individual nuclear segmentation, CD4 and CD8 were selected as cytoplasmic markers using real-time tuning. Minimum cytoplasm and membrane thresholds of cells were set.

4. Cellular Phenotyping

The last and very important step in image analysis is cell phenotyping (Figure 3.2). Training of inForm based on a small set of different biomarkers classifies these cells in the WSS image. TSA based mfIHC helps identification of low expressing epitopes by tagging them with the brightest fluorophores and vice versa.

Batch processing

After completing a set of training of a project, remaining Stamps were batch analyzed based on this project. Each time point and mouse strain type were trained for a particular project and ultimately batch analyzed. To further check the quality of image analysis and to ensure data integrity, each Stamp was reviewed and removed from batch analysis if found unsuitable.

Data visualization and spatial analysis

Data from batch analyzed set of Stamps was merged into summary data files and graphed using GraphPad Prism version 9.5.1 (GraphPad software, La Jolla, CA) and the R software v.3.6.3. To explore the potential of image analysis data, the spatial distribution of different immune phenotypes was analyzed at 35-, 63- and 77-days post infection. For this purpose, the X and Y coordinates of each phenotype in the image analysis process were generated and spatially plotted using phenoptrReports (Akoya Biosciences) built-in the R software v.3.6.3. To investigate the cell interactions, the nearest neighbor distance was calculated and presented as a median distance from CD4 and CD8 to each phenotype included in the panels. Further, the mean immune cell counts in a radius of 100 µm from a single CD4 and CD8 cell was performed.

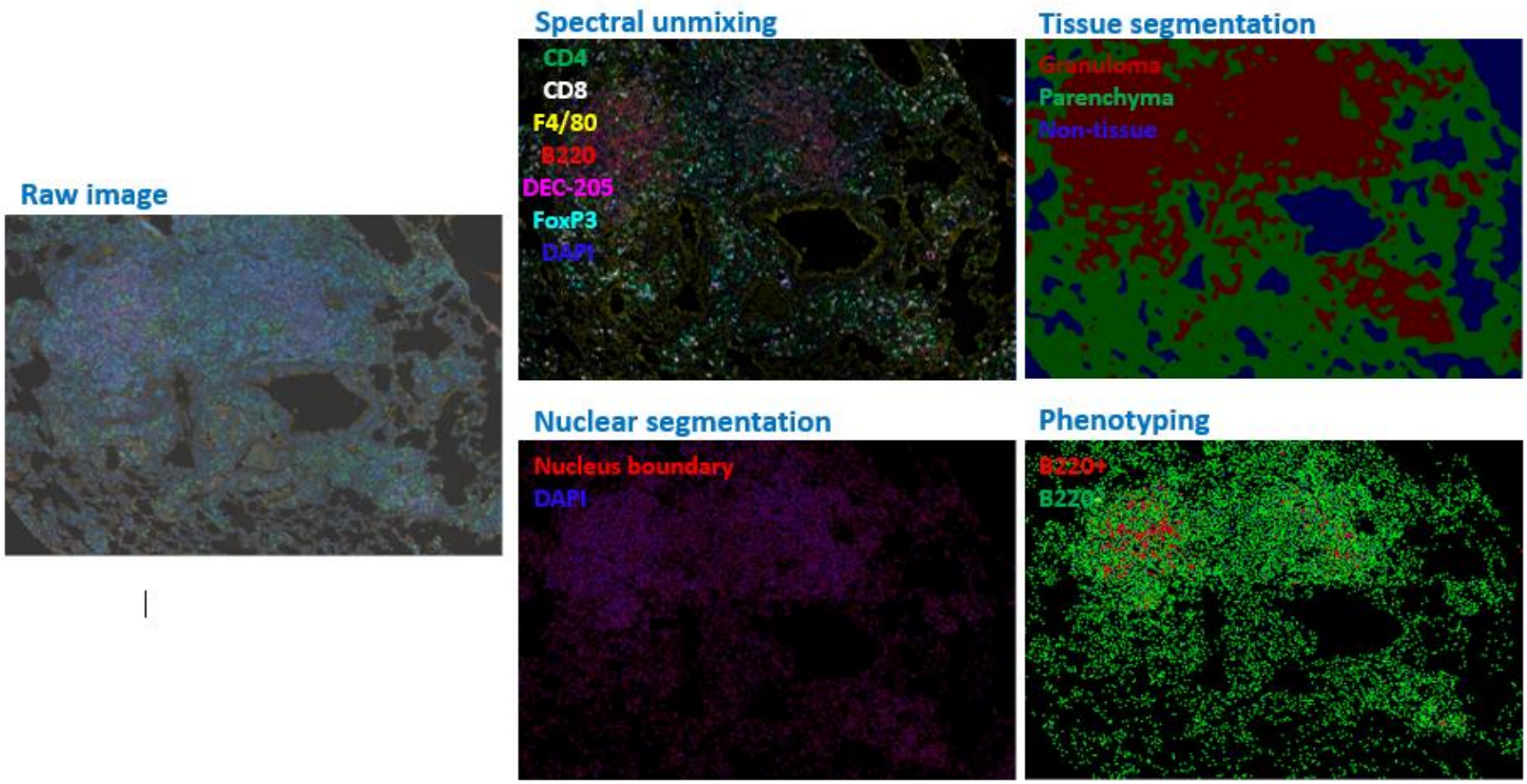

Figure 3.2. Image analysis using inForm software. Raw images can be processed for analysis in 4 different steps. Spectral unmixing is done based on the emission spectra of the respective fluorophore. Tissue segmentation relies on deep learning pattern recognition algorithms. Nuclear segmentation through deep learning approach is based mainly on the DAPI marker in the image. Phenotyping identifies different cells based on the training for a small set of different cells.

Statistical analysis

Bacterial burden data were expressed as CFU which were Log_{10}-transformed and analyzed using GraphPad Prism version 9.5.1 (GraphPad software, La Jolla, CA). The statistical analysis was performed using a Tukey's multiple comparison test as part of one-way ANOVA. Lesion score, total cell phenotypes and their cell densities were plotted using GraphPad Prism while the cell densities were Log_{10}-transformed. Nearest neighbor median distance and count with 100 µm radius were calculated based on the matrix of X and Y coordinates of each cell and visualized as heatmap using R studio.

Results

This project was conducted to study *in situ* immuno-pathogenesis of TB using the BALB/c and C3HeB/FeJ TB models. The lungs from both murine TB models were collected and prepared to measure the bacterial burden (CFU), lesion score and the spatial and temporal distribution of immune cells several times over the course of the infection. A comparative investigation was also conducted to study differences between each stage of TB disease recapitulated by each mouse TB model.

Temporal changes in lung bacterial burden of the BALB/c TB model

As shown in Figure 3.3, the lung bacterial burden at 35-, 63- and 77-days post infection were 6.37 ± 0.08, 6.08 ± 0.13 and 5.03 ± 0.41 log_{10} CFU respectively. Overall, the CFU decreased with time and a significant difference was observed for CFU at 35 and 63 days to 77 days post infection. However, no significant difference was observed for CFU between 35- and 63-days post infection.

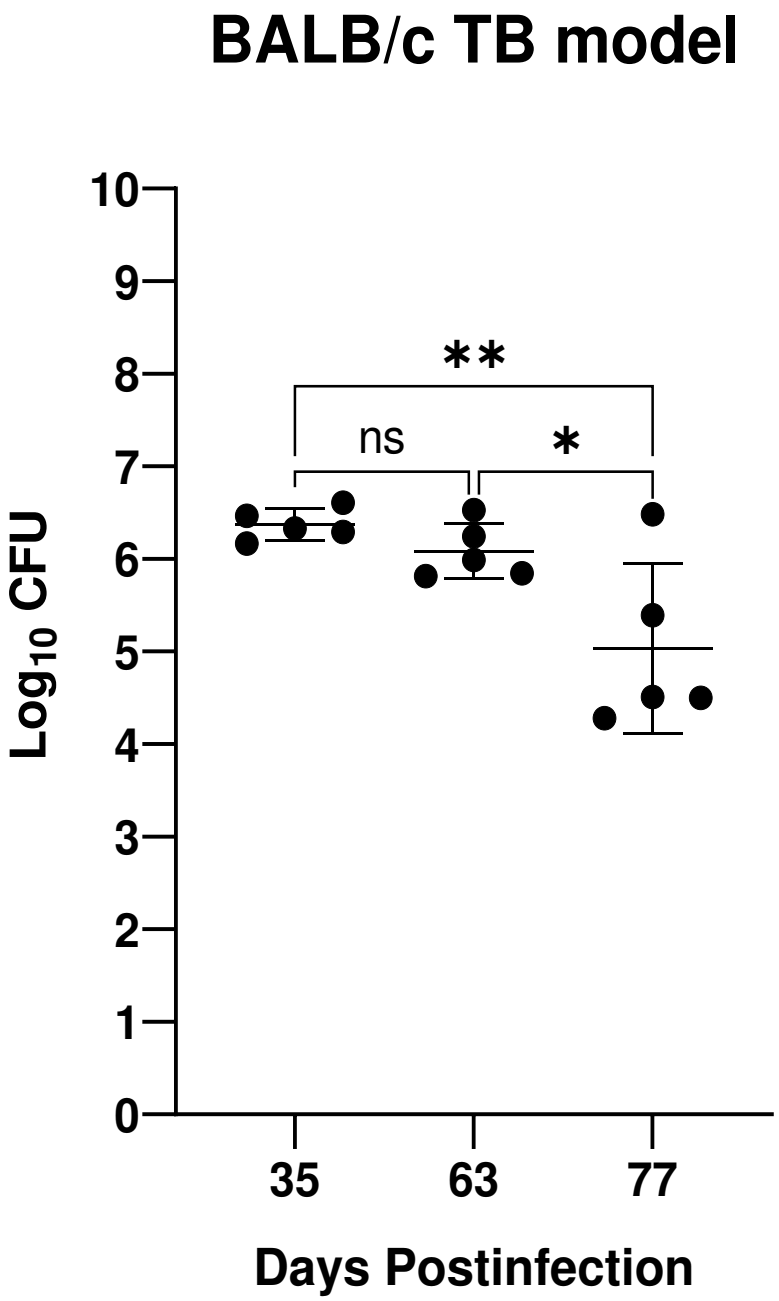

Figure 3.3. Bacterial burden (measured as $\log_{10}$ CFU per lung is in Y-axis) in Mtb infected BALB/c mice at different time points post infection. The lungs were homogenized, serially diluted and plated on 7H11 agar. The CFU was enumerated after 4-6 weeks of incubation and analyzed using one-way ANOVA. Statistical differences between timepoints were established using Tukey's multiple comparison test. * $p < 0.05$, ** $p < 0.001$

Temporal changes in lung lesion burdens in the BALB/c TB model

The lung lesion score at increased time post infection was calculated based on the size of granulomas versus uninvolved tissue. The H&E images of lung tissues at 35-, 63- and 77-days post-infection are shown in Figure 3.4. and their lesion scores are given in Figure 3.5. Figure 3.4 A-C show representative images highlighting examples of granulomas (hexagons) and unaffected parenchymal tissue (arrows). As the infection progresses in time, the granuloma increased in size leaving a smaller proportion of unaffected parenchymal tissue as depicted by their lesion scores given in Figure 3.5. For lesion scoring, the unrelated lymphoid (oval) and cardiac tissue (rectangle) were removed from the algorithm.

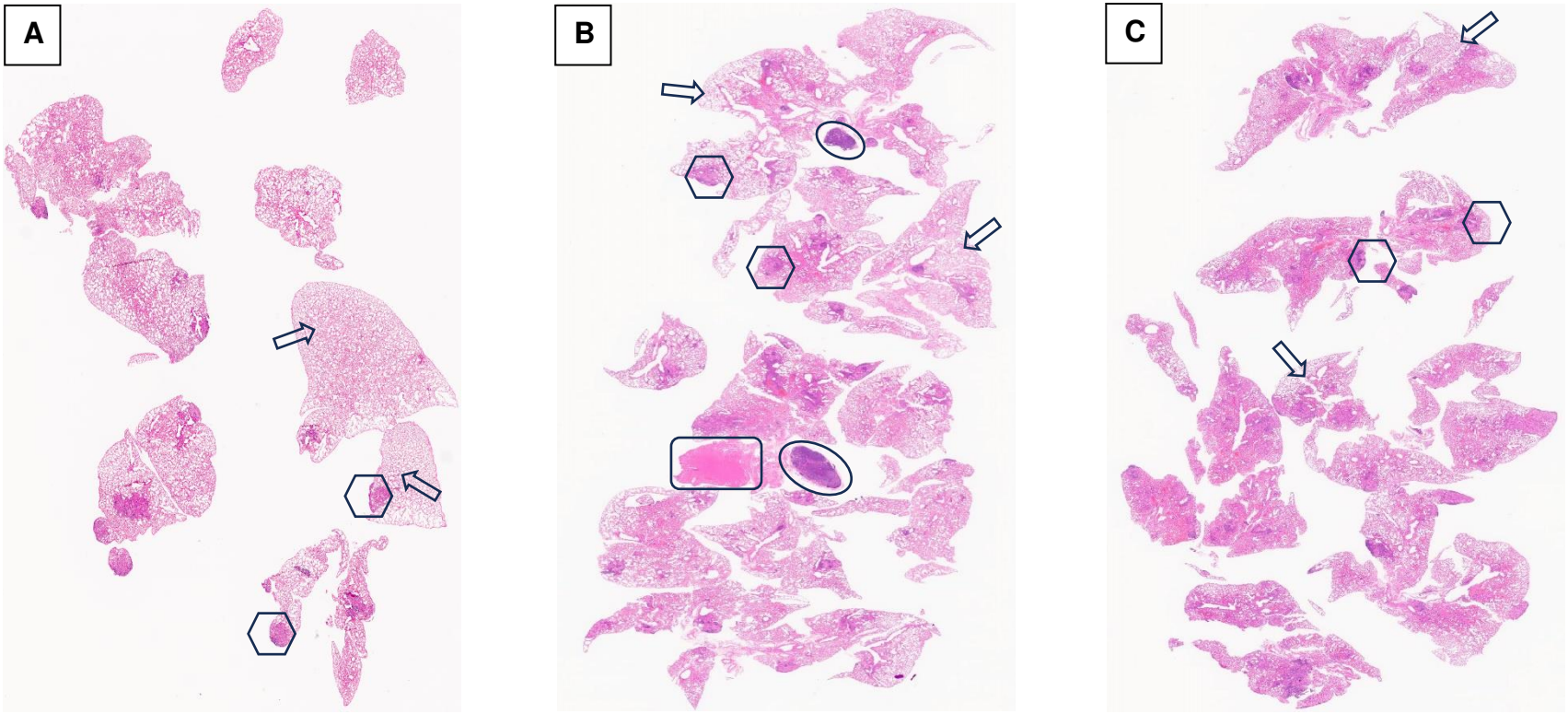

Figure 3.4. Temporal changes in the lung histopathology of Mtb infected BALB/c mice. Lung tissues were collected on day 53 (A), 63 (B) and 77 (C) post infection. (A-C) Arrows show examples of regions selected as unaffected parenchymal tissue while hexagons represent examples of regions identified as granulomas. In (B), the rectangle corresponds to the cardiac tissue while ovals select for the lymphoid tissue that were also harvested with the same sample. H&E, 20x

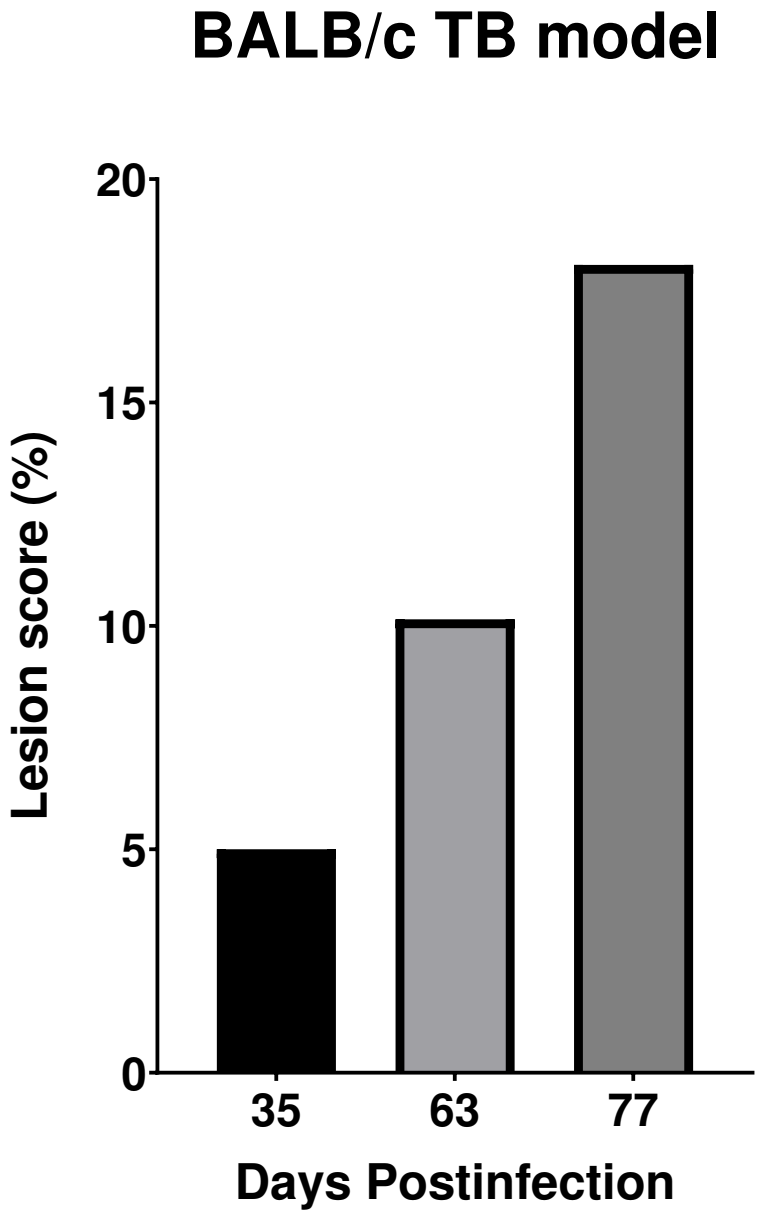

Figure 3.5. Temporal changes in the lung lesion score of Mtb infected BALB/c mice. A gradual increase in the lung lesion score was observed as reflected by their histopathology images in Figure 3.4.

Temporal Changes within lung immune cell populations in the BALB/c TB model

In the first step, the whole lung tissue containing different granulomas, inflammatory regions and unaffected parenchymal tissue were analyzed to determine temporal changes of their immune cellular composition. The sections were stained with mfIHC for 2 different panels of immune markers along with DAPI as a nuclear marker. Staining panel 1 consists of CD4, CD8, Foxp3, B220, DEC-205 and F4/80 while panel 2 encompasses CD4, CD8, IFNγ, IL-10, CD11c and Ly6G. The granulomas and inflammatory regions were segmented from the rest of the unaffected parenchymal tissue and thereby collectively termed as the lesions. The total number of several immune phenotypes from mfIHC staining panel 1 and panel 2 were counted in lesions and parenchymal tissue from samples obtained at day 35, 63 and 77 post infection and their individual counts are given in Figures 3.6 and 3.7 respectively. The results demonstrated that most of the immune cell populations were present in Mtb affected or lesions area while there were a smaller number of cells in the unaffected parenchymal tissue except IFNγ+ and IL-10+ cells that were more predominant in unaffected parenchymal. Overall, in both panels, there was an increased trend in the total count of each phenotype except for Ly6G+ (neutrophils) which showed a slightly decreasing trend. However, CD4+ positive cells (T helper), F4/80+ (macrophages) along with IFNγ+ and IL-10+ cells remained the most abundant cells throughout the all-time points.

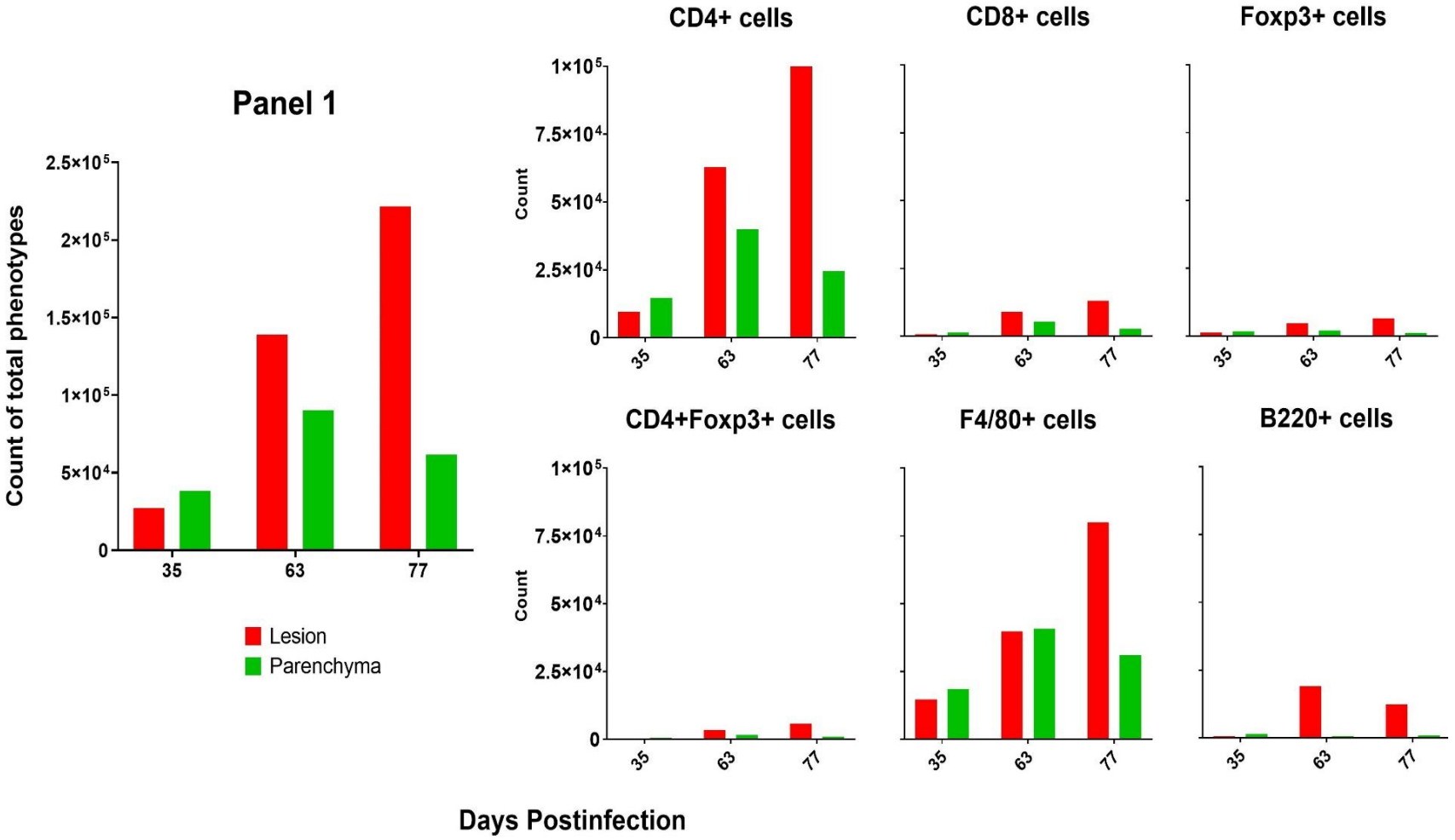

Figure 3.6. Temporal changes in the immune cell phenotypes (panel 1) in the whole lung tissue in BALB/c mice infected with Mtb. The immune cells were counted in lesion (red) and unaffected parenchymal (green) tissue at 35-, 63- and 77-days post infection.

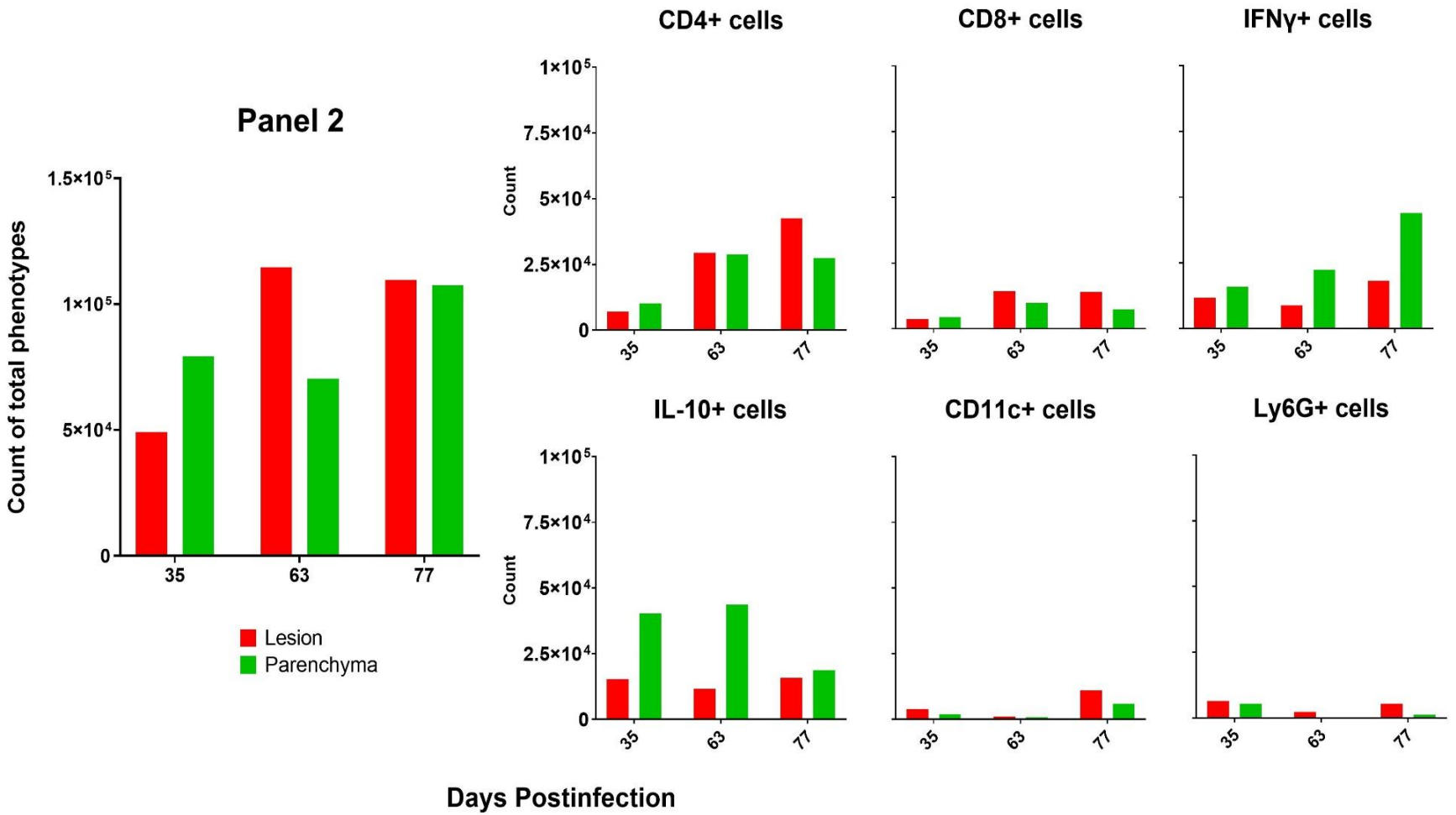

Figure 3.7. Temporal changes in the immune cell phenotypes (panel 2) in the whole lung tissue in BALB/c mice infected with Mtb. The immune cells were counted in lesion (red) and unaffected parenchymal (green) tissue at 35-, 63- and 77-days post infection.

Temporal changes within granulomas immune cell populations in the BALB/c TB model

In the next step, changes in the immune cell infiltrates within the granuloma structure were characterized at increasing times post infection. For this purpose, we first selected the representative granulomas from the whole lung tissue at 35-, 63- and 77-days post infection and determined the total cell count. It is pertinent to mention that the selected granulomas may not accurately reflect their true size in just a 5 µm thick section and it can also vary with sectioning dimensions.

The sections were also stained with mfIHC for 2 different panels of immune markers along with DAPI as a nuclear marker. Staining panel 1 consists of CD4, CD8, Foxp3, B220, DEC-205 and F4/80 while panel 2 encompasses CD4, CD8, IFNγ, IL-10, CD11c and Ly6G.

Panel 1

Figure 3.8 reflects a full composite image from a selected granuloma and displays six different immune cell markers along with DAPI staining in panel 1. In the same figure, each subset is shown in the single-color composite image. The co-expression of CD4+ and Foxp3+ cells was also measured and counted. Using the inForm tissue Finder software, the granuloma tissue was separated from the unaffected parenchymal tissue, then segmented at the cellular level and finally phenotyped as per the respective markers used. Since the cellular segmentation was based on the DAPI staining in a 5 µm thick section, the detection and segmentation of large cells such as

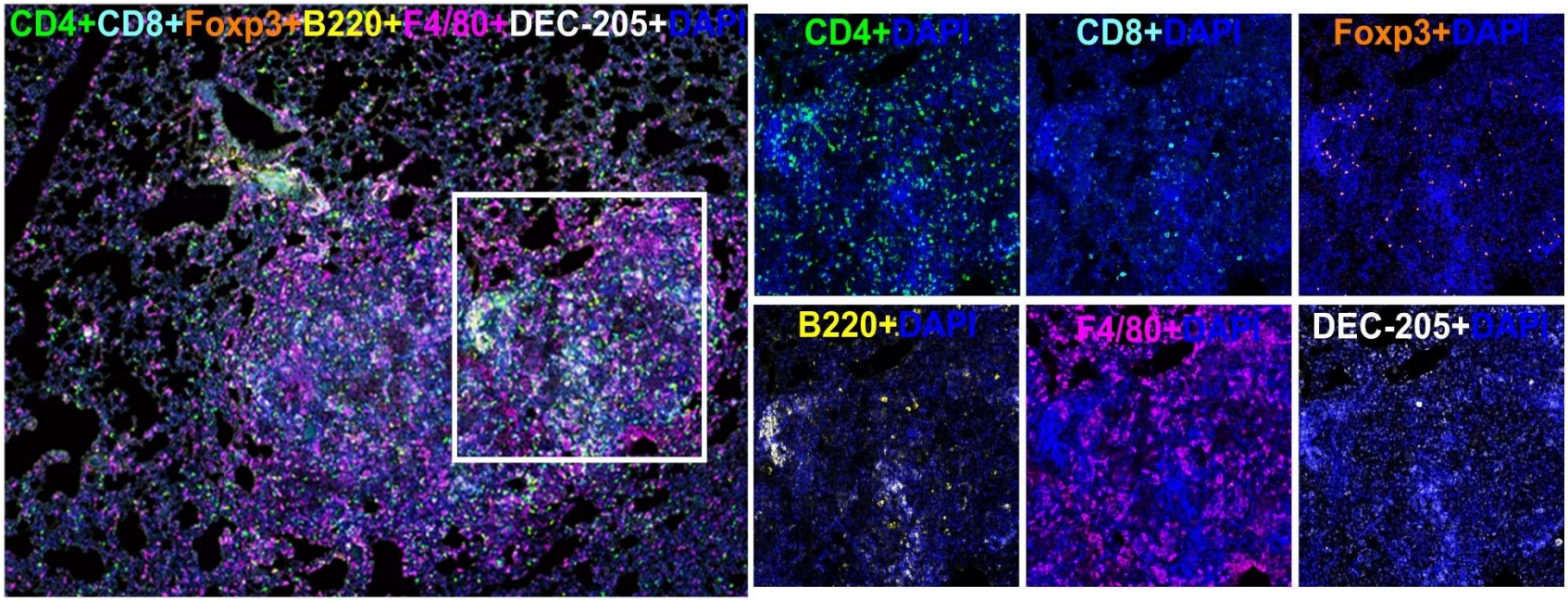

Figure 3.8. A composite image of a representative cellular TB granuloma stained with multiplex immunohistochemistry panel 1 displays different immune cell markers along with DAPI. The subsets show single-color composite image of individual markers with DAPI showing distribution of each immune cell population within a granuloma.

F4/80+ macrophages and DEC-205+ DCs is not always accurate and often only partially observed.

Figure 3.9 shows the changes in the immune cells of panel 1 except for DEC-205 antibodies. Generally, an increasing trend in the count of cells was observed as infection progressed in time suggesting a continuous recruitment of immune cells into the granulomas. In response to Mtb infection and as time post infection progressed, the granulomas showed significant increases in the number of CD4+ cells, B220+ cells along with the F4/80+ cells. However, there was no significant increase in the cell count from day 35 to day 77 post infection for CD8+, Foxp3+ and CD4+/Foxp3+ cells. Furthermore, based on the spread of the standard deviation for each of the cell populations shown in Figure 3.9, all granulomas were very similar and homogenous (low standard deviation) in terms of numbers of CD4+, Foxp3+ and F4/80+ positive cells whereas the content of CD8+, and B220+ was more variable between granulomas (large standard deviations). These data suggest that as time post infection progressed there was increased recruitment and numbers of T cells (CD4+ cells), B lymphocytes (B220+ cells) and macrophages (F4/80+cells) within the granulomas while the number of cytotoxic T cells (CD8+cells) and regulatory cells (Foxp3+ and CD4+/Foxp3+ cells) remained steady. Furthermore, while the immune microenvironments responsible for recruitment of CD4+, Foxp3+ and F4/80+ are similar among granulomas, there are differences between granulomas microenvironments responsible for recruiting CD8+ and B220+ cells.

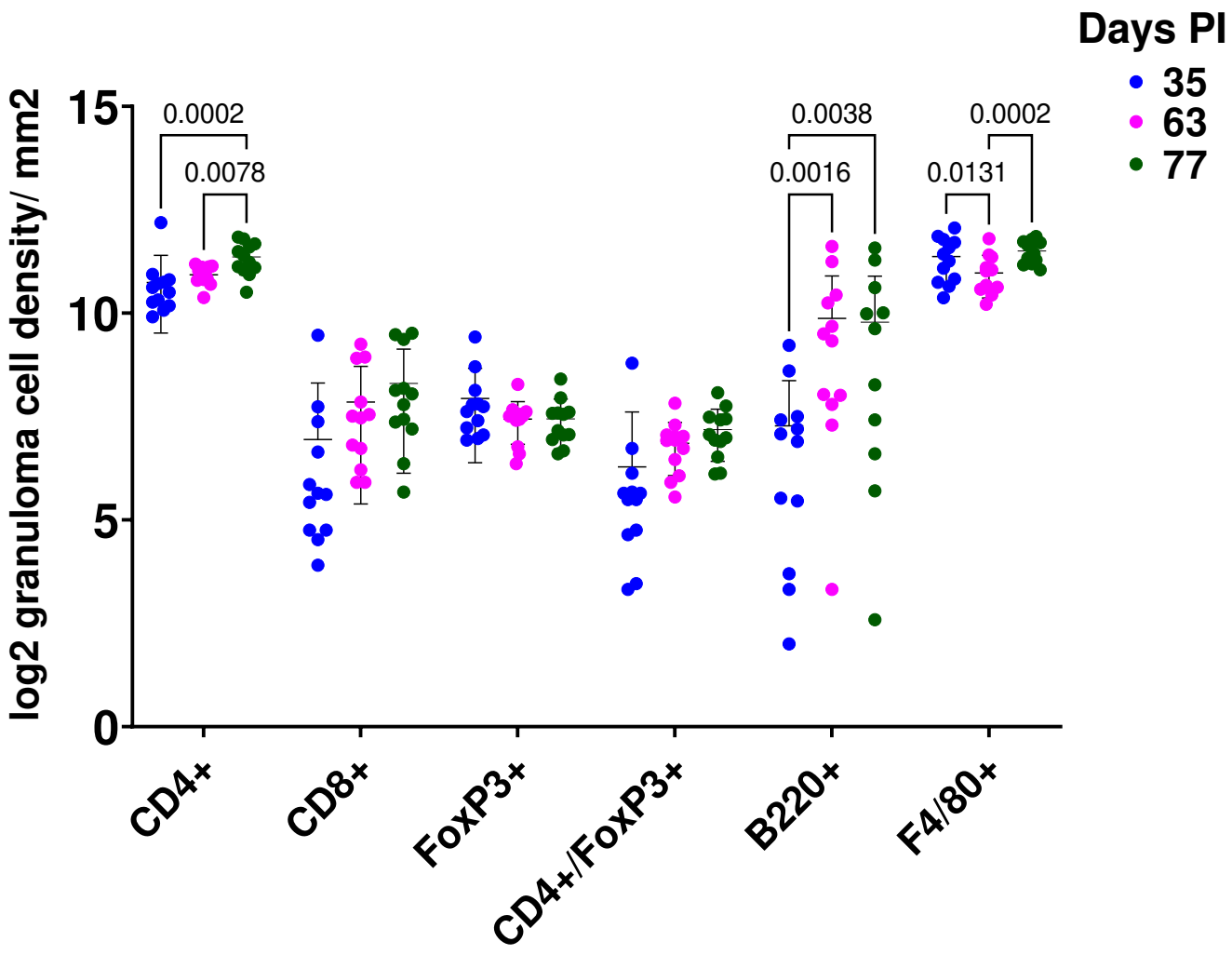

Figure 3.9. Temporal changes in the immune cell phenotypes (panel 1) in selective lung granulomas in BALB/c mice infected with Mtb. The immune cells were counted at 35-, 63- and 77-days post infection and the results were evaluated using one-way ANOVA and Tukey's multiple comparison test. $p < 0.05$

Panel 2

Like in panel 1, Figure 3.10 also shows a full composite image of different immune cell markers given in panel 2. The single-color composite image from each marker of panel 2 is also shown. The co-expression of CD4+ and IFNγ+ cells was also measured and counted. The same strategy of panel 1 for tissue and cell segmentation was followed in panel 2 using the inForm tissue Finder software and the cells were phenotyped as per the respective markers used.

Figure 3.11 shows temporal changes over the course of the infection in immune cells when stained with panel 2. Like in panel 1, CD4 and CD8 markers are also used in panel 2 to check if mfIHC staining is consistent and reproduces the same results irrespective of the fluorophores used for these antibodies. Interestingly, the results for CD4 and CD8 in panel 2 were similar to the results presented in panel 1 and the count of CD4 cells has increased significantly with time post infection but no difference was observed in CD8 count. The change in the count of CD4+ and CD8+ cells between both panels was attributed to differences in tissue sectioning (not being the consecutive sections) and the use of two different fluorophores even though the same set of algorithms was applied to all images (Figure 3.12). IFNγ+ and IL-10+ secreting cells and CD11c+ cells showed a significant drop in their cell counts after 35 days and then recovered at 77 days post infection. Of notice is also the wide standard deviation in the IFNγ+ and IFNγ+/CD4+, suggesting large heterogeneity in abundance of these cells among different granulomas. Ly6G+ cells expressed a slight decrease in their count, but it remained statistically non-significant during time post infection.

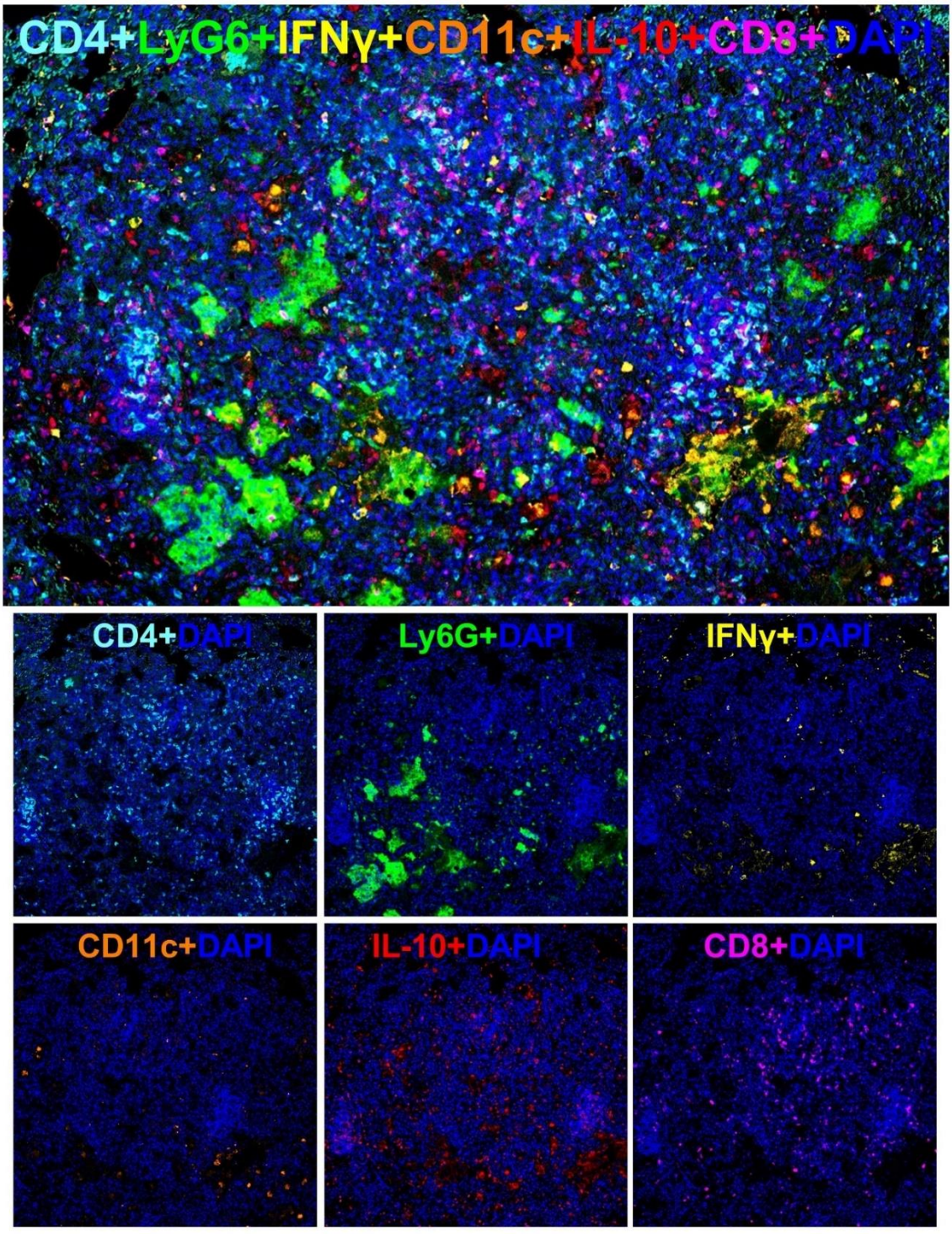

Figure 3.10. A composite image of a representative cellular TB granuloma stained with multiplex immunohistochemistry panel 1 displays different immune cell markers along with DAPI. The subsets show single-color composite image of individual markers with DAPI showing distribution of each immune cell population within a granuloma.

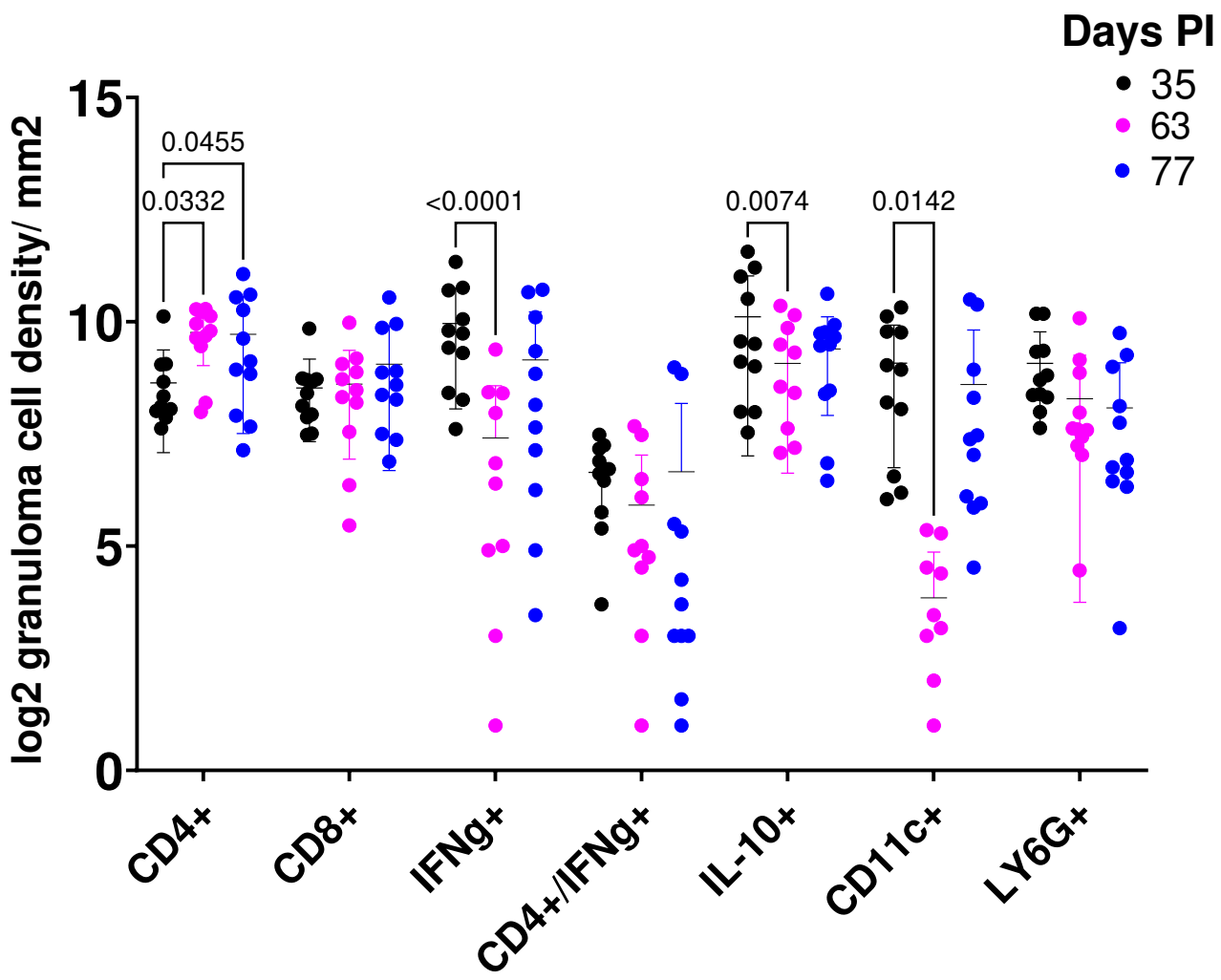

Figure 3.11. Temporal Changes in the immune cell phenotypes (panel 2) in selective lung granulomas in BALB/c mice infected with Mtb. The immune cells were counted at 35-, 63- and 77-days post infection and the results were evaluated using one-way ANOVA and Tukey's multiple comparison test. $p < 0.05$

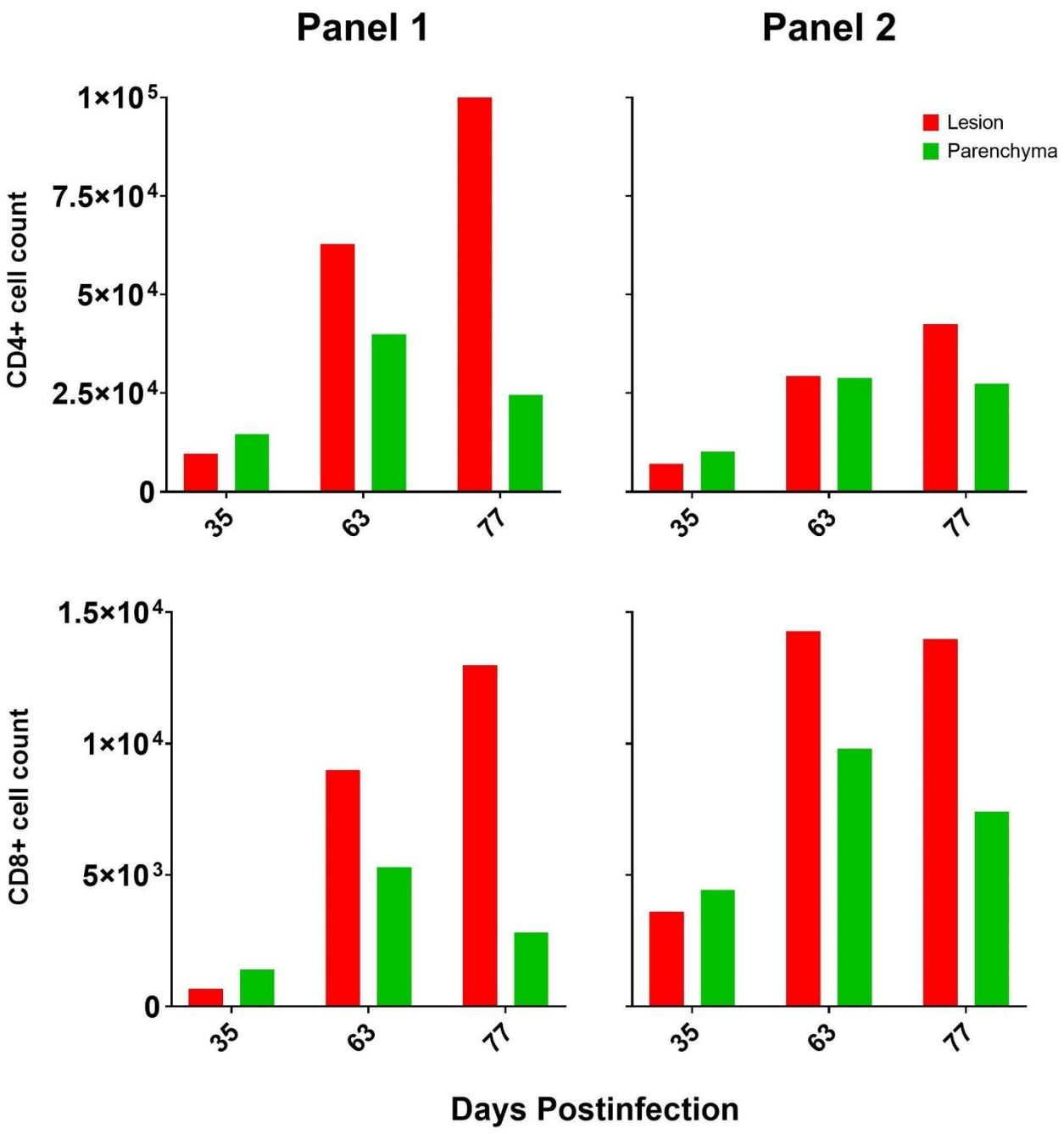

Figure 3.12. CD4+ and CD8+ cell count for mfIHC staining panel 1 and 2 at 35-, 63- and 77-days post infection in lesion and parenchymal tissue.

Temporal and Spatial distribution of immune cell populations in the BALB/c TB model

Further, the spatial distribution of different immune phenotypes from image analysis data was analyzed at 35-, 63- and 77-days post infection in the affected (lesion) and unaffected (parenchyma) tissue. As shown above, during the course of infection, most of the immune cells were located within the lesions as compared to the unaffected parenchymal tissue. However, while most immune cells (CD4+, CD8+, Foxp3+, IFNγ+, IL-10+, Ly6G+…) were interspaced as single cells across the granuloma, it was noticed that the B220+ cells (B cells) formed clusters of cells that become clearly visible and well distinguished at later stage of infection (day 77 PI) though there were a few B cells in the beginning (day 35 PI) (Figure 3.13).

The X and Y coordinates of each cell phenotype were generated and then plotted in the R software v.3.6.3 (Figure 3.13). Based on the matrix of X and Y coordinates of each cell, the median distance from CD4+ and CD8+ cells to different cell phenotypes were calculated as the nearest neighbor distance (µm) both in lesion and parenchymal tissue with time post infection (Figure 3.14). The results showed that the median distance in lesion from CD4+ (T helper cell) and CD8+ (cytotoxic T lymphocytes) to Ly6G+ (neutrophils) increased abruptly from 35 days to 63 days post infection (33.28 to 169.76 µm and 35.28 to 181.87 µm respectively) and parenchyma (51.79 to 402.17 µm and 55.96 to 342.26 µm respectively). The median distance from CD4+ and CD8+ (T lymphocytes) to B220+ (B lymphocytes) while drastically increased from 35 days to 63 days post infection in parenchymal tissue (132.91 to 287.87 µm and 103.60 to 268.10 µm respectively), however, there was a slight decrease in this distance for the lesion

(81.71 to 75.02 µm and 87.02 to 86.83 µm respectively). These findings were also supported by our data (Figure 3.15) counting the mean number of immune cells within 100 µm radius of a single CD4+ and CD8+ T lymphocytes in both tissue types with time post infection. The data from affected (lesion) tissue at 35 days to 63 days post infection presented a marked decrease in the mean count of Ly6G+ neutrophils within 100 µm radius from a single CD4+ (14.38 to 1.81) and CD8+ (9.03 to 1.35) cells. Contrary, the mean count of B220+ (B lymphocytes) within 100 µm radius of a single CD4+ and CD8+ T lymphocytes manifested a sharp increase (2.92 to 30.44 and 1.96 to 22.45 respectively).

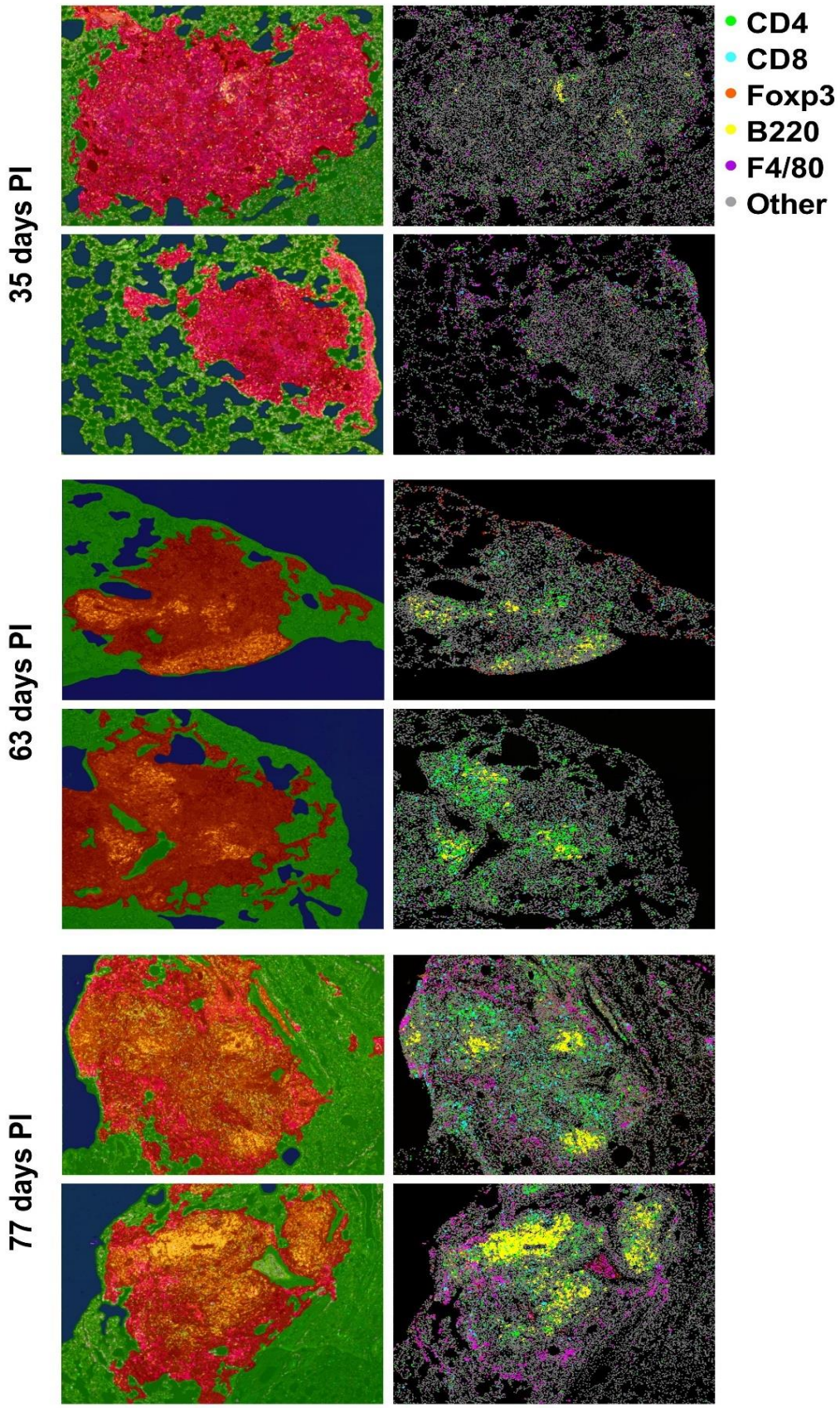

Figure 3.13. Temporal changes in the mapping of immune phenotypes in the lung tissue of Mtb infected BALB/c mice over time post infection (PI). (left column) lesion (red) and parenchyma (green) tissues are segmented from the non-tissue (blue) regions. (right column) Immune phenotypes are highlighted with different colors.

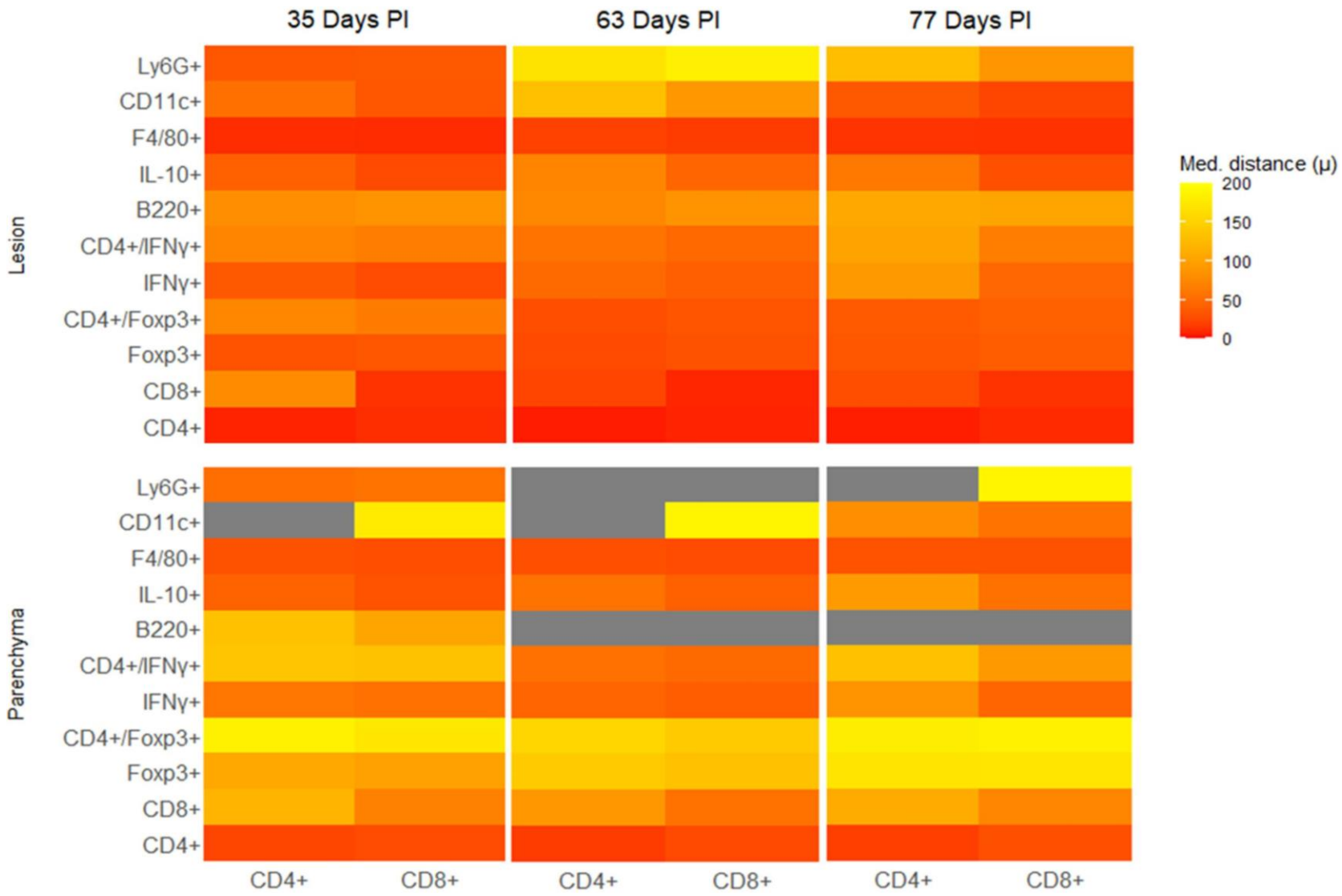

Figure 3.14. Nearest neighbor distance from CD4+ and CD8+ cells to other phenotypes with time post infection (PI). The distance in µm was measured as the median distance in lesion and parenchymal tissue.

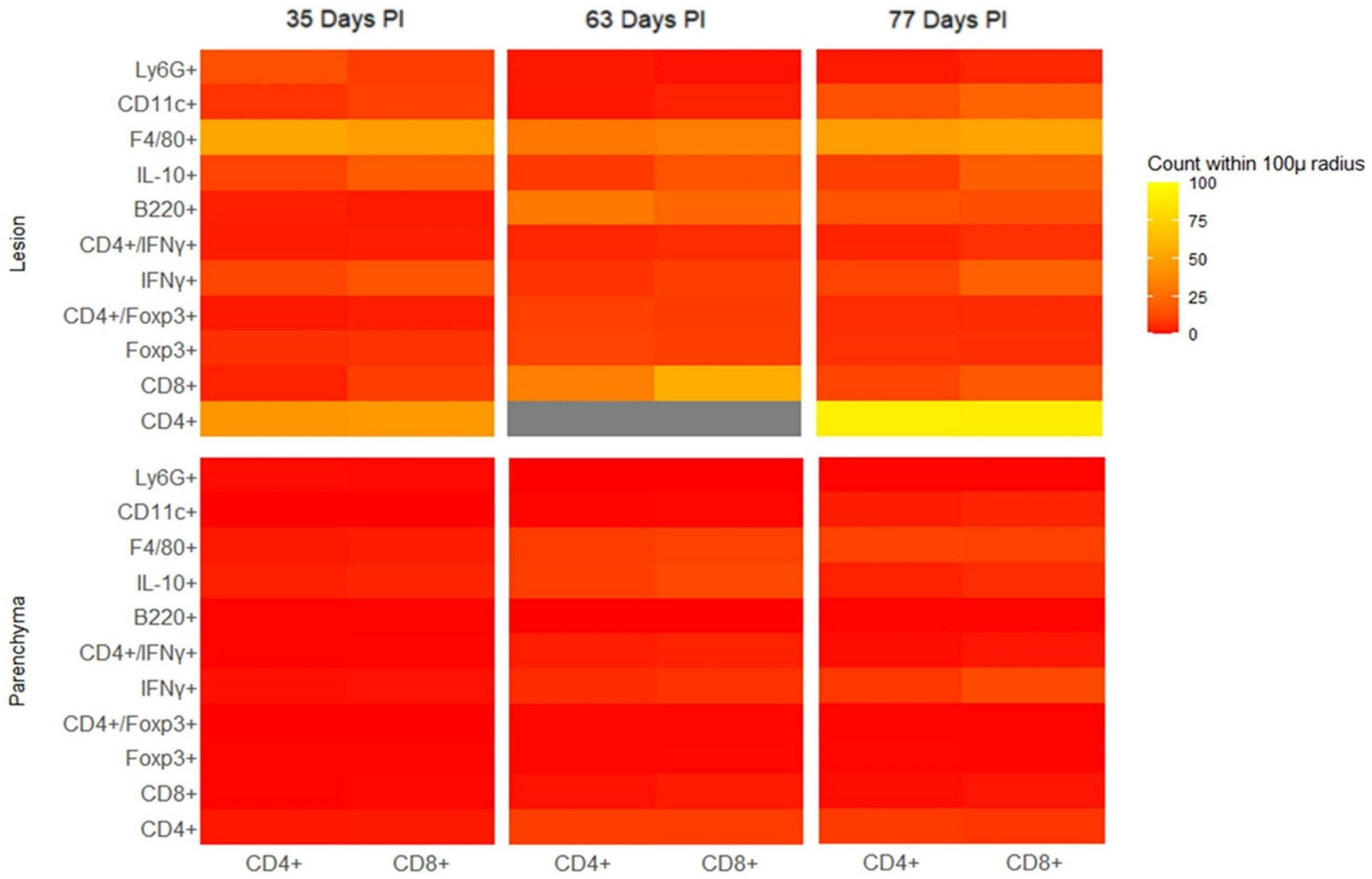

Figure 3.15. Count of cells from CD4+ and CD8+ cells to other phenotypes with time post infection (PI). The mean count of different phenotypes within 100 µm radius of a single CD4+ and CD8+ cells was calculated in lesion and parenchymal tissue.

Temporal Changes in the lung bacterial burden in the C3HeB/FeJ TB model

As in BALB/c mice, the lung bacterial burden in term of CFU was also enumerated in C3HeB/FeJ mice at 63- and 91-days post infection (7.08 ± 0.24 and 7.13 ± 0.24 $\log_{10}$) respectively. Contrary to the BALB/c mice, no significant difference was observed for CFU in C3HeB/FeJ mice between both time points as shown in Figure 3.16.

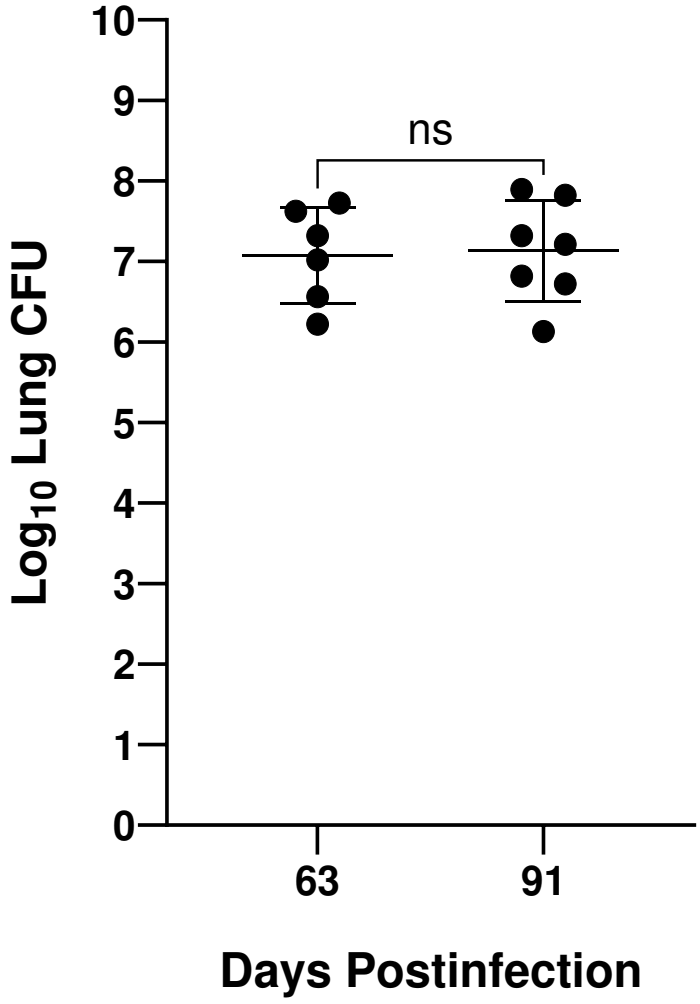

Figure 3.16. Bacterial burden (measured as $\log_{10}$ CFU per lung is in Y-axis) in Mtb infected C3HeB/FeJ mice at 63- and 91-days post infection. The lungs were homogenized, serially diluted at 10-fold and plated on 7H11 agar. The CFU was enumerated after 4-6 weeks of incubation and evaluated using one-way ANOVA and Tukey's multiple comparison test. $p < 0.05$

Temporal Changes in the lung lesion burden in the C3HeB/FeJ TB model

Similar to BALB/c mice, the lung lesion score from H&E images of the C3HeB/FeJ mice lungs tissue at 35-, 63- and 77-days post infection was measured and is shown in Figure 3.17. The lesion score increased as the infection progressed with time from 85% to 92%.

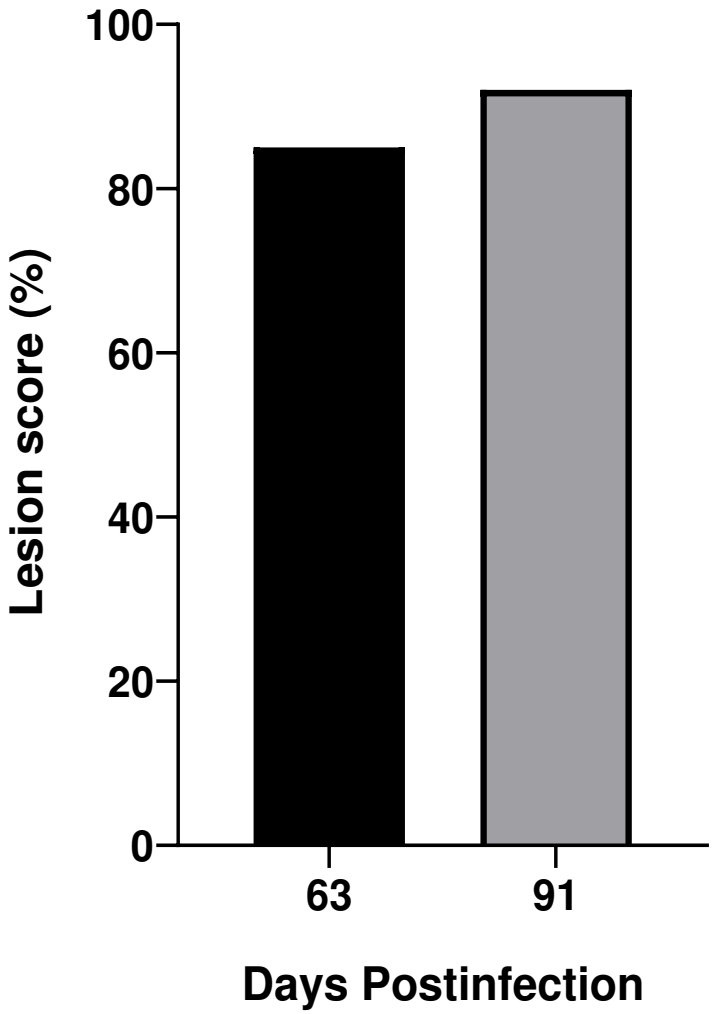

Figure 3.17. Temporal changes in the lung lesion score of Mtb infected C3HeB/FeJ mice. An increase in the lung lesion score was observed from day 63 to 91 post infection.

Discussion

In this study, we optimized three different automated mfIHC panels using TSA system and a set of immune markers to identify various types of immune cells associated with the lesions and unaffected parenchymal tissue in the lungs of Mtb infected BALB/c and C3HeB/FeJ mice. We performed the whole slide image analysis of the lung tissues using the inForm tissue Finder software which allowed us to assess the reproducibility of the data by quantifying and comparing various cell phenotypes at different times post infection in both TB models. We also analyzed the immune microenvironment (IME) of different types of granulomas, the hallmark of TB, and the temporal and spatial cellular distribution of those different phenotypes.

Human TB pathology manifests a diverse spectrum of granulomatous lesions and unfortunately no single animal model recapitulates the broader range of these lesions (32,33). We chose the BALB/c and C3HeB/FeJ murine TB models because of their unique pathological and disease outcomes. Briefly, both TB models are representative of a long-term Mtb chronic infection that develops lung granulomatous lesions. BALB/c mice produce uniform cellular lung granulomas containing macrophages and lymphocytes that restrain Mtb within intracellular compartments (34). However, C3HeB/FeJ mice display a diverse spectrum of lesions ranging from cellular granulomas seen in BALB/c model to neutrophil enriched granulomas and to highly organized encapsulated caseous necrotic lesions surrounded by a rim of macrophages and lymphocytes (24,35,36). In the latter case, the caseum contains abundant extracellular bacilli (24,36,37) in a similar fashion to necrotic granulomas found in some human TB patients. Therefore, to understand the development of lung granulomas and

their corresponding immune responses with the time PI, both murine chronic TB models were employed (38–40). The data from histopathological findings (Figure 3.4), lesion score (Figure 3.5) and bacterial burden (Figure 3.3) reflect the granuloma spectrum of BALB/c mouse model as explained above. However, the analysis of images from C3HeB/FeJ mouse model is still in progress while writing this dissertation.

Our image analysis data from the whole lung tissue slide from BALB/c TB model demonstrate that most of the immune cell populations identified were located within the lesions or affected tissue compared to unaffected otherwise healthy parenchymal tissue (Figure 3.6 and 3.7) as determined by the previous murine and human TB studies (8,10,26). Further, we observed an orderly recruitment of different immune cells within these lesions as the time of infection progressed that is in line with the previous reports (41). Generally, an increasing trend was observed in the count of nearly all phenotypes with time post infection, however, this trend was significantly distinct for CD4+ (T helper cells), F4/80+ (macrophages), B220+ (B cells) and IFNγ+ cells and these results are in line with the previous report measuring this count using flow cytometry (26). On the other hand, the count of Ly6G+ neutrophils both in the lesions and parenchymal tissue decreased with time post infection while the IL-10 secreting cells showed nearly the similar response throughout infection.

Next, we determined the composition of the immune cells within the granulomas of the BALB/c TB model to see if the immunological heterogeneity is present. The results showed that these granulomas are predominated by T (CD4+ helper cells, CD8+ cytotoxic cells and Foxp3+ regulatory cells) and B (B220+) lymphocytes, macrophages (F4/80+) and abundant with neutrophils (Ly6G+) (Figure 3.9 and 3.11). Furthermore,

with time post infection, CD4+ and Foxp3+ (T cells), F4/80+ (macrophages) and Ly6G+ (neutrophils) demonstrated a uniform distribution within different granulomas compared to CD8+ (T cells), B220+ (B cells) and IFNγ secreting cells which showed a heterogenous distribution. This heterogenous distribution indicates the different IME of these histologically similar granulomas with time post infection as the previous human and animal studies described this immunological heterogeneity even in the same lung (8,10,22,42–44). In addition, the increasing trend in CD4+Foxp3 (T regulatory cells) reflect a local suppressive environment of inflammatory cells within granulomas which has been previously shown (31,45).

The histological pattern of immune cell distribution showed marked diversity with time post infection. In the beginning (day 35 post infection), there were fewer CD4 and CD8 (T cells) in the affected (lesion) area compared to healthy parenchyma (Figure 3.12) as described previously (26) suggesting the accumulation of these cells in perivascular and peribronchiolar regions to demonstrate the initiation of a granulomatous response. With the development of granulomas (day 63 and 77 post infection), an influx of these cells, especially CD4 cells along with F4/80 macrophages was observed, suggesting the migration of these cells from parenchyma to the affected (lesions) area. Contrary, the distribution pattern of CD8 cells suggest their slow migration with fewer cells involved in granuloma composition. B220 cells, however, showed the opposite trend and their number increased with time and they aggregate in the form of clusters within granulomas as shown previously (46). Therefore, a typical advanced cellular granuloma in BALB/c mice contained F4/80 macrophages in the

periphery while CD4 and CD8 cells uniformly distributed and B220 cells make clusters of B cells in granulomas (Figure 3.13).

The spatial analysis of the images has been performed to calculate the nearest neighbors of and count within CD4 and CD8 cells. The increased median distance for Ly6G+ neutrophils and decreased distance for B220 cells within granuloma suggest their functional relation and their protective role especially for B220 cells in immunity. These findings are further supported by count within data where more B220 cells were present within a 100µm granuloma radius of CD4 and CD8 cells.

In summary, this study showed temporal changes for several immune cells along with the changes in their spatial distribution in Mtb infected BALB/c lung tissue. As the infection progressed in time, immune phenotypes became involved in the affected (lesion) areas. Moreover, the histologically similar granulomas manifested complexity in their immune cell composition mainly due to the presence of adaptive immune responses. The advanced cellular granulomas in the BALB/c TB model mainly predominated by CD4 and CD8 T cells, Ly6G stained neutrophils, B220 B cells and all these were surrounded by F4/80 macrophages. Combining the spatial and temporal data in addition to the mere cell counts helps uncover the interactions and relationships of different immune cells to have deeper insights into the immunity process which is the next target of this project.

References

1. WHO. Global TB report. 2022.
2. Moule MG, Cirillo JD. *Mycobacterium tuberculosis* Dissemination Plays a Critical Role in Pathogenesis. Front Cell Infect Microbiol. 2020;10:1–12.
3. WHO. Global TB Report 2021.
4. Cadena AM, Fortune SM, Flynn JL. Heterogeneity in tuberculosis. Nat Rev Immunol. 2017;17(11):691–702.
5. Higgins DM, Sanchez-Campillo J, Rosas-Taraco AG, Higgins JR, Lee EJ, Orme IM, et al. Relative Levels of M-CSF and GM-CSF Influence the Specific Generation of Macrophage Populations during Infection with *Mycobacterium tuberculosis* . J Immunol. 2008;180(7):4892–900.
6. Silva Miranda M, Breiman A, Allain S, Deknuydt F, Altare F. The tuberculous granuloma: An unsuccessful host defence mechanism providing a safety shelter for the bacteria? Clin Dev Immunol. 2012;2012.
7. Flynn JL, Chan J, Lin PL. Macrophages and control of granulomatous inflammation in tuberculosis. Mucosal Immunol. 2011;4(3):271–8.
8. McCaffrey EF, Donato M, Keren L, Chen Z, Delmastro A, Fitzpatrick MB, et al. The immunoregulatory landscape of human tuberculosis granulomas. Nat Immunol. 2022;23(2):318–29.
9. Pai M, Behr MA, Dowdy D, Dheda K, Divangahi M, Boehme CC, et al. Tuberculosis. Nat Rev Dis Prim. 2016;2.
10. Carow B, Hauling T, Qian X, Kramnik I, Nilsson M, Rottenberg ME. Spatial and temporal localization of immune transcripts defines hallmarks and diversity in the tuberculosis granuloma. Nat Commun [Internet]. 2019;10(1):1–15. Available from: http://dx.doi.org/10.1038/s41467-019-09816-4
11. Roca FJ, Ramakrishnan L. TNF dually mediates resistance and susceptibility to mycobacteria via mitochondrial reactive oxygen species. Cell. 2013;153(3):521–34.
12. Flynn JL, Chan J. Immunology of Tuberculosis. Annu Rev Immunol. 2001;19:93–129.
13. Cooper AM. Cell-mediated immune responses in tuberculosis. Annu Rev Immunol. 2009;27:393–422.
14. Sasindran SJ, Torrelles JB. *Mycobacterium tuberculosis* infection and inflammation: What is beneficial for the host and for the bacterium? Front Microbiol. 2011;2(JAN):1–16.
15. Cooper AM, Mayer-Barber KD, Sher A. Role of innate cytokines in mycobacterial infection. Mucosal Immunol [Internet]. 2011;4(3):252–60. Available from:

http://dx.doi.org/10.1038/mi.2011.13

16. Geldmacher C, Ngwenyama N, Schuetz A, Petrovas C, Reither K, Heeregrave EJ, et al. Preferential infection and depletion of *Mycobacterium tuberculosis*-specific CD4 T cells after HIV-1 infection. J Exp Med. 2010;207(13):2869–81.

17. Laennec RTH. A treatise on the diseases of the chest. First Amer. Philadelphia: William Brown Printer, Philadelphia; 1823.

18. Ford CB, Lin PL, Chase MR, Shah RR, Iartchouk O, Galagan J, et al. Use of whole genome sequencing to estimate the mutation rate of *Mycobacterium tuberculosis* during latent infection. Nat Genet. 2011;43(5):482–8.

19. Lin PL, Ford CB, Coleman MT, Myers AJ, Gawande R, Ioerger T, et al. Sterilization of granulomas is common in active and latent tuberculosis despite within-host variability in bacterial killing. Nat Med. 2014;20(1):75–9.

20. Subbian S, Tsenova L, Kim MJ, Wainwright HC, Visser A, Bandyopadhyay N, et al. Lesion-specific immune response in granulomas of patients with pulmonary tuberculosis: A pilot study. PLoS One. 2015;10(7):1–21.

21. Lenaerts A, Barry CE, Dartois V. Heterogeneity in tuberculosis pathology, microenvironments and therapeutic responses. Immunol Rev. 2015;264(1):288–307.

22. Abengozar-Muela M, Esparza M, Garcia-Ros D, Vásquez C, Echeveste J, Idoate M, et al. Diverse immune environments in human lung tuberculosis granulomas assessed by quantitative multiplexed immunofluorescence. Mod Pathol. 2020;33(12):2507–19.

23. Cronan MR. In the Thick of It: Formation of the Tuberculous Granuloma and Its Effects on Host and Therapeutic Responses. Front Immunol. 2022;13.

24. Irwin SM, Driver E, Lyon E, Schrupp C, Ryan G, Gonzalez-Juarrero M, et al. Presence of multiple lesion types with vastly different microenvironments in C3HeB/FeJ mice following aerosol infection with *Mycobacterium tuberculosis*. Dis Model Mech. 2015;8(6):591–602.

25. Kramnik I, Beamer G. Mouse models of human TB pathology: roles in the analysis of necrosis and the development of host-directed therapies. Semin Immunopathol. 2016;38(2):221–37.

26. Gonzalez-Juarrero M, Turner OC, Turner J, Marietta P, Brooks J V., Orme IM. Temporal and spatial arrangement of lymphocytes within lung granulomas induced by aerosol infection with *Mycobacterium tuberculosis*. Infect Immun. 2001;69(3):1722–8.

27. Gonzalez-Juarrero M, Shim TS, Kipnis A, Junqueira-Kipnis AP, Orme IM. Dynamics of Macrophage Cell Populations During Murine Pulmonary Tuberculosis. J Immunol. 2003;171(6):3128–35.

28. Junqueira-Kipnis AP, Turner J, Gonzalez-Juarrero M, Turner OC, Orme IM.

Stable T-Cell Population Expressing an Effector Cell Surface Phenotype in the Lungs of Mice Chronically Infected with *Mycobacterium tuberculosis*. Infect Immun. 2004;72(1):570–5.

29. Ordway D, Henao-tamayo M, Orme IM, Gonzalez-juarrero M, Ordway D, Henao-tamayo M, et al. Foamy macrophages within lung granulomas of mice infected with *Mycobacterium tuberculosis* express molecules characteristic of dendritic cells and antiapoptotic markers of the TNF receptor-associated factor family. J Immunol. 2005;175(6):3873–81.

30. Ordway D, Harton M, Henao-tamayo M, Montoya R, Orme IM, Gonzalez-juarrero M. Enhanced macrophage activity in granulomatous lesions of immune mice challenged with *Mycobacterium tuberculosis*. J Immunol. 2006;176(8):4931.

31. Ali MZ, Dutt TS, Macneill A, Walz A. A Modified BPaL Regimen for Tuberculosis Treatment replaces Linezolid with Inhaled Spectinamides. bioRxiv [Preprint]. 2023;

32. Singh AK, Gupta UD. Animal models of tuberculosis: Lesson learnt. Indian J Med Res [Internet]. 2018;147:456–63. Available from: http://www.ncbi.nlm.nih.gov/pubmed/23144490

33. Gonzalez-Juarrero M, Lukka PB, Wagh S, Walz A, Arab J, Pearce C, et al. Preclinical Evaluation of Inhalational Spectinamide-1599 Therapy against Tuberculosis. ACS Infect Dis. 2021;7(10):2850–63.

34. De Groote MA, Gilliland JC, Wells CL, Brooks EJ, Woolhiser LK, Gruppo V, et al. Comparative studies evaluating mouse models used for efficacy testing of experimental drugs against *Mycobacterium tuberculosis*. Antimicrob Agents Chemother. 2011;55(3):1237–47.

35. Robertson GT, Ramey ME, Massoudi LM, Carter CL, Zimmerman M, Kaya F, et al. Comparative Analysis of Pharmacodynamics in the C3HeB/FeJ Mouse Tuberculosis Model for DprE1 Inhibitors TBA-7371, PBTZ169, and OPC-167832. Antimicrob Agents Chemother. 2021;65(11):e00583-21.

36. Driver ER, Ryan GJ, Hoff DR, Irwin SM, Basaraba RJ, Kramnik I, et al. Evaluation of a mouse model of necrotic granuloma formation using C3HeB/FeJ mice for testing of drugs against *Mycobacterium tuberculosis*. Antimicrob Agents Chemother. 2012;56(6):3181–95.

37. Lanoix JP, Lenaerts AJ, Nuermberger EL. Heterogeneous disease progression and treatment response in a C3HeB/FeJ mouse model of tuberculosis. Dis Model Mech. 2015;8(6):603–10.

38. Harper J, Skerry C, Davis SL, Tasneen R, Weir M, Kramnik I, et al. Mouse model of necrotic tuberculosis granulomas develops hypoxic lesions. J Infect Dis. 2012;205(4):595–602.

39. Irwin SM, Gruppo V, Brooks E, Gilliland J, Scherman M, Reichlen MJ, et al. Limited activity of clofazimine as a single drug in a mouse model of tuberculosis

exhibiting caseous necrotic granulomas. Antimicrob Agents Chemother. 2014;58(7):4026–34.

40. Aly S, Wagner K, Keller C, Malm S, Malzan A, Brandau S, et al. Oxygen status of lung granulomas in *Mycobacterium tuberculosis*-infected mice. J Pathol. 2006;210:298–305.

41. Tsai MC, Chakravarty S, Zhu G, Xu J, Tanaka K, Koch C, et al. Characterization of the tuberculous granuloma in murine and human lungs: Cellular composition and relative tissue oxygen tension. Cell Microbiol. 2006;8(2):218–32.

42. Gideon HP, Phuah JY, Myers AJ, Bryson BD, Rodgers MA, Coleman MT, et al. Variability in Tuberculosis Granuloma T Cell Responses Exists, but a Balance of Pro- and Anti-inflammatory Cytokines Is Associated with Sterilization. PLoS Pathog. 2015;11(1):1–28.

43. Lin PL, Rodgers M, Smith L, Bigbee M, Myers A, Bigbee C, et al. Quantitative comparison of active and latent tuberculosis in the cynomolgus macaque model. Infect Immun. 2009;77(10):4631–42.

44. Upadhyay S, Mittal E, Philips JA. Tuberculosis and the art of macrophage manipulation. Pathog Dis. 2018;76(4):1–12.

45. Scott-Browne JP, Shafiani S, Tucker-Heard G, Ishida-Tsubota K, Fontenot JD, Rudensky AY, et al. Expansion and function of Foxp3-expressing T regulatory cells during tuberculosis. J Exp Med. 2007;204(9):2159–69.

46. Dutt TS, Karger BR, Fox A, Youssef N, Dadhwal R, Ali MZ, et al. Mucosal exposure to non-tuberculous mycobacteria elicits B cell-mediated immunity against pulmonary tuberculosis. Cell Rep [Internet]. 2022;41(11):111783. Available from: https://doi.org/10.1016/j.celrep.2022.111783

CHAPTER 4

Conclusion

Discussion

Tuberculosis (TB) is a disease that affects people of all ages. Historically, it has been responsible for more morbidity and mortality than any other human pathogen and still today it stands as a leading disease by a single infectious agent. The incidence of TB in developed nations has been falling steadily since the last decade due to modern sanitation practices and chemotherapeutic treatments. However, this decline is inadequate to combat the current global burden of TB. The coinfection due to exquisite synergism of human immunodeficiency virus (HIV) with the increased susceptibility to Mtb and revitalization of latent TB (1) and malnutrition (2) are the challenges in increased burden of this disease especially in undeveloped nations. In addition, multidrug resistance is one of the enormous global crises today and is one of the limiting factors in controlling this disease (3). After the early Golden Era of TB drug discovery from mid-1940s through mid-1960s the standard TB chemotherapy regimen transformed TB from a potentially deadly disease to a curable disease within a course of up to 9 months. However, soon after this achievement the emergence of drug-resistant strains of Mtb were documented (4–6). Although the stability of mycobacterial genome making spontaneous mutations that induce drug resistance is a rare event. These mutations and the persistent nature of Mtb leading to the necessity of long and complex nature of TB treatment comprising of several oral medications and injectables result in a high healthcare cost and, ultimately, poor outcomes of the failed treatment

regimens collectively rendered patient noncompliance – a major cause of multidrug resistant (MDR) and extensively drug resistant (XDR) TB in undeveloped countries.

TB involves a complex interaction between host immune defense and bacterial virulence factors however *Mycobacterium tuberculosis* (Mtb, the causative agent of TB) has evolved special mechanisms to hijack the host defense systems through which it undergoes active replication. This host-bacterial interface activates the recruitment of immune cells and in advanced disease state these cells are surrounded by a fibrotic tissue layer and ultimately transformed into a lesion structure called granuloma, a hallmark pathological structure of TB. Human TB manifests a diverse and dynamic spectrum of TB lesions characterized by lesion heterogeneity, ranging from inflammatory up to destructive necrotic lesions with cavity which is mostly acellular and may contain caseum. Even though TB is one of the oldest diseases in the world with decades of research, the role of granuloma is not clear, and its role could either be host-protective or otherwise based on its distinctly diverse immune microenvironments. Owing to the scarcity of human samples, animal modeling is the best and essential method for research purposes to recapitulate and understand the complexities in human TB lesions.

Currently the cure rate of MDR- and XDR-TB has dropped significantly to below 50% while the treatment duration has tremendously increased up to 2 years or greater which lead to restricted treatment options for such patients. After the research of last more than five decades since the discovery of last anti-TB drug, a novel all-three-oral 6-month regimen was approved by the United States Food and Drug Administration in 2019 consisting of bedaquiline (B), pretomanid (Pa) and linezolid (L) referred to as the

BPaL or Nix-TB regimen based on the results obtained from the Nix-TB trial. This trial was conducted in South Africa on patients with XDR-TB as well as treatment-intolerant or non-responsive MDR-TB, including HIV positive patients with a CD4 count of 50 or higher. The outcome of this trial was incredible (about 90%) though many patients observed high rate of toxicities associated adverse effects (AEs). Among the BPaL regimen, long-term administration of linezolid acted as a blatant agent for inducing bone marrow myelosuppression (48%), peripheral neuropathy, optic neuritis (81%) and anemia (37%) in patients. The incidence of anemia is reported as high as up to 62.5% in MDR- and XDR-TB patients and the onset of this effect can occur 2 weeks to 2 months post linezolid administration. The ZeNix trial based on several studies (7–10) adjusted the BPaL regimen to a linezolid dose of 600mg that was half of what had been used in the Nix-TB trail. This trial showed remarkable favorable outcomes in 84-91% patients in shorter duration of treatment with fewer AEs than those observed in the Nix-TB trial. Apart from AEs, several studies have also raised awareness of high doses of linezolid leading to development of linezolid resistant Mtb strain. In this scenario, researchers are exploring shorter regimens with no or least AEs with the aim to encourage patient adherence and prevent recrudescence or the evolution of further drug resistance.

In this thesis we attempted to overcome linezolid-associated AEs and proposed to replace linezolid in the BPaL regimen with spectinamide 1599 (S), another protein synthesis inhibitor, as a BPaS regimen. Spectinamide 1599 is one of the series of semisynthetic analogues of spectinomycin antibiotic which has a very high safety margin with respect to ototoxicity and nephrotoxicity. Linezolid-induced toxicity has been

observed due to its binding with the host mitochondrial ribosomes while spectinamides do not show such binding. Also, the spectinamides evade drug efflux by Rv1258c transporters present on the surface of Mtb. These both properties equipped spectinamides with potent anti-tubercular activity and reduced potential AEs and due to their ability to be active under hypoxic conditions and with no cross-resistance with other anti-TB drugs, they have shown tremendous outcomes against MDR- and XDR-Mtb strains when administered as aerosolized liquid formulation. Therefore, we hypothesize that inhalational administration of spectinamide 1599 if combined with BPa (BPaS regimen) has higher or similar efficacy than the BPaL regimen with no AEs observed during administration of the BPaL regimen. To prove this hypothesis, we had three aims, and their details are given below.

In aim 1 (Chapter 2), two preclinical murine TB models such as C3HeB/FeJ and BALB/c were chronically infected with a low dose of Mtb Erdman strain and treated with monotherapy of linezolid or spectinamide 1599 and combination of BPa, BPaL or BPaS regimens for 4 weeks. The analysis of bacterial burdens between treatment and untreated groups was done to determine the comparative efficacy of drug treatments. The BALB/c TB model represents a long term Mtb chronic infection that develops multiple and homogenous lung granulomatous lesions formed by cellular aggregations that restrain the bacilli within the intracellular compartments. The C3HeB/FeJ TB model, on the other hand, also develops into a chronic infection but their lungs exhibit a heterogenous spectrum of granulomatous lesions including cellular lesions (as in the BALB/c TB model) in addition to caseous necrotic lesions surrounded by a fibrotic rim. The caseum of these necrotic lesions creates a hypoxic environment and contains abundant extracellular bacilli

in a similar fashion to necrotic lesions found in some human TB patients. These lesions having fibrotic, necrotic, and hypoxic environment create barriers to drug penetration and challenge multidrug therapeutic outcomes. As no single animal model reflects the wide spectrum of human TB pathology, therefore, to better understand the broader implications of drug efficacy and drug associated AEs in scenarios without (BALB/c) and with (C3HeB/FeJ) necrotic lesions both murine TB models were used. The Aim 1 results, combined from 3 independent studies done in C3HeB/FeJ model while 2 studies in BALB/c, are in accordance with the lesions spectrum of both TB models where more robust reduction in lung and spleen bacterial burden was observed in the absence (BALB/c) versus the presence (C3HeB/FeJ) of necrotic lesions. Monotherapy of linezolid or spectinamide 1599 showed limited or no efficacy, the BPa, BPaL or BPaS combination regimens significantly reduced lung bacterial burden up to 4 $\log_{10}$ CFU and these results are in line with the previous findings (11,12). Though the BPa regimen showed similar efficacy as to other combination regimes (BPaL and BPaS), however, to avoid development of drug resistance in Mtb a three-drug regimen is preferred. Therefore, we conclude that the potent antimicrobial effect of the BPaL and BPaS regimens promote similar bactericidal effects by improving the pathological outcomes in chronic TB murine models lacking or featuring advanced pulmonary pathology.

Aim 2 (Chapter 2) focuses on the investigation of major AEs reported in the Nix-TB trial using the BALB/c and C3HeB/FeJ TB models (used in Aim 1). For this purpose, five approaches were employed which include 1) the live body weight 2) lung lesion burden 3) complete blood count (CBC) profile 4) bone marrow histopathology 5) evaluation of immune cells and the cytokines and chemokines at local and systemic

levels. The extent of weight loss is an important preclinical and clinical parameter in TB patients because it determines severity of the disease progression. Compared to monotherapy of linezolid or spectinamide 1599, linezolid-containing (BPaL) regimen significantly decreased the live body weight in both murine TB models and results are supported by the previous studies (13,14) finding an inverse relationship between body weight and linezolid exposure in human patients. Moreover, quantitative histopathological assessment revealed an improvement in lung lesion burden of BPaL and BPaS treated mice compared to untreated animals. Though both regimes overall decreased lung lesion burden compared to untreated control at 4-weeks, existence of lung lesions emphasizes continuation of the treatment for longer duration. To the best of our knowledge, no comprehensive study on CBC profile of both murine TB models has been done before. Results of the present study indicated that out of 20 peripheral blood parameters, monotherapy of linezolid at 4-weeks significantly increased red blood cell distribution width-standard deviation (RDWs) and decreased mean corpuscular hemoglobin concentration (MCHC). In addition, combination of BPaL at 4-weeks showed a significant drop in hemoglobin (HGB) and mean platelet count (MPV) and presented similar results for RDWs and MCHC as in monotherapy of linezolid. All these changes in BPaL but not in BPa and BPaS treatment groups suggest development of mild anemia though RBC counts remained within reference intervals for all mice during 4-week time course. Myeloid to erythroid cell ratio (M:E) in the examination of bone marrow histology provides information about the relative proportions of myeloid lineage (granulocytes, monocytes, and their precursors) to erythroid lineage. The BPa and BPaL regimens significantly altered M:E in C3HeB/FeJ TB model by suppressing myeloid and inducing erythroid

lineages. Importantly, the BPaS treatment did not show any difference in the content of M:E when compared to UnRx control. Based on these results, we conclude that spectinamide 1599 combined with BPa recovers the altered M:E ratio seen in other treatment groups. Furthermore, the comparative analysis of 26 cytokines and chemokines of bone marrow supernatants from BPaL and BPaS treatment groups revealed significantly higher concentrations of most proinflammatory cytokines and chemokines including IL-1β, IL-12p70 and TNF-α in BPaL treated animals than BPaS. These results by BPaL regimen especially for IL-1β could be the attributable cause of the AEs. Additionally, the analysis of bone marrow revealed a significant reduction in population of immune cell subsets during treatments where increase in T lymphocytes (CD45+CD3+) and CD19+ B lymphocytes (CD45+CD3-CD19+B220-) suggesting changes associated with the adaptive immunity. Spatial mapping of immune cells in the lungs also revealed an increase in lymphocytes; T (CD4, CD8 and Foxp3) and B (B220) cells in both treatment groups. Collectively, a low lung and spleen bacterial burden correlates with reduced number of neutrophil associated marker (Ly6G) cells while a gradual increase and changes in location of CD8, CD4, Foxp3 and B220 positive cells in the lungs. These results suggest that the BPaL and BPaS regimens promote the immune system's equilibrium by reducing inflammation and enhancing the adaptive immune responses. The immune phenotype comparative analysis between both regimens did not reveal significant difference in changes of immune cell populations except for a higher count of F4/80 marker in BPaS treated animals than in BPaL. Based on the results from five parameters analyzed, we conclude that the BPaS regimen is safer than the BPaL in chronic murine TB models.

Aim 3 (Chapter 3) highlights the development of 7-color panels for multiplex fluorescence immunohistochemistry (mfIHC) and quantification of immune responses post infection over the time using inForm Tissue Finder software. The untreated lung samples from both murine TB models (used in Aim 1) were processed for histology and their 5 µm sections were stained with 3 different 7-color panels using Opal Tyramide Signal Amplification technique. The mfIHC slides were scanned for whole slide imaging using automated multispectral PhenoImager HT and image analysis was done using Phenochart and inForm Tissue Finder software. While the analysis of lung samples from C3HeB/FeJ mice is in progress, the results obtained from Mtb infected BALB/c mice lungs showed dynamic temporal changes for different immune phenotypes and in their spatial distribution. Although granulomas may appear similar under a microscope their immune cell composition is quite complex, and the adaptive immune response is playing a significant role in shaping this complexity. For example, T (CD4, CD8 and Foxp3 T) cells, Ly6G stained neutrophils, B220 B cells and F4/80 macrophages were present in a mature BALB/c granuloma and with time post infection their recruitment within granulomas increased uniformly compared to parenchymal tissue where IFNγ and IL-10 secreting cells were abundant. B220 B cells showed increased but heterogeneous distribution among the advancing granulomas in the form of clusters. The spatial analysis showed an increased median distance for Ly6G neutrophils when measured from CD4 and CD8 cells, whereas this distance to B220 B cells was decreased. The spatial and temporal data in addition to the mere cell counts helps uncover the interactions and relationships of different immune cells to have deeper insights into the immunity process and we are learning more about these interactions.

References

1. Komrower D, Thillai *M. tuberculosis* and HIV co-infection. Clin Tuberc A Pract Handb. 2015;157–70.
2. Ockenga J, Fuhse K, Chatterjee S, Malykh R, Rippin H, Pirlich M, et al. Tuberculosis and malnutrition: The European perspective. Clin Nutr. 2023;42(4):486–92.
3. Wright A, Zignol M, Van Deun A, Falzon D, Gerdes SR, Feldman K, et al. Epidemiology of antituberculosis drug resistance 2002-07: an updated analysis of the Global Project on Anti-Tuberculosis Drug Resistance Surveillance. Lancet. 2009;373(9678):1861–73.
4. Crofton J, Mitchison D. Streptomycin resistance in tuberculosis. Br Med J. 1948;1009–15.
5. Canetti G. Present aspects of bacterial resistance in tuberculosis. Vol. 92, American Review of Respiratory Disease. 1965. p. 687–703.
6. Conway H. Prevelance of drug resistance in previously untreated patients.pdf. Am Rev Respir Dis. 1964;89(3):327–32.
7. Lund FE, Randall TD. Effector and regulatory B cells: modulators of CD4+ T cell immunity. Nat Rev Immunol. 2010;10(4):236–47.
8. Imperial MZ, Nedelman JR, Conradie F, Savic RM. Proposed Linezolid Dosing Strategies to Minimize Adverse Events for Treatment of Extensively Drug-Resistant Tuberculosis. Clin Infect Dis. 2022;74(10):1736–47.
9. Mase A, Lowenthal P, True L, Henry L, Barry P, Flood J. Low-Dose Linezolid for Treatment of Patients With Multidrug-Resistant Tuberculosis. Open Forum Infect Dis. 2022;9(12):1–10.
10. Bigelow KM, Tasneen R, Chang YS, Dooley KE, Nuermberger EL. Preserved efficacy and reduced toxicity with intermittent linezolid dosing in combination with bedaquiline and pretomanid in a murine tuberculosis model. Antimicrob Agents Chemother. 2020;64(10).
11. Williams K, Minkowski A, Amoabeng O, Peloquin CA, Taylor D, Andries K, et al. Sterilizing activities of novel combinations lacking first- and second-line drugs in a murine model of tuberculosis. Antimicrob Agents Chemother. 2012;56(6):3114–20.
12. Nuermberger EL, Martínez-Martínez MS, Sanz O, Urones B, Esquivias J, Soni H, et al. GSK2556286 Is a Novel Antitubercular Drug Candidate Effective In Vivo with the Potential To Shorten Tuberculosis Treatment. Antimicrob Agents Chemother. 2022;66(6).
13. Gonzalez-Juarrero M, Lukka PB, Wagh S, Walz A, Arab J, Pearce C, et al. Preclinical Evaluation of Inhalational Spectinamide-1599 Therapy against

Tuberculosis. ACS Infect Dis. 2021;7(10):2850–63.

14. Wasserman S, Denti P, Brust JCM, Abdelwahab M, Hlungulu S, Wiesner L, et al. Linezolid pharmacokinetics in South African patients with drug-resistant tuberculosis and a high prevalence of HIV coinfection. Antimicrob Agents Chemother. 2019;63(3).